KINETIC DESCRIPTION OF THE ENERGETIC PARTICLES AND WAVES IN FUSION PLASMAS INTERACTION BETWEEN

David Zarzoso

Kinetic description of the interaction between energetic particles and waves in fusion plasmas

by

David Zarzoso

A dissertation submitted for the degree of

Doctor of Philosophy

in

Plasma Physics

Ecole Doctorale de l'Ecole Polytechnique

Dr. Yanick Sarazin	.....	PhD Advisor
Dr. Rémi Dumont	.....	CEA Advisor
Prof. Peter Beyer	.....	Referee
Dr. Sergei Sharapov	.....	Referee
Dr. Carlos Hidalgo	.....	Senior Researcher at CIEMAT
Prof. Jean-Marcel Rax	.....	Chair of PhD Committee

October 2009 - September 2012

Abstract

Controlling the turbulence in magnetic fusion devices is essential for the steady-state production of energy. Also, nuclear reactions and external heating generate energetic particles. When energetic particles and turbulence coexist, their mutual interaction has to be taken into account. The effect of turbulence on energetic particle transport has already been analysed, with the conclusion that the energetic particle transport is weakly affected by turbulence. On the contrary, the impact of energetic particles on turbulence has been so far little explored and constitutes the main focus of this thesis. We investigate two critical issues: (1) the properties of one of the generation mechanisms of energetic particles and (2) the impact of energetic particles on turbulence.

The generation of energetic particles is studied in ICRH discharges. We quantify the energetic particle kinetic effects on the discharge properties. For this purpose, we introduce the velocity anisotropy, which is essential to model ICRH scenarios, characterized by perpendicular heating rather than parallel. This is done by means of a full-wave 3D solver called EVE coupled to a module called AQL. This module solves the Fokker-Planck equation in both parallel and perpendicular directions in velocity space. The coupling EVE$-$AQL provides the self-consistent response of the plasma in two ITER scenarios: second harmonic DT heating and first harmonic DT(^{3}He) heating. The importance of the anisotropy is evidenced by the formation of a long tail in the distribution function for high perpendicular velocities, modifying the properties of the discharge.

The impact of energetic particles on electrostatic turbulence is evidenced by means of the full-f 5D gyrokinetic GYSELA code. This is done in two steps. First, the excitation of a particular class of energetic modes in the acoustic range of frequency (EGAMs) is demonstrated. These modes are particularly attractive in the framework of turbulence regulation, since they lead to an oscillatory radial electric shear which can potentially saturate the turbulence. We predict a theoretical linear threshold for the excitation of EGAMs that is verified numerically in neoclassical GYSELA simulations. In addition, the structure of the distribution function is found to impact the excitation and saturation of the modes. Second, EGAMs are excited for the first time in global, full-f and flux-driven turbulent simulations. For this purpose, a heating source is implemented in GYSELA. The effects of this source on turbulence are predicted analytically and corroborated numerically, in particular the possibility of turbulence suppression. In the simulations presented in this thesis, EGAMs are found to interact with turbulence in an extremely complex way. In particular, it is found that a control of turbulence with externally driven oscillating sheared flows is not straightforward. We focus our analysis on two observed phenomena. First, turbulence propagates radially in the presence of EGAMs. Second, the turbulent transport is modulated at the EGAM frequency.

Résumé

Le contrôle de la turbulence dans les tokamaks est essentiel dans le cadre de la production d'énergie en régime stationnaire. Par ailleurs, les réactions nucléaires et les systèmes de chauffage produisent des particules énergétiques. Lorsque turbulence et particules énergétiques coexistent, leur interaction doit être prise en compte. L'effet de la turbulence sur le transport des particules énergétiques a déjà été analysé, avec la conclusion que les particules énergétiques sont peu sensibles à la turbulence. Par contre, l'effet des particules énergétiques sur la turbulence a été peu étudié jusqu'à présent. Ceci constitue le cadre de ce manuscrit. Nous analysons deux problématiques: (1) la génération de particules énergétiques et (2) l'impact de ces particules sur la turbulence.

La génération de particules énergétiques est étudiée dans le cadre des décharges ICRH. Nous quantifions l'effet des particules énergétiques sur les propriétés des décharges et introduisons aussi la possibilité d'une anisotropie dans l'espace de vitesses, essentielle pour la modélisation de scénarios ICRH, caractérisés par un chauffage principalement perpendiculaire. Ceci est fait à travers le couplage d'un code *full-wave* 3D appelé EVE et d'un module appelé AQL. Ce module résout léquation de Fokker-Planck en vitesse parallèle et perpendiculaire. Le couplage fournit la réponse du plasmas dans deux scénarios ITER: second harmonique DT et premier harmonique DT(^{3}He). L'importance de l'anisotropie est mise en évidence par la formation d'une queue dans la fonction de distribution à des vitesses perpendiculaires élévées, ce qui modifie les propriétés de la décharge.

L'effet des particules énergétiques sur la turbulence est mis en évidence à travers le code *full-f* global et gyrocinétique GYSELA. Ceci est fait en deux étapes. Dans un premier temps, nous démontrons l'excitation d'une classe de mode de particules énergétiques dans le domaine de la fréquence acoustique (EGAMs). Ces modes se traduisent par l'excitation d'un cisaillement oscillant du champ électrique radial, qui pourrait potentiellement contribuer à la stabilisation de la turbulence. Nous donnons une prédiction linéaire pour le seuil d'excitation, qui est vérifiée numériquement dans des simulations néoclassiques dans GYSELA. Par ailleurs, nous montrons que la structure de la fonction de distribution dans l'espace de vitesse perpendiculaire a un impact important sur l'excitation et saturation des modes. Dans un second temps, les EGAMs sont excités pour la première fois en la présence de turbulence avec un code global *full-f* dans des simulations à forçage par le flux. Pour ce faire, nous implémentons une source de chauffage dans GYSELA, dont les effets sur la turbulence sont étudiés analytiquement et vérifiés dans les simulations. En particulier, nous trouvons que la source peut conduire à une réduction de la turbulence. Dans les simulations que nous présentons ici, les EGAMs et la turbulence interagissent d'une manière extrêmement complexe. Notamment, nous montrons que le contrôle de la turbulence à travers un cisaillement oscillant excité par des particules énergétiques n'est pas immédiat. Nous détaillons deux mécanismes observés. D'une part, la turbulence semblerait se propager en la présence d'EGAMs. D'autre part, le transport turbulent est modulé à la fréquence EGAM.

Foreword

This manuscript does not give any introduction to nuclear physics or nuclear fusion reactions and implies that the reader is already familiar with the concept of *tokamak*. It does not cover all the subjects that attracted my interest during the last three years. In particular, the experimental analysis of the ELM size scaling in JET hybrid discharges is not included.

Throughout this thesis, I was seized by some mathematical and physical reflections, mainly those related to the nature of the distribution function, the interpretation of the Landau damping, the effects of a source term in gyrokinetics and some other phenomena that I have observed but for which I have not provided a complete explanation yet. I have considered instructive to include all these reflections and observations so that they do not fall into obscurity, so that they remain written down on the same document as my main research: my PhD manuscript.

Acknoledgments / Remerciements/Agradecimientos

Arrivé à la fin de cette thèse, je ne peux que regarder les trois années (voire quatre si l'on compte mes stages) qui se sont écoulées avec émotion, fierté et le désir de travailler à nouveau un jour avec ces collègues et amis qui m'ont tellement aidé, encouragé, enseigné et soutenu dans absolument tous les moments de cette période de ma vie. C'est sans doute pour cela que, en regardant ces dernières années, je ne peux que remercier tous ceux et celles qui ont été là pour moi.

Tout d'abord, je tiens à remercier Alain Bécoulet de m'avoir acueilli au sein de l'IRFM et à Xavier Litaudon de m'avoir *managé* (si ce mot existe en français) pendant ces années dans son service, le SCCP. Merci à Tuong d'avoir été présent: même si au début son bureau n'était pas dans le même bâtiment, on le croisait fort souvent à la pause café du 1er étage du bâtiment 513, ce qui nous rejouisait sincèrement. Leurs soutiens et conseils lors des discussions dans les couloirs, bureaux ou entre les bâtiments m'ont toujours aidé. Merci à eux.

Merci à mes deux rapporteurs, Sergei Sharapov et Peter Beyer, d'avoir accepté cette tâche, d'avoir lu le manuscrit en profondeur. Merci pour leurs avis, leurs conseils et leurs discussions. Merci à Carlos Hidalgo d'avoir emmené avec lui une petite partie de mon cher pays à mon jury de thèse. Je tiens à remercier aussi Jean-Marcel Rax, qui a été présent dans ma formation en fusion depuis ma 3ème année à l'X. Merci d'avoir accepté d'être le président de mon jury.

Un grand merci à Yanick, qui a commencé à m'apprendre ce qu'est la recherche un jour du mois d'avril de la lointaine année 2008. Merci à lui, qui m'a si bien guidé sur cette route de la physique des plasmas, de la fusion magnétique, de la science, mais aussi ailleurs. C'est grâce à lui que j'ai décidé de faire une thèse à l'IRFM et je lui en remercie, car cela a été une expérience unique... à faire, comme dirait un de mes professeurs à l'X (et je crois qu'il se sent visé), au moins une fois dans sa vie. Merci à Rémi, avec qui j'ai eu aussi la chance de travailler, avec qui j'ai pu m'initier à l'art du chauffage et des particules énergétiques. Merci pour son soutien permanent, surtout dans ces moments de faiblesse scientifique qu'il m'a aidé à surmonter. Merci pour sa patience lorsqu'il m'expliquait les chemins inextricables d'EVE (et de l'ancien QDQL!). Merci de croire en moi. Ce fut un véritable plaisir de travailler avec ces deux grands chercheurs.

Merci aux permanents de l'équipe GYSELA, pour leur amitié, sympathie et disponibilité. Merci à Xavier Garbet, pour ces longues discussions autour de la physique (notamment de la physique des (E)GAMs), pour sa sagesse et son expérience, mais aussi pour son lexique irréprochable qui, loin d'être superfétatoire, était fort instructif (il comprendra). Merci pour ses cours de FLE avancé et ses mots... que dis-je *mots*, phrases! du jour... mmm voire du mois!! (il comprendra aussi) et malgré tout le mal que l'on puisse dire

des blagues de Xavier, il faut quand-même (hélas... oui) reconnaître qu'elles étaient parfois un peu drôles et qu'elles rendaient l'ambiance un peu plus détendue aux moments les plus scientifiquement chargés. Merci à lui. Merci aussi à Philippe Ghendrih, pour nos discussions parfois un peu philosophiques, parfois un peu existentielles sur l'avenir d'un X dans la recherche, merci de m'avoir appris à toujours me mettre en question. Virginie... que puis-je dire pour la remercier? Je crois que je devrais la remercier au moins une fois par *bug* introduit dans le code, mais soyons honnêtes, la recherche avance grâce aux erreurs... et aux petites soirées GYSELA entre amis! ;-) Chantal, *c'est encore moi*, mais cette fois-ci je viens uniquement pour dire merci, merci d'avoir été là et de m'avoir aidé tout le long de ce chemin numérique. Merci aussi à Guillaume Latu pour son aide précieuse dans le développement de GYSELA.

Merci à mes amis thésards du 513 (par ordre de bureau, étage et bâtiment): Farah, Maxime, Stanislas, Grégoire, Hugo, Jérémie, François-Xavier, Thomas, Antoine (Strugarek), Dmytro, Antoine (Merle), Timothée, François, Didier, Marc (Coatanea-Gouachet), Gaël... et à ceux qui étaient un peu plus loin: Mélanie, Rémi (Dachicourt), Pierre, Stéphanie (Panayotis). Merci aux postdocs et nouveaux embauchés Shimpei, Guilhem, Olivier, Patrick et Eric, avec qui j'ai eu l'occasion de partager des moments de travail, mais aussi de détente. Merci aussi à ces personnes avec qui j'avais l'habitude de discuter dans les couloirs, à la pause café, à la cantine ou même en conférence: Roland, Emmanuel, Patrick (Maget), Marina, Gloria, Maurizio, Gerardo, Jerónimo, Yves, Joan, Laurent, Marc, Frédéric, Clarisse, Christel, Pascale (Hennequin), Pascale (Monier-Garbet), Laure, Dominique. Merci à Valérie et Stéphanie (Beaufils), pour m'avoir si bien aidé avec ces lourdes (mais fort nécéssaires) démarches admisnistratives, mais surtout pour leurs sourires et humours inépuisables. Et maintenant que je parle de démarches administratives... ce paragraphe ne serait pas complet sans remercier mon amie Christine (elle comprendra pourquoi je dis cela), la première personne que j'ai vue en arrivant au bâtiment 513 le premier jour de mon premier stage en fusion. Elle m'a soutenu pendant qu'elle était au CEA, mais aussi après.

Enfin, merci à ceux qui ont toujours été un soutien proche, même dans la distance... gracias a mis padres, que me han animado siempre a hacer aquello en lo que yo creía, aquello que me gustaba. Gracias a mis hermanos y a mi hermana, que me han apoyado en todo y han creído siempre en mí. Por último, gracias a Julie, que tanto me ha ayudado durante esta tesis, que tanto me ha animado mostrándome la vida de otra manera y que tanto ha tenido que soportar hasta ver estas páginas publicadas. Sin ellos, no habría podido terminar este manuscrito.

Une fois j'ai lu un livre où l'on affirmait que derrière chaque livre il y a tout un univers et toute une vie à découvrir. Maintenant que j'ai écrit ce manuscrit, je crois avoir compris pourquoi...

Contents

List of Figures

Chapter 1

Introduction: a brief insight into energetic particles, instabilities and mathematical framework of this thesis

> La pensée n'est qu'un éclair au milieu de la nuit. Mais c'est cet éclair qui est tout.
>
> Henri Poincaré (1854-1912)

Contents

Understanding the complex behaviour of a magnetized plasma to achieve the steady-state production of energy by means of nuclear fusion is a hard task. Therefore, this introduction aims at giving a brief description of the fundamentals that will be used throughout this manuscript to model the behaviour of magnetized plasmas. In section 1.1 the magnetic field inside a tokamak as well as the mathematical model and tools are presented. Some comments on the particle orbits in a tokamak are given in section 1.2. The motivation of the present research is explained by introducing in section 1.3 the concept of energetic particles and the main instabilities that are considered in this thesis. Finally, in section 1.4 the outline of the manuscript is presented.

1.1 Mathematical description of a fusion plasma

Within this section the basic equations to describe the behaviour of a magnetized plasma are given as well as the hypothesis of simplification. Many of the developments written herein can be found in classical textbooks for plasma physics and tokamaks such as [1, 2, 3, 4, 5] and these references will not be explicitly cited in the remainder of this introduction, except in special cases.

1.1.1 Magnetic field and geometry in tokamaks

The equilibrium magnetic field inside a tokamak can be expressed, under the assumption of axisymmetry, as

$$\mathbf{B}_{\text{eq}} = \boldsymbol{\nabla}\psi \times \boldsymbol{\nabla}\varphi + I\left(\psi\right)\boldsymbol{\nabla}\varphi \tag{1.1}$$

where φ is the toroidal angle, ψ is the poloidal magnetic flux and I is the current function $I = R^2\mathbf{B}_{\text{eq}} \cdot \boldsymbol{\nabla}\varphi$. In practice, this magnetic field lines have a helix form and are rolled up on the so-called magnetic surfaces, labeled by the flux ψ, mathematically expressed by

$$\psi = \frac{1}{2\pi}\iint \mathrm{d}\mathbf{S}_{\Sigma_\theta} \cdot \mathbf{B}_{\text{eq}} \tag{1.2}$$

with $\mathrm{d}\mathbf{S}_{\Sigma_\theta}$ the surface element, as illustrated in figure 1.1, where we give an schematic view of a cross-section of a tokamak. The magnetic flux surface ($\psi = \text{cst}$) is represented by a dashed circle and the vector $\boldsymbol{\nabla}\psi$ is orthogonal to this surface. In the same figure, we represent the coordinate Z and the major radius R. Note that the image given in this figure corresponds to a tokamak with circular poloidal cross section and concentric flux surfaces. However, the expressions 1.1 and 1.2 are valid for any geometry, in particular for situations where the magnetic flux surfaces are elongated and not concentric.

A measure of the helicity of the magnetic field is given by the *safety factor* q defined as

$$q\left(\psi\right) = \frac{\mathbf{B}_{\text{eq}} \cdot \boldsymbol{\nabla}\varphi}{\mathbf{B}_{\text{eq}} \cdot \boldsymbol{\nabla}\theta} \tag{1.3}$$

where the poloidal angle θ has been chosen so that q depends only on the poloidal flux ψ. The fact that q depends only on ψ allows one to write $\mathbf{B}_{\text{eq}} \cdot \boldsymbol{\nabla}\theta = (\boldsymbol{\nabla}\psi \times \boldsymbol{\nabla}\varphi) \cdot \boldsymbol{\nabla}\theta = Iq^{-1}R^{-2}$, meaning that this magnetic topology defines a direct system of coordinates (χ, θ, φ) with a Jacobian $\mathcal{J} = qR^2/I$ and $\chi \equiv -\psi$. The total magnetic field in the tokamak is the superposition of this equilibrium magnetic field and the magnetic field resulting from the interaction between the heating waves and particles composing the plasma. These general expressions will be used in chapter 2 for an ITER-like geometry. In chapters

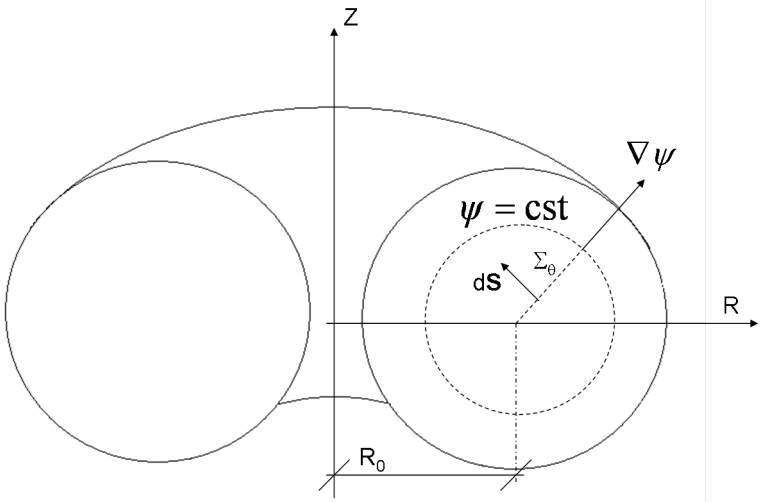

Figure 1.1: Schematic view of a tokamak.

3 and 4, we will make use of a simplified circular geometry like in figure 1.1, valid in the large aspect ratio limit $\varepsilon \ll 1$, where $\varepsilon = \frac{r}{R}$ is the inverse of the aspect ratio. In addition, in figure 1.1 the Grad-Shafranov shift has been neglected. In that case, the magnetic field can be expressed as

$$\mathbf{B}_{\text{eq}} = B_\theta \mathbf{e}_\theta + B_\varphi \mathbf{e}_\varphi \tag{1.4}$$

where

$$B_\varphi = \frac{B_0 R_0}{R} = \frac{B_0 R_0}{R_0 + r\cos\theta}, \quad B_\theta = \frac{r B_\varphi}{R_0 q\left(r\right)} \tag{1.5}$$

with R_0 represented in figure 1.1.

In this simplified geometry, the poloidal angle θ is the same as the geometric angle and the poloidal flux ψ has been replaced by the minor radius r. Both ψ and r represent radial coordinates and are linked to each other by the relation $\mathrm{d}\psi = -B_\theta R \mathrm{d}r$. In particular, when ψ increases, r decreases.

1.1.2 Physical model: Maxwell and Vlasov equations

The electromagnetic field in a plasma satisfies the Maxwell equations [6]

$$\nabla \cdot \mathbf{D} = \rho \tag{1.6}$$
$$\nabla \cdot \mathbf{B} = 0 \tag{1.7}$$
$$\nabla \times \mathbf{E} = -\frac{\partial \mathbf{B}}{\partial t} \tag{1.8}$$
$$\nabla \times \mathbf{H} = \mathbf{j} + \frac{\partial \mathbf{D}}{\partial t} \tag{1.9}$$

where $\mathbf{D}$ is the electric displacement, $\mathbf{E}$ the electric field, $\mathbf{H}$ the magnetic field, $\mathbf{B}$ the magnetic induction, ρ the charge density and $\mathbf{j}$ the current density. The constitutive relations

of the medium are

$$\mathbf{D} = \epsilon_0 \mathbf{E} + \mathbf{P} \tag{1.10}$$
$$\mathbf{B} = \mu_0 \mathbf{H} + \mathbf{M} \tag{1.11}$$

where $\epsilon_0 = 8.85 \cdot 10^{-12} F \cdot m^{-1}$ is the vacuum permittivity and $\mu_0 = 4\pi \cdot 10^7 H \cdot m^{-1}$ is the vacuum permeability. In the following, we will call $\mathbf{B}$ the magnetic field and will not make the distinction between $\mathbf{H}$ and $\mathbf{B}$. These equations are coupled to the Newton equation [7] together with the expression of the Lorentz force

$$m_j \frac{\mathrm{d}^2 \mathbf{x}_j}{\mathrm{d}t^2} = eZ_j \left(\mathbf{E} + \mathbf{v}_j \times \mathbf{B} \right) \tag{1.12}$$

where m_j and eZ_j are the mass and the charge of the j-th particle. The density ρ and the current $\mathbf{j}$ are expressed in terms of the position $\mathbf{x}_j$ as follows

$$\rho(\mathbf{x}, t) = \sum_j eZ_j \delta \left(\mathbf{x} - \mathbf{x}_j(t) \right) \tag{1.13}$$
$$\mathbf{j} = \sum_j eZ_s \frac{\mathrm{d}\mathbf{x}_j}{\mathrm{d}t} \tag{1.14}$$

where we have made use of the Dirac distribution δ. These equations constitute a system of partial differential equations on the unknowns $\mathbf{E}$, $\mathbf{B}$, $\mathbf{D}$, $\mathbf{M}$, $\mathbf{j}$, ρ and $\mathbf{x}_j$ and need to be solved for all the particles in the system.

Statistical approach

Integrating the previous equations for a system with many particles is very demanding. Another approach consists in describing statistically the physical system. To do so, one needs to consider that we can only have access to the probability for a particle to be in the volume element $\mathbf{Z} + \mathrm{d}\mathbf{Z}$ (both space and velocity) in the time interval $t + \mathrm{d}t$. This probability for a species s is measured by the so-called probability distribution function F_s as follows

$$\mathbb{P}\left([\mathbf{Z}, \mathbf{Z} + \mathrm{d}\mathbf{Z}], [t, t + \mathrm{d}t] \right) = F_s(\mathbf{Z}, t)\, \mathrm{d}\mathbf{Z}\mathrm{d}t \tag{1.15}$$

This statistical description is called kinetic description and represents a simplification of the reality. In what follows, the probability distribution function will be referred to only as the distribution function. A very well-known theorem that gives the evolution of any distribution function when the particle motion is constrained by a Lagrangian displacement $\boldsymbol{\xi}$ is the Lagrange theorem[1], which states that the finite variation of the distribution function is the result of a convection and a diffusion in phase-space, namely

$$\Delta F_s = -\frac{\partial}{\partial \mathbf{Z}} \cdot \boldsymbol{\xi} F_s + \frac{1}{2} \frac{\partial}{\partial \mathbf{Z}} \cdot \frac{\partial}{\partial \mathbf{Z}} \cdot \boldsymbol{\xi} \otimes \boldsymbol{\xi} F_s \tag{1.16}$$

The proof of this theorem can be found in Ref. [2]. Dividing the previous equation by a time increment δt and taking the limit $\delta t \to 0$ one obtains the Fokker-Planck equation

$$\frac{\partial F_s}{\partial t} = -\frac{\partial}{\partial \mathbf{Z}} \cdot \frac{\boldsymbol{\xi}}{\delta t} F_s + \frac{\partial}{\partial \mathbf{Z}} \cdot \frac{\partial}{\partial \mathbf{Z}} \cdot \frac{\boldsymbol{\xi} \otimes \boldsymbol{\xi}}{2\delta t} F_s \tag{1.17}$$

[1] This theorem constitutes a general result in the Theory of Elasticity

But in this equation, F_s is not the only unknown since the displacement $\boldsymbol{\xi}$ needs to be determined as well. Depending on the nature of the displacement, the Fokker-Planck equation can be rewritten differently, but will always contain the same information, i.e. the evolution of the distribution function. The Fokker-Planck equation may be rewritten as follows

$$\frac{\partial F_s}{\partial t} = \left.\frac{\partial F_s}{\partial t}\right|_{E,B} + \left.\frac{\partial F_s}{\partial t}\right|_{s'} \tag{1.18}$$

where the subscript E, B represents the displacement due to the electromagnetic field and the subscript s' represents the displacement due to the interaction with all the populations, i.e. slowing-down and isotropisation on the existing species. If we consider that no interactions between particles exist, i.e. $\partial_t F_s|_{s'} = 0$, the evolution of the distribution function is governed only by the electromagnetic field, i.e. $\partial_t F_s = \partial_t F_s|_{E,B}$. Making this term vanish leads to the well-known Vlasov equation

$$\left.\frac{\partial F_s}{\partial t}\right|_{E,B} = 0 \Leftrightarrow \frac{\partial F_s}{\partial t} + \mathbf{v}\cdot\nabla F_s + \frac{\mathrm{d}\mathbf{v}}{\mathrm{d}t}\cdot\frac{\partial F_s}{\partial \mathbf{v}} = 0 \tag{1.19}$$

where the phase space has been split into velocity space and position space and $m_s \mathrm{d}\mathbf{v}/\mathrm{d}t = eZ_s\left(\mathbf{E} + \mathbf{v}\times\mathbf{B}\right)$. This means that the Vlasov equation expresses the invariance of the distribution function along the particle trajectory in the absence of Coulomb interactions with other particles, namely

$$\frac{\mathrm{d}F_s}{\mathrm{d}t} = 0 \tag{1.20}$$

The displacement due to the interaction with all the species (including $s - s$ interaction) leads to the Landau equation. Since the species are described in a statistical way, the tensors in equation (1.17) are averaged over many realizations. In addition, the particle-particle interaction will take place only in the impulsion space. The Landau equation reads

$$\left.\frac{\partial F_s}{\partial t}\right|_{s'} = -\frac{\partial}{\partial \mathbf{p}}\cdot\frac{\langle\delta\mathbf{p}\rangle}{\delta t}F_s + \frac{\partial}{\partial \mathbf{p}}\cdot\frac{\partial}{\partial \mathbf{p}}\cdot\frac{\langle\mathbf{p}\otimes\mathbf{p}\rangle}{2\delta t}F_s \tag{1.21}$$

The first term on the right-hand side of equation (1.21) represents a friction or a slowing-down on the other species. The second term represents a diffusion. In particular, the pitch-angle scattering present in this second term leads to the isotropisation of the velocity distribution. The coefficients $\langle\delta\mathbf{p}\rangle/\delta t$ and $\langle\delta\mathbf{p}\delta\mathbf{p}\rangle/2\delta t$ are called the *Spitzer-Chandrasekhar* coefficients and will be detailed in the next chapter. Note that this structure where a diffusion operator is identified is also underlying beneath the Vlasov equation. The obtention of this diffusion due to the electromagnetic field will also be obtained in the next chapter within the framework of the *quasi-linear* approach.

The spatial and the velocity coordinates lead to a six dimensional space where the physical system is described. In addition, the temporal variable t is to be taken into account. The Maxwell and the Vlasov equations can be solved self-consistently by introducing the relation

$$\rho = \sum_s \rho_s = \sum_s \int F_s \mathrm{d}^3\mathbf{v} \tag{1.22}$$

Hamiltonian formalism for the Vlasov equation: action-angle variables

We know that the motion of a charged particle can be described by Hamilton's equations (see appendices B and D)

$$\dot{\mathbf{q}} = \frac{\partial \mathcal{H}}{\partial \mathbf{p}} \tag{1.23}$$

$$\dot{\mathbf{p}} = -\frac{\partial \mathcal{H}}{\partial \mathbf{q}} \tag{1.24}$$

In addition, the Vlasov equation, which describes the statistical motion of particles in an electromagnetic field, can be rewritten as follows

$$\frac{\partial F}{\partial t} + \dot{\mathbf{q}} \cdot \frac{\partial F}{\partial \mathbf{q}} + \dot{\mathbf{p}} \cdot \frac{\partial F}{\partial \mathbf{p}} = 0 \tag{1.25}$$

where the distribution function in the $(\mathbf{q}, \mathbf{p}, t)$ space is related to the distribution function in the $(\mathbf{x}, \mathbf{v}, t)$ by $m^3 F(\mathbf{q}, \mathbf{p}, t) = F(\mathbf{x}, \mathbf{v}(\mathbf{p}), t)$. Injecting Hamilton's equations in 1.25 leads to the Hamilton formulation of the Vlasov equation

$$\frac{\partial F_s}{\partial t} - [\mathcal{H}, F_s] = 0 \tag{1.26}$$

where $\mathcal{H} = 1/2 m_s v^2 + e\phi$ is the Hamiltonian of the particles taking into account their interaction with the electrostatic field and $[A, B] = \partial_{\mathbf{q}} A \partial_{\mathbf{p}} B - \partial_{\mathbf{p}} A \partial_{\mathbf{q}} B$ is the Poisson Bracket. This formulation reveals extremely useful and powerful when performing coordinate transformations. However, as explained in appendix D, the transformations that are interesting are called *canonical transformations*, which lead to a system of canonical variables and therefore keep the motion equations invariant. In particular, the existence of a canonical transformation leading to a system $(\boldsymbol{\alpha}, \mathbf{J})$ such that the *momenta* $\mathbf{J}$ are invariant and the *positions* $\boldsymbol{\alpha}$ depend linearly on the time reveals interesting for the analysis of a Hamiltonian system. In this case, Hamilton equations imply

$$\dot{\mathbf{J}} = -\partial_{\boldsymbol{\alpha}} \mathcal{H} = 0 \Rightarrow \mathbf{J} = \mathbf{J}_0 \tag{1.27}$$

$$\boldsymbol{\alpha} = \boldsymbol{\Omega} t + \boldsymbol{\alpha}_0 \Rightarrow \dot{\boldsymbol{\alpha}} = \partial_{\mathbf{J}} \mathcal{H} = \boldsymbol{\Omega} \tag{1.28}$$

where $\boldsymbol{\Omega}$ are the eigenfrequencies of the physical system. Therefore, such a system is characterized by a Hamiltonian that depends only on the actions and is consequently a motion invariant, i.e. $\mathrm{d}_t \mathcal{H} = 0$. This system of canonical variables will be called *action-angle* variables and the linear evolution of the angles will be useful to introduce time scale separation for the different physical phenomena present in the system. In particular, as we will see later on in this chapter, the existence of an ordering in the eigenfrequencies leads to the gyro-kinetic description of the plasma, which presents the advantage of reducing the dimension of the phase space. For the moment, it is interesting to recall that the existence of invariants in a dynamical system is related to Poincaré's work[2] and gives rise to the concept of *non integrability in the sense of Poincaré*. More generally, according to Liouville-Arnold theorem, the integrability in the sense of Poincaré is equivalent to the

[2]Henri Poincaré (Nancy, France, 1854-Paris, France, 1912) published his *Three bodies problem together with the dynamics equations* and later his *New methods of celestial mechanics*. He introduced in 1890 the concept of non integrability as the absence of N analytic first integrals of the motion in involution (a bijection which is its own inverse bijection) in a dynamical system with N degrees of freedom.

existence of a first kind generating function providing a canonical transformation leading to the action-angle variables, characterized by the invariance of the generalized momenta or actions and the system is described by a Hamiltonian that depends only on the actions. With these action-angle variables, the phase space acquires a structure of N-dimensional tori described by the actions. These tori are called the *Kolmogorov-Arnold-Moser (KAM) tori*. According to the existence of the Poincaré-Helmholtz invariant, one can define the actions as

$$J_i = \frac{1}{2\pi} \oint_{C_i} \mathbf{p} \cdot \mathrm{d}\mathbf{q} \tag{1.29}$$

where C_i ($i = 1, \cdots, N$) are N independent contours on each torus. The derivation of these variables for a tokamak is detailed in the appendix D and will not be revisited here. In the following, we will make use of these angle-action variables formalism whenever analytical calculations are performed, especially to derive the quasi-linear diffusion operator and to analyse the wave-particle interaction and the marginal stability of ITG modes.

1.1.3 Stationary, equilibrium and perturbed distribution functions

It is legitimate to ask oneself about the nature of the solution of the Vlasov equation. The first comment that can be made is that the solution must be physical in the sense that its integral over the whole phase space must reflect some physical properties and therefore remain finite at any time. If we define the segment $\mathbb{I}_{2\pi} = [0, 2\pi[$, in the action-angle formalism, this condition is mathematically expressed as

$$\frac{1}{(2\pi)^3} \int_{\mathbb{R}^3 \times \mathbb{I}_{2\pi}^3} F_s \, \mathrm{d}^3\mathbf{J} \mathrm{d}^3\boldsymbol{\alpha} < \infty, \, \forall t > 0 \tag{1.30}$$

Physically, this condition means that the number of particles must be finite at any time. For convenience, we introduce the inner product

$$\langle F, G \rangle_{\boldsymbol{\alpha}\mathbf{J}} = \frac{1}{(2\pi)^3} \int_{\mathbb{R}^3 \times \mathbb{I}_{2\pi}^3} FG \, \mathrm{d}^3\mathbf{J} \mathrm{d}^3\boldsymbol{\alpha} \tag{1.31}$$

and we define the space of distribution functions

$$L^2(\Omega_f) = \{F : \Omega_f \to \mathbb{R}, \, \langle F, F \rangle_{\boldsymbol{\alpha}\mathbf{J}} < \infty, \, \forall t\} \tag{1.32}$$

where $\Omega_f = \mathbb{R}^3 \times \mathbb{I}_{2\pi}^3 \times \mathbb{R}_+$. Once the solution (if any) of the Vlasov equation is defined, let us note $\Omega_{\mathrm{eq}} = \mathbb{R}^3 \times \mathbb{R}_+$ and define the subspace of *equilibrium distribution functions* as

$$L^2_{\mathrm{eq}}(\Omega_{\mathrm{eq}}) = \{F : \Omega_{\mathrm{eq}} \to \mathbb{R}, \, \langle F, F \rangle_{\mathbf{J}} < \infty, \, \forall t\} \tag{1.33}$$

where the inner product $\langle \, , \, \rangle_{\mathbf{J}}$ is defined as

$$\langle F, G \rangle_{\mathbf{J}} = \int_{\mathbb{R}^3} F \, G \mathrm{d}^3\mathbf{J} \tag{1.34}$$

The algebraically complemented subspace called subspace of *perturbed distribution functions*, $\tilde{L}^2(\Omega_f)$, can be introduced as the subspace satisfying

$$L^2(\Omega_f) = L^2_{\mathrm{eq}}(\Omega_{\mathrm{eq}}) \oplus \tilde{L}^2(\Omega_f) \tag{1.35}$$

$$L^2_{\mathrm{eq}}(\Omega_{\mathrm{eq}}) \cap \tilde{L}^2(\Omega_f) = \{0\} \tag{1.36}$$

with the natural isomorphism

$$\phi_{\Omega_f,\Omega_{\rm eq}} : L^2_{\rm eq}\left(\Omega_{\rm eq}\right) \times \tilde{L}^2\left(\Omega_f\right) \to L^2\left(\Omega_f\right), \ \left(F_{\rm eq}, \delta F\right) \to F_{\rm eq} + \delta F \tag{1.37}$$

and the projection $\langle \cdots \rangle_{\boldsymbol{\alpha}}$ of $L^2\left(\Omega_f\right)$ on $L^2_{\rm eq}\left(\Omega_{\rm eq}\right)$ along $\tilde{L}^2\left(\Omega_f\right)$

$$\langle \cdots \rangle_{\boldsymbol{\alpha}} : L^2\left(\Omega_f\right) \to L^2_{\rm eq}\left(\Omega_{\rm eq}\right), \ F \to F_{\rm eq} \equiv \langle F \rangle_{\boldsymbol{\alpha}} = \frac{1}{\left(2\pi\right)^3} \int_{\mathbb{I}^3_{2\pi}} F \mathrm{d}^3\boldsymbol{\alpha} \tag{1.38}$$

which satisfies the property $\langle \cdots \rangle^2_{\boldsymbol{\alpha}} = \langle \cdots \rangle_{\boldsymbol{\alpha}}$. The following property naturally stems from the previous definitions

$$\forall\, \delta F \in \tilde{L}^2\left(\Omega_f\right) \Rightarrow \langle \delta F \rangle_{\boldsymbol{\alpha}} = 0 \tag{1.39}$$

We use now the notation $\Omega_{\rm stat} = \mathbb{R}^3$ and define the subspace of *stationary distribution functions* as

$$L^2_{\rm stat}\left(\Omega_{\rm stat}\right) = \left\{F : \Omega_{\rm stat} \to \mathbb{R}, \langle F, F \rangle_{\mathbf{J}} < \infty\right\} \tag{1.40}$$

with the corresponding algebraically complementary subspace satisfying

$$L^2_{\rm eq}\left(\Omega_{\rm eq}\right) = L^2_{\rm stat}\left(\Omega_{\rm stat}\right) \oplus \tilde{L}^2_{\rm eq}\left(\Omega_{\rm eq}\right) \tag{1.41}$$

$$L^2_{\rm stat}\left(\Omega_{\rm stat}\right) \cap \tilde{L}^2_{\rm eq}\left(\Omega_{\rm eq}\right) = \{0\} \tag{1.42}$$

and the projection $\langle \cdots \rangle_T$ which physically constitutes an average over a finite time T

$$\langle F \rangle_T = \frac{1}{T} \int_t^{t+T} F \mathrm{d}t' \tag{1.43}$$

This time-average makes sense only when the following condition is satisfied

$$\frac{\mathrm{d}}{\mathrm{d}t} \lim_{T\to\infty} \frac{1}{T} \int_t^{t+T} F \mathrm{d}t' = 0 \tag{1.44}$$

Finally, the whole vector space where the solution exists is decomposed into a direct sum of subspaces as

$$L^2\left(\Omega_f\right) = L^2_{\rm stat}\left(\Omega_{\rm stat}\right) \oplus \tilde{L}^2_{\rm eq}\left(\Omega_{\rm eq}\right) \oplus \tilde{L}^2\left(\Omega_f\right) \tag{1.45}$$

and any solution of the Vlasov equation can be decomposed into an equilibrium which evolves in time and a perturbation which contains the dependence on the angle variables and evolves in time. The stationary solution (i.e. statistical equilibrium) exists only when the condition 1.44 is fulfilled

$$F\left(\mathbf{J}, \boldsymbol{\alpha}, t\right) = \begin{cases} F_{\rm stat}\left(\mathbf{J}\right) + F_{\rm eq}\left(\mathbf{J}, t\right) + \delta F\left(\mathbf{J}, \boldsymbol{\alpha}, t\right), & \text{if condition 1.44 satisfied.} \\ F_{\rm eq}\left(\mathbf{J}, t\right) + \delta F\left(\mathbf{J}, \boldsymbol{\alpha}, t\right), & \text{otherwise.} \end{cases} \tag{1.46}$$

Any element of $L^2_{\rm stat}\left(\Omega_{\rm stat}\right)$ is a solution of the Vlasov equation if and only $[\mathcal{H}_{\rm stat}, F_{\rm stat}] = 0$ for the time-independent Hamiltonian $\mathcal{H}_{\rm stat}$. The latter condition means that the Hamiltonian related to the stationary solution is a motion invariant, since $\partial_t \mathcal{H} = \mathrm{d}_t \mathcal{H}$. Therefore, it must be a function of motion invariants only. This is equivalent to the integrability of the system. If the solution reduces to an element of $L^2_{\rm stat}$, then the system is integrable. However, this is not the general case, where the Hamiltonian is decomposed as follows

$$\mathcal{H} = \mathcal{H}_{\rm stat} + \delta\mathcal{H} \tag{1.47}$$

with $\delta\mathcal{H}$ the perturbation of the Hamiltonian. In this case, we can say that if a stationary solution exists, it is solution of the Vlasov equation corresponding to the integrable part of the Hamiltonian $\mathcal{H}_{\text{stat}}$. The remainder of the solution corresponds to the non-integrable system and can be decomposed into an equilibrium part which evolves in time [3] and a perturbation. The application of this to a tokamak is straightforward. The axisymmetry guarantees the invariance of the toroidal momentum $J_3 = P_\varphi$. In the adiabatic limit, which is the framework of this thesis, magnetic momentum is also an invariant. In addition, the second action, which is a canonical momentum, is also an invariant. Therefore, if the Hamiltonian does not evolve in time and the axisymmetry is not broken, the motion is integrable and will be referred to as *unperturbed motion*. The Hamiltonian depends only on the three actions. By definition of the Poisson bracket, the stationary condition imposes $\partial_{\mathbf{J}}\mathcal{H}_{\text{stat}} \cdot \partial_{\boldsymbol{\alpha}} F_{\text{stat}} = 0$. Therefore, this solution satisfies $F_{\text{stat}} = F_{\text{stat}}(\mathbf{J})$. Let us assume now that the initial condition is $F(t=0) = F_{\text{stat}}(\mathbf{J}) + \delta F(\mathbf{J}, \boldsymbol{\alpha})$, with $|\delta F| \ll F_{\text{stat}}$. The perturbation part gives rise to a perturbation of the electrostatic potential and to an equilibrium part. Then for another instant, the solution evolves towards $F(t=\delta t) = F_{\text{eq}}(\mathbf{J}, \delta t) + \delta F(\mathbf{J}, \boldsymbol{\alpha}, t=\delta t)$. If the stationary part of the initial condition is stable, the perturbations will disappear and the equlibrium will converge towards F_{stat}. Otherwise, the perturbations will be increased, the electrostatic will depend on time and will not therefore be a motion invariant any longer. No solution in L^2_{stat} is possible and one needs to look for the solution in the whole space

$$F(t) = F_{\text{eq}}(\mathbf{J}, t) + \delta F(\mathbf{J}, \boldsymbol{\alpha}, t) \tag{1.48}$$

The equilibrium part of the solution evolves following the quasi-linear theory described in the next chapter, until a saturation is achieved. The existence of the saturation can be explained by stating that the energy of the physical system is finite and the perturbations cannot grow indefinitely. The saturation is defined as the state at which the perturbation stops growing. We will come back in detail to the different saturation mechanisms in the next chapter. Let us for the moment mention here that for $t \to \infty$, the saturation can be described by a stationary state F_{stat} (the existence of this stationary state is not guaranteed, as mentioned before), a faster evolution governed by an equilibrium $F_{\text{eq}}(t)$ and the perturbation δF, whose module is upper-bounded. The stationary distribution function represents the closest stationary state and the equilibrium distribution function represent the deviation with respect to that stationary state (if any). In any case, $|\delta F_{t\to\infty}|$ can remain constant (stationary saturation), oscillate (oscillating saturation) or tend to zero (damped saturation). The oscillating saturation can also be decomposed into a periodic saturation (the oscillations of the perturbation can be defined by a period) or quasi-periodic (there is no well-defined period and the oscillations exhibit a chaotic behaviour). In what follows, we will consider that $\mathcal{H}_{\text{stat}} \equiv \mathcal{H}_{\text{eq}}$, i.e. the decomposition into stationary, equilibrium and perturbations does not apply to the Hamiltonian. Therefore, the time dependence of the Hamiltonian will appear only in the perturbation $\delta\mathcal{H}$ and the Hamiltonian is decomposed as $\mathcal{H} = \mathcal{H}_{\text{eq}}(\mathbf{J}) + \delta\mathcal{H}(\boldsymbol{\alpha}, \mathbf{J}, t)$.

1.1.4 Gyrokinetic description

The motion of a particle in the magnetic field 1.1 can be described using its spatial coordinates $\mathbf{x}$ and its velocity $\mathbf{v}$. Without any loss of generality, this motion can be decomposed

[3] This time evolution of an equilibrium could seem somewhat paradoxical and will be given either by the quasi-linear formalism described in the next chapter or by the wave-particle trapping mechanism detailed in chapter 3.

into a guiding-center motion and a *gyromotion* around the magnetic field lines. The latter one is characterized by a time scale $\Omega_1 \equiv \partial_{J_1}\mathcal{H}_{\rm eq}$, namely the cyclotron frequency. Therefore, we can write

$$\mathbf{x}\left(t\right) = \mathbf{x}_{\rm gc}\left(t\right) + \boldsymbol{\rho}_L\left(t\right) \tag{1.49}$$

$$\mathbf{v}\left(t\right) = \mathbf{v}_{\rm gc}\left(t\right) + \mathbf{v}_\perp\left(t\right) \tag{1.50}$$

where the subscript *gc* stands for guiding-center. The gyro-motion represents the circular motion of the particle around the magnetic field line with a radius given by $\rho_{\mathbf{L}}\left(t\right) = \frac{m\mathbf{v}_\perp(t)}{eB}$, called the ion Larmor radius.

The gyro-kinetic theory is appropriate in the adiabatic limit (see appendix A), i.e. under the assumption that $\Omega_1 \gg \Omega_2, \Omega_3$ and that spatial variations in the perpendicular direction in an ion Larmor radius scale are smaller than variation in large scales. In this case, any characteristic frequency ω will be smaller than the cyclotron frequency and a separation between fast gyro-motion and slow guiding-centre motion is possible. We can therefore introduce the *small* parameter

$$\epsilon_\omega = \frac{\omega}{\Omega_1} \sim \rho_\star \ll 1 \tag{1.51}$$

where $\rho_\star = \rho_i/a$ is the ion Larmor radius normalized to the minor radius. With this hypothesis, one can perform a gyro-average operation (an average over the cyclotron motion) and reduce the *standard* 6D Fokker-Planck equation to the 5D gyrokinetic equation on the guiding-centre distribution function $\bar{F}\left(\mathbf{x}_{\rm gc}, v_{\rm gc\|}, \mu, t\right)$, which depends on the guiding-centre position $\mathbf{x}_{\rm gc}$, the parallel velocity $v_{\rm gc\|}$ and the magnetic momentum of the charged particles around the magnetic field line $\mu = \frac{mv_\perp^2}{2B}$. The gyrokinetic equation reads

$$\frac{\partial \bar{F}}{\partial t} + v_{\rm gc\|}\nabla_\| \bar{F} + \mathbf{v}_{\rm gc\perp}\cdot\boldsymbol{\nabla}_\perp \bar{F} + \dot{v}_{\rm gc\|}\frac{\partial \bar{F}}{v_{\rm gc\|}} = 0 \tag{1.52}$$

where $\nabla_\|$ and $\boldsymbol{\nabla}_\perp$ are respectively the gradients along the parallel and transverse directions of the magnetic field. It is important to realize that the guiding-centre transformation leading to the gyrokinetic equation does not provide any canonicity, i.e. the equation 1.52 cannot be written in the form 1.26. Nevertheless, as explained in the appendix D, one can obtain the action-angle system from the expression of the guiding-centre Lagrangian. Note that, in the adiabatic limit, the magnetic momentum is a motion invariant and will be called adiabatic invariant in the following. This property will be used in chapters 3 and 4. From a mathematical point of view, the gyro-average operator is expressed as

$$J_0 \cdot \equiv \frac{1}{2\pi}\oint_{\rho_i = cst} \cdot \,\mathrm{d}\varphi_c \tag{1.53}$$

where φ_c is the gyro-phase and the integral is performed over the cyclotron motion. In this expression, we assume that the Larmor radius is constant, i.e. that the projection of the trajectory onto the perpendicular direction is closed. This is true up to the first order in $\rho_\star$. The notation for the gyro-average operator might be somewhat misleading if one considers that the integral represents only an average over the gyro-phase, i.e. if one assumes that $\oint \cdots \mathrm{d}\varphi_c \equiv \int_0^{2\pi} \cdots \mathrm{d}\varphi_c$. Actually, for a quantity $A\left(\mathbf{x}\right)$, one can Taylor-expand around the guiding-centre position as $A\left(\mathbf{x}\right) = \mathrm{e}^{\boldsymbol{\rho}_i\cdot\boldsymbol{\nabla}} A|_{\mathbf{x}_{\rm gc}}$ and the gyroaverage reads

$$J_0 \cdot A = \frac{1}{2\pi}\int_0^{2\pi} \mathrm{e}^{\boldsymbol{\rho}_i\cdot\boldsymbol{\nabla}} A|_{\mathbf{x}_{\rm gc}} \mathrm{d}\varphi_c \tag{1.54}$$

Since the ion Larmor radius depends on the gyro-phase, even if the quantity does not depend on the gyro-phase we find $J_0 \cdot A \neq A$. This means in particular that $J_0^2 \neq J_0$ and therefore the gyro-average operator is not a projector. This property is important, since it means that the whole gyrokinetic theory is not built only by projecting the Fokker-Planck equation onto a five-dimensional space. In the remainder of this thesis, we will avoid using the notation $\bar{\cdot}$ for the guiding-centre distribution function and assume that all quantities are considered in the gyrokinetic framework.

1.2 Particle orbits in a tokamak

As shown in appendix D, the motion of the guiding-centre can be described with three actions and three angles. The actions are motion invariants, meaning that they are conserved along the guiding-centre trajectory. The parallel velocity of the guiding-centre can be written in terms of the energy, which is an exact invariant in the unperturbed motion, and the adiabatic invariant, which is an invariant at the 0^{th} order in $\rho_\star$

$$v_\parallel = \pm\sqrt{\frac{2}{m}\left(E - \mu B\right)} = \pm\sqrt{\frac{2E}{m}}\sqrt{1 - \Lambda + \Lambda\frac{r}{R_0}\cos\theta} \tag{1.55}$$

where $\Lambda = \frac{\mu B_0}{E}$ is an adiabatic invariant called pitch angle. If the parallel velocity never vanishes, the particle is called *passing particle*. For a constant positive parallel velocity, the conservation of the toroidal momentum $P_\varphi = e\psi + mRv_\parallel$ implies that the poloidal flux decreases when the major radius increases. Therefore, the minor radius increases. The same reasoning can be made for a constant negative parallel velocity. This means that the orbits of passing particles are shifted with respect to the magnetic flux surface. This shift can be calculated by the invariance of the toroidal momentum and yields

$$\Delta r = \frac{mv_\parallel}{qeZB_0} \tag{1.56}$$

whose sign depends on the sign of the parallel velocity. If the energy and the adiabatic invariant of a particle satisfy

$$\frac{R_0}{r}\left|1 - \frac{1}{\Lambda}\right| \leq 1 \tag{1.57}$$

the parallel velocity vanishes at a given position (r, θ), the particle bounces back and the parallel velocity changes its sign. These particles are called trapped particles and the projection of their trajectory onto the poloidal cross section has a banana shape. This is the reason why these particles are also called banana particles. The orbit width of a banana particle is given by

$$\delta_b = \frac{qmv_\parallel}{\varepsilon eZB_0} \tag{1.58}$$

Figure 1.2 shows an example of the projection of passing (left) and banana (right) orbits onto the poloidal cross section. Note that highly energetic trapped particles may exhibit large banana orbits, with δ_b comparable to the minor radius of the tokamak. This represents a major concern in the confinement of particles in magnetic fusion devices, especially when energetic passing particles becomes trapped.

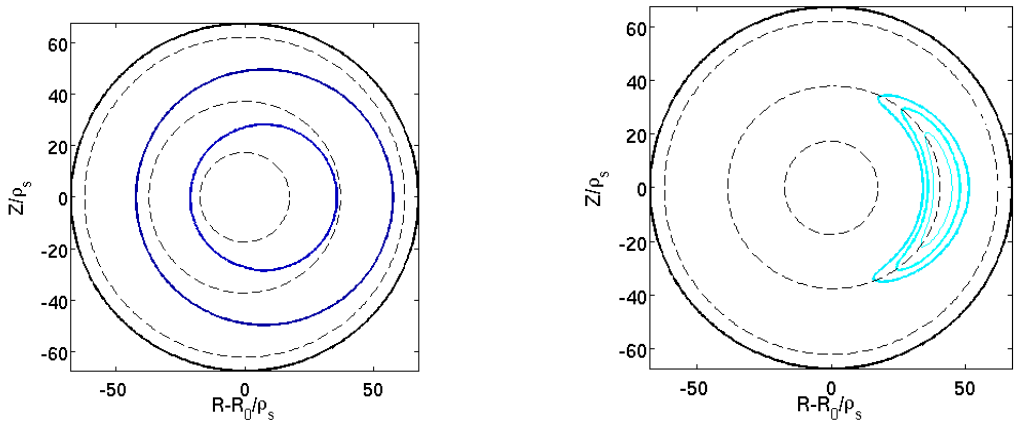

Figure 1.2: Schematic view of the projection of passing (left) and banana (right) orbits onto the poloidal cross section of a tokamak. Magnetic flux surfaces are given by concentric dashed lines.

1.3 Main instabilities analysed in this thesis

Particles and energy released by nuclear fusion reactions must be sufficiently well confined so as to achieve steady-state operation regimes. The confinement of energy can be estimated by the ratio of the internal energy of the plasma to the lost power

$$\tau_E = \frac{W_{\text{int}}}{P_{\text{loss}}} \tag{1.59}$$

A measure of the tokamak performance is given by the amplification factor $\mathcal{Q}$ [8][4]

$$\mathcal{Q} = \frac{P_{\text{fus}}}{P_{\text{add}}} = \frac{5}{\frac{\tau_{\text{Lawson}}}{\tau_E} - 1} \tag{1.60}$$

where the Lawson time is defined as $\tau_{\text{Lawson}} = W_{\text{int}}/P_\alpha$ and P_α is the power contained in the alpha particles released by nuclear fusion reactions. Here we have approximated the total power released by nuclear reactions by $P_{\text{fus}} = 5P_\alpha$. Under the assumption that the electron pressure equals the ion pressure, one can express the Lawson time as $\tau_{\text{Lawson}} = 15pVP_{\text{fus}}^{-1}$, with p the pressure and V the volume of the plasma. The ignition conditions are given by $\tau_E = \tau_{\text{Lawson}}$, i.e. $\mathcal{Q} \to \infty$. ITER must have a confinement such that $\mathcal{Q} = 10$ in short pulses, i.e. the energy confinement time must be of the order of the second. The internal energy is reduced when the losses are increased. These losses can be due to energetic particles such as α particles that are deconfined before transferring their energy to thermal particles. But they can also be due to turbulent transport of energy. Therefore, analysis of both energetic particles and turbulence to reduce these losses is essential for the next step fusion devices. We hereafter give a brief insight into these two phenomena that will be considered in the remainder of this thesis.

[4]John D. Lawson called this parameter R, for the ratio of the energy released in a hot gas to the energy supplied.

1.3.1 Energetic particle modes

Strictly speaking, energetic particles are those having an energy which is much greater than the thermal energy, i.e. $E \gg E_{\text{th}} = k_B T$, where k_B is the Boltzmann constant $k_B = 1.38 \cdot 10^{-23} \text{m}^2\,\text{Kg}\,\text{s}^{-2}\,\text{K}^{-1}$. In the following, no disctinction will be made between temperature and thermal energy, such that temperatures will be expressed in energy units. A plasma in thermodynamical equilibrium can be represented by an isotropic Maxwellian-Boltzmann distribution function $F_{MB} \propto \text{e}^{-E/k_B T}$. Due to the exponential decay with the energy, the effect of highly energetic particles on the physics of such a system is not expected to be significant with respect to the impact of thermal particles. However, if the population of energetic particles is increased, the distribution function may considerably depart from this thermodynamical equilibrium and the exponential decay modified, leading to important effects that will constitute the main research of this thesis. This situation is not far from reality, since in the core of tokamak plasmas, energetic particles naturally exist, generated by nuclear fusion reactions, neutral beam injection (NBI) and radio frequency (RF) waves

- *Nuclear fusion reactions*. In a plasma, there are mainly four nuclear reactions that may happen, but the one retained for the next fusion devices such as ITER is the D(T,α)n reaction, where D stands for deuterium and T stands for tritium. Here, the α particles are produced with an energy of 3.56 MeV and the neutrons are accelerated up to 14.03 MeV. Steady-state ignition in thermonuclear plasmas will be achieved only if the energy of α particles is recovered to heat the background plasma.

- *Neutral Beam Injection*. The physical mechanism of acceleration by NBI relies upon the transfer of momentum by means of Coulomb collisions between charged species. However, one cannot directly send charged particles into a plasma since they would be sent back. One needs to inject neutral particles that will penetrate across the magnetic field lines. By means of ionization processes, they will become high-energy ions and finally they will slow down by Coulomb collisions on the thermal species. In that way, the beam energy is transferred to the plasma.

- *Radio Frequency heating*. RF waves have two range of frequencies: ion cyclotron frequency and lower hybrid frequency. The whole chapter 2 will be devoted to the ion cyclotron frequency heating.

Some problems regarding these energetic particles have attracted the interest of plasma physicists in the last years, such as their neoclassical and turbulent transport. But probably the most analysed issue is the confinement of α particles, since the steady-state ignition in thermonuclear plasmas depends on the heating efficiency achieved by the α particles slowing down on thermal species. In addition, the loss of confinement of these particles results in serious damage of the plasma facing components (PFCs). This loss of confinement has been found to be mostly due to energetic particle modes, i.e. modes excited by the energetic particles themselves, such as Toroidal Alfvén Eigenmodes (TAEs) and fishbones instabilities [9, 10, 11]. In this thesis we will focus on a special kind of modes, localized in the acoustic frequency range like the TAEs. However, in our case, the modes will be electrostatic, i.e. the magnetic field remains unperturbed and the oscillations occur only in the electrostatic potential at a frequency close to the acoustic frequency. The paradigm of acoustic mode in tokamaks is the so-called geodesic acoustic mode (GAM) [12] and it has been recently found that it can be driven unstable by

energetic particles [13, 14]. Previous experimental works on the JET tokamak to these findings were reported in [15, 16], where oscillations of the $n = 0$ mode in the acoustic range of frequencies were attributed to an inverted slope of the distribution function. The main difference between electrostatic and electromagnetic energetic particle modes comes from the effect on the particle confinement. Whereas energetic particles are sensitive to radial perturbations of the magnetic field such as in TAEs and fishbones, they are less affected by radial perturbations of the electrostatic potential. A heuristic explanation for this can be given by considering the diffusivity in the perpendicular direction to the magnetic field lines $\chi_\perp \sim \left\langle \delta v_\perp^2 \right\rangle \tau_c$, where τ_c is a correlation time. In the case of radial perturbations of the magnetic field, $\delta v_\perp \sim v_\parallel B^{-1} \delta B$, whereas for radial perturbations of the electrostatic field, the perpendicular velocity does not depend on $v_\parallel$ and scales as $\delta v_\perp \sim B^{-1} \delta E_\theta$. the correlation time in both cases is expressed as $\tau_c \sim L_c / v_\parallel$, where L_c is a correlation length. Therefore, the perpendicular diffusivities can be estimated for the electromagnetic modes and for the electrostatic modes respectively as follows

$$\chi_{\perp,\mathrm{EM}} \sim \left\langle \left(\frac{\delta B}{B} \right)^2 \right\rangle L_c v_\parallel \tag{1.61}$$

$$\chi_{\perp,\mathrm{ES}} \sim \left\langle \left(\frac{\delta E_\theta}{B} \right)^2 \right\rangle \frac{L_c}{v_\parallel} \tag{1.62}$$

We do not give here more details about electrostatic modes, since they will be studied deeply in chapters 3 and 4.

1.3.2 Drift-wave and interchange instabilities as the origin of turbulent transport

The energy flux can be modeled by a diffusive behaviour in the perpendicular direction quantified by the effective diffusivity χ_{eff}

$$Q_{\mathrm{loss}} = -\chi_{\mathrm{eff}} n_i \frac{\mathrm{d}T_i}{\mathrm{d}r} \tag{1.63}$$

When one considers only the diffusivity predicted by neoclassical theory, the values of the energy transport are ten times smaller than the ones obtained in present fusion devices. The difference has been found to correspond to the so-called anomalous transport or turbulent transport and it is now widely accepted that radial transport of both particles and energy is mainly dominated by small scale (micro-scale) instabilities [17]. Therefore, suppressing or limiting the turbulent transport in tokamaks would lead to high performance operating regimes, characterized by high energy confinement time. Micro-scale instabilities leading to turbulent transport in strongly magnetized plasmas are represented by the drift-wave instability, schematically illustrated in figure 1.3. Let us consider a plasma in a magnetic field $\mathbf{B} = B\mathbf{e}_z$, with a gradient electron density $\nabla n = \mathrm{d}_x n \mathbf{e}_x$. Let us introduce a density perturbation $\delta n\,(y)$ and an electric field $\mathbf{E} = E_y \mathbf{e}_y$. Both the density perturbation and the electric field oscillate along the y-direction. Let us consider the configuration given in the figure, where the electric field combined with the magnetic field produces an $E \times B$ velocity oriented outwards in the region where $\delta n > 0$ and inwards in the region where $\delta n < 0$. Under these circumstances, taking into account the direction of the gradient of the electron density, the density in the regions where $\delta n > 0$ will increase and the density in the regions where $\delta n < 0$ will decrease. This mechanism leads to an

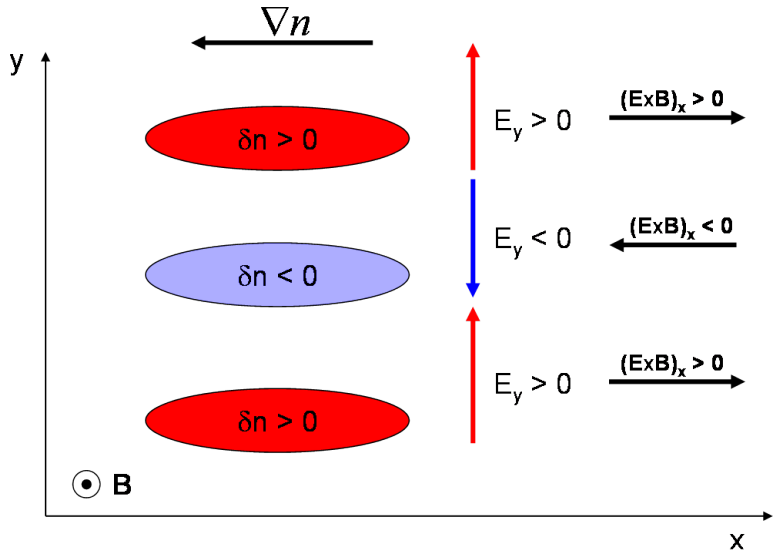

Figure 1.3: Schematic representation of the drift wave instability

amplification of the initial perturbation. The frequency of the resulting instability can be calculated by projecting the continuity equation onto a Fourier mode $\delta n_{k_y,\omega} = \mathrm{e}^{i(k_y y - \omega t)}$ and using the Boltzmann response

$$-i\omega\delta n_{k_y,\omega} = i\frac{T_e}{eB}\frac{\delta n}{n}k_y\frac{\mathrm{d}n}{\mathrm{d}x} \Rightarrow \omega = \omega_* = k_y\frac{T_e}{eB}L_n^{-1} \tag{1.64}$$

where $L_n^{-1} = -n^{-1}\mathrm{d}_x n$ and ω_* is the diamagnetic frequency of electrons. However, in the core of tokamaks, microinstabilities leading to turbulent transport are mostly driven by the ion temperature gradient (ITG) and not by the density gradient, even if the underlying mechanisms are similar to each other, i.e. an initial temperature perturbation is amplified due to the transport of hot and cold regions of plasma by the $E \times B$ velocity.

Together with these instabilities, another kind of instability exists in tokamaks, called interchange instability. It is due to both large radial gradients and inhomogeneous magnetic field. A heuristic analysis like the one done to explain the drift-wave instability is illustrated in figure 1.4. Let us consider a poloidal cross section with a density and toroidal magnetic field profiles given in the lower panel of the figure. The low field side (LFS) is characterized by decreasing density ($\boldsymbol{\nabla} n \cdot \mathbf{e}_x < 0$) and the high field side (HFS) is characterized by increasing density ($\boldsymbol{\nabla} n \cdot \mathbf{e}_x > 0$). Let us assume the existence of small convective cells, i.e. isopotential lines, represented by the dashed ellipses. These isopotential lines enclose regions of positive (red) and negative (blue) perturbations. In between two convective cells, the $E \times B$ velocity is oriented outwards or inwards depending on the region (see figure) and this orientation does not depend on the charge of particles. However, the curvature velocity is oriented upwards for ions and downwards for electrons. The motion of ions and electrons is represented by red (for ions) and blue (for electrons) dashed arrows. Note that ions filling the positive perturbation regions in the LFS are more numerous than ions filling the negative perturbation regions. This means that in the LFS ions will in average fill the regions of positive perturbations and electrons will in average fill the regions of negative perturbations and initial perturbations will be amplified in the LFS. Conversely, they will be damped in the HFS. This damping of perturbations is illustrated by small ellipses in figure 1.4.

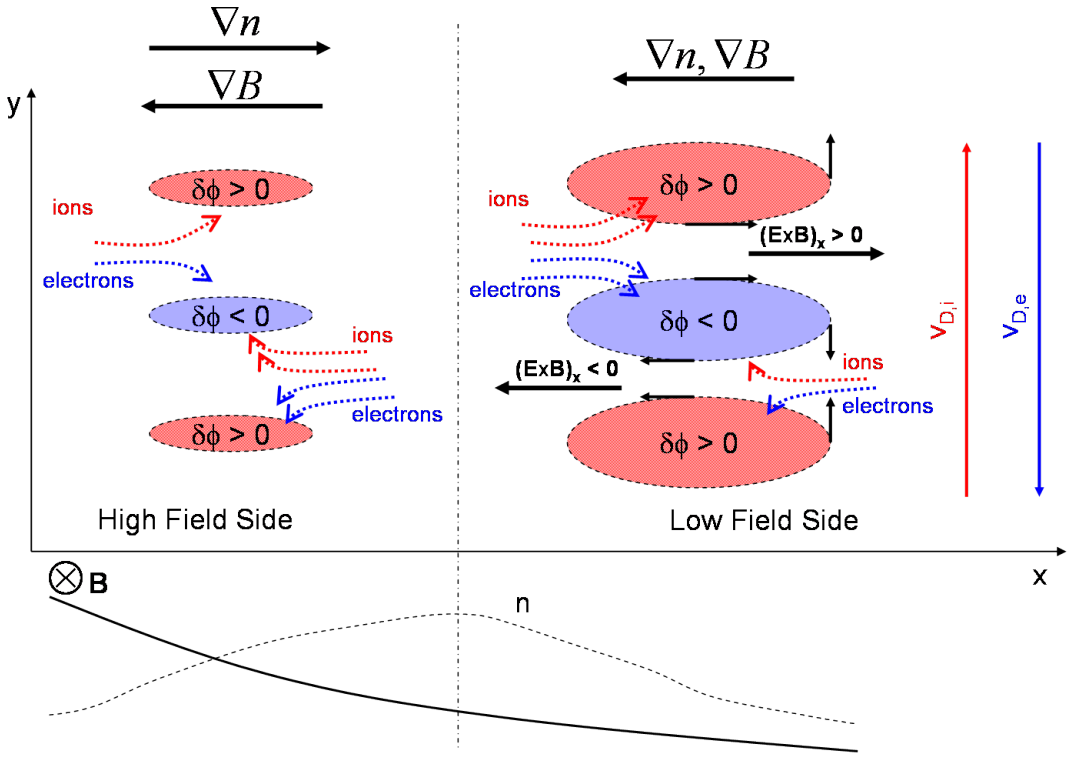

Figure 1.4: Schematic representation of the interchange instability in a tokamak

1.4 Outline of this thesis

In order to analyse the previously mentioned issues, this thesis is organized as follows. In chapter 2 the question of energetic particle generation in ICRH scenarios is tackled. This is done selfconsistently by means of a full-wave 3D code called EVE coupled to a Fokker-Planck module called AQL to describe the plasma-wave interaction in the presence of binary Coulomb collisions. Special attention is devoted to the construction of the quasi-linear diffusion operator from the wave solution to highlight the effect of energetic particles. Simulations with ITER-relevant parameters are performed and presented to analyse the impact of energetic particles on the heating and current drive efficiencies as well as on the structure of the distribution function in velocity space. A well-known property that is recovered in this chapter is that the distribution function in the presence of energetic particles develops a tail localized at suprathermal energies. This is characteristic of RF heating scenarios but also of NBI heating scenarios and can result in the excitation of energetic particle modes. Such a physics issue is analysed in chapter 3 in the framework of electrostatic modes in the acoustic frequency range, namely geodesic acoustic modes. The exact dispersion relation in cylindrical geometry is solved and the role of energetic particles in the mode excitation is explained, leading to the so-called energetic geodesic acoustic modes (EGAMs), for which a linear threshold is predicted with the variational principle and verified in gyrokinetic simulations with the full-f and 5D GYSELA code. Although our theoretical approach does not include nonlinear effects, these are present in the simulations and are explored in the context of both saturation and nonlinear excitation of linearly stable modes. This analysis is done in the absence of turbulence and diamagnetic effects. However, these effects are ubiquitous in real situations and need to

be taken into account for a complete description of the energetic particle modes. This naturally leads to the analysis presented in chapter 4. In particular, we explain the necessity of implementing a source term in the gyrokinetic model. This source is used in the presence of finite temperature gradients but without turbulence to build slowly the energetic particle distribution function and excite EGAMs. Finally, turbulence is taken into account and a more real situation where energetic particles, turbulence and EGAMs exist all together and interact with each other is analysed in detail for the first time in global full-f gyrokinetic flux-driven simulations. In particular, a turbulence propagation is observed and attributed to the coupling of propagating fronts and coherent oscillations of the temperature gradient at the EGAM frequency. The modulation of the turbulence by EGAMs is also studied therein.

Chapter 2

Generation of energetic particles by Ion Cyclotron Resonant Heating

> La nature agit toujours par les voies les plus courtes et les plus simples.
>
> Pierre de Fermat (1607?-1665)

Contents

2.1 Introduction: Ion Cyclotron Resonant Heating

In the activated phase of ITER, the plasma will consist of deuterium (D) and tritium (T) and the reaction rate is proportional to the cross section, which depends on the temperature and peaks at ~ 70 keV. Therefore, in order to have enough nuclear fusion reactions, the ion temperature in the core of the tokamak must be sufficiently high. For this reason, it is important to conceive systems that heat the fuel. Among the different heating systems envisioned for the next fusion devices, the Ion Cyclotron Resonant Heating (ICRH) or the heating within the Ion Cyclotron Range of Frequency (ICRF) is the one which provides heating of ions. Therefore, it is expected that this heating will constitute an essential element for the performance of ITER. One of the main features of this system is the generation of very energetic particles, which can excite some modes in the plasma, namely the energetic particle modes, that can potentially eject them from the very inner regions of the core plasma towards the edge. These energetic particles can also coexist and interact with turbulence, which is the motivation of the present manuscript. However, before analysing this interaction, we consider necessary to give in this chapter a kinetic description of the generation of these energetic ions in realistic heating scenarios and analyse the effects of this fast population on the heating properties and current drive efficiency. The way the energy of the wave is absorbed by the plasma species and how the energy absorbed by the energetic ions is redistributed among the thermal species is analysed in detailed in the following sections. Let us for the moment introduce the basic concepts that are needed to understand the whole chapter.

2.1.1 The wave absorption

The physical mechanism behind the ICRF heating relies upon the fact that a wave generated with a frequency ω will be absorbed by those ions whose cyclotron frequency $\omega_{\rm ci}$ is close to ω. Therefore, this mechanism is also called *cyclotron damping*. Taking into account the dependence of the magnetic field on the major radius, one can find the position of the so-called resonance layer

$$\omega_{\rm ci} = \frac{eB}{m_i} = \frac{eB_0R_0}{m_iR} = \omega \Rightarrow R_{\rm res} = \frac{eB_0R_0}{m_i\omega} \tag{2.1}$$

with B_0 and R_0 the magnitude of the magnetic field and the major radius on the magnetic axis, respectively. Therefore, one can control the position of the resonance layer by modifying the frequency of the wave that is sent to the plasma. Strictly speaking, the resonance condition is written as

$$\omega = p\omega_{\rm ci} + k_\parallel v_\parallel \tag{2.2}$$

where p represents the harmonic of the cyclotron damping and $k_\parallel v_\parallel$ introduces the modification of the resonance by Doppler shift, which is more significant for highly passing ions. It is obtained under the assumption that the unperturbed motion of ions between two resonant points is uniform, as explained in the next section. If $p = 1$, the damping mechanism will be called *fundamental* cyclotron damping or *fundamental* heating. If $p > 1$ the mechanism is called *harmonic* cyclotron damping or *harmonic heating*. In this chapter we will consider only fundamental ($p = 1$) and second harmonic ($p = 2$) heating. In addition, plasmas composed of several species will be analysed. In such plasmas, the wave energy can be absorbed either by the majority ions or by the minority ions. The

heating scenario where the wave energy is mainly absorbed by minority ions is called *minority heating*. It is important to realize that second harmonic minority heating does not require very low concentration of resonant ions, whereas for fundamental minority heating low concentrations are mandatory. However, second harmonic requires that the resonant species has a finite perpendicular temperature, as will be highlighted later on in this chapter. Finally, note that the absorption of the wave can also be related to the electron damping by means of the electron Landau effect (see next chapter for a discussion on the Landau damping). Another possible scenario corresponds to the mode-conversion. The parameters introduced here (minority ions concentration, harmonic and wave frequency) give to the experimentalist powerful tools to optimize the heating of the plasma and the position of the power deposition layer.

2.1.2 Energy transfer via Coulomb collisions and diffusion

In the previous subsection, we have discussed the wave absorption mechanism by the different species in a fusion plasma. The so-called minority heating has been introduced. This concept leads to the heating of mainly one species (the minority ions), but it is important to note that electrons and majority ions will absorb a part of the wave energy. This heating system remains however useless if no energy exchange between the different species exists. Indeed, sometimes, minority ions are introduced in order to increase the efficiency of the absorption, but these ions are not necessarily the reacting ones. If this is the case, they must transfer their energy to the reacting species. This will be done through the Coulomb collisions in the Fokker-Planck equation 1.18. As will be explained later on in this chapter, this equation can be written as follows

$$\frac{\partial F_s}{\partial t} = \left.\frac{\partial F_s}{\partial t}\right|_{\mathrm{QL}} + \left.\frac{\partial F_s}{\partial t}\right|_{\mathrm{coll}} \tag{2.3}$$

where the first term on the right-hand side corresponds to the quasi-linear diffusion mechanism and the second term represents the Coulomb collision operator. When writing the Fokker-Planck equation under this form, we state that the quasi-linear diffusion term is equivalent to the term describing the interaction between particles and the electromagnetic field, which has been explained in the introduction of this manuscript, i.e.

$$\left.\frac{\partial F_s}{\partial t}\right|_{E,B} \approx \left.\frac{\partial F_s}{\partial t}\right|_{\mathrm{QL}} \tag{2.4}$$

Both terms will be obtained in the next paragraphs. Let us note that no losses are not considered in this thesis, which represents a rather strong hypothesis, especially for highly energetic particles if one considers their large orbit width. In the following sections we will explain in detail each of the terms on the right-hand side of equation 2.3.

Linear and quasi-linear descriptions of the plasma response

As explained before in this manuscript, the plasma response is given by coupling the Maxwell equations (electromagnetic description) to the Vlasov equation (kinetic description). The latter one, in the angle-action variables formalism, reads

$$\frac{\mathrm{d}F_s}{\mathrm{d}t} = \frac{\partial F_s}{\partial t} - [H_s, F_s] = 0 \tag{2.5}$$

where $[A,B] = \partial_{\alpha_i} A \partial_{J_i} B - \partial_{\alpha_j} B \partial_{J_j} A$ represents the Poisson bracket. The distribution function F_s and the hamiltonian $\mathcal{H}_s$ may be decomposed into an equilibrium part and a perturbation as follows

$$F_s = F_{s,\mathrm{eq}} + \delta F_s \tag{2.6}$$

$$\mathcal{H}_s = \mathcal{H}_{s,\mathrm{eq}} + \delta \mathcal{H}_s \tag{2.7}$$

Owing to the quasi-periodicity of a tokamak, the perturbations may be projected onto a Fourier basis as follows

$$F_s = F_{s,\mathrm{eq}}\left(\mathbf{J},t\right) + \sum_{\omega,\mathbf{n}\neq\mathbf{0}} \delta F_{s,\omega,\mathbf{n}}\left(\mathbf{J}\right) e^{i(\mathbf{n}\cdot\alpha-\omega t)} \tag{2.8}$$

$$\mathcal{H}_s = \mathcal{H}_{s,\mathrm{eq}}\left(\mathbf{J}\right) + \sum_{\omega,\mathbf{n}\neq\mathbf{0}} \delta \mathcal{H}_{s,\omega,\mathbf{n}}\left(\mathbf{J}\right) e^{i(\mathbf{n}\cdot\alpha-\omega t)} \tag{2.9}$$

This system may be analysed by reducing the equilibrium distribution function to a time independent function, i.e. we identify the equilibrium with a statistical equilibrium $\mathrm{eq} \leftrightarrow \mathrm{stat}$, following the notation given in the introduction of this thesis. This definition of equilibrium is legitimate if one considers that the equilibrium term usually refers to a state where nothing changes. Under this hypothesis, ignoring collisions and injecting equations 2.6 and 2.7 into equation 2.5 one can obtain the so-called linear response of the plasma, i.e. an equation on the perturbation

$$\delta F_{s,\omega,\mathbf{n}} = -\frac{\mathbf{n}\cdot\partial_{\mathbf{J}} F_{s,\mathrm{eq}}}{\omega - \mathbf{n}\cdot\mathbf{\Omega}_s} \delta \mathcal{H}_{s,\omega,\mathbf{n}} \tag{2.10}$$

where $\Omega_s = \partial_{\mathbf{J}} \mathcal{H}_{s,\mathrm{eq}}$ is the eigenfrequency, which satisfies the Hamilton equation $\Omega_s = \dot{\alpha}_s$. More realistic approaches are obtained when nonlinear effects are taken into account. These nonlinear effects are extremely important in physics, since they constitute the only way for an instability to saturate. The saturation of an instability has been introduced in the previous chapter and is analysed in detail in the next one. An intermediate state between linear and nonlinear approaches is the quasi-linear description. The beginning of the quasi-linear theory in plasma physics goes back to the 60's [18, 19, 20], when physicists wondered how large could the amplitude of an instability grow in time. In we consider the time-dependence of F_{eq}, the Fourier decompositions 2.8 and 2.9, injected into the Vlasov equation, allows one to obtain a diffusion equation for the equilibrium distribution function

$$\frac{\partial F_{s,\mathrm{eq}}}{\partial t} = \frac{\partial}{\partial \mathbf{J}} \cdot \left(\mathbf{D}_s^{\mathrm{QL}} \cdot \frac{\partial F_{s,\mathrm{eq}}}{\partial \mathbf{J}} \right) \tag{2.11}$$

where $\mathbf{D}_s^{\mathrm{QL}}$ is a second-order tensor called the quasi-linear diffusion operator. The expression of this operator is given by

$$\mathbf{D}_s^{\mathrm{QL}} = i \left\langle \sum_{\omega,\mathbf{n}\neq\mathbf{0}} \frac{\mathbf{n}\otimes\mathbf{n}}{\omega - \mathbf{n}\cdot\mathbf{\Omega}_s} |\delta \mathcal{H}_{s,\omega,\mathbf{n}\neq\mathbf{0}}|^2 \right\rangle_{\boldsymbol{\alpha}} \tag{2.12}$$

where $\langle \cdots \rangle_{\boldsymbol{\alpha}} \equiv \frac{1}{(2\pi)^3} \int \cdots \mathrm{d}^3\boldsymbol{\alpha}$ is the orbit-average (over the three angles). To obtain this equation, we have assumed (i) that the amplitude of the perturbations $|\delta \mathcal{H}_{s,\omega,\mathbf{n}}|$ is not so large as to invalidate their linear dependence 2.10 (ii) that the number of modes is sufficiently large so that all the modes contribute to provide an efficient diffusion without interacting with each other and (iii) that the evolution of the equilibrium is slow compared

to the real frequencies $\Re(\omega)$. Although expression 2.11 seems extremely simple (we have simply obtained a diffusion equation), important comments need to be made. Strictly speaking, the quasi-linear diffusion operator that we have derived here actually represents a source term in the Fokker-Planck equation, coming from the interaction between heating waves and particles. This is not obvious when one restricts the analysis to the kinetic description of the plasma. However, as stated earlier, the plasma response must include also the self-consistent evolution of the electromagnetic field *via* the Maxwell equations. This electromagnetic field appears in the quasi-linear diffusion operator by means of the perturbed Hamiltonian $\delta\mathcal{H}_s$. Therefore, the diffusion that we obtain here is nothing but the evolution of the equilibrium distribution function due to the heating waves. It is actually this evolution which makes it possible the saturation of instabilities when many modes that do not interact with each other are present in the physical system. Note that this modification does not mean that the actions are not invariant any longer. The actions remain invariant, but only from the point of view of the unperturbed motion. The quasi-linear diffusion coefficient includes a resonance $\omega = \mathbf{n}\cdot\mathbf{\Omega}_s$, which means that the interaction between the wave and the particles will not occur everywhere in the phase-space. Therefore, a particle characterized by the invariants J_1, J_2, J_3 will move along its trajectory with no modification of any of its invariants until it reaches a position in the phase-space where the interaction with the heating wave is possible. At that moment, there will be a transfer of energy and momentum from the wave to the particle (particle heating or mode damping) or from the particle to the wave (particle cooling or mode excitation). In addition, the tensorial structure of the diffusion coefficient reflects the possibility of anisotropic heating. In this chapter, in order to build the diffusion coefficient, we will express the distribution function in terms of the adiabatic invariant $\Lambda = \mu B_{(0)}/E$, the kinetic energy E, which is an invariant of the unperturbed motion, and the toroidal momentum P_φ, strictly invariant if the axisymmetry is not broken. This last condition is verified especially in non turbulent regimes. When turbulence develops, axisymmetry is broken and the previous invariance does not hold any longer.

Coulomb collision operator

In the previous chapter we introduced the Landau equation as the equation describing the evolution of the distribution function of particles s, F_s, when the displacement $\boldsymbol{\xi}$ is due to the Coulomb interactions between the species s and s'. In this case, one can show that the friction and diffusion coefficient are expressed in terms of the distribution function of species $F_{s'}$ as (see e.g. [2])

$$\frac{\langle\delta\mathbf{p}\rangle}{\delta t} = -C\frac{1}{m}\int F_{s'}(\mathbf{p}')\,\frac{\mathbf{v}-\mathbf{v}'}{|\mathbf{v}-\mathbf{v}'|^3}\mathrm{d}\mathbf{p}' \tag{2.13}$$

$$\frac{\langle\delta\mathbf{p}\delta\mathbf{p}\rangle}{\delta t} = C\int F_{s'}(\mathbf{p}')\,\frac{\mathbf{I}|\mathbf{v}-\mathbf{v}'|^2-(\mathbf{v}-\mathbf{v}')(\mathbf{v}-\mathbf{v}')}{|\mathbf{v}-\mathbf{v}'|^3}\mathrm{d}\mathbf{p}' \tag{2.14}$$

$$\tag{2.15}$$

where $C = e^4 Z_s^2 Z_{s'}^2 \Lambda/(4\pi\varepsilon_0)$ and $m = m_s m_{s'}/(m_s+m_{s'})$. These expressions are general and usually useless unless explicit distribution functions $F_{s'}$ are considered. Therefore, depending on the hypothesis of the population of species s', different expressions for the friction and diffusion coefficients can be obtained. In this chapter, we solve the Fokker-Planck equation only for one single species (the fast ions) and consider that the other

species (ions and electrons) are modelled by Maxwellian distribution functions. It is interesting to note here that although ions can absorb most of the wave power, they eventually transfer a non negligible fraction of the absorbed power to electrons. The energy transferred from energetic ions to thermal electrons *via* collisions is not necessarily lost, since it remains in the plasma. Let us recall that the critical energy at which the power transferred from fast ions to thermal electrons equals that transferred from fast ions to thermal ions is given by [21]

$$E_c = 14.8 A T_\mathrm{e} \left(\sum_s \frac{n_s Z_s^2}{n_\mathrm{e} A_s} \right)^{2/3} \tag{2.16}$$

2.2 A brief description of the 3D full-wave solver EVE. Towards the coupling with a Fokker-Planck module

EVE is a full-wave solver based on a variational formulation, in which a first order expanded version of the Hamiltonian has been implemented. For a brief introduction into the variational principles, the reader is encourage to spend some time at exploring the appendix B and the reference given therein. Let us here assume that this introduction is already known and let us state that, mathematically, the charge and current conservations, i.e. Maxwell-Gauss and Maxwell-Ampère laws, are equivalent to the variational formulation

$$\delta \mathcal{L} = \delta \int \mathrm{d}^3\mathbf{x} \left(\mathbf{j}\left(\mathbf{A}, \phi\right) \cdot \mathbf{A}^\dagger - \rho\left(\mathbf{A}, \phi\right) \phi^\dagger \right) = 0, \; \forall \left(\mathbf{A}^\dagger, \phi^\dagger \right) \tag{2.17}$$

where $\mathcal{L} = \mathcal{L}_\mathrm{maxw} + \mathcal{L}_\mathrm{ant} + \sum_s \mathcal{L}_{\mathrm{part},s}$. The expression of $\mathcal{L}_{\mathrm{part},s}$ is defined in terms of the distribution function by means of the linear approach explained in the previous section. The decomposition of the distribution function into an equilibrium part and a perturbation leads to the following simplified expression for the particle functional

$$\mathcal{L}_{\mathrm{part},s} = \mathcal{L}^\mathrm{nres}_{\mathrm{part},s} + \mathcal{L}^\mathrm{res}_{\mathrm{part},s} \tag{2.18}$$

where the resonant part comes from the denominator $\omega - \mathbf{n} \cdot \mathbf{\Omega}$. This resonant functional may be simplified by considering that the unperturbed particle motion is uniform at each resonant point.

In practice, EVE returns an electromagnetic field $(\mathbf{E}, \mathbf{B})$ and the absorbed power for each species for a given magnetic equilibrium and a given distribution function F_s [22]. In order to have a self-consistent problem, this electromagnetic field must be used to calculate the quasi-linear diffusion coefficient 2.12. Then, the Fokker-Planck equation for the energetic species can be solved, where the balance between the quasi-linear diffusion and the collisions dictates the evolution of the distribution function $F_{\mathrm{eq},h}$. Assuming that the electromagnetic field resulting from the heating evolves in a time-scale longer than the time-scale of the evolution of the distribution function, one can integrate the Fokker-Planck equation to obtain a time evolution of $F_{\mathrm{eq},h}$. This assumption does not mean that the time evolution obtained is physical. It is only used for comparison between different heating scenarios to analyse the dynamics of the energetic tail formation. The real evolution of $F_{\mathrm{eq},h}$ and $(\mathbf{E}, \mathbf{B})$ must be given by solving the Maxwell equations and the Fokker-Planck equation at each time step. The calculation of the quasi-linear diffusion coefficient and the resolution of the Fokker-Planck equation are integrated into a unique

module called AQL. Once AQL has obtained a steady-state distribution function, we can inject the equivalent Maxwellian into EVE to obtain another electromagnetic field and new absorbed powers, which will be injected into AQL again and so on. This iterative coupling EVE-AQL is schematically represented in figure 2.1. In this figure we show also that AQL solves the Fokker-Planck equation in an *iterative* way. These iterations are related only to the time evolution of the distribution function, as was explained earlier.

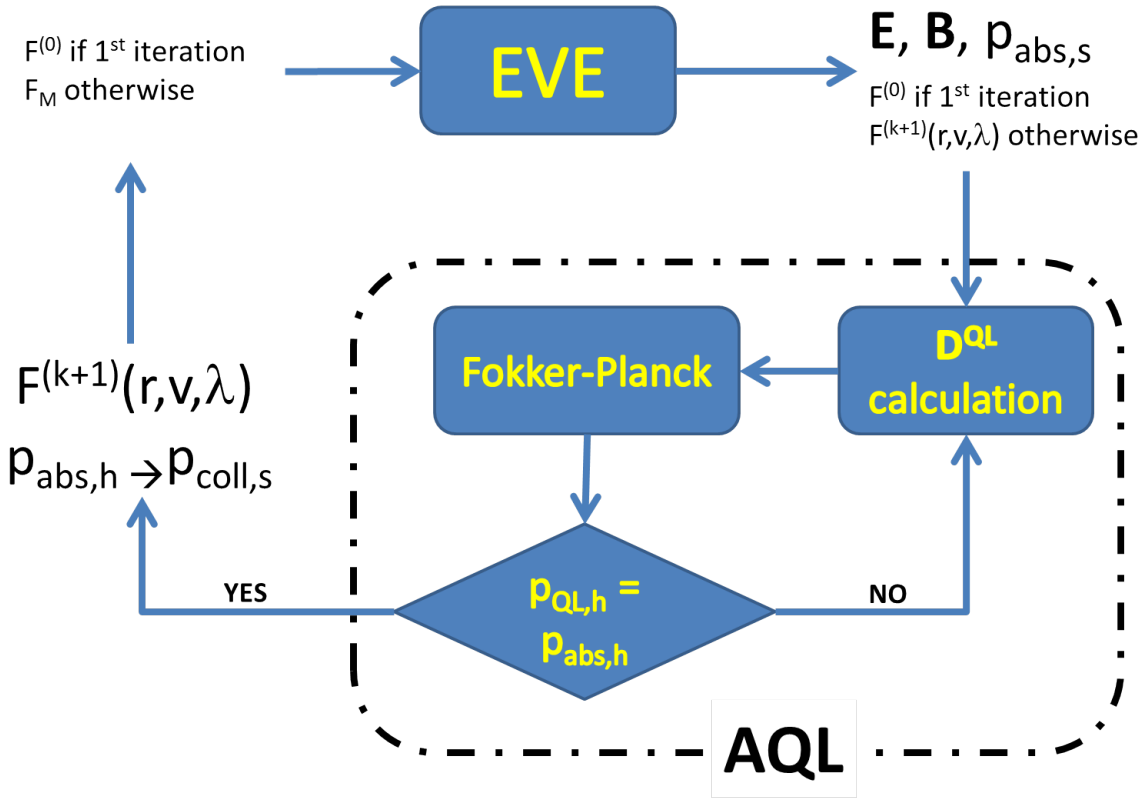

Figure 2.1: Schematic representation of the coupling between EVE and AQL

2.3 AQL: anisotropic quasi-linear Fokker-Planck module

In this section we analyse the bounce-averaged Fokker-Planck equation in the quasi-linear approximation. As discussed in the previous section, the electromagnetic field is an output from the EVE code. Another output is the linear absorbed power for each species $p_{\mathrm{abs,s}}$. The main input consists of a Maxwellian distribution function. However, in ICRH scenarios, generation of fast particles leads to distribution functions presenting a fast tail, which means that the final distribution may depart from a Maxwellian. In particular, since the interaction between the particle and the wave occurs through the cyclotron motion, strong perpendicular heating is expected. The solution given by EVE must be coupled to the Fokker-Planck equation

$$\frac{\partial F_{s,\mathrm{eq}}}{\partial t} = \frac{\partial}{\partial \mathbf{J}} \cdot \left(\mathbf{D}_s^{\mathrm{QL}} \cdot \frac{\partial F_{s,\mathrm{eq}}}{\partial \mathbf{J}} \right) + \sum_{s'} \langle \mathcal{C} \left(F_{s,\mathrm{eq}}, F_{s'} \right) \rangle \tag{2.19}$$

which is solved only for the heated species, whose equilibrium distribution function is noted F_h. No loss term is accounted for. This constitutes a rather strong approximation, since the wave energy (completely absorbed by the plasma) must be redistributed *via* the Coulomb collisions during the evolution of the distribution function and, once the steady state is reached, the power absorbed by the heated species must equal the power which is redistributed by collisions among the thermal species. To obtain this, one can multiply the equation 2.19 by the kinetic energy of the energetic particles and integrate over the whole velocity space, which gives the energy conservation

$$\frac{\mathrm{d}}{\mathrm{d}t}\frac{1}{2}m_h\int \mathrm{d}^3\mathbf{v}v^2F_h = p_{\mathrm{QL},h} + \sum_{s'} p_{\mathrm{coll},s'} \tag{2.20}$$

where $p_{\mathrm{QL},h}$ is the quasi-linear power of the heated species, defined as follows

$$p_{\mathrm{QL},h} = \int \mathrm{d}^3\mathbf{v}\frac{m_h v^2}{2}\frac{\partial}{\partial \mathbf{J}}\cdot\left(\mathbf{D}_h^{\mathrm{QL}}\cdot\frac{\partial F_{s,\mathrm{eq}}}{\partial \mathbf{J}}\right) \tag{2.21}$$

and $p_{\mathrm{coll},s'}$ is the power transferred *via* the Coulomb collisions from the heated species to the thermal species s'

$$p_{\mathrm{coll},s'} = \int \mathrm{d}^3\mathbf{v}\frac{m_h v^2}{2}\left\langle \mathcal{C}\left(F_{s,\mathrm{eq}}, F_{s'}\right)\right\rangle \tag{2.22}$$

Under the assumption that EVE gives the correct linear absorbed power for the heated species, $p_{\mathrm{abs,h}}$, and that for each instant this linear power equals the quasi-linear power, namely

$$p_{\mathrm{abs},h} = p_{\mathrm{QL},h},\ \forall\, t > 0 \tag{2.23}$$

we can derive the following condition in steady state

$$p_{\mathrm{abs},h} = -\sum_{s'} p_{\mathrm{coll},s'} \tag{2.24}$$

In this section, we derive the collision and diffusion operators that have been implemented in AQL. We also explain the method used to solve the Fokker-Planck equation, leading to a system of coupled partial differential equations in time and energy. Finally, the physical meaning of each term in these equations is analysed together with the boundary conditions.

2.3.1 Quasi-linear diffusion operator implemented in AQL

In what follows, the quasi-linear diffusion operator will be noted

$$\langle D_w(F_h, D_0)\rangle \equiv \frac{\partial}{\partial \mathbf{J}}\cdot\left(\mathbf{D}_h^{\mathrm{QL}}\cdot\frac{\partial F_h}{\partial \mathbf{J}}\right) \tag{2.25}$$

where the parameter D_0 will be justified later. The action-angle description is a powerful tool to understand the particle trajectories and highlight the physics of wave-particle resonance, but this approach is little convenient to make analytical progress in order to give physical results that will be compared to experiments. It is therefore more intuitive to express the diffusion operator in terms of the adiabatic invariants $\mathbf{I} = (E, \Lambda, P_\varphi)$, where $\Lambda = \frac{\mu B_{(0)}}{E}$ and $B_{(0)}$ is the amplitude of the magnetic field on the magnetic axis. Defining the metric tensor as follows

$$g_{ij} = \frac{\partial J_i}{\partial I_j} \tag{2.26}$$

we can find the components of the quasi-linear diffusion operator in the $\mathbf{I}$ basis

$$D^{\mathrm{QL}}_{h,E\Lambda} = \frac{1}{E}\left(\frac{p\omega_{\mathbf{c},h}}{\omega}-\Lambda\right)D^{\mathrm{QL}}_{h,EE} \tag{2.27}$$

$$D^{\mathrm{QL}}_{h,\Lambda\Lambda} = \frac{1}{E^2}\left(\frac{p\omega_{\mathbf{c},h}}{\omega}-\Lambda\right)^2 D^{\mathrm{QL}}_{h,EE} \tag{2.28}$$

$$D^{\mathrm{QL}}_{h,EP_\varphi} = D^{\mathrm{QL}}_{h,P_\varphi E} = \frac{\pi}{\omega_b}\frac{n}{\omega}D^{\mathrm{QL}}_{h,EE} \tag{2.29}$$

$$D^{\mathrm{QL}}_{h,\Lambda P_\varphi} = D^{\mathrm{QL}}_{h,P_\varphi \Lambda} = \frac{n}{\omega}\left(\frac{p\omega_{\mathbf{c},h}}{\omega}-\Lambda\right)D^{\mathrm{QL}}_{h,EE} \tag{2.30}$$

$$D^{\mathrm{QL}}_{h,P_\varphi P_\varphi} = \frac{\pi}{\omega_b}\frac{n^2}{\omega^2}D^{\mathrm{QL}}_{h,EE} \tag{2.31}$$

The component $D^{\mathrm{QL}}_{h,EE}$ is straightforwardly calculated since $\partial_{\mathbf{J}}E = \mathbf{\Omega}$. Using the expression 2.12 and taking into account the Plemelj formula for the resonance, one obtains

$$D^{\mathrm{QL}}_{h,EE} = \pi\omega^2\sum_{\mathbf{n}}\delta\left(\omega-\mathbf{n}\cdot\Omega\right)\left|\delta\mathcal{H}_{h,\omega,\mathbf{n}\neq\mathbf{0}}\right|^2 \tag{2.32}$$

The determination of the components of the diffusion operator in terms of $\left(v_\parallel, v_\perp\right)$ at the resonance leads to the following ordering between the perpendicular and the parallel components

$$D^{\mathrm{QL}}_{h,v_\perp v_\perp} = \frac{1}{m_h v_\perp}\left(p\frac{\omega_{\mathrm{c},h}}{\omega}\right)^2 D^{\mathrm{QL}}_{h,EE} \gg D^{\mathrm{QL}}_{h,v_\parallel v_\parallel} = \frac{1}{m_h v_\parallel}\left(1-p\frac{\omega_{\mathrm{c},h}}{\omega}\right)^2 D^{\mathrm{QL}}_{h,EE} \tag{2.33}$$

when $\omega \sim p\omega_{\mathrm{c},h}$, which means that the diffusion occurs mainly in the perpendicular direction. Therefore, ICRH system provides heating mainly in the perpendicular direction and we will retain only the component $D^{\mathrm{QL}}_{h,v_\perp v_\perp}$ in the following, so that the quasi-linear diffusion operator acting on the equilibrium distribution function is rewritten as

$$\langle D_w(F_h, D_0)\rangle = \frac{1}{v_\perp}\frac{\partial}{\partial v_\perp}v_\perp D^{\mathrm{QL}}_{h,v_\perp v_\perp}\frac{\partial F_h}{\partial v_\perp} \tag{2.34}$$

Writing the perpendicular velocity in terms of v and $\lambda = \frac{v_\parallel}{v}$

$$v_\perp = v\left(1-\lambda^2\right)^{1/2} \tag{2.35}$$

allows one to express the quasi-linear diffusion operator as follows

$$\begin{aligned}\langle D_w(F_h, D_0)\rangle = \frac{1-\lambda^2}{v^2}\frac{\partial}{\partial v}\left[vD^{\mathrm{QL}}_{h,v_\perp v_\perp}\left(v\frac{\partial F_h}{\partial v}-\lambda\frac{\partial F_h}{\partial \lambda}\right)\right] - \\ \frac{1}{v^2}\frac{\partial}{\partial\lambda}\left[\lambda\left(1-\lambda^2\right)D^{\mathrm{QL}}_{h,v_\perp v_\perp}\left(v\frac{\partial F_h}{\partial v}-\lambda\frac{\partial F_h}{\partial\lambda}\right)\right]\end{aligned} \tag{2.36}$$

The last step is the calculation of the component $D^{\mathrm{QL}}_{h,v_\perp v_\perp}$, given by

$$D^{\mathrm{QL}}_{h,v_\perp v_\perp}(u,\lambda) = D_0\sum_{res}\left|E_+ J_{p-1}\left(\frac{k_\perp u(1-\lambda^2)^{1/2}}{\omega_{\mathrm{c},h}}\right)+E_- J_{p+1}\left(\frac{k_\perp u(1-\lambda^2)^{1/2}}{\omega_{\mathrm{c},h}}\right)\right|^2 \tag{2.37}$$

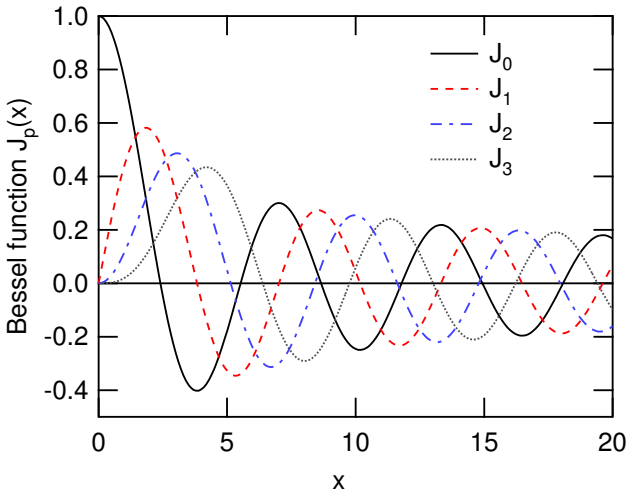

Figure 2.2: Bessel functions of the first kind and order $p \in \{0, 3\}$

where D_0 represents a normalization factor, E_+ and E_- are the components of the electric field in the complex basis and J_p is the Bessel function of the first kind of order p, plotted in figure 2.2. The coefficient D_0 is chosen to recover the absorbed power, i.e. to satisfy equation 2.23. In that respect, the iterations that we have represented in figure 2.1 reflect the evolution of D_0 and $F_{\mathrm{eq},s}$. This is due to the fact that the steady state is characterized by the non-evolution of the distribution function and therefore by the non-evolution of the coefficient D_0. It means that during the time evolution of the distribution, both F_h and D_0 evolve together and at each time step the absorbed power $p_{\mathrm{abs},h}$ must equal the quasi-linear estimated power $p_{\mathrm{QL},h}$ and the coefficient D_0 must be recalculated to satisfy this assumption. Therefore the iterative loop in AQL is explained as follows. We know the distribution function before starting the internal AQL iterations. We know the absorbed power $p_{\mathrm{abs},h}$, which remains constant during the whole AQL loop since it is an output from EVE. We can therefore calculate a first value of D_0 which makes it possible that $p_{\mathrm{QL},h} = p_{\mathrm{abs},h}$ at $t = 0$. Then we solve the Fokker-Planck equation and obtain a distribution function at the next time step $t = \Delta t$. The coefficient D_0 is recalculated at $t = \Delta t$ so that the absorbed power equals the quasi-linear power for the new distribution function. This process ends up when neither the distribution function nor D_0 evolve any longer.

Note that taking into account the left circularly polarized component E_- is essential to correctly include the effect of energetic particles. This is a significant improvement with respect to more simplified modules employed in other ICRF codes. In this expression we have made use of the quasi-local approximation for the Hamiltonian $|\delta\mathcal{H}_{h,\omega,\mathbf{n}\neq 0}|^2$ and assumed that the wave-particle interaction occurs at a single poloidal angle $\theta = \theta_{\mathrm{res}}$ where the absorption of the wave power is maximum.

2.3.2 Collision operator

For the sake of simplicity, the assumption will be made that the thermal species are modeled by a Maxwellian distribution function. In this case, the collision operator may be written as follows [23]

$$\sum_{s'} \langle \mathcal{C}\left(F_{s,\mathrm{eq}}, F_{s'}\right)\rangle \equiv \langle \mathcal{C}\left(F_h\right)\rangle = \frac{1}{u^2}\frac{\partial}{\partial u}u^2\left(\mathcal{D}_{h,uu}\frac{\partial F_h}{\partial u} - \mathcal{F}_{h,u}F_h\right) + \frac{1}{u^2}\frac{\partial}{\partial \lambda}\mathcal{D}_{h,\lambda\lambda}\frac{\partial F_h}{\partial \lambda} \quad (2.38)$$

In this expression, u is the velocity scaled to the thermal velocity $v_{\mathrm{th},h}$ of the energetic ions. The collision coefficients have the following expressions

$$\mathcal{D}_{h,uu} = \frac{1}{2u}\sum_{s'\neq h}\frac{\nu^{h/s'}}{\nu_h}\Psi(u_{s'}) \quad (2.39)$$

$$\mathcal{F}_{h,u} = -\sum_{\beta\neq h}\frac{\nu^{h/s'}T_h}{\nu_h T_{s'}}\Psi(u_{s'}) \quad (2.40)$$

$$\mathcal{D}_{h,\lambda\lambda} = \frac{1}{2u}\left(1-\lambda^2\right)\sum_{s'\neq h}\frac{\nu^{h/s'}}{\nu_h}\Theta(u_{s'}) \quad (2.41)$$

where $u_{s'}$ is the velocity of the s'-th species normalized to its thermal velocity. For the heated species, the thermal velocity will be obtained from the temperature before heating. $\nu^{h/s'}$ is the collision frequency between species s' and h and ν_h is the collision frequency of the species h with reference thermal background ions. The first coefficient refers to diffusion in energy space. The second one represents a drag term, meaning that particles with different velocities tend to equal their energies by accelerating the slowest one and slowing-down the most energetic one. Both coefficients are written in terms of the function

$$\Psi(u) = \frac{1}{u}\left(-\frac{2}{\sqrt{\pi}}ue^{-u^2} + Erf(u)\right) \quad (2.42)$$

where Erf is the error function. The third coefficient is derived from Ψ and reads

$$\Theta(u) = \frac{2}{u\sqrt{\pi}}u^2e^{-u^2} + \frac{1}{u^2}\left(u^2-\frac{1}{2}\right)\left(-\frac{2}{\sqrt{\pi}}ue^{-u^2} + Erf(u)\right) \quad (2.43)$$

It makes sense only when pitch-angle scattering is accounted for. This coefficient is not needed when the distribution function is assumed isotropic.

2.3.3 Projecting the Fokker-Planck equation onto Lagrange polynomial basis

To solve the system 2.23-2.19 we assume that the distribution function can be decomposed in an orthogonal polynomial basis as follows

$$F_h(u,\lambda,t) = \sum_{m=0}^{L} F_{h,m}(u,t)P_m(\lambda) \quad (2.44)$$

where m is the degree of the polynomials. This decomposition allows one to decouple the variables u and λ and is, in principle, exact as long as the number of polynomials $L \to \infty$. Nevertheless, the resolution of the Fokker-Planck equation would be impossible from a numerical point of view and one needs therefore to truncate the number of

polynomials and choose an *arbitrary* $L < \infty$. This choice makes the numerical resolution easier since the initial 2D problem is reduced to a 1D problem. However, this is a strong approximation and potentially leads to some inconsistencies regarding the properties of the distribution function in a few situations. For example, small negative values can be encountered, which are artificially set to zero. In the following, for the sake of clarity, both the Einstein notation and the upper limit L will be assumed for the sums. Expression 2.44 is then rewritten as

$$F_h(u,\lambda,t) = F_{h,m}(u,t)P_m(\lambda) \tag{2.45}$$

The collision and diffusion operators become

$$\langle \mathcal{C}(F_h)\rangle = \frac{1}{u^2}\frac{\partial}{\partial u}u^2\left(\mathcal{D}_{h,uu}\frac{\partial F_{h,m}(u,t)}{\partial u}P_m(\lambda) - \mathcal{F}_{h,u}F_{h,m}(u,t)P_m(\lambda)\right) + \frac{1}{u^2}\frac{\partial}{\partial \lambda}\mathcal{D}_{h,\lambda\lambda}F_{h,m}(u,t)\frac{\mathrm{d}P_m(\lambda)}{\mathrm{d}\lambda} \tag{2.46}$$

$$\langle D_w\left(F_h, D_0\right)\rangle = \frac{1-\lambda^2}{u^2}\frac{\partial}{\partial u}\left[uD^{\mathrm{QL}}_{h,v_\perp v_\perp}\left(u\frac{\partial F_{h,m}(u,t)}{\partial u}P_m(\lambda) - \lambda F_{h,m}(u,t)\frac{\mathrm{d}P_m(\lambda)}{\mathrm{d}\lambda}\right)\right] - \frac{1}{u^2}\frac{\partial}{\partial \lambda}\left[\lambda\left(1-\lambda^2\right)D^{\mathrm{QL}}_{h,v_\perp v_\perp}\left(u\frac{\partial F_{h,m}(u,t)}{\partial u}P_m(\lambda) - \lambda F_{h,m}(u,t)\frac{\mathrm{d}P_m(\lambda)}{\mathrm{d}\lambda}\right)\right] \tag{2.47}$$

We can then multiply these two operators by P_n for $n = 0, \cdots, L$, integrate between $\lambda = -1$ and $\lambda = 1$ and separate the derivatives following their order, so that we can write the following set of partial differential equations

$$\left\{\frac{\partial F_{h,m}}{\partial t} = \alpha^{(2)}_{h,m,n}(u)\frac{\partial^2 F_{h,m}}{\partial u^2} + \alpha^{(1)}_{h,m,n}(u)\frac{\partial F_{h,m}}{\partial u} + \alpha^{(0)}_{h,m,n}(u)F_{h,m}\right\}_{n=0,\ldots,L} \tag{2.48}$$

where the α coefficients are defined as

$$\alpha^{(2)}_{h,m,n}(u) = \mathcal{D}_{h,uu}\|P_m\|^2\delta_{mn} + D_{00,m,n}(u) \tag{2.49}$$

$$\alpha^{(1)}_{h,m,n}(u) = \left(\frac{1}{u^2}\frac{\mathrm{d}}{\mathrm{d}u}\left(u^2\mathcal{D}_{h,uu}\right) - \mathcal{F}_{h,u}\right)\|P_n\|^2\delta_{mn} + \frac{1}{u^2}\frac{\mathrm{d}}{\mathrm{d}u}\left(u^2 D_{00,m,n}(u)\right) - \frac{1}{u}\left(D_{10,m,n}(u) - D_{01,m,n}(u)\right) \tag{2.50}$$

$$\alpha^{(0)}_{h,m,n}(u) = \frac{1}{u^2}\left[\left\langle P_n, \frac{\partial}{\partial\lambda}\left(\mathcal{D}_{h,\lambda\lambda}\frac{\mathrm{d}P_m}{\mathrm{d}\lambda}\right)\right\rangle_\lambda - \frac{\mathrm{d}}{\mathrm{d}u}\left(u^2\mathcal{F}_{h,u}\|P_n\|^2\delta_{mn} + uD_{10,m,n}(u)\right) - D_{11,m,n}(u)\right] \tag{2.51}$$

where $\langle a, b\rangle_\lambda \equiv \int_{-1}^{1} ab\mathrm{d}\lambda$ and the following integrated diffusion coefficients are defined

$$D_{00,m,n}(u) = \int_{-1}^{1}(1-\lambda^2)D^{\mathrm{QL}}_{h,v_\perp v_\perp}P_mP_n\mathrm{d}\lambda \tag{2.52}$$

$$D_{10,m,n}(u) = \int_{-1}^{1} \lambda(1-\lambda^2) D^{\mathrm{QL}}_{h,v_\perp v_\perp} \frac{\mathrm{d}P_m}{\mathrm{d}\lambda} P_n \mathrm{d}\lambda \tag{2.53}$$

$$D_{01,m,n}(u) = \int_{-1}^{1} \lambda(1-\lambda^2) D^{\mathrm{QL}}_{h,v_\perp v_\perp} P_m \frac{\mathrm{d}P_n}{\mathrm{d}\lambda} \mathrm{d}\lambda \tag{2.54}$$

$$D_{11,m,n}(u) = \int_{-1}^{1} \lambda^2(1-\lambda^2) D^{\mathrm{QL}}_{h,v_\perp v_\perp} \frac{\mathrm{d}P_m}{\mathrm{d}\lambda} \frac{\mathrm{d}P_n}{\mathrm{d}\lambda} \mathrm{d}\lambda \tag{2.55}$$

After having obtained the system 2.48, it is useful to verify whether the particular case of an isotropic problem leads to the distribution function already used in the literature [24]. For this, we write $F_h \equiv F_{\mathrm{iso}} = F_{h,0}$. Under the assumption of isotropy, the α-coefficients are simplified as follows

$$\alpha_h^{(2)}(u) = 2\mathcal{D}_{h,uu} + D_{00}(u)$$

$$\alpha_h^{(1)}(u) = 2\left(\frac{1}{u^2}\frac{\mathrm{d}}{\mathrm{d}u}\left(u^2\mathcal{D}_{h,uu}\right) - \mathcal{F}_{h,u}\right) + \frac{1}{u^2}\frac{\mathrm{d}}{\mathrm{d}u}u^2 D_{00}(u)$$

$$\alpha_h^{(0)}(u) = \frac{2}{u^2}\frac{\mathrm{d}}{\mathrm{d}u}u^2\mathcal{F}_{h,u}$$

where the subscripts m, n have been dropped off for the sake of clarity. In this case, the effect of the quasi-linear diffusion has been included only in $D_{00,m,n}(u)$, which represents an average over the pitch-angle of the quasi-linear diffusion coefficient, i.e. $D_{00,m,n}(u) = \int_{-1}^{1}(1-\lambda^2)D^{\mathrm{QL}}_{h,v_\perp v_\perp}\mathrm{d}\lambda$. The equations 2.48 in steady state reduce to a single equation

$$\frac{\mathrm{d}}{\mathrm{d}u}\left(u^2\left(D_{00} + 2\mathcal{D}_{h,uu}\right)\frac{\mathrm{d}F_h}{\mathrm{d}u} - 2u^2\mathcal{F}_{h,u}F_h\right) = 0 \tag{2.56}$$

whose first integration together with the condition that the distribution function and its derivative are finite at $u = 0$ lead to the equation

$$u^2\left(D_{00} + 2\mathcal{D}_{h,uu}\right)\frac{\mathrm{d}F_h}{\mathrm{d}u} - 2u^2\mathcal{F}_{h,u}F_h = 0 \tag{2.57}$$

which is straightforwardly integrated into (only if $D_{00} + 2\mathcal{D}_{h,u} \neq 0$)

$$F_h(u) = F_h(u=0)\exp\int_0^u \frac{2\mathcal{F}_{h,u}}{D_{00} + 2\mathcal{D}_{h,u}}\mathrm{d}u' \tag{2.58}$$

which is exactly the distribution function used in [24]. It is interesting to make some comments on the physical meaning of each α-coefficient. To do so, the case of an isotropic distribution function is especially useful. Indeed, equation (2.56) reflects that the coefficient $\alpha^{(2)}_{h,m,n}$ can be interpreted as a pure diffusion term resulting from the energy diffusive part of the collision operator and the pitch-angle averaged quasi-linear diffusion coefficient. This average naturally stems from the energy diffusive part of the quasi-linear diffusion operator. The coefficient $\alpha^{(1)}_{h,m,n}$ contains information from the drag and energy diffusion coefficients of the collision operator and also information from the quasi-linear diffusion coefficient through the pitch-angle averaged coefficient and from the cross-derivatives. The coefficient $\alpha^{(0)}_{h,m,n}$ is the only one containing the effect of the pitch-angle scattering.

Boundary conditions and Legendre polynomials

In order to have a non-vanishing solution, the system 2.48 needs a set of non-vanishing boundary conditions. The Fokker-Planck equation in $\{u, \lambda\}$ space has the following boundary conditions:

$$\begin{aligned} \partial_\lambda F_h(u=0,\lambda) &= 0 \\ \partial_u F_h(u=0,\lambda) &= 0 \\ F_h(u=\infty,\lambda) &= 0 \end{aligned} \tag{2.59}$$

The first condition represents an axisymmetry at the origin of energies and means that the distribution function is isotropic at very low energies. In addition, we assume that the distribution function is even in λ, i.e. there are as many particles with positive parallel velocity as particles with negative parallel velocity. The system 2.48 is solved numerically following a finite difference method. In this case, the u space must be bounded in order to create a finite grid $\{u_p\}_{p=0,\dots,N}$. Taking into account the fact that the velocity grid must be finite, the boundary conditions can be written as follows

$$\begin{aligned} &\{F_{h,m}\left(u=0,t\right)=0\}_{m>0} \\ &F_{h,m}\left(u=u_{-1},t\right) = F_{h,m}\left(u=u_0,t\right) \\ &F_{h,m}(u=u_{N+1},t)=0 \end{aligned} \tag{2.60}$$

The initial boundary condition will be given by a Maxwellian distribution function. The form of the coefficient 2.51 suggests that the right choice for the polynomial decomposition consists of taking the Legendre polynomials basis with even degree to satisfy the symmetry in $v_\parallel$, as proposed in [25]. However, the final expression of the α coefficients that we obtain here differs from the one reported in [25]. The choice of Legendre polynomials allows us to write the $\alpha^{(0)}$ coefficient as follows

$$\alpha^{(0)}_{h,m,n}(u) = \frac{1}{u^2}\left[-\frac{1}{2u}\Theta_c(u)\|P_n\|^2 n(n+1)\delta_{mn} - \frac{\mathrm{d}}{\mathrm{d}u}\left(u^2\mathcal{F}_{h,u}\|P_n\|^2\delta_{mn} + uD_{10,m,n}(u)\right) - D_{11,m,n}(u)\right] \tag{2.61}$$

where $\Theta_c(u) = \sum_{\beta\neq h}\frac{\nu^{h/\beta}}{\nu_h}\Theta(u_\beta)$. Note that $F_{h,n=0}\left(u=0,t\right)$ is not determined by the boundary conditions. Since no particle transport exists, it will be calculated to ensure the conservation of density, i.e.

$$n_h = 2\pi v_{\mathrm{th}}^3 \int_0^\infty \int_{-1}^1 F_{h,m}\left(u,t\right) P_m\left(\lambda\right)\, u^2 \mathrm{d}u\mathrm{d}\lambda,\ \forall t \tag{2.62}$$

As mentioned before in this chapter, the Fokker-Planck equation is solved by using finite central differences in velocity u and forward differences in time t. In addition, to ensure the convergence of the method, the time evolution of the distribution function will be solved implicitly. The discretization in velocity leads to a linear system of the form

$$\mathbf{M}\cdot\mathbf{F}^{(k+1)} = \mathbf{B}^{(k)} \tag{2.63}$$

where the superscripts refer to the discretization in time. The details of the discretization as well as the construction of the stiffness matrix $\mathbf{M}$ and boundary conditions vector $\mathbf{B}$ are explained in appendix C.

2.4 Heating in ITER scenarios: analysis of the anisotropy and efficiency of the ion heating and current drive

In this section, the Maxwell and Fokker-Planck equations are solved self-consistently by performing iterations between EVE and AQL. The time-dependence of the distribution function is obtained inside AQL. This is done for different heating scenarios. This section aims at giving a quantitative approach of the quasi-linear effects of energetic particles. We demonstrate in particular that the inclusion of these effects leads to important modifications of the ion distribution function, which departs considerably from the usual isotropic Maxwellian distribution function. The convergence of the method when increasing the number of Legendre polynomials is verified. We also identify scenarios where the ions are more efficiently heated and analyse the generation of toroidal current by means of ion cyclotron waves. Finally, some issues on the limitations of the model are addressed. Two ITER ICRH scenarios are simulated and compared in this section:

- Second harmonic (p=2) tritium heating (DT) scenario.
- First harmonic or fundamental (p=1) helium 3 minority heating DT(^{3}He) scenario.

In the DT heating scenario, the present species are electrons, deuterium, tritium, thermal ^{4}He and energetic α particles. In the DT(^{3}He) heating scenario, we replace 2% of the thermal ^{4}He population by ^{3}He. In both scenarios, the power absorbed by the heated species is prescribed, $p_{\mathrm{abs,h}} = 10$ MW. We choose a spatial grid with 460 points in the radial direction inside the plasma volume, 53 in the vacuum region and 512 points in the poloidal direction. The Fourier transforms in this direction is performed with the poloidal wavenumbers $-64 < m < 64$, whereas in the toroidal direction only two modes $n = \pm 30$ are considered. The ITER ICRH antenna has 24 straps, divided into 8 poloidal triplets, connected by pairs. For more information on the structure of the ITER antenna, the interested reader can read the reference [26]. The parallel velocity grid has 1024 points and the λ grid 401 points. The time step is $\nu_{\mathrm{h}\to\mathrm{D}}\Delta\tau = 4$, where $\nu_{\mathrm{h}\to\mathrm{D}} \equiv \nu_{\mathrm{h}}$ has been introduced earlier in this chapter.

2.4.1 Analysis of the anisotropy and distribution of power

The first point that we want to verify is that the solution of the Fokker-Planck equation (without any EVE-AQL iteration) converges when increasing the number of Legendre polynomials. This convergence is quantified by the ratio between the perpendicular and the parallel energy, namely $W_\perp/W_\parallel$. These energies are defined as follows

$$\left\{ \begin{array}{c} W_\perp \\ W_\parallel \end{array} \right\} = 2\pi a^2 m_h \pi v_{\mathrm{th}}^5 \int_0^1 \rho \mathrm{d}\rho \int_0^\infty \mathrm{d}u \int_{-1}^1 \mathrm{d}\lambda \left\{ \begin{array}{c} 1-\lambda^2 \\ \lambda^2 \end{array} \right\} F\left(u,\lambda,t=\infty\right) u^2 \qquad (2.64)$$

where a is the minor radius, ρ is the normalized minor radius, i.e. $\rho = r/a$, and m_h is the mass of the heated species. This ratio can be interpreted as a measure of the anisotropy. In ITER simulations, this anisotropy is less important than in Tore Supra simulations.

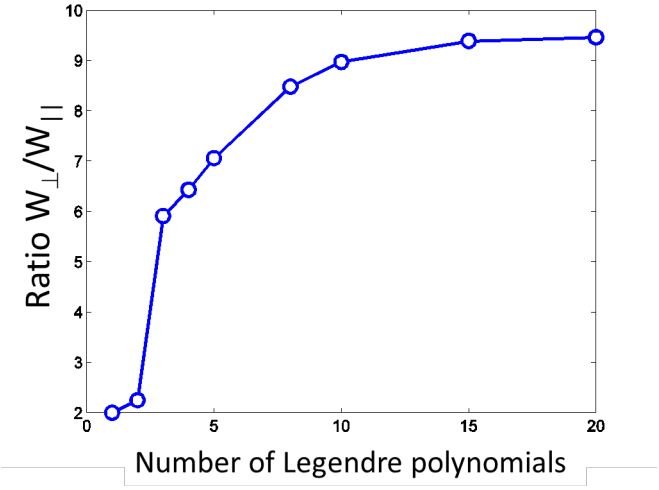

Figure 2.3: Dependence of the anisotropy on the number of Legendre polynomials for typical Tore Supra parameters

Therefore, the number of polynomials for Tore Supra discharges represents an upper limit of the number of polynomials to be used. For typical Tore Supra parameters, we can see in figure 2.3 that a convergence is achieved for $L \approx 20$. Therefore, in the following, we will choose $L = 20$ for all the calculations, meaning that the maximum degree of the polynomials is 40.

We present now the results corresponding to the convergent iterations between EVE and AQL. In the case of the DT heating scenario, we illustrate the evolution of the ion distribution function of the energetic ions (i.e. Tritium) during the first iteration between EVE and AQL for $\lambda = \pm 1$ (only parallel velocity) and $\lambda = 0$ (only perpendicular velocity) in figures 2.4a and 2.4b respectively. The initial distribution function is represented by a thick black line and the final one by a thick dashed red line. We can observe that for both scenarios, the distribution function exhibits an energetic tail which is more important for perpendicular velocities. This is consistent with the fact that the ion cyclotron waves provide heating mainly in the perpendicular direction. Figures 2.4c and 2.4d show the evolution of the distribution function during the second iteration between EVE and AQL. From these figures, we can conclude that the iterative coupling EVE-AQL converges very quickly and only very few iterations (typically 4 or 5) between the two codes are enough to achieve a self-consistent steady-state solution. In figure 2.5 we represent the same evolution, but in the DT(^{3}He) heating scenario. In this scenario, we have found as well that the final distribution function of the first iteration EVE-AQL differs little from the final distribution function of the last iteration. Therefore, the equivalent of the figures 2.4c and 2.4d is not given in this manuscript for the DT(He^3) scenario. The same energetic tail for particles with mainly perpendicular energies can be observed in this scenario.

Several differences can be observed between both scenarios. **The first difference is related to the dynamics of the energetic tail**. We can observe that the energetic tail for $\lambda = 0$ in the DT scenario after $\sim 4\nu^{-1}_{T\to D}$ is close to the final one. However, in the minority heating, only after $\sim 40\nu^{-1}_{He^3\to D} = 10\nu^{-1}_{T\to D}$ does the energetic tail approach the final one. This means that the dynamics of the He^3 tail is between 2 and 3 times slower than the dynamics of the T tail, due to the different ion charge.

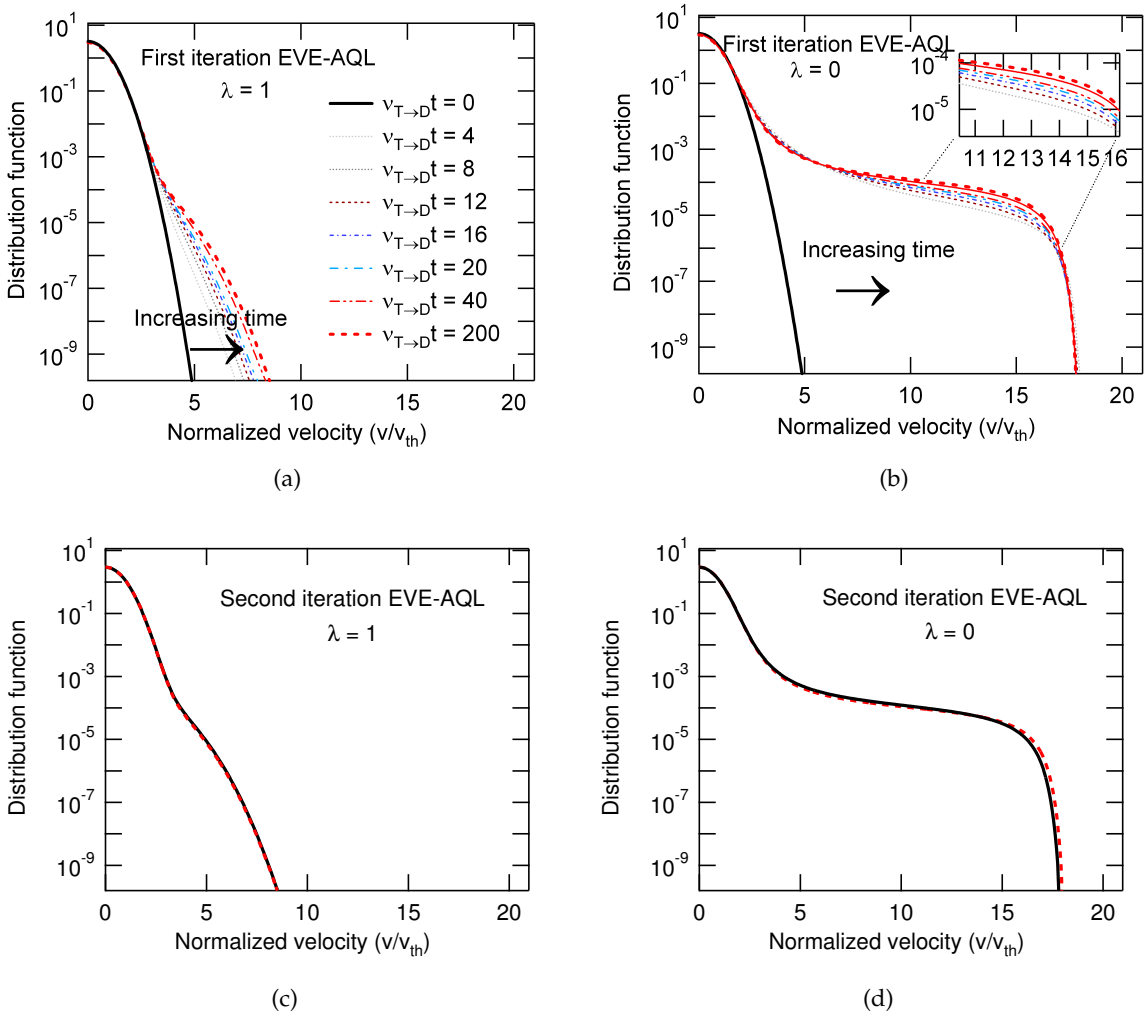

Figure 2.4: Evolution of the Tritium distribution function in the DT heating scenario. Top: first iteration between EVE and AQL. Bottom: second iteration between EVE and AQL.

The second difference is observed in the energy of fast particles in both scenarios. In the DT heating scenario, the energetic tail reaches energies up to $E \sim 225\,E_{\rm th}$, whereas in the minority heating scenario, the tail covers ions with $E \sim 625\,E_{\rm th}$. This difference comes from the fact that in first harmonic minority cyclotron damping, there is more power available per resonant particle, only because the ^{3}He density is smaller than the tritium density. Nevertheless, let us note that this kind of (very energetic) trapped particles might be weakly confined, especially in small devices. However, our analysis cannot deal with this kind of issues for which a Monte Carlo module together with a loss term should be developed.

The third difference is related to the harmonic of the cyclotron absorption. In the DT(^{3}He) case, the heating is characterized by the fundamental harmonic $p = 1$. Therefore, the Bessel functions appearing in the quasi-linear diffusion operator are J_0 and J_2. In the case DT, the harmonic is $p = 2$ and therefore, the Bessel functions are J_1 and J_3. Since $J_0(0) = 1$ and $J_m(0) = 0$ for $m \in \{1, 2, 3\}$, the T distribution function around $u = v/v_{\rm th} = 0$ is weakly modified, whereas the ^{3}He distribution function for vanishing

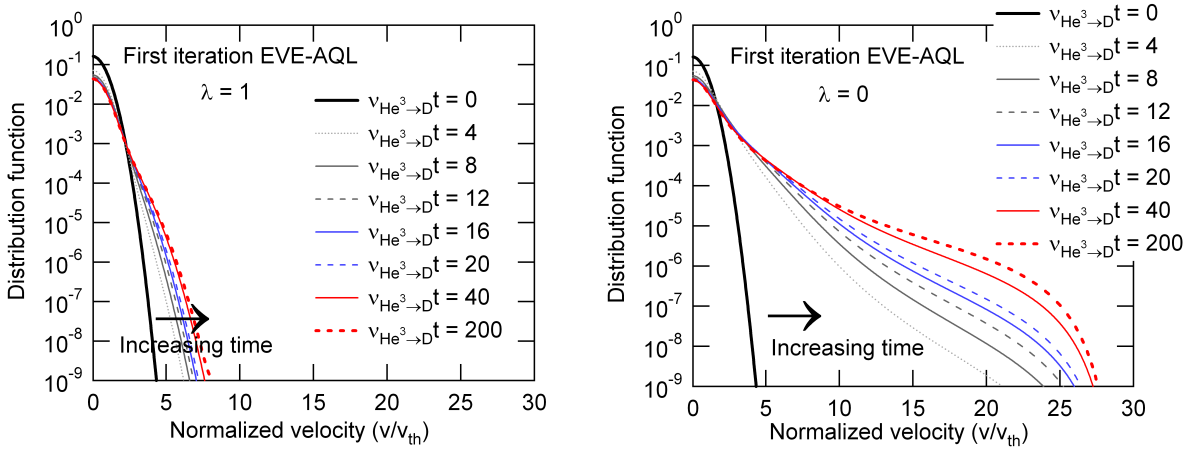

(a) (b)

Figure 2.5: Evolution of the He^3 distribution function in the DT(^{3}He) heating scenario

energies is strongly modified due to the action of the J_0 Bessel function.

The distribution of the absorbed energy among the different species allows one to quantify how much absorbed power remains in the heated species after collisions. This analysis is interested since sufficiently high temperatures of reacting species must be achieved for nuclear fusion. An estimate can be made by means of the power transferred by collisions, calculated as follows

$$p_{\text{coll,s}} = \pi m_h v_{\text{th}}^5 \int_0^\infty u^2 \mathrm{d}u \int_{-1}^1 \mathrm{d}\lambda \left\langle \mathcal{C}\left(F_h, F_s\right)\right\rangle \tag{2.65}$$

For the DT heating scenario, we show in figure 2.6a the power absorbed in steady state by the plasma *via* wave damping. In figure 2.6b the deposition and redistribution among the different species of the power absorbed by the energetic ions is given. These curves correspond to the last iteration between EVE and AQL, namely the 5^{th} one.

One can observe that the power absorbed by tritium is mainly localized in the inner radial positions. We also observe that the power absorbed by electrons per volume unit for $\rho > 0.2$ is greater than the one absorbed by tritium. The redistribution of the energy by collisions is quantified as follows. In this scenario, we have obtained that 28.57% of the power absorbed by tritium is transferred *via* the collisions to the electrons, 29.28% is transferred to the deuterium, 19.58% to the ^{4}He and 22.57% remains in the tritium population. **This means that only 1.5 MW are directly available for the reacting species**. In the minority heating scenario, as expected, the wave energy is mainly absorbed by the minority species, i.e. ^{3}He. This is shown in figure 2.7a. The absorption by electrons has been slightly reduced with respect to the DT scenario, as well as the absorption by tritium. The remaining power has been absorbed by ^{3}He. In this case, the power transferred by collisions to the electrons is 23.70% of the total absorbed power. 29.86% is transferred to deuterium, 24% to tritium, 17.55% to ^{4}He and only 4.90% remains in the energetic particles population. **This means that in the minority heating scenario, 2.4 MW are available for the reacting species**. We have therefore increased the direct heating of the reacting species by a factor 1.6. However, as explained earlier, **this does not mean that the heating efficiency is increased by the same factor, since the energy that is transferred by collisions remains in the plasma and is not lost**. We can observe that

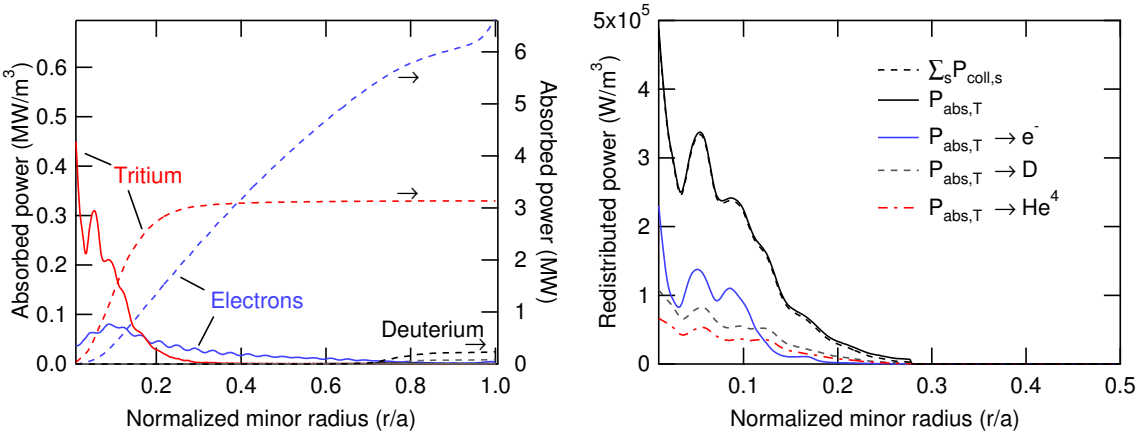

(a) (b)

Figure 2.6: Absorbed power in the DT heating scenario and redistribution of the power absorbed by T among the different species.

the integrated absorbed power for electrons increases slightly when approaching $\rho = 1$. This might be due to the limitations of the model and deserves further analysis and improvement.

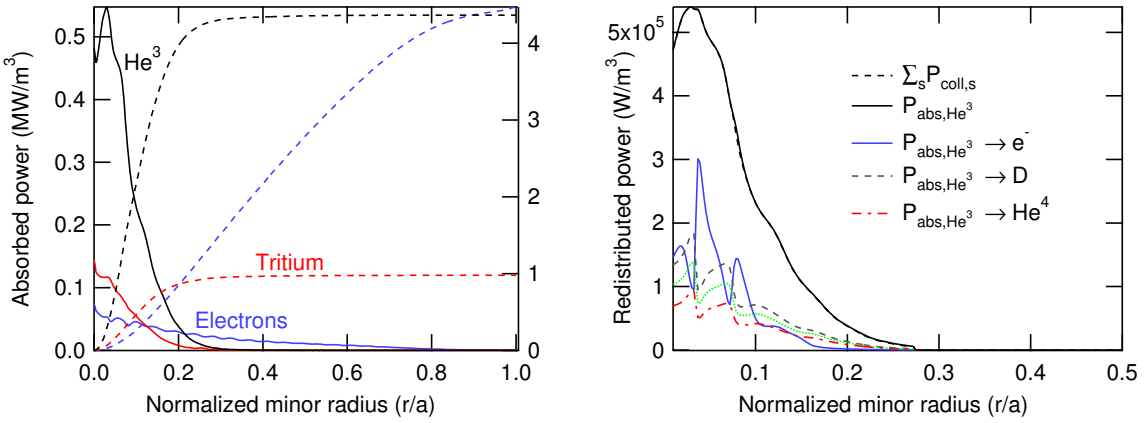

(a) (b)

Figure 2.7: Absorbed power in the DT(^{3}He) heating scenario and redistribution of the power absorbed by ^{3}He among the different species.

2.4.2 Kinetic effects on the generation of toroidal current by ICRH

In order to generate energy from nuclear fusion reactions, the ions in the core region of the tokamak must be efficiently heated, as stated in the previous paragraphs. In that respect, analysis of the heating of reacting species was the aim of the last subsection. However, another issue that must be taken into account is the stationary operating regime of present and future fusion devices in the context of the fusion reactors for commercial

production. The steady-state regimes in fusion plasmas relies upon the capability of the poloidal magnetic field $\mathbf{B}_p$ to confine the charged particles. This poloidal field depends on the toroidal current following the Ampère's law. In the framework of toroidal current production, one can consider a tokamak as a transformer with primary winding (the inner poloidal field coils or Ohmic heating coils) and a secondary winding (the plasma inside the vacuum vessel). When the current in the primary winding is increased, the plasma responds by increasing the toroidal current. This current generation method is called inductive current drive. However, this method only provides pulsed discharges and the necessity to operate in steady-state regimes [27] led more than fifty years ago to other methods of current drive [28], the so-called non-inductive current drive.

The first of these methods was proposed by Ohkawa in 1970 [29] and consisted of neutrals injection that would transfer momentum to electrons and ions, making it possible to operate without any inductive electric field. Therefore, this mechanism relies upon the direct injection of toroidal momentum. Subsequent works in this direction provided new clues to generate current with no external torque injection. The first of these works, carried out by Wort in 1971 [30], suggested that a traveling wave with a parallel phase velocity lower than the electron thermal velocity could result in a momentum transfer from the wave to electrons. The counterpart consisting of momentum transfer from thermal electrons to thermal ions through collisions was also considered. To overcome this difficulty, it was proposed to inject another wave that would transfer momentum to thermal ions, i.e. a traveling wave with a phase velocity equal to the ion thermal velocity. The final required RF power was estimated at $56\,MW$.

More recent analysis in this direction was carried out by Fisch in 1980 [31]. The acceleration of electrons by high phase velocity waves was proposed by Fisch [32] and analysed numerically by both Karney and Fisch [33] with the solution of a two-dimensional Fokker-Planck equation. In this case, the velocity at which electrons and waves interact with each other is higher than the thermal velocity. Therefore, the electrons carrying the toroidal current barely transfer their energy to ions through collisions. In this way, contrary to the mechanism proposed by Wort, the current can be maintained during long discharges with relatively low input power. This method has been extensively used from the beginning of the 80s to the present fusion devices in the context of the lower hybrid current drive (LHCD) [34, 35, 36]. An alternative approach was proposed by Fisch and Boozer, consisting of high phase velocity waves with no net toroidal momentum. They determine an analytical expression for the current drive efficiency [37]. This mechanism relies upon the existence of an asymmetry in the plasma resistivity. This asymmetry leads to different collisional regimes depending on the direction the electrons move and has been envisioned under the name of electron cyclotron current drive (ECCD) [38, 39, 40, 41, 42, 43, 44, 45, 46]. As explained before, the different heating scenarios that are currently considered for ITER operation include the minority heating. The possibility of efficiently sustaining non-inductive generated toroidal current in minority heating scenarios was pointed out by Fisch [47]. It relies upon the preferential absorption of the traveling wave by the minority ions. Some other works followed on the analysis of the minority heating current drive both experimentally [48, 49] and numerically [50]. Although certainly present in minority heating scenarios, in the following we will not consider the effect of the wave absorption by the minority species on the current generation. Concerning in particular the numerical works on the non inductive current drive in fusion plasmas, many kinetic effects are to be taken into account when modeling the efficiency. Some of these were introduced from the very beginning by Harvey in 1981 to

consider the nonlinear effects and loss terms due to magnetic field stochasticity [51]. The reduction of current due to trapped electrons was subsequently demonstrated by Cordey *et al* in 1982 [52] and later generalized to trapped ions in 1983 by Chiu *et al* [53]. Nevertheless, as for the minority-species heating, we will not consider in the following kinetic effects related to trapped ions.

Fast waves in the ion cyclotron range frequency have also been envisioned for non-inductive toroidal current drive. This mechanism is referred to as fast wave current drive (FWCD) [54]. The main advantage that these waves present with respect to the LH waves is the deeper penetration to the centre of the plasma, where density is higher. After absorption on the thermal electrons by Landau damping, toroidal current can be efficiently sustained. This subsection aims only at comparing different heating scenarios in terms of FWCD when the energetic particle effects are taken into account in the kinetic equation. This will be done by calculating the current drive efficiency following the semi-analytical formula proposed by Ehst and Karney in 1991 [55]

$$\eta_n = \eta_0 \left(Z_{\text{eff}}, w\right) R\left(\epsilon, w\right) C\left(\epsilon, \theta, w\right) M\left(\epsilon, \theta, w\right) \tag{2.66}$$

where

$$\eta_0 \left(Z_{\text{eff}}, w\right) = \frac{23.82}{w\left(0.678 + Z_{\text{eff}}\right)} + \frac{8.26}{Z_{\text{eff}}^{0.707}} + \frac{8w^2}{Z_{\text{eff}} + 5}$$

$$R\left(\epsilon, w\right) = 1 - \frac{\epsilon^{0.77}\sqrt{12.25 + w^2}}{3.5\epsilon^{0.77} + w}$$

$$C\left(\epsilon, \theta, w\right) = 1 - \mathrm{e}^{-\left(0.0987\frac{\left(1-\lambda_t^2\right)w^2}{\lambda_t^2}\right)^{2.48}}$$

$$M\left(\epsilon, \theta, w\right) = 1 + 12.3\left(\frac{\lambda_t}{w}\right)^3$$

where $w = \omega k_{\parallel}^{-1} v_{\text{e,th}}^{-1} \approx \omega R n^{-1} v_{\text{e,th}}^{-1}$, λ_t the cosine of the pitch angle below which particles are trapped, ϵ the inverse of the aspect ratio and Z_{eff} the effective ion charge defined as

$$Z_{\text{eff}}\left(r\right) = \frac{\sum_s n_s\left(r\right) Z_s^2}{\sum_s n_s\left(r\right) Z_s} \tag{2.67}$$

The total toroidal current, as a function of the radial position is calculated following Jaeger *et al* [56]

$$\frac{j_{\text{FW}}}{P_{\text{ICRH}}} \equiv J_{\parallel}\left(\rho\right) = \frac{19.19 \cdot 10^{15}}{\log \Lambda} \frac{k_B T_e\left(\rho\right)}{e n_e\left(\rho\right)} \sum_n |\sigma_n|^2 J_{\parallel,n}\left(\rho\right) \tag{2.68}$$

where $J_{\parallel,n}\left(\rho\right) = \left\langle \eta_n P_{\text{abs},e,n}\left(\rho, \theta\right)\right\rangle_\theta$ and $|\sigma_n|^2$ is the antenna weighting factor. This current is expressed in $A \cdot W^{-1} \cdot m^{-2}$. Figures 2.8a and 2.8b illustrate the radial dependence of the fast wave current drive efficiency for the DT and DT(He^3) heating scenarios respectively. The different curves represent the efficiency calculated at each EVE-AQL iteration. One can observe that the most important change is obtained between the first and second iterations for both scenarios. After the second iteration the radial profiles barely evolve. **The main difference between these two scenarios is that the total parallel current per injected power in minority heating is reduced by** 40% **with respect to the DT scenario**.

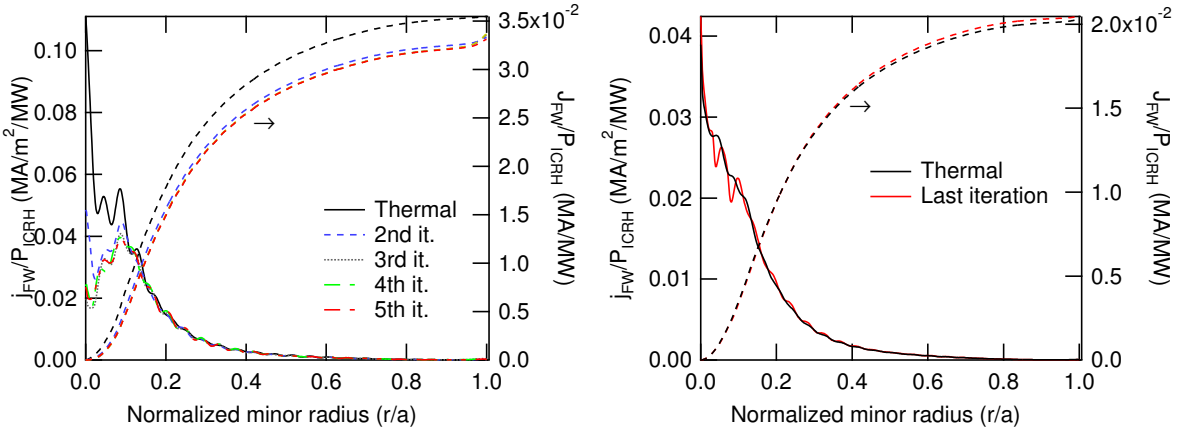

(a) (b)

Figure 2.8: Fast Wave Current Drive efficiency for both heating scenarios considered in this chapter, DT (left) and DT(^{3}He) (right).

2.4.3 Energetic particle effects on the heating and current drive efficiencies

As we have explained earlier, **the term E_- is essential in order to describe the physics of the energetic particles**. In this subsection we will analyse the modification of the previous results when cancelling the contribution of the left circularly polarized component of the electric field, namely E_-. The most important difference is observed in the DT heating scenario. In the case of minority heating, no significant differences have been observed. Therefore, in this subsection we will only analyse the DT heating scenario. We represent in figure 2.9a with solid (resp. dashed) lines the absorbed power when the E_- component is not (resp. is) accounted for. One can observe that electrons absorb more power when the effect of the left circularly polarized electric field is not considered. Nevertheless, as we can see in figure 2.9b, the power transferred by collisions to the electrons is reduced in the case without E_- (solid lines) with respect to the case with E_-. We have found that the power transferred from tritium to electrons has been decreased by 20.34% with respect to the case where the left circularly polarized component of the electric field is taken into account. This difference in the energy transferred by collisions to the electrons has been almost equally redistributed among the remaining species: 37.23% of the power is transferred to deuterium, 25.41% is transferred to ^{4}He and 29.13% remains in the tritium population. Therefore, although electrons are less indirectly heated without the effect of E_-, some of the energy is recovered by α particles. **The overall heating performance is therefore decreased when considering the effect of energetic particles, since more than 50% of the energy of the reacting ions goes to the electrons due to the effect of E_-**. However, a model where eventual very energetic particles losses are accounted for [1] should provide more realistic situations where the mentioned effect is less critical. Further studies need to be carried out to determine the effective contribution of very energetic particles in the overall heating of the reacting species.

Finally, **the fast wave current drive is also modified and slightly increased when the effect of the left circularly polarized component E_- is not considered**, as observed in figure 2.10a. This is due to the fact that electrons absorb more power in the inner

[1] Due either to orbit width effects or to energetic particle modes.

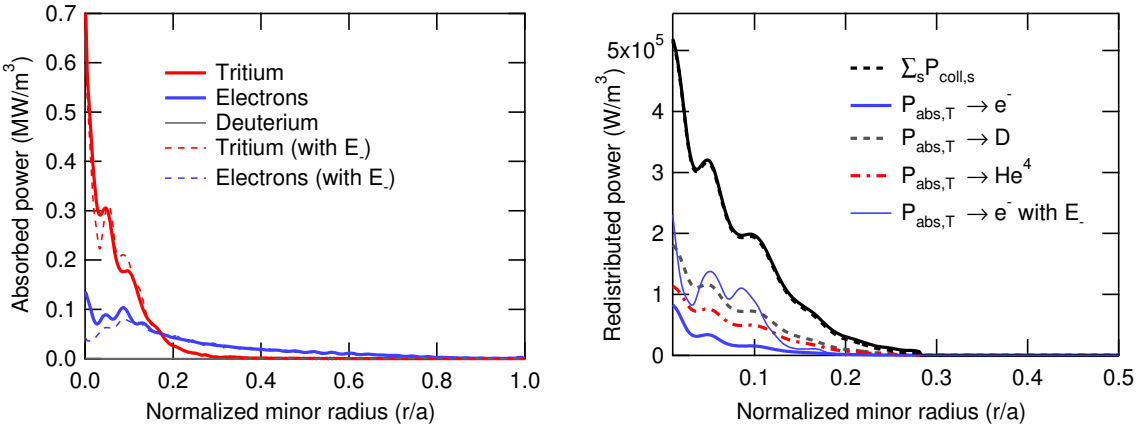

(a) (b)

Figure 2.9: Aborbed power (left) and redistribution of the absorbed power (right) for the DT scenario depending on whether the component E_{-} is or is not accounted for.

radial region. We can understand these differences by looking at the structure of the distribution function of the heated species. In figure 2.10b we observe the final tritium distribution function for both cases with E_{-} (thick lines) and without E_{-} (thin lines with open squares). The distribution function is plotted for particles with only parallel (resp. perpendicular) velocity, i.e. $\lambda = \pm 1$ (resp. $\lambda = 0$). The effect of the E_{-} component is clearly observed by looking at the energetic tail. The inclusion of this component acts like an additional fast particle source, pumping passing particles at $E \sim 4E_{\rm th}$ and injecting them at $E \sim 7E_{\rm th}$ and pumping trapped particles at $E \sim 5E_{\rm th}$ and injecting them at $E \sim 10E_{\rm th} - 18E_{\rm th}$.

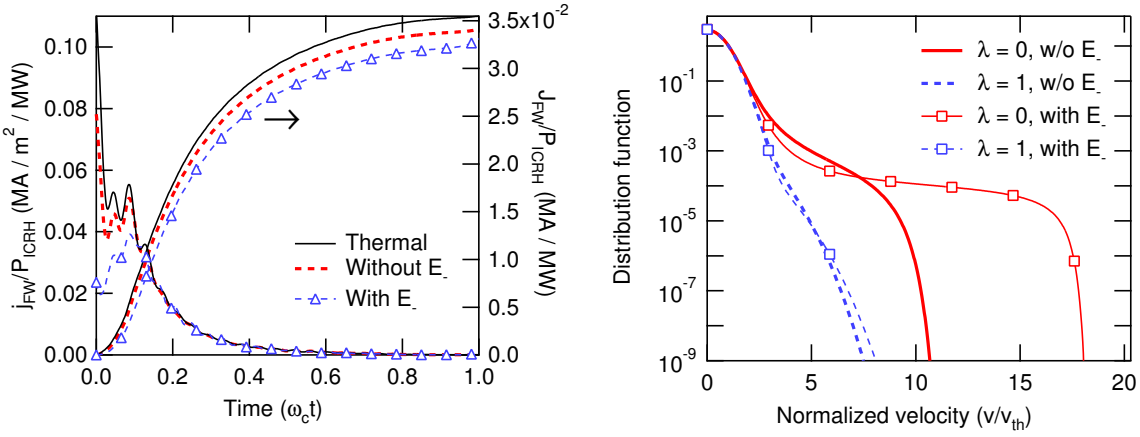

Figure 2.10: (Left) Fast Wave Current Drive efficiency for both heating scenarios considered in this chapter. Comparison between the cases *with* and *without* E_{-}. (Right) Steady-state tritium distribution function for passing ($\lambda = \pm 1$) and deeply trapped ($\lambda = 0$) particles.

2.4.4 Properties and limitations of the model

The model we use presents several limitations, both from the physical and numerical point of view. From the physical point of view, the limitations have been mentioned throughout the whole chapter. For instance, the model we consider is based on a bounce-averaged Fokker-Planck equation. Therefore, no orbits effects are considered. In particular, the radial transport induced by the ion cyclotron damping on the banana particles is completely neglected [57]. For the calculation of the current drive, we are estimating only a fraction of the total toroidal current carried by the electrons. This fraction corresponds to the current driven by direct absorption of the wave by electrons. However, as we have seen, in the case of minority heating, some of the current can also be driven directly by minority ions, which has not been considered. Nevertheless, this current tends to be negligible with respect to the fast wave current.

Another important limitation is the assumption that the distribution function can be decomposed onto a Legendre polynomial basis. By doing this and integrating later with respect to the pitch-angle, we are neglecting the particle trapping effects, which become important for very large energies. For relatively low energies, the isotropic assumption is satisfying and provides a sufficient description of the plasma response. For intermediate energies, the decomposition we have made is legitimate, although one must be careful when drawing conclusion from this analysis. In particular, the decomposition onto the polynomial basis introduces some properties that cannot be found in distribution functions. For instance, for very large energies, the distribution function can have negative values, which are artificially set to zero in this chapter.

Finally, we have already pointed out that an additional term representing the losses should be added to the right-hand side of the Fokker-Planck equation. The interest of this term is twofold. First, it represents the losses of very energetic ions, which can potentially be deconfined in real devices due to orbit width effects and energetic particle modes. Second, it would make it possible that the absorbed power that cannot be redistributed among the thermal species goes to an external thermal sink. Why the absorbed power cannot be effectively redistributed by collisions can be understood as follows. When solving the Fokker-Planck equation 2.19 we are using a certain number of boundary conditions. If this number is the correct one, the equation has a unique solution F_h. However, an external constraint is given by condition 2.23. This condition is strictly not needed to have the solution of 2.19. Therefore, we are imposing too many conditions to the distribution function of the heated species. The whole problem 2.19-2.23 for each instant should be interpreted as a way to find the point (D_0, F_h) solution of the optimization problem

$$\min_{p_{\mathrm{QL},h}=p_{\mathrm{abs,h}}} \left| p_{\mathrm{QL},h} + \sum_{s'} p_{\mathrm{coll},s'} \right|$$

This is schematically represented in figure 2.11. The set of possible solutions of the Fokker-Planck equation satisfying the boundary conditions and $\int \mathrm{d}^3\mathbf{v} F_h = n_h$ is given by the dark blue plane. The set of stationary solutions satisfying $\sum_{s'} p_{\mathrm{coll},s'} + p_{\mathrm{QL},h} = 0$ is given by the light blue area enclosed by the black dashed line. The initial condition is given by the black point inside the dark blue region. Depending on the boundary conditions, the solution evolves in time following the black thin line and always around the yellow dotted line, on which the condition $p_{\mathrm{QL},h} = p_{\mathrm{abs,h}}$ is satisfied. If the yellow dotted line encounters the black dashed line, the solution of the problem exists. Otherwise, one can only find the point where the distance between the yellow line and the dashed line is

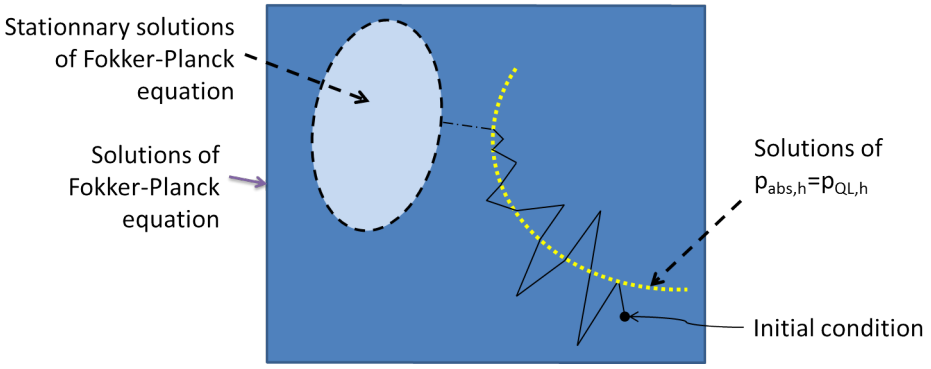

Figure 2.11: Schematic representation of the evolution of the energetic particle distribution function.

minimum. Special care must be taken during the evolution of the distribution function, since once the minimum point is reached, any numerical perturbation could lead to a divergent solution depending on the nature of the minimum.

2.5 Summary

In this chapter we have reported on results from the coupling between a full-wave 3D solver called EVE and an anisotropic Fokker-Planck module called AQL to model the ICRF heating in toroidal fusion devices. The basic mechanisms of wave absorption, quasi-linear diffusion and Coulomb collisions have been introduced and the method to solve the Fokker-Planck equation taking into account the anisotropy introduced by the cyclotron damping has been detailed. These two codes have been applied to two ITER RF heating scenarios: second harmonic DT heating and fundamental DT(^{3}He) heating. It has been found that the introduction of kinetic effects that complement the wave absorption description is essential to obtain important properties such as the anisotropy of the energetic tail in the distribution function. The redistribution of the absorbed energy among the thermal species has been analysed. As far as the generation of current is concerned, the fundamental heating provides fast wave current reduced by 40% with respect to the second harmonic scenario. The effect of energetic particles has been analysed as well through the left circularly polarized component of the electric field. It turns out that no significant difference is appreciated in the minority heating. However, in the second harmonic heating, the energetic tail is reduced when switching off artificially the left circularly polarized electric field. This leads to an increase of the fast wave current drive efficiency. Finally, the limitations of the model have been pointed out, especially the absence of a losses term in the Fokker-Planck equation. It has been invoked that the time evolution of the energetic particle distribution function should be understood as a way to find the solution of an optimization problem, equivalent to the equations solved in this chapter. The presence of the loss term has been justified by stating that the power absorbed by the energetic ions cannot always be redistributed among the present thermal species. Therefore, the additional loss term constitutes a kind of relaxation condition for the mathematical problem.

Chapter 3

Collisionless theory of geodesic acoustic modes driven by energetic ions

> The man who has got up a formula is at the mercy of his memory, while the man who has thought out a principle may keep his mind clear of formulæ.
>
> J. C. Maxwell (1831-1879)

Contents

3.1 Introduction: geodesic acoustic modes in tokamaks

Geodesic acoustic modes (in the following *GAMs*) have been since their discovery by Winsor *et al* in 1968 [12] a major subject of discussion in the fusion community. Their importance is mainly due to recent publications where it is claimed that these modes appear to interact in some way with plasma turbulence [58, 59, 60, 61, 62, 63]. In particular, experiments in the DIII-D tokamak have revealed that GAMs might play a role in suppressing background turbulence [64]. In this context, the nonlinear excitation of GAMs by drift waves has been extensively studied in the literature [65, 66, 67, 68, 69, 70, 71, 72]. As we will see later on in this chapter, GAMs are Landau damped and this damping decreases with the safety factor. Therefore, the damping in the core tends to be stronger than in the edge region, which implies that GAMs are mainly observed in experiments close to the edge [73]. This high damping in the inner region of the tokamak makes it difficult to analyse their interaction with the core turbulence. In addition, if the only way one can observe GAMs in steady-state scenarios is *via* the nonlinear generation by turbulence, then any external control of their excitation would be highly improbable. Though the interaction between GAMs and turbulence is beyond the scope of this chapter, we will give the first elements of the linear GAM excitation by external means and the nonlinear effects present in their saturation. To do so, we will be inspired by the very recent works reporting on the excitation of GAMs by energetic ions [13, 14, 15, 74, 75]. These new modes are called energetic GAMs (EGAMs). We will show that their amplitude can be controlled by injecting energetic ions. In this chapter we assume that no turbulence exists, which simplifies the analysis and enables the study of the nonlinear saturation of EGAMs. This chapter is structured as follows. In the present section, we give a heuristic approach of the origin of GAMs and their damping. In section 3.2, a fully kinetic dispersion relation for GAMs is derived and solved numerically. A variational approach is detailed and used to predict the linear threshold for EGAM excitation. This linear threshold is explicitly calculated for two examples of distribution function. In section 3.3, the gyrokinetic code used in this thesis is introduced. The predicted linear thresholds is recovered in gyrokinetic simulations presented in section 3.4. The nonlinear saturation is analysed and quantified in section 3.5. Finally, open questions on the excitation of the modes in regimes under the linear threshold are discussed in section 3.6.

3.1.1 The magnetic curvature as the origin of GAMs

Strictly speaking, GAMs are oscillations of the electrostatic potential at the so-called GAM frequency that we will derive in detail in the next section. For the moment, let us make only a heuristic approach to show that these modes are naturally present in toroidal devices. Let us consider the axisymmetric component of the electrostatic potential ϕ_{00}. The radial electric field is written as $E_r = -\partial_r \phi_{00}$ and gives a poloidal flow $v_\theta \approx E_r/B$, with B the toroidal magnetic field. In general, this poloidal flow is not divergenceless. This means, that a density perturbation δn in the θ direction exists following the continuity equation. This perturbation is proportional to $-\partial_\theta v_\theta$. The derivative with respect to θ of the poloidal flow is

$$\partial_\theta v_\theta = -\frac{E_r}{B^2}\partial_\theta B \tag{3.1}$$

In a tokamak $B = B_0\,(1+\epsilon\cos\theta)$, which implies that $\delta n \propto \epsilon\frac{E_r}{B_0}\sin\theta$. This density perturbation generates an up-down asymmetric pressure perturbation $\delta p \sim \sin\theta$, repre-

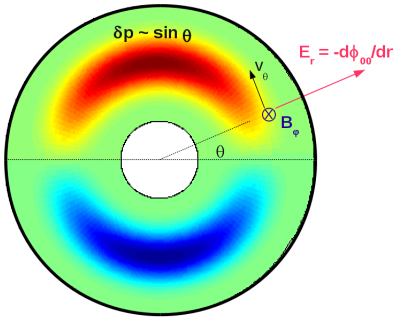

Figure 3.1: Schematic representation of a tokamak poloidal cross-section. The two lobes (red and blue) represent the pressure perturbation. This up-down asymmetric structure scaling as $\sim \sin\theta$ comes from the geodesic curvature naturally present in toroidal devices. This topological origin gives rise to the name of Geodesic Acoustic Mode (GAM).

sented by the red (positive) and blue (negative) regions in figure 3.1. This perturbation gives rise to a radial current of the form $J_r \sim \frac{1}{B}\partial_\theta \delta n$. The radial current brings particles across the magnetic surfaces, leading to an electric field which provides the restoring force. The competition between the initial electric field and the *induced* electric field results in oscillations of the axisymmetric poloidal flows. These oscillations are called GAMs. As we have shown in a very easy way, they exist naturally in a tokamak plasma because the poloidal flows are coupled to up-down asymmetric pressure perturbations through the geodesic curvature.

3.1.2 Heuristic approach to the linear wave-particle interaction and the Landau damping

The GAMs that we have introduced are a special case of modes that can be found in an ionised medium. These modes can interact with the particles that constitute the plasma and are either damped or excited. Historically, this interaction is known in a more general way as the wave-particle interaction. In this section, we give some elements for the analysis of this interaction between a wave, characterized by a frequency and a wavenumber (ω, k), and the plasma. For this purpose, we use a simple model consisting of the Vlasov equation with one dimension in space and one dimension in velocity. In addition no magnetic field is considered, so that the Vlasov equation reads

$$\frac{\partial F}{\partial t} + v\frac{\partial F}{\partial x} + E\left(x,t\right)\frac{\partial F}{\partial v} = 0 \tag{3.2}$$

where charge and mass are set to unity for the sake of simplicity. We decompose now the distribution function into an equilibrium part and a perturbed distribution function as follows $F = F_{\text{eq}} + \delta F$ and assume that the electric field E is a first-order quantity with respect to the perturbation, i.e. $E = \mathcal{O}\left(\delta F\right)$. This assumption is justified if one considers that the Vlasov equation is coupled to the Poisson equation

$$\frac{\partial E}{\partial x} = -\int \mathrm{d}v \delta F \tag{3.3}$$

We can perform a Fourier transform in space and write the linearized Vlasov equation

for the perturbed distribution function

$$\frac{\partial \delta F_k}{\partial t} + ikv\delta F_k + ik\phi_k \frac{\partial F_{\text{eq}}}{\partial v} = 0 \tag{3.4}$$

A subsequent Fourier transform (obviously in time) would naturally introduce the term $\omega - kv$ and if one decides to express $F_{k,\omega}$ in terms of the equilibrium distribution function an originally-non-existing singularity stems from the division by $\omega - kv$. Such a division is strictly only allowed from a purely mathematical point of view if the condition $\omega - kv \neq 0$ is always satisfied. Otherwise, the nature of the perturbed distribution function (which must absolutely be analytic if it really represents a physical solution) is modified. Afterwards, using the theory of complex functions is the only way to overcome this "error". For the moment we will not bring our discussion to such an abstract mathematical framework, but will try to give the general physical idea of the interaction between particles and waves. To do so, the equation (3.4) can be easily solved by convolution

$$\delta F_k = \delta F_k\left(t=0\right) - ik\int_0^t \mathrm{e}^{-ikv(t-t')}\phi_k \frac{\partial F_{\text{eq}}}{\partial v}\mathrm{d}t' \tag{3.5}$$

Let us now assume that $\partial_v F_{\text{eq}}$ does not depend on time and let us write $f\left(t\right) = i\int_0^t \mathrm{d}t' k\phi_k \mathrm{e}^{ikvt'}$. Note that this function includes the information of the electric field and depends also on k and v, but for the sake of clarity we will only write explicitly the dependence on t. Combining equations (3.3) and (3.5) the electrostatic potential yields

$$-k^2\int \mathrm{d}\omega\phi_{k,\omega}\mathrm{e}^{i\omega t} = \int \mathrm{d}v\delta F_k\left(t=0\right) - \int \mathrm{d}\omega\mathrm{d}v\mathrm{e}^{i(\omega-kv)t}\hat{f}\left(\omega\right)\frac{\partial F_{\text{eq}}}{\partial v} \tag{3.6}$$

The definition of the Dirac delta function can be straightforwardly used to conclude that only particles with a velocity $v = \omega/k$, for $k \neq 0$, will be resonant in the context of the interaction between the electric field and the equilibrium. Note that this interaction is mathematically represented here by the product $\hat{f}\left(\omega\right)\partial_v F_{\text{eq}}$. This previous analysis can be understood as an effort to explain the origin of the resonance without introducing any singularity into the equations. When t becomes large in equation (3.5), the perturbed distribution function in velocity space will become more granulated, due to the term e^{-iktv}. This granulation introduces an important phenomenon in physics called *phase mixing*, which represents a destructive interference and therefore a loss of information contained in the perturbed distribution function for different values of v. This concept has been invoked in the literature as the equivalent of the Landau damping, however the latter one is found to be a particular case of the former one. The Landau effect was demonstrated for the first time in collisionless plasmas by Lev Davidovich Landau in 1946. This was done by making use of the Laplace transform in time to solve the linearized Vlasov equation. As mentioned earlier in this paragraph, this method introduces singularities in the physical system that were not present originally. Landau, in his original paper, performed an analytic continuation of the integral $\int \mathrm{d}v\mathcal{G}_{k,\omega}$, with $\mathcal{G}_{k,\omega} = \left(\omega - kv\right)^{-1}$, i.e. he tried to recover the initial analyticity of the solution. He proceeded by introducing a term $\pm io^+F_k$ in equation (3.4) which leads to a modified function $\tilde{\mathcal{G}}_{k,\omega} = \left(\omega - kv \pm io^+\right)^{-1}$. The sign of the new term depends on whether we integrate above or below the pole $v = \omega/k$ and the main (astonishing) result was that any initial plasma oscillation would be damped. This effect has been extensively analysed in the last 60 years and was not generally accepted till its experimental discovery [76], for it did not conveniently explain how energy can be

lost in collisionless plasmas. To shed some light on this paradox, in the meanwhile, important theoretical works were published aiming at giving an explanation of the physical mechanisms of such a phenomenon. In particular, an alternative solution for the initial value problem (3.4) was proposed by Van Kampen [77]. He obtained normal modes, eigenfunctions of the equation

$$(\omega - kv)\,\delta F_{\omega,k} = k^{-1}\int \mathrm{d}v \delta F_{\omega,k}\partial_v F_{\mathrm{eq}} \tag{3.7}$$

normalized so that $\int \mathrm{d}v\delta F_{\omega,k}\partial_v F_{\mathrm{eq}} = 1$. The function $\mathcal{G}_{k,\omega}$ can be interpreted as a distribution, i.e. in the sense of Schwartz, and one should therefore keep in mind that it only makes sense when using a test function φ_0 multiplied by $\mathcal{G}_{k,\omega}$. Finally, using the Lebesgue integral $\int \mathrm{d}\omega \mathcal{G}_{k,\omega}\varphi_0$ and the prescription of Dirac the eigenfunction reads, for $\omega \in \mathbb{R}$ and $\partial_v F_{\mathrm{eq}} \neq 0$ [77]

$$\delta F_{\omega,k} = \mathcal{PV}\frac{1}{\omega - kv} + \lambda(v)\,\delta(\omega - kv) \tag{3.8}$$

with $\delta(\omega - kv)$ the Dirac function and $\lambda(v)$ a function of v given by the normalization condition. If there is a velocity v_n for which $\partial_v F_{\mathrm{eq}}(v_n) = 0$ and $\lambda(v_n) = 0$ for $v_n \in \mathbb{R}$, the eigenfunction reduces to

$$\delta F_{\omega,k,n} = \frac{1}{\omega_n - kv} \tag{3.9}$$

with $\omega_n = kv_n$. This eigenfunction is the same as in the case $\omega \in \mathbb{C}$. These normal modes satisfy the property of completeness, i.e. any initial plasma oscillation may be decomposed as a linear combination of these modes. The particularity of these modes is that each single mode represents an undamped oscillation, which seems inconsistent with Landau prediction. Actually, these modes do not represent any physical solution. Therefore, they make sense only when any initial perturbation is expanded onto the complete basis of Van Kampen. The expected damping is recovered only when considering that a sufficiently large band of these modes is excited via this decomposition, i.e. when the initial perturbation is expressed in terms of $N \gg 1$ Van Kampen modes, characterized by different frequencies $\omega_1, \ldots, \omega_N$. The amplitude of the perturbation will tend to decrease with time due to the phase mixing between the N modes, quantified by $(\omega_i - \omega_j)\,t$. Then one would expect that after a finite time t_{echo} large enough, all the modes will have the same phase, i.e. $(\omega_i - \omega_j)\,t_{\mathrm{echo}} = 2\pi n_{i,j}$, with $n_{i,j} \in \mathbb{N}$ for all $i, j = 1, \ldots, N$. This phenomenon, which is related to the reversibility of the mechanism, is known as *plasma wave echo* and has indeed been observed experimentally [78]. Note that the echo time t_{echo} increases with N. In particular, if $N \to \infty$, then $t_{\mathrm{echo}} \to \infty$ and reversibility is lost. As we have pointed out before, the mechanism is reversible, which means that no loss of energy is possible and therefore the Landau damping must only be understood as a redistribution of the initial energy among all the modes characterizing the initial perturbation. The word *damping* appears only when the term $\pm io^+ F_k$ is introduced in the kinetic equation, representing a Krook-like collision operator, coming in a rather natural way from an analytic continuation of the integral $\int \mathrm{d}\omega \mathcal{G}_{k,\omega}$. This is consistent with the loss of reversibility produced by a infinite number of Van Kampen modes. Indeed, $N \to \infty$ is equivalent to an open system, since any closed system will have a finite number of modes. The open system can be equivalently characterized by an external sink of energy, represented by the collision operator.

We have already seen that the interaction between particles (more exactly the equilibrium) and waves comes from the term $\partial_v F_{\mathrm{eq}}$. In order to understand in a very intuitive

way why this term is important for the wave-particle interaction, let us consider the same 1D problem where a particle of mass m and charge eZ moves in the electric field $E(x,t)$, written under the form

$$E(x,t) = E_0 \cos(kx(t) - \omega t) \tag{3.10}$$

where E_0, k and ω are given. If we assume that the position evolves as $x(t) = x_0 + v_0 t$, the motion of the particle satisfies

$$m\frac{\mathrm{d}v}{\mathrm{d}t} = eZE_0 \cos((kv_0 - \omega)t + kx_0) \tag{3.11}$$

The time derivative of the kinetic energy of the particle yields

$$\frac{\mathrm{d}E}{\mathrm{d}t} = mv\frac{\mathrm{d}v}{\mathrm{d}t} = \frac{(eZE_0)^2}{m} t\cos^2(kx_0) + v_0\frac{eZE_0}{m}\cos(kx_0) \tag{3.12}$$

where we have considered that the initial velocity of the particle is close to the phase velocity of the wave, i.e. $\omega - kv_0 \to 0$. This is consistent with the resonant condition that we have found earlier in this paragraph. For small times, the kinetic energy yields

$$E(t) \approx v_0\frac{eZ}{m}E_0 t\cos(kx_0) \tag{3.13}$$

which means that the particle will gain or lose energy linearly depending on the initial position x_0. If a particles has an initial velocity $\omega/k+\delta v$, then by giving some of its energy to the wave it will become more resonant. Conversely, if a particle has an initial velocity $\omega/k - \delta v$, then by taking energy from the wave it will become more resonant. A plasma is composed of many particles and therefore collective process need to be considered. A plasma in thermodynamical equilibrium is described by a Maxwellian distribution function. Therefore, for a given velocity ω/k, the plasma will always have more particles with a velocity $\omega/k - \delta v$ than $\omega/k + \delta v$. This means that a wave in a Maxwellian plasma will be damped. This heuristic approach has been developed in one dimension, namely v, and leads to the important conclusion that an inversion of population is needed in order to excite a mode (ω, k). Mathematically, this is expressed by the condition $\partial_v F > 0$ at $v = \omega/k$. In section 3.2, we will extend this analysis in a more rigorous way to derive a condition for the mode excitation in the context of GAMs

3.1.3 Wave-particle trapping *vs* quasi-linear diffusion

The energy transferred from particles to waves leads to an increase of the perturbations. Without any loss of generality, we can define the instability as a phenomenon where the amplitude of the perturbations $\delta\mathcal{H}_{\omega,\mathbf{n}}$ and $\delta F_{\omega,\mathbf{n}}$ increases due to a drive coming from the equilibrium (linearly unstable) or from the perturbations themselves (nonlinearly unstable). If nothing prevents the instability from developing, the amplitude of the perturbations will grow indefinitely. However, the energy of the physical system must be finite. Therefore, one expects that a mechanism of saturation exists leading to a balance between driving and damping terms. This can be understood by considering the general expression of the evolution of a mode $\delta\mathcal{H}_{\omega,\mathbf{n}}$

$$\partial_t \delta\mathcal{H}_{\omega,\mathbf{n}} = \gamma_{\omega,\mathbf{n}}(F_{\mathrm{eq}})\,\delta\mathcal{H}_{\omega,\mathbf{n}} + \sum_{\omega',\mathbf{n}'} \Gamma_{\omega,\mathbf{n},\omega',\mathbf{n}'}\delta\mathcal{H}_{\omega',\mathbf{n}'}\delta\mathcal{H}_{\omega-\omega',\mathbf{n}-\mathbf{n}'} \tag{3.14}$$

One of the saturation mechanism affects directly the perturbations by nonlinear coupling of the different existing modes, modifying the second term on the right-hand side of expression 3.14. This term reflects the nonlinear damping and balance the linear damping provided by the first term. However, another possible mechanism of saturation is related to the modification of the equilibrium. If the linear growth rate $\gamma_{\omega,\mathbf{n}}$ is positive only when some conditions are fulfilled by the equilibrium distribution function, making this function evolve further from these conditions results in a damping of the instability (in a decrease of the linear growth rate, actually). In this case, the first term in expression 3.14 reflects a linear damping balancing the nonlinear drive given by the second term. The evolution of the equilibrium may be accomplished nonlinearly by means of two mechanisms: quasi-linear diffusion and wave-particle trapping. The former one has already been introduced in the previous chapter in the context of quasi-linear evolution of the equilibrium distribution function. As invoked there, this theory appeared when physicists asked themselves about the mechanism of saturation of an instability. By looking at the equation 2.11, it is obvious that the quasi-linear theory provides a saturation mechanism *via* a diffusion of the equilibrium in the presence of a large spectrum $(\mathbf{n}, \omega)$ where the modes do not interact with each other.

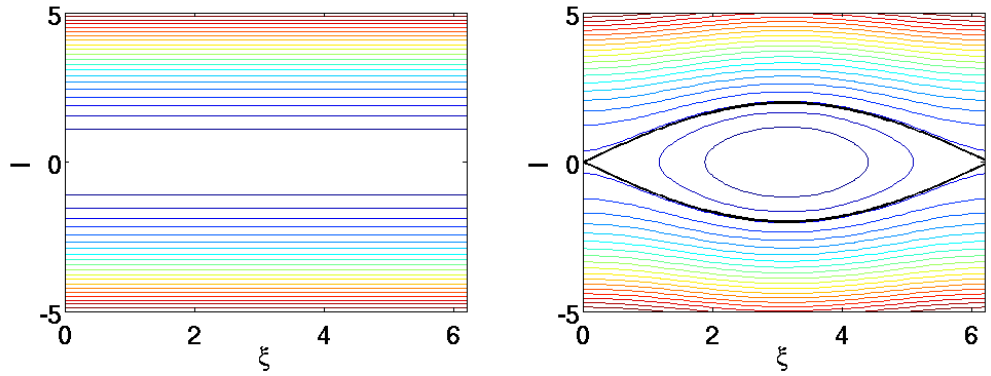

Figure 3.2: Illustration of the wave-particle trapping mechanism.

The wave-particle trapping is present in systems where there is only one mode $(\omega, \mathbf{n})$ or few monochromatic modes, which are phase coherent. The mechanism is illustrated in figure 3.2. In this case, under the assumption that the motion of particles interacting with the mode is described by an effective Hamiltonian $\mathcal{K} = \frac{1}{2}I^2 - h\cos\xi$, one can state that particles follow trajectories where $\mathcal{K} = cst$, represented by isocontours in figure 3.2. In addition there are two classes of orbits: passing ($\mathcal{K} > h$, represented by open trajectories) and trapped ($-h < \mathcal{K} < h$, represented by closed trajectories). These orbits are divided in the phase space by the surface $\mathcal{K} = h$, called separatrix. The separatrix is represented by a thick black line in figure 3.2b. Particles following trapped orbits are *trapped* in the potential well. At the beginning of the linear growth phase of the instability, all particles are passing, as represented in figure 3.2a, and resonant particles (those satisfying $\omega - kv = 0$) interact with the mode. As the amplitude of the mode grows, the term $h\cos\xi$ becomes important, the potential well deeper and therefore the population of trapped particles is increased. The situation is then illustrated by figure 3.2b. Particles around the resonant velocity transfer some of their energy to the mode during half a cycle of the

trapped orbit, but they recover this energy during the remaining half of the cycle. The amplitude of the mode stops growing when the potential well is large enough to cancel the linear growth rate, which occurs by means of a flattening of the distribution function. Therefore, a wave-particle trapping mechanism results in a flattening of equilibrium profiles. However, the reciprocal statement is in general false, i.e. a flattening of equilibrium profiles is not necessary due to a wave-particle trapping mechanism, since a quasi-linear diffusion may also lead to this flattening. The wave-particle trapping mechanism will be invoked in the context of the saturation of energetic ion driven GAMs in section 3.5.

3.2 Linear theory of GAM excitation

In this section, we give the fundamental elements to understand the excitation of GAMs by means of energetic ions. For this purpose, we firstly derive and solve numerically the exact dispersion relation of GAMs in a Maxwellian background by coupling the gyrokinetic equation to the quasineutrality condition. Secondly, written under a variational form, the quasi-neutrality condition allows one to obtain a condition for the excitation of the mode, leading to the positiveness of the slope of the distribution function in the energy space. Finally, two examples of distribution functions are analysed.

3.2.1 Exact dispersion relation of GAMs in a Maxwellian background

The guiding-centre distribution function F, solution of the Vlasov equation, is written as the sum of an equilibrium distribution function F_{eq} and a perturbed distribution function δF. As we show in appendix E, the perturbation δF may be written under the form

$$\delta F = F_{eq}\left(T_i \partial_H \log F_{eq} J_0 \cdot \phi + G\right) \tag{3.15}$$

where F_{eq} is defined as $F_{eq} = \langle F \rangle_{\theta,\varphi}$, ϕ is the electric potential normalized to T_i/e (an arbitrary equilibrium ion temperature), $J_0\cdot$ is the usual gyro-average operator, $\langle\cdot\rangle_{\theta,\varphi}$ represents an average over flux surfaces and G the non adiabatic part of the perturbed distribution function, solution of the following gyrokinetic equation (appendix E)

$$\partial_t G - [\mathcal{H}_{\mathrm{eq}}, G] = -T_i \partial_{\mathcal{H}} \log F_{\mathrm{eq}} \partial_t J_0 \cdot \phi \tag{3.16}$$

where $\mathcal{H}_{\mathrm{eq}}$ is the equilibrium Hamiltonian. In this expression, we have assumed that the electrostatic modes are axisymmetric, i.e. $n_3 = 0$. In addition, in the remainder of this chapter, no radial dependence will be accounted for. This assumption constitutes a strong simplification, but allows one to perform analytic calculations to predict a linear threshold that will be compared to gyrokinetic simulations later on in this chapter. Therefore, equation 3.16 represents the most simplified model to described the excitation and damping of GAMs. The radial dependence will be considered in the next chapter in the context of ITG modes. In order to make analytic progress, in the calculations presented in the following sections, trapping effects are not considered in the Vlasov equation. This is justified in the large aspect ratio limit $R/a \to \infty$, since the correction due to trapped particles is of the order $\mathcal{O}(\epsilon)$, with $\epsilon = r/R$. As we will see in section 3.4, the choice of a more realistic value of the aspect ratio ($R/a = 3.2$) does not introduce significant deviations with respect to the predicted linear threshold. The Poisson bracket is expressed in terms of the guiding-centre velocity as $[\mathcal{H}_{\mathrm{eq}}, G] = -v_{\parallel}\nabla_{\parallel} G - \mathbf{v}_D \cdot \boldsymbol{\nabla}_{\perp} G$. Considering

only axisymmetric modes, the parallel gradient reads $\nabla_\parallel = q^{-1}R^{-1}\partial_\theta$. In cylindrical geometry, $\boldsymbol{\nabla}_\perp = \partial_r \mathbf{e}_r + r^{-1}\partial_\theta \mathbf{e}_\theta$. Considering the simplified equilibrium 1.5, the curvature term reads (see appendix A)

$$\mathbf{v}_D \cdot \boldsymbol{\nabla}_\perp G = -\frac{mv_\parallel^2 + \mu B}{eBR}\left(\frac{1}{r}\cos\theta\partial_\theta G + \sin\theta\partial_r G\right)$$

Since the modes we consider have low poloidal wavenumber, the second term on the right-hand side of the previous expression will be neglected. Taking the Fourier transform in time and radial position, and ignoring trapping effects the linearized gyrokinetic equation may be expressed as follows

$$\left\{i\omega_t\partial_\theta + \omega\right\} G - \omega_d \sin(\theta)\, G = -T_i\partial_{\mathcal{H}} \log F_{eq}\omega J_0 \cdot \phi \tag{3.17}$$

where $\omega_d = K_r v_d$, $\omega_t = \frac{v_\parallel}{qR}$ and

$$v_d = -\frac{mv_\parallel^2 + \mu B}{eBR} \tag{3.18}$$

In these expressions, which are also found for instance in [75], K_r is the radial wavevector, $v_\parallel$ is the parallel velocity, q is the safety factor, R is the major radius, μ is the adiabatic invariant and B is the amplitude of the magnetic field. We consider now an electrostatic potential and a distribution function of the form

$$\mathcal{S} = \mathcal{S}_0 + \mathcal{S}_1 \mathrm{e}^{i\theta} + \mathcal{S}_{-1}\mathrm{e}^{-i\theta} \tag{3.19}$$

where $\mathcal{S} = \phi, G$. Identifying the coefficients of each Fourier mode in equation 3.17, one can write

$$\underbrace{\begin{pmatrix} \omega+\omega_t & -i\frac{\omega_d}{2} & 0 \\ i\frac{\omega_d}{2} & \omega & -i\frac{\omega_d}{2} \\ 0 & i\frac{\omega_d}{2} & \omega-\omega_t \end{pmatrix}}_{\mathbf{M}} \begin{pmatrix} G_{-1} \\ G_0 \\ G_1 \end{pmatrix} = -T_i\partial_H \log F_{eq}\omega \begin{pmatrix} J_0\cdot\phi_{-1} \\ J_0\cdot\phi_0 \\ J_0\cdot\phi_1 \end{pmatrix} \tag{3.20}$$

The inverse of the matrix $\mathbf{M}$ is

$$\mathbf{M}^{-1} = \frac{1}{\det\mathbf{M}}\begin{pmatrix} \omega(\omega-\omega_t) - \frac{\omega_d^2}{4} & i\frac{\omega_d}{2}(\omega-\omega_t) & -\frac{\omega_d^2}{4} \\ -i\frac{\omega_d}{2}(\omega-\omega_t) & \omega^2-\omega_t^2 & i\frac{\omega_d}{2}(\omega+\omega_t) \\ -\frac{\omega_d^2}{4} & -i\frac{\omega_d}{2}(\omega+\omega_t) & \omega(\omega+\omega_t) - \frac{\omega_d^2}{4} \end{pmatrix} \tag{3.21}$$

where the determinant of the matrix is

$$\det\mathbf{M} = \omega(\omega+\omega_t)\left(\omega - \omega_t - \frac{\omega_d^2}{2(\omega+\omega_t)}\right) \tag{3.22}$$

We consider now a potential of the GAM form, i.e. $\phi_1 = -i|\phi_1|$ and $\phi_{-1} = -\phi_1$. For simplicity we will write from now on $|\phi_1| \equiv \phi_1$. Therefore, an electrostatic potential of the GAM form (GAM symmetry) is written as

$$\phi = \phi_0 + 2\phi_1\sin\theta \tag{3.23}$$

The axisymmetric perturbation G_0 then reads

$$G_0 = \frac{-T_i\partial_{\mathcal{H}}\log F_{eq}}{\omega - \omega_t - \frac{\omega_d^2}{2(\omega+\omega_t)}}\left[(\omega-\omega_t)J_0\cdot\phi_0 + \frac{\omega\omega_d}{\omega+\omega_t}J_0\cdot\phi_1\right] \tag{3.24}$$

and the side-bands

$$G_1 = \frac{-T_i \partial_{\mathcal{H}} \log F_{eq}}{\omega - \omega_t - \frac{\omega_d^2}{2(\omega+\omega_t)}} \left(\frac{\omega_d}{2} J_0 \cdot \phi_0 + \omega J_0 \cdot \phi_1 \right) \tag{3.25}$$

$$G_{-1} = \frac{-T_i \partial_{\mathcal{H}} \log F_{eq}}{\omega + \omega_t - \frac{\omega_d^2}{2(\omega-\omega_t)}} \left(\frac{\omega_d}{2} J_0 \cdot \phi_0 + \omega J_0 \cdot \phi_1 \right) \tag{3.26}$$

Note that ω_t is odd in $v_\parallel$. Therefore, in order to have the GAM symmetry for the non adiabatic distribution function, the component G_{-1} must be obtained from G_1 by changing the parallel velocity $v_\parallel$ in its opposite $-v_\parallel$, i.e. $G_{-1}\left(v_\parallel\right) = -G_1\left(-v_\parallel\right)$. Finally, one finds the following relation

$$\begin{pmatrix} G_0 \\ G_1 \end{pmatrix} = \frac{-T_i \partial_{\mathcal{H}} \log F_{eq}}{\omega - \omega_t - \frac{\omega_d^2}{2(\omega+\omega_t)}} \begin{pmatrix} \omega - \omega_t & \frac{\omega\omega_d}{\omega+\omega_t} \\ \frac{\omega_d}{2} & \omega \end{pmatrix} \cdot \begin{pmatrix} J_0 \cdot \phi_0 \\ J_0 \cdot \phi_1 \end{pmatrix} \tag{3.27}$$

Equation (3.27) is in principle the exact solution, but it raises technical difficulty. Indeed, the division by a term that may vanish is only justified if we regularize the solution to recover its analytic character. This will be done by introducing the plasma dispersion function. If the plasma contains only thermal passing particles, a reasonable assumption of the equilibrium distribution function F_{eq} is

$$F_{eq} \equiv F_{eq,i} = \frac{n_i}{\left[2\pi T_i/m\right]^{3/2}} e^{-\frac{m v_\parallel^2 + 2\mu B}{2T_i}} \tag{3.28}$$

In this case, the definition of the temperature stems from the gradient of the equilibrium distribution function

$$-T_i \partial_{\mathcal{H}} \log F_{eq,i} = 1 \tag{3.29}$$

The dispersion relation of GAMs is obtained by using the electro-neutrality condition

$$\frac{T_i}{T_e}\left(\phi - \phi_0\right) - \frac{1}{n_i} \boldsymbol{\nabla}_\perp \cdot \left(\frac{m n_i}{eB^2} \boldsymbol{\nabla}_\perp \phi \right) = \frac{1}{n_i} \int \mathrm{d}^3\mathbf{v} J_0 \cdot F - 1 \tag{3.30}$$

The second term on the right-hand side represents the polarisation density, which can be projected onto a Fourier mode to give

$$-\frac{1}{n_i} \boldsymbol{\nabla}_\perp \cdot \left(\frac{m n_i}{eB^2} \boldsymbol{\nabla}_\perp \phi \right) \to K_r^2 \frac{m T_i}{e^2 B^2} \phi \tag{3.31}$$

where we have neglected the derivatives of n_i. The gyro-average operator J_0 and the square of the gyro-average operator J_0^2 can be expressed in terms of K_r as

$$J_0 \approx 1 - \frac{1}{2} K_r^2 \frac{m T_i}{e^2 B^2} \frac{\mu B}{T_i} \quad J_0^2 \approx 1 - K_r^2 \frac{m T_i}{e^2 B^2} \frac{\mu B}{T_i} \tag{3.32}$$

where the perpendicular gradients of B^{-1} and T_i have been neglected. The right-hand side of the electro-neutrality equation can be written as

$$\frac{1}{n_i} \int \mathrm{d}^3\mathbf{v} J_0 \cdot F - 1 \approx \frac{1}{n_i} \int \mathrm{d}^3\mathbf{v} F_{\mathrm{eq}} J_0 \cdot G - \frac{1}{n_i} \int \mathrm{d}^3\mathbf{v} F_{\mathrm{eq}} J_0^2 \phi \tag{3.33}$$

Using the expression for J_0^2 in 3.32, the polarisation density and the term $\sim K_r^2$ in 3.33 cancel out. The electroneutrality equation can finally be written for the $m = 0$ and $m = 1$ modes respectively as follows

$$-\phi_0 + \langle J_0 \cdot G_0 \rangle = 0 \tag{3.34a}$$

$$-\phi_1 + \langle J_0 \cdot G_1 \rangle = \frac{T_i}{T_e}\phi_1 \tag{3.34b}$$

where the brackets in this case represent an average over the velocity space, i.e. $\langle \cdot \rangle = \frac{1}{n_i}\int \cdot F_{eq} d^3\mathbf{v}$.

Taking the gyro-average of equation 3.27 and using the two previous expressions representing the electro-neutrality condition, we can derive a system of the form $\tilde{\mathbf{M}} \cdot \boldsymbol{\phi} = \mathbf{0}$, which has a non trivial solution if and only if $\det\left(\tilde{\mathbf{M}}\right) = 0$, leading to the kinetic dispersion relation of GAMs

$$\left\{1 - \left\langle J_0^2 \cdot \right\rangle - \frac{1}{2}\left\langle \frac{\omega_d^2}{\omega^2 - \omega_t^2} \right\rangle\right\}\left\{1 + \frac{T_i}{T_e} - \left\langle \frac{\omega}{\omega - \omega_t} \right\rangle\right\} = \frac{1}{2}\left\langle \frac{\omega_d}{\omega - \omega_t} \right\rangle^2 \tag{3.35}$$

where we have made use of the symmetry of F_{eq} in $v_\parallel$. Under the assumption of thermal passing particles, i.e. using equation 3.28, one can perform a first integration over μ to express the dispersion relation in terms of a normalized parallel velocity. After integration, this dispersion relation is written as follows

$$\left\{1 - \frac{1}{2}\left\langle \frac{\zeta^4 + 2\zeta^2 + 2}{\Omega^2 - \zeta^2/q^2} \right\rangle\right\}\left\{1 + \frac{T_i}{T_e} - \left\langle \frac{\Omega}{\Omega - \zeta/q} \right\rangle\right\} = \frac{1}{2}\left\langle \frac{\zeta^2 + 1}{\Omega - \zeta/q} \right\rangle^2 \tag{3.36}$$

where ζ is the parallel velocity normalized to the thermal velocity $c_{si} = \sqrt{T_i/m_i}$, and the frequency is normalized to the sound frequency, $\Omega = \omega R/c_{si}$. This equation may be rewritten in terms of the plasma dispersion function [79] $Z(x) = \frac{1}{\sqrt{\pi}}\int \frac{e^{-u^2}}{u-x} du$ under the form

$$\begin{gathered}\left\{1 + \frac{q^2}{2\chi}\sum_{\epsilon=-1,+1}\epsilon\left[I_4(\epsilon\chi) + I_2(\epsilon\chi) + \frac{1}{2}Z(\epsilon\chi)\right]\right\}\{1 + \tau + \chi Z(\chi)\} = \\ q^2\left\{I_2(\chi) + \frac{1}{2}Z(\chi)\right\}^2\end{gathered} \tag{3.37}$$

where $\chi = q\Omega/\sqrt{2}$, $\tau = T_i/T_e$ and

$$I_{2p}(\chi) \equiv \frac{1}{\sqrt{\pi}}\int_{\mathbb{R}} \frac{u^{2p}e^{-u^2}}{u - \chi} du = \chi^{2p} Z(\chi) + \sum_{k=0}^{p-1} \mu_{2k}\chi^{2(p-k)-1}$$

$$\mu_{2k} \equiv \frac{1}{\sqrt{\pi}}\int_{\mathbb{R}} u^{2k}e^{-u^2} du = \frac{1}{2^k}\prod_{l=1}^{k}\left[2(k-l)+1\right]$$

After multiplication by χ, some algebra allows one to recast this equation as follows

$$\mathcal{D}(\chi) = \left\{\chi + q^2 Z_1(\chi)\right\}\{1 + \tau + \chi Z(\chi)\} - q^2\chi Z_2(\chi)^2 = 0 \tag{3.38}$$

where

$$Z_1(\chi) = \left(\chi^4 + \chi^2 + \frac{1}{2}\right)\frac{Z(\chi) - Z(-\chi)}{2} + \chi\left(\chi^2 + \frac{3}{2}\right) \tag{3.39a}$$

$$Z_2(\chi) = \chi + \left(\chi^2 + \frac{1}{2}\right) Z(\chi) \tag{3.39b}$$

A similar dispersion relation has already been reported by Watari et al [80]. If one applies the symmetry properties of the plasma dispersion function this equation can be solved numerically. Figure 3.3 shows a contour plot of the inverse of $|\mathcal{D}|$, i.e. $|\mathcal{D}|^{-1}$, for $q = 3$. The poles of $|\mathcal{D}|^{-1}$ provide the complex frequencies solution of equation 3.38.

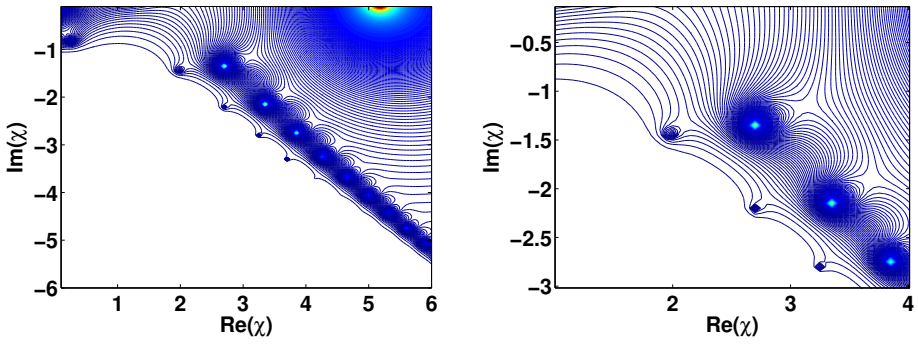

(a) (b)

Figure 3.3: (3.3a) Contour plot of $|\mathcal{D}|^{-1}(\chi)$ showing the two branches of isolated poles for $\Im(\chi) < 0$. (3.3b) Magnified view showing the lowest frequency damped modes.

Note that the pole $\chi = 0$, which could be erroneously identified to the stationary zonal flow, does not represent any physical solution. It simply stems from the multiplication by χ of equation 3.37, which is only valid if $\chi \neq 0$. We find another pole close to the real axis representing the usual GAM, whose frequency is estimated around $\chi \approx 5.1$, i.e. $\Omega \approx 2.4$. In addition, there exists a damped mode with very low real frequency. Moreover, two branches of isolated infinite poles have been observed, corresponding to highly damped modes and satisfying $\Im(\chi) \approx \Re(\chi)$.

Taking now the fluid limit, i.e. $\Omega = \omega R/c_{si} \gg 1/q$ of the dispersion relation, one finds the following real frequency

$$\omega^2 = \left(2\tau^{-1} + \frac{7}{2} + \frac{1}{\tau q^2}\right)\left(\frac{c_{si}}{R}\right)^2 \tag{3.40}$$

This dispersion relation is identical to the one obtained by Watari et al [81] and allows one to recover the undamped GAM with $\Omega \approx 2.4$ for $q = 3$.

The expression 3.40 shows that the GAM frequecy is close to the acoustic frequency $\sim c_{\rm si}/R$, which justifies the classification of GAMs as *acoustic frequency range modes*. This is a common feature between the GAMs and the well-known Beta-Alfvén Eigenmodes (BAEs) [82, 83, 84, 85]. Therefore, distinguishing experimentally between these two modes by means of their frequency reveals impossible and one must use the mode structure for this purpose. As we have explained, the poloidal structure of GAMs is given by the component $\sin\theta$. This means that if a mode within the acoustic range frequency is observed in the equatorial plane of the tokamak, one can conclude that it is undoubtly related to BAE oscillations.

3.2.2 Variational approach to predict the damping and excitation of GAMs

The electro-neutrality condition can be written under a variational form (see Appendix B) which states that the functional

$$\Xi = -\int \mathrm{d}^3\mathbf{x}\delta n_i\phi^\dagger + \tau\int \mathrm{d}^3\mathbf{x}n_i\left|\phi-\phi_0\right|^2 \tag{3.41}$$

is extremum for any variation of ϕ. Here electrons are assumed adiabatic. The perturbed ion density is the integral of the perturbed distribution function

$$\delta n_i = \int \mathrm{d}^3\mathbf{v}J_0\cdot\delta F = \int \mathrm{d}^3\mathbf{v}\left(T_i\partial_H\log F_{eq}J_0^2\cdot\phi + J_0\cdot G\right)F_{eq} \tag{3.42}$$

Thus, the functional Ξ is expressed in terms of the non adiabatic part as follows

$$\Xi = -\int \mathrm{d}^3\mathbf{x}\mathrm{d}^3\mathbf{v}\left(T_i\partial_H\log F_{eq}J_0\cdot\phi+G\right)F_{eq}\phi^\dagger + 2\tau n_i\int \mathrm{d}^3\mathbf{x}\left|\phi_1\right|^2 \tag{3.43}$$

The factor 2 in the adiabatic response of electrons comes from the integral of $|\phi_1\mathrm{e}^{i\theta}+\phi_{-1}\mathrm{e}^{-i\theta}|^2$ and making use of the GAM symmetry $\phi_{-1}=-\phi_1$

$$\int \mathrm{d}^3\mathbf{x}\left|\phi-\phi_0\right|^2 = \int \mathrm{d}^3\mathbf{x}|\phi_1\mathrm{e}^{i\theta}+\phi_{-1}\mathrm{e}^{-i\theta}|^2 = \int \mathrm{d}^3\mathbf{x}4\sin^2\theta\left|\phi_1\right|^2 = 2\int \mathrm{d}^3\mathbf{x}\left|\phi_1\right|^2$$

If we neglect the term $\sim\omega_d^2\sim K_r^2$ in the denominator of equation 3.27 and assume the parity of the solution, the expression for the resonant part of the functional 3.43 reads

$$\Xi_{\mathrm{res}} = 2\int d^3\mathbf{x}\left\langle\frac{T_i\partial_H\log F_{eq}}{\omega^2-\omega_t^2}\left|\frac{\omega_d}{2}J_0\cdot\phi_0+\omega J_0\cdot\phi_1\right|^2\right\rangle \tag{3.44}$$

where we have used only the non adiabatic part of the response.

This compact variational form allows one to draw very general conclusions. The imaginary part of this function is proportional to the exchange of energy between particles and waves. In other words, it represents the Landau damping of GAMs in the particular case of a plasma containing only thermal passing particles. This imaginary part involves a δ function centered on the resonance $\omega = v_\parallel/qR$. If a marginal mode exists, this imaginary part must vanish for real ω. A close inspection shows that this can only be true if the resonance disappears, i.e. if we can neglect the parallel velocity with respect to the frequency: $\omega\gg\omega_t$, which leads to $\Omega\equiv\omega R/c_{si}\gg 1/q$, which is in fact the condition for application of the fluid theory. Hence GAMs will be Landau damped in a Maxwellian background except if $\omega_{GAM}\gg c_{si}/qR$.

The exchange of energy between resonant particles and waves per volume and time unit is given by the relation $\frac{d\mathcal{E}}{dt}=2\omega n_iT_i\Im\left(\mathcal{L}\right)$, where $\Xi=\int d^3\mathbf{x}\mathcal{L}$ and $\Im\left(\mathcal{L}\right)$ is the imaginary part of $\mathcal{L}$. A positive value of $\frac{d\mathcal{E}}{dt}>0$ means heating of ions, i.e. mode damping. We can now use the equations 3.27 and 3.34b in the fluid limit ($\omega\gg\omega_t,\omega_d$) to find the relation

$$\phi_1 = -\frac{K_r\rho_{si}}{\tau\Omega}\phi_0 \tag{3.45}$$

which leads together with equation 3.44 to the following expression for the density of exchanged energy per volume and time unit

$$\frac{d\mathcal{E}}{dt} = -\frac{\pi}{2}T_i^2\frac{c_{si}}{R}K_r^2\rho_{si}^2\left|\phi_0\right|^2 4\pi c_{si}^3\int_0^\infty\left(\bar{\mu}+q^2\Omega^2+2\tau\right)^2\partial_HF_{eq}|_{|\zeta|=q\Omega}d\bar{\mu} \tag{3.46}$$

where $\bar{\mu}=\frac{\mu B}{T_i}$ is the perpendicular energy normalized to the thermal energy, the normalized frequency $\Omega=\omega R/c_{si}$ is given by the dispersion relation and $\rho_{si}=\frac{mc_{si}}{eB}$ is

the thermal Larmor radius. In the following, equation 3.46 will be called quasi-linear exchange of energy between waves and particles, but note that this nomenclature does not necessarily refer to any kind of quasi-linear saturation. If the plasma contains only thermal ions, i.e. $T_i \partial_H \log F_{eq} = -1$, the density of exchanged power reads

$$\frac{d\mathcal{E}_i}{dt} = \sqrt{\frac{\pi}{2}} \left[1 + \left(1 + q^2\Omega^2 + 2\tau\right)^2\right] q e^{-\frac{q^2\Omega^2}{2}} n_i T_i \frac{c_{si}}{R} K_r^2 \rho_{si}^2 \left|J_0 \cdot \phi_0\right|^2 \tag{3.47}$$

The quantity given by equation 3.47 is always positive, which means that the mode is naturally damped in a Maxwellian background. This is due to the fact that the distribution function of thermal particles has a negative derivative with respect to the energy. This phenomenon is the well-known GAM Landau damping. It is important to note that the Landau damping is not restricted to the especial case of GAMs treated here. In our case, GAMs are damped because they naturally exist in toroidal devices, as explained throughout this chapter. These GAMs are characterized by a frequency ω_{GAM} and a parallel wavenumber $k \approx qR^{-1}$ (see dispersion relation 3.38). Therefore, particles with parallel velocity $v_{\parallel} \approx q^{-1} R \omega_{\mathrm{GAM}}$ will resonate with GAMs and the modes will be damped if the derivative of the distribution function with respect to the energy at the resonant velocity is negative. The density of exchanged power 3.47 will be called in the following quasi-linear exchange of energy between particles and waves. However, the word quasi-linear refers here only to the fact that a saturation of the mode can occur due to a modification of the equilibrium distribution function, as we will later on in this chapter. However, the saturation must not be understood as a quasi-linear saturation because as we will show there is only one single eigenmode, whereas quasi-linear diffusion/saturation requires many modes (see previous chapter).

3.2.3 Linear excitation of GAMs by energetic particles

The damping of the modes in a Maxwellian background may be offset by a positive derivative of the distribution function at the resonance, i.e. at $|\zeta| = q\Omega$. Let us consider the general case of equation 3.17, with the condition 3.29 not satisfied for the whole plasma, but only for the bulk. The equilibrium distribution function may be decomposed as follows

$$F_{eq} = F_{eq,i} + F_{eq,h} \tag{3.48}$$

where $F_{eq,h}$ is the fast ions distribution function (h stands for h). In this case, it is easily shown that the mode is excited when

$$\int_0^{\infty} g\left(\bar{\mu}\right) \partial_H F_{eq,h}|_{|\zeta|=q\Omega} d\bar{\mu} \geq \frac{n_i e^{-\frac{q^2\Omega^2}{2}}}{T_i \sqrt{\frac{\pi}{2}} 4\pi c_{si}^3} \left[1 + \left(1 + q^2\Omega^2 + 2\tau\right)^2\right] \tag{3.49}$$

where $g\left(\bar{\mu}\right) = \left(\bar{\mu} + q^2\Omega^2 + 2\frac{T_e}{T_i}\right)^2$.

This condition allows us to determine the kind of particles which contribute to the excitation of the mode. A necessary condition of excitation is the existence of an interval $[\bar{\mu}_1, \bar{\mu}_2]$ such that for all $\bar{\mu} \in [\bar{\mu}_1, \bar{\mu}_2]$ the derivative of the equilibrium distribution function satisfies $\partial_H F_{eq,h}|_{|\zeta|=q\Omega} > 0$. Within this interval, the left-hand side of equation 3.49 is positive. Therefore, particles with perpendicular energies in between $\bar{\mu}_1$ and $\bar{\mu}_2$ will excite the mode. The compensation by this positiveness of both the negativeness outside this

interval and the Landau damping may be mathematically expressed by equation 3.49. Thus, this condition may be rewritten under the form

$$\int_{\bar{\mu}_1}^{\bar{\mu}_2} g\left(\bar{\mu}\right) \partial_H F_{eq,h} d\bar{\mu}|_{|\zeta|=q\Omega} \geq \left| \int_{\bar{\mu}\notin[\bar{\mu}_1,\bar{\mu}_2]} g\left(\bar{\mu}\right) \partial_H F_{eq,h}|_{|\zeta|=q\Omega} d\bar{\mu} \right| + \frac{n_i e^{-\frac{q^2\Omega^2}{2}}}{T_i \sqrt{\frac{\pi}{2}} 4\pi c_{si}^3} \left[1 + \left(1 + q^2\Omega^2 + 2\tau\right)^2\right] \tag{3.50}$$

Furthermore, even if $\partial_H F_{eq,h}|_{|\zeta|=q\Omega} > 0 \,\forall\, \bar{\mu} \in \mathbb{R}_+$, the dependence of the equilibrium function on the perpendicular energy may strongly modify the value of the left-hand side of equation 3.49. Thus, **a convenient choice of the distribution function in μ could lead to a scenario where GAMs are more efficiently excited**. In order to use these results and to make further analytical calculations we need to assume an explicit equilibrium distribution function for fast ions. In the next sections we will apply these results to two typical NBI heated fast ions distribution functions: a Maxwellian distribution shifted in $v_{||}$ (in the following called *bump-on-tail*), which will allow us to obtain an explicit expression for the threshold condition, and a slowing-down distribution function modulated by a pitch-angle distribution (in the following called *slowing-down*). Note that the slowing-down distribution represents a more realistic fast ion distribution, where trapping particle effects are included resulting in the pitch-angle dependence. This is not the case for the bump-on-tail distribution. However, the interest of this more academic example can be seen when considering that the fast particle source presently implemented in GYSELA (see next chapter) leads to a bump-on-tail-like distribution. Therefore, analysis of this distribution together with the comparison with a more experiment-relevant case reveals essential on the route towards the next chapter.

Application to two types of distribution function

Let us firstly consider the case of a fast ions population described by a double-beam bump-on-tail distribution function. This kind of distribution can be mathematically represented by the following expression

$$F_{eq,h} = F_{M,h} e^{-\frac{\overline{\zeta}^2}{2\hat{T}_h}} \cosh\left(\frac{\overline{\zeta}\zeta}{\hat{T}_h}\right) \tag{3.51}$$

with $F_{M,h} = \frac{n_h}{\left(2\pi T_i \hat{T}_h/m\right)^{3/2}} e^{-\frac{\zeta^2+2\bar{\mu}}{2\hat{T}_h}}$. This expression is close to the one used by Dannert et al [86]. Here, $\overline{\zeta}$ represents the mean parallel velocity of the injected ions normalized to the thermal velocity and $\hat{T}_h$ the fast ions temperature normalized to the bulk temperature. Figure 3.4 illustrates an example of such a bump-on-tail distribution function.

The fact that we use a *double-beam* distribution is related to the hypothesis of symmetry in parallel velocity, namely $F_{\text{eq}}\left(v_{\|}\right) = F_{\text{eq}}\left(-v_{\|}\right)$. This symmetry is also important in order to analyse the excitation and saturation of EGAMs in the absence of supplementary effects such as the toroidal rotation. This is an important hypothesis, since it allows one to make analytical calculations leading to a tractable expression for the linear excitation threshold. However, experimental conditions may depart from this ideal situation, either due to the injection of parallel torque by neutral beams, or due to the turbulence induced intrinsic plasma rotation [87]. The importance of analysing the effect of the rotation on the onset of EGAMs has been pointed out by Berk *et al.* [74] and will not be discussed in

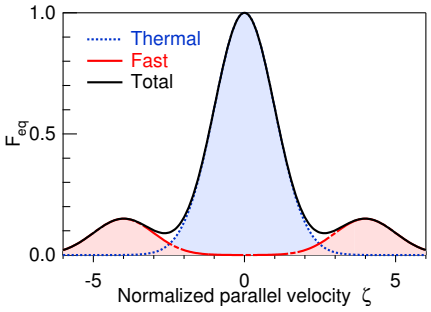

Figure 3.4: Example of double-beam bump-on-tail distribution function (red dashed line) in a Maxwellian background (blue dotted line). Black solid line represents the total ion population.

the following. In order to apply the linear threshold calculated above, we need to determine the derivative of this fast ions equilibrium distribution with respect to the energy at the resonance, which reads

$$\partial_E F_{eq,h}|_{|\zeta|=q\Omega} = \frac{F_{M,h}|_{|\zeta|=q\Omega}}{T_i \hat{T}_h} e^{-\frac{\overline{\zeta}^2}{2\hat{T}_h}} \cosh\left(\frac{\overline{\zeta} q\Omega}{\hat{T}_h}\right)\left[\frac{\overline{\zeta}}{q\Omega}\tanh\left(\frac{\overline{\zeta} q\Omega}{\hat{T}_h}\right) - 1\right] \tag{3.52}$$

One may derive a necessary condition for fast ions to excite GAMs. This derivative is positive provided that

$$\overline{\zeta}^2 > \hat{T}_h \tag{3.53}$$

The sufficient condition on the fast ion concentration for the EGAMs to become unstable may be derived from expression 3.49. This leads to the following criterion

$$\frac{n_h}{n_i} \geq \frac{\hat{T}_h^{1/2} e^{-\left(1-\frac{1}{\hat{T}_h}\right)\frac{q^2\Omega^2}{2}} e^{\frac{\overline{\zeta}^2}{2\hat{T}_h}}}{\cosh\left(\frac{\overline{\zeta} q\Omega}{\hat{T}_h}\right)\left[\frac{\overline{\zeta}}{q\Omega}\tanh\left(\frac{\overline{\zeta} q\Omega}{\hat{T}_h}\right) - 1\right]} \frac{1+\left[1+2\tau+q^2\Omega^2\right]^2}{1+\left[1+2\frac{\tau}{\hat{T}_h}+\frac{q^2\Omega^2}{\hat{T}_h}\right]^2} \tag{3.54}$$

The parameters that allow one to control the fast ion population are n_h, $\hat{T}_h$ and $\overline{\zeta}$. As may be deduced from the criterion 3.54), the linear threshold depends on the fast ions temperature $\hat{T}_h$. Figure 3.5 shows the dependence of the fast ions concentration on the mean velocity for four different values of $\hat{T}_h$. For numerical simulations, small values of $\hat{T}_h$ would require high resolution in $v_\parallel$-space. In addition, the right-hand side of Eq.(3.54) flattens around a minimum located between $\overline{\zeta} = 3.5$ and $\overline{\zeta} = 4.5$. Thus, in order to use reasonable values of fast pressure and numerical resolution, a good compromise is to take $\hat{T}_h$ around $\hat{T}_h^{\lim} = 1$ and the mean velocity within the interval $3.5 < \overline{\zeta} < 4.5$.

Another distribution function may be considered, taking into account the coupling between the heating in $v_\parallel$-space and the heating in μ-space. Let us analyse the excitation of modes by a fast ion population described by a slowing-down distribution function [13, 75]

$$F_{eq,h} = \frac{n_h}{E^{3/2} + E_c^{3/2}} e^{-\left(\frac{\Lambda-\Lambda_0}{\Delta\Lambda}\right)^2} H_E\left(E_b - E\right) \tag{3.55}$$

where $\Lambda = \frac{\mu B_0}{E}$, E_c is the critical energy of heated ions, introduced in the previous chapter, E_b is the birth energy of the fast ions and H_E is the Heaviside step function. Here, B_0 represents the amplitude of the magnetic field on the magnetic axis.

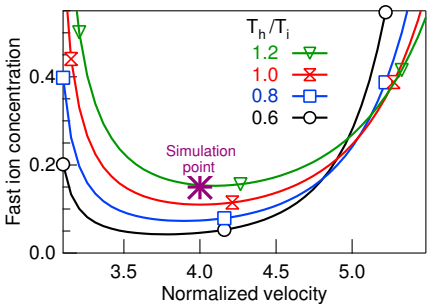

Figure 3.5: Dependence of the linear threshold on the injection velocity and fast ions temperature. The case of a resonant velocity $q\Omega = 3$ is considered here. Parameters used in the simulation of section 3.4 to recover the linear threshold are indicated by an asterisk in this figure.

In this case, the derivative (in the sense of distributions) with respect to the energy at the resonance reads

$$\partial_E F_{eq,h}|_{|\zeta|=q\Omega} = \left(\frac{(\Lambda-\Lambda_0)\Lambda}{\Delta\Lambda^2} - \frac{3}{4}\frac{E^{3/2}}{E^{3/2}+E_c^{3/2}}\right)\frac{2F_{eq,h}}{E} H_E\left(E_b - E\right) - \frac{n_h}{E^{3/2}+E_c^{3/2}} e^{-\left(\frac{\Lambda-\Lambda_0}{\Delta\Lambda}\right)^2} \delta\left(E - E_b\right) \tag{3.56}$$

We can inject this expression into equation 3.49 to determine the linear threshold for excitation. The integration is performed numerically and Figure 3.6 shows the projection of this threshold in the $(n_h/n_i, E_c)$ plane, for several values of E_b. $\Delta\Lambda$ and Λ_0 are equal to 0.2 and 0.5 respectively in each case. These values have been taken from Ref. [13].

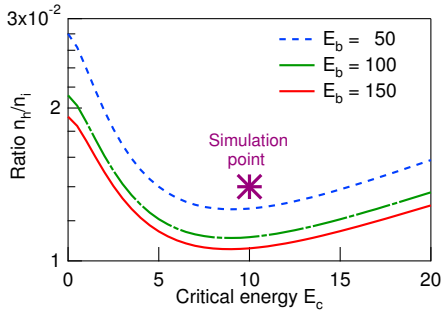

Figure 3.6: Dependence of the linear threshold on critical and birth energies in the case of $\Delta\Lambda = 0.2$, $\Lambda_0 = 0.5$ and a resonant velocity $q\Omega = 3$. Parameters of the simulation are indicated by an asterisk.

We observe that the minimum fast ion concentration for EGAM excitation decreases with the birth energy. The linear threshold has been analysed for different values of Λ_0 as well. We have identified numerically an interval $[\Lambda_{0,min}, \Lambda_{0,max}(E_b)]$ in which the excitation is possible for any critical energy. This is illustrated in figure 3.7. If $\Lambda_0 < \Lambda_{0,min} \approx 0.38$, the minimum value of E_c for excitation does not depend on E_b, i.e. there is a fast ion concentration leading to the excitation of the mode for any E_c and E_b. The only term in the expression 3.56 which contributes to the positiveness of the derivative is the difference $\Lambda - \Lambda_0$. One can derive a sufficient condition for the inexistence of a $E_c < \infty$. Indeed, if $\Lambda - \Lambda_0 < 0$ for the less stabilizing particles, then the minimum value

of E_c for excitation must diverge. This condition is satisfied if $\Lambda_0 > \Lambda_b = 1 - \frac{q^2\Omega^2}{2E_b}$, which has been obtained for particles with E_b. The divergence of E_c for EGAM excitation is shown in figure 3.7. Note that the condition that we have derived is a sufficient condition. Therefore, it is more restrictive than the condition given by figure 3.7. For instance, a birth energy of $E_b = 50$ would give $\Lambda_b \approx 0.9$, whereas in figure 3.7 we obtain $\Lambda_b \approx 0.8$.

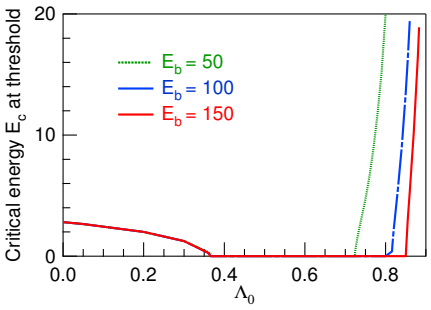

Figure 3.7: Threshold of E_c for GAM excitation as a function of the birth energy and Λ_0 at $q\Omega = 3$.

We can analyse the contribution of the fast ions to the equation 3.49 by looking at the derivative of the equilibrium function with respect to the energy. Figure 3.8a shows the dependence of this derivative on the adiabatic invariant for $\Delta\Lambda = 0.2$ and $\Lambda_0 = 0.5$. It turns out that the particles that excite the mode satisfy $\bar{\mu} > \frac{q^2\Omega^2}{2}$. Such a result suggests that **trapped particles should play a role in destabilizing the EGAMs**. However, one should keep in mind that the whole derivation, starting from equation 3.17, did not include the trapped particle physics. In that respect, numerical simulations will reveal particularly helpful in order to assess the excitability of EGAMs from a slowing-down equilibrium function.

One can perform the definite integral in equation 3.49 between 0 and $\bar{\mu}$ and calculate the value of $\bar{\mu}$ for which this balance equation is satisfied. Figure 3.8b illustrates the evolution of the integral (solid line) and the value of the right-hand side (dashed line) of equation 3.49 for $E_b = 100$, $E_c = 10$ and $n_h/n_i = 0.012$. **The excitation condition is satisfied only when particles with very high perpendicular energy are considered. This results in a major difficulty when studying this instability by means of numerical simulations, because of the large number of grid points required in perpendicular energy**.

3.3 The GYSELA code

GYSELA [88] solves the standard gyrokinetic equation for the full-f ion guiding-centre distribution function, consistently with the modern gyrokinetic formulation [89]. The simplified magnetic topology consists of concentric toroidal magnetic flux surfaces with circular poloidal cross-sections. In particular, the Shafranov shift is not account for in the simulations, which is justified since it is not expected to play a role in the dynamics of $n = 0$ modes such as EGAMs. The electrostatic limit is considered, and electrons are assumed adiabatic. The self consistent system consists of the gyrokinetic equation

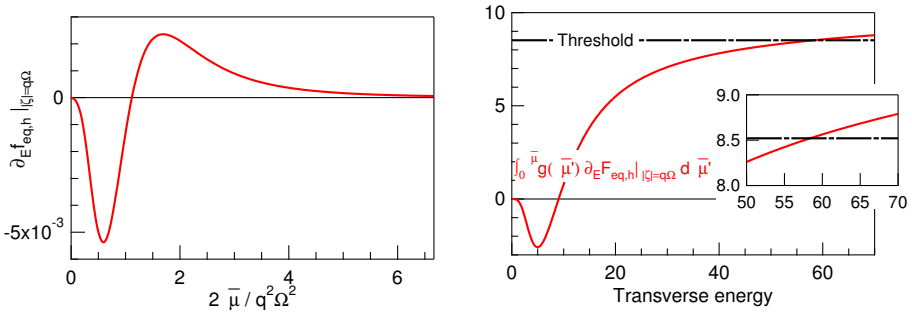

Figure 3.8: (3.8a) Derivative of the equilibrium distribution function with respect to the energy as a function of the perpendicular energy. (3.8b) Left-hand side (solid line) and right-hand side (dashed line) of equation 3.49. When the solid line is above the dashed line, excitation of GAMs by fast ions is possible.

coupled to quasi-neutrality condition:

$$B_{\parallel}^{*}\partial_t F + \nabla\cdot\left(B_{\parallel}^{*}\,\dot{\mathbf{x}}_G\;F\right) + \partial_{v_{G\parallel}}\left(B_{\parallel}^{*}\,\dot{v}_{G\parallel}\;F\right) = \mathcal{C}(F) + S \tag{3.57a}$$

$$B_{\parallel}^{*}\,\dot{\mathbf{x}}_G = v_{G\parallel}\mathbf{B}^{*} + \mathbf{b}\times\nabla\Xi/e \tag{3.57b}$$

$$B_{\parallel}^{*}\,\dot{v}_{G\parallel} = -\mathbf{B}^{*}\cdot\nabla\Xi/m_i \tag{3.57c}$$

$$\frac{e}{T_{e,eq}}\left(\phi - \langle\phi\rangle\right) - \frac{1}{n_{eq}}\nabla_{\perp}.\left(\frac{m_i n_{eq}}{eB^2}\nabla_{\perp}\phi\right) = \frac{n_G - n_{eq}}{n_{eq}} \tag{3.57d}$$

with $\nabla\Xi = \mu\nabla B + e\nabla\bar{\phi}$ and $\mathbf{B}^{*} = \mathbf{B} + (m_i/e)\,v_{G\parallel}\nabla\times\mathbf{b}$. No collisions are accounted for in the present chapter, i.e. $\mathcal{C}(F) = 0$. The source term S drives the system out of equilibrium by injecting energy and will not be considered either in this chapter. For a more detailed description of the sources implemented in GYSELA, the reader can go deeper into the next chapter. The gyro-averaged electric potential is represented by $\bar{\phi}$. In GYSELA, the current effects are taken into account by means of the quantity $B_{\parallel}^{*} = \mathbf{B}^{*}\cdot\mathbf{b}$, with $\mathbf{b} = \mathbf{B}/B$. The guiding-centre density is defined by: $n_G = \iint \mathcal{J}_v \mathrm{d}\mu\mathrm{d}v_{G\parallel}(J_0\cdot F)$, with $\mathcal{J}_v = 2\pi B_{\parallel}^{*}/m_i$ the Jacobian in the velocity space. F is replaced by the equilibrium component F_{eq} when computing n_{eq}. Finally, $\langle\phi\rangle$ stands for the flux surface average of the electric potential. In the following, the electric potential is normalized to the electron equilibrium temperature ($\phi \to e\phi/T_{e,eq}$) and the guiding-center density is normalized to the equilibrium density ($n_G \to n_G/n_{eq}$).

Fluctuations characterized by $(m,n) \neq (0,0)$ vanish at both radial boundaries $r = r_{min}$ and $r = r_{max}$, with m and n the poloidal and toroidal wave numbers respectively. As far as the $(m,n) = (0,0)$ is concerned, Dirichlet boundary conditions are used for the electric potential at $r_{\min}$ and $r_{\max}$, $\phi_{00}(r_{\min,\max}) = 0$. The conditions imposed to F_{00} are $\partial_r F_{00}(r_{\min}) = 0$ and $F_{00}(r_{\max}, t) = F_{eq}(r_{\max}, t = 0)$. The initial distribution function is decomposed as follows:

$$F(t=0) = F_{eq}\,(E) + \delta F = F_{eq,i} + F_{eq,h} + \delta F \tag{3.58}$$

where the equilibrium distribution function $F_{eq,i}$ is given by the expression 3.28. If the contribution of hot particles is taken into account, then $F_{eq,h}$ is given either by 3.51 or by

3.55. Otherwise, $F_{eq,h} = 0$. The initial perturbation δF is up-down asymmetric:

$$\delta F = \varepsilon\left(r\right) F_{eq}\left(E\right) \sin\theta \tag{3.59}$$

with ε the amplitude of the initial perturbation. The amplitude $\varepsilon(r)$ is a gaussian that vanishes at both boundaries and has a maximum value of 10^{-3}. Note that $F_{eq,i}$ and $F_{eq,h}$ are constant radially at $t = 0$ for the simulations reported in the following, such that these two distribution functions depend only on E and μ. In particular, these simulations do not exhibit any ITG-driven turbulence (Ion Temperature Gradient). In addition, since the equilibrium distribution function depends on the motion invariants, time evolution results from the initial perturbation ε only.

3.4 Linear gyrokinetic simulations

Within the model described before, numerical simulations with and without fast ions have been carried out. The linear threshold predicted analytically by means of a variational approach is recovered, as detailed below. The two fast ion distribution functions introduced in section 3.2 have been implemented in GYSELA. Figure 3.9a illustrates the time evolution of the mode ϕ_{10} in the absence of fast ions at the radial position $r = \frac{r_{min}+r_{max}}{2}$ around which the safety factor takes a constant value. The usual GAM real frequency is recovered as highlighted in figure 3.9b. The mode is Landau-damped as predicted in section 3.2.

The collisionless damping of zonal flows evolving as oscillations of GAMs has been firstly demonstrated by Rosenbluth et al [90] and subsequently widely investigated with gyrokinetic theory and simulations by Sugama et al [91]. Later published results have proved the consistency of GYSELA code with the predicted collisionless damping [88, 92]. In our simulations without energetic ions, we have observed that, the collionless damping of zonal flows is recovered as long as a $(m, n) = (0, 0)$ initial perturbation of the distribution function is applied. If this perturbation is only nonlinearly excited via the coupling of the modes $m = -1$ and $m = 1$, the mode ϕ_{00} is fully damped.

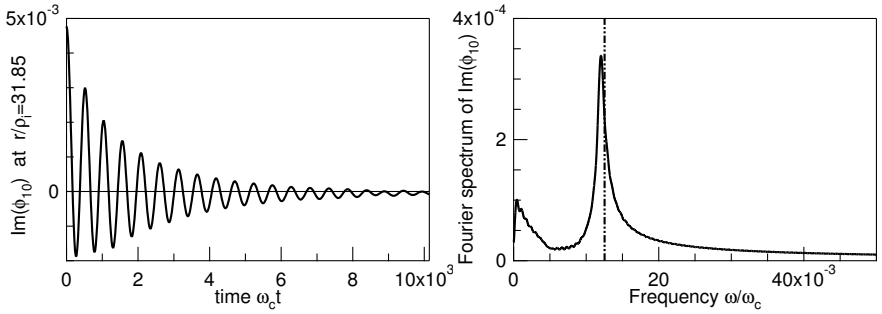

Figure 3.9: Damping of ϕ_{10} at the GAM frequency without fast particles (left) and FFT of the mode (right). GAM frequency is represented by a vertical dashed line.

In order to obtain the linear threshold of the EGAM excited by a bump-on-tail equilibrium function, the following set of parameters has been chosen (see figure 3.5)

$$\hat{T}_h = 1,\ \overline{\zeta} = 4,\ n_h = 0.15 n_i \tag{3.60}$$

We observe in figure 3.10 that the mode is indeed marginally stable and oscillates at a smaller frequency (ω_{EGAM}) than the standard GAM frequency (ω_{GAM}). We find $\omega_{EGAM} \approx 0.5\omega_{GAM}$, i.e. $q\Omega \approx 3$ for a safety factor $q \approx 3$, which is consistent with the hypothesis of the section 3.2. In addition, we observe the presence of a mode at a frequency closer to ω_{GAM}. This mode is indeed the standard GAM which is highly damped by fast ions due to the fact that $\partial_E \left(F_{eq,i} + F_{eq,h}\right)|_{|\zeta|=q\Omega_{GAM}} < \partial_E F_{eq,i}|_{|\zeta|=q\Omega_{GAM}} < 0$.

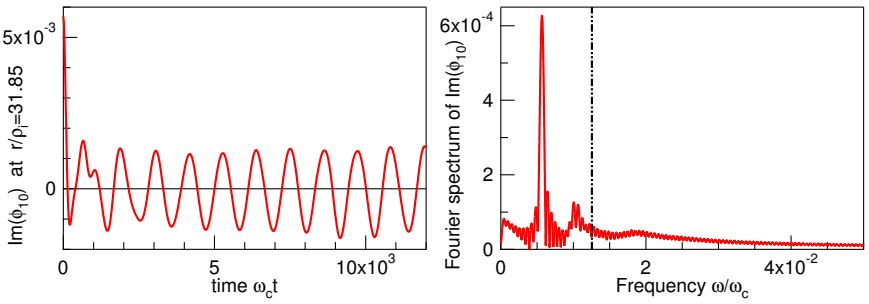

(a) (b)

Figure 3.10: Steady-state oscillations of ϕ_{10} at the EGAM frequency with energetic particles. In this example, the parameters of the bump-on-tail distribution function have been set to $n_h = 0.15n_i$, $\overline{\zeta} = 4$ and $\hat{T}_h = 1$. The standard GAM frequency is given by a vertical dashed line.

In the case of a slowing-down distribution function, the parameters for the simulations are (see figure 3.6)

$$\Lambda_0 = 0.2,\ \Delta\Lambda = 0.5,\ E_b = 50,\ E_c = 10,\ n_h = 0.014n_i \tag{3.61}$$

The parameters of the pitch-angle part have been selected following the results illustrated in figure 3.7, where we have shown that there is an interval of Λ_0 in which the excitation is possible for any value of E_b and E_c. The upper limit in velocity space of numerical simulations constraints the maximum birth energy. Here we have used $-10 \leq v_{\|} \leq 10$ and $0 \leq \mu \leq 50$, so that the maximum value of the birth energy is $E_b = 50$. The critical energy has been chosen equal to 10 since this value is representative of the critical energy of fast ions in NBI heated plasmas. The parameter n_h, which is proportional but not equal to the density, has been selected equal to 0.014, close to the predicted linear threshold. Figure 3.11 shows the oscillations of the undamped mode ϕ_{10} close to the usual GAM frequency and no other modes have been observed in this case.

A possible explanation for the absence of the EGAM frequency can be found in Ref. [13], where the ratio between the particle bounce frequency to the standard GAM frequency is introduced as a critical parameter for the excitation of EGAMs. This ratio is estimated as $Z \sim E_h/(2.75q^2T)$, where E_h is the energetic particle energy and T the plasma temperature [13]. Here E_h is to be calculated for $\Lambda = 0$. If we assume that only resonant particles must be considered, it turns out this parameter differs from one simulation to another in the safety factor value. For the bum-on-tail instability Z is four times smaller than in the slowing-down instability. Therefore, the bump-on-tail distribution function is potentially more efficient than the slowing-down distribution regarding the excitation of the EGAM frequency. However, when using for the slowing-down distribution function the same safety factor as for the bump-on-tail, the criterion for instability is not satisfied

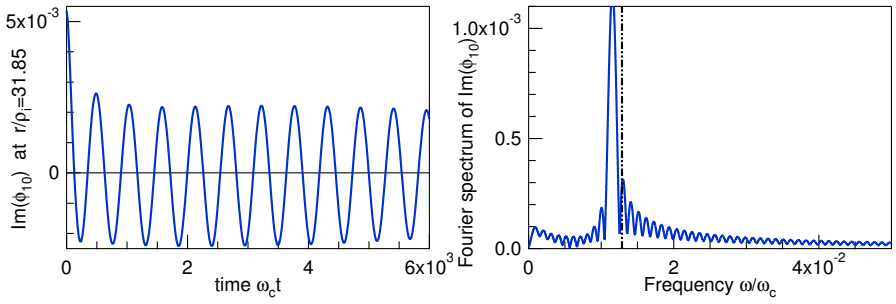

(a) (b)

Figure 3.11: Steady-state oscillations of ϕ_{10} at the EGAM frequency with fast particles. The parameters of the slowing-down distribution function have been set to $n_h = 0.014 n_i$, $\Lambda_0 = 0.2$, $\Delta\Lambda = 0.5$, $E_b = 50$, $E_c = 10$.

due to the damping of passing particles and EGAMs cannot be excited. This is an issue that should be completely explored in future GYSELA simulations.

The radial structure of the mode has been analysed in the literature [13], where the equation on the perturbed radial electric field is derived and a global structure deduced. Here we show in figure 3.12 the imaginary part of the mode ϕ_{10} as a function of r/ρ_i at four different instants of the simulation taken during one EGAM cycle for both types of distribution functions. Boundary conditions force the instantaneous electric potential to vanish at $r = r_{min}$ and $r = r_{max}$. A global structure is observed, which is consistent with the fact that the equilibrium profiles do not depend on the radial position. Let us recall here that this constitutes a major limitation of the model. The impact of finite temperature gradient and a more general scenario where EGAMs and turbulence interact with each other are addressed in the next chapter of this thesis.

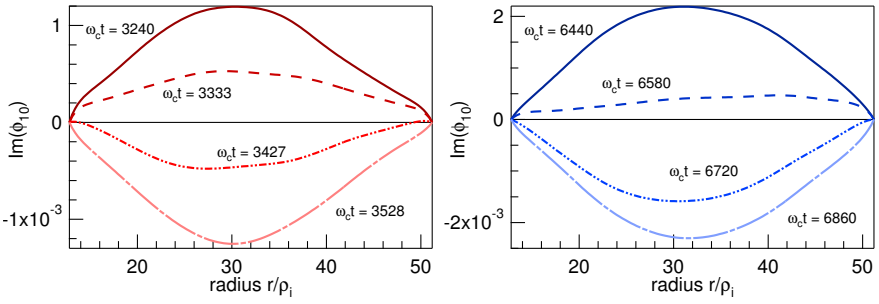

(a) (b)

Figure 3.12: Radial structure of the mode ϕ_{10} for a bump-on-tail (left) and a slowing-down (right) distribution functions.

For both distribution functions, a density scan has been performed in order to explore the region beyond the linear threshold and obtain the dependence of the real frequency and the linear growth rate on the fast ion concentration. We have selected ratios between the fast ion concentration and the thermal particles concentration up to 0.4. Figure 3.13 illustrates the results of the density scan during the linear excitation of the mode. Two branches have been identified when fast ions are modelled by a bump-on-tail distribu-

tion function: the GAM branch, which is highly damped by the presence of energetic particles as explained before in this paper, and the EGAM branch, which is excited by the anisotropy of the distribution function. In the case of a slowing-down distribution, only the GAM branch is observed and no other mode appears. The existence of these branches was theoretically predicted by Fu [13] and confirmed by Qiu et al [75]. However, our results slightly differ from the ones reported by Fu [13] since the stable GAM branch always exhibits a finite damping rate. This is due to the fact that we use for both thermal and fast particles a fully kinetic model and that the increase of n_h/n_i results in more negative values of the slope of the distribution function at $|\zeta| = q\Omega_{GAM}$. In addition, the EGAM branch exists even for fast ion density below the threshold, but this branch is highly damped. **We observe that the real frequency of the existing modes decreases with the fast ion concentration for both classes of fast ion distributions. In addition, the unstable modes exhibit positive linear growth rates which increase with the concentration** in agreement with Fu [13]. Finally, the linear growth rate for a concentration above the linear threshold is similar for both fast ion distributions.

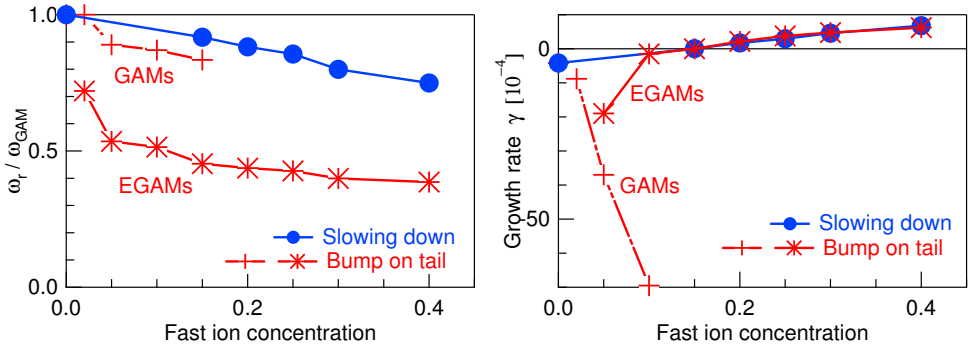

Figure 3.13: Dependence of the real frequency (left) and the linear growth rate (right) on the fast ion concentration for both classes of distributions considered in this chapter. We observe that the real frequency (resp. the linear growth rate) decreases (resp. increases) with the concentration.

3.5 Nonlinear saturation of energetic-ion-driven GAMs: energy transfer mechanism *vs* wave-particle trapping

In the previous section, we have recovered the predicted linear threshold for EGAM excitation and observed that beyond this value the linear growth rate is positive, as expected. This means that the amplitude of the mode will grow and, as analysed in the introduction of this chapter, a mechanism that prevents the amplitude from growing indefinitely must exist. This mechanism is characterized by nonlinear effects that will either modify directly the second term on the right hand side of equation 3.14 or modify the equilibrium and therefore indirectly the growth rate. The kinetic simulations presented in this chapter are suitable for this kind of analysis and enable the study of (nonlinear) saturation, in particular in the framework of EGAM excitation. The saturation of EGAMs has been pointed out very recently in the literature as a possible mechanism providing the explanation of fluctuations at the second harmonic $2\omega_{\mathrm{EGAM}}$ [93]. The aim of this section

is to provide for the first time numerical evidence of the saturation of EGAMs. We will in particular analyse in detail the saturation in the case of the two distribution functions introduced before.

In figure 3.14a we have plotted, for $n_h = 0.3n_i$ the time evolution of the mode $n = 0$ for four different values of m ($m \leq 3$), excited by a bump-on-tail. We observe that the linear growth rate is the same for all the poloidal modes we have considered here. In addition, the linear regime ends at $\omega_c t \approx 10^4$ for all the poloidal Fourier components. Beyond this time, the saturation is reached and the amplitudes of the poloidal modes do not grow any longer. Note that, in our simulations, the non axisymmetric wave numbers $n \neq 0$ are not excited and the time evolution of the poloidal modes in the case of the bump-on-tail is the same for all m, meaning that there is no energy exchange between the modes. Actually, each of these m mode numbers is part of the same eigenvector, corresponding to $n = 0$. These results show that the linear terms dominate the excitation of the mode. If there is only one single eigenmode growing linearly, wave-particle trapping is the only way it can saturate as we will see in the following. Figure 3.14b shows a similar behaviour for the slowing-down distribution function. However, in this case, we can observe that the growth phase of the mode is not characterized by a single linear growth rate γ. This result indicates that **even if the excitation is also dominated by linear effects in the case of the slowing-down distribution, nonlinearities are already present and may affect the way the mode saturates. This constitutes the main difference regarding the dynamics of the excitation and saturation of the energetic GAMs excited by the two distribution functions considered in this chapter** and, as we will see later, this is likely due to different structures in the μ-space.

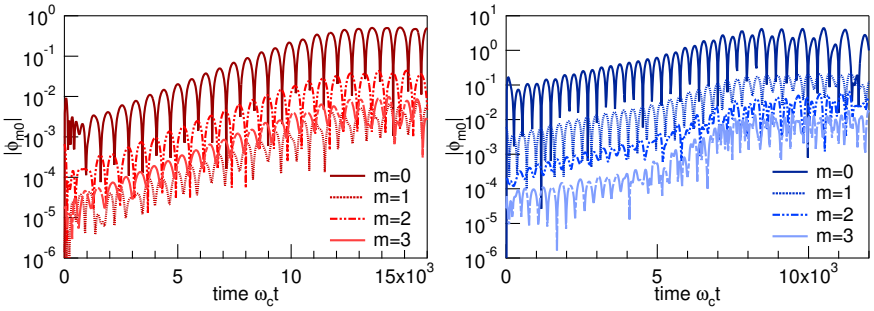

Figure 3.14: Time evolution of the Fourier components $m \leq 3$ for the bump-on-tail (left) and the slowing-down (right) distribution functions. Linear excitation occurs up to $\omega_c t \approx 10^4$. After that time, saturation appears for all the modes, but no energy exchange betweeen the modes exists.

To analyse this, we can firstly quantify the saturation level for each distribution function. This level is defined as the value of the electrostatic potential after saturation. The density scan performed in this section gives a quantification of this level as a function of the fast ion concentration. Figure 3.15 shows the level of saturation of the instability for both distribution functions. This level increases with the concentration in the case of fast ions modelled by a bump-on-tail distribution but it does not depend on the content of fast ions for the slowing-down instability. We hereafter give an explanation for this behaviour.

As established in collisionless regime by O'Neil [94] and later generalized by Berk *et al.* [95] in the presence of an external wave damping and a collision operator, the

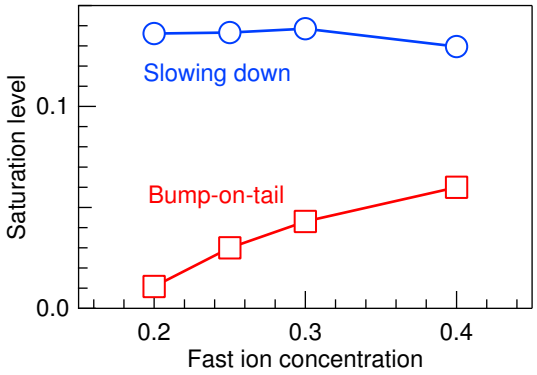

Figure 3.15: Level of saturation for the two distribution functions considered in this chapter.

wave-particle trapping mechanism can be understood as a competition between the linear growth rate of the wave, γ, and the trapping frequency, ω_b. When the wave trapping frequency reaches the linear growth rate the mode saturates. In the case of the bump-on-tail, we have noticed that the saturation can only occur by means of the wave-particle trapping. Therefore, the saturation level should satisfy $\phi_{sat} \sim \gamma_L^2$, following O'Neil [94]. The growth rate depends in its turn on the fast ion concentration as illustrated in figure 3.13b and has been found to be constant during all the excitation phase. One may conclude that the saturation level will increase with the fast ion concentration, which is consistent with figure 3.15. However, we observe that the scaling $\phi_{sat} \sim \gamma_L^2$ is not recovered and for high densities the saturation level appears to be smaller than the one expected from the mentioned scaling. Further work needs to be done in this direction to explain this behaviour.

The wave-particle trapping can be described, in the absence of frequency sweeping, by the formation of an island in phase-space. Trajectories are defined by the conservation of the Hamiltonian. When an island is created, particles following the closed orbits (trapped orbits) will give energy during $\Delta t = \pi\omega_b^{-1}$ and will recover this energy during the remaining half-cycle. It is obvious that when the frequency ω_b is of the order of the linear growth rate, the mode cannot grow any longer.

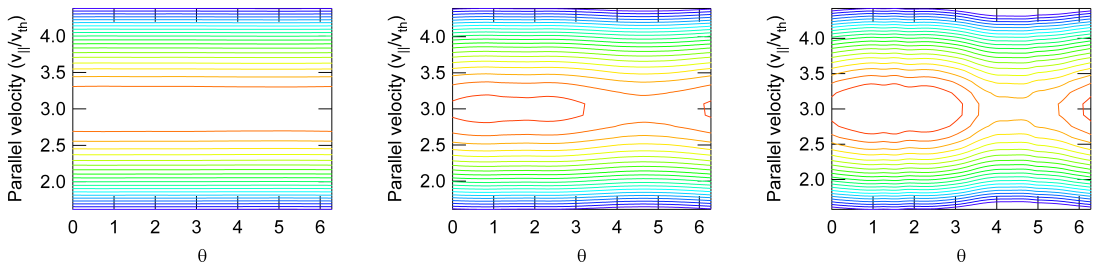

(a) $\omega_c t = 5000$ (b) $\omega_c t = 10000$ (c) $\omega_c t = 15000$

Figure 3.16: Isocontours of the effective Hamiltonian in the case of the bump-on-tail instability at different instants of the simulation for $n_h = 0.3 n_i$.

The formation of the phase-space island in the case of the bump-on-tail distribution

function is captured in figure 3.16, where isocontours of the effective Hamiltonian are given. The effective Hamiltonian can be obtained by means of the action-angle set of variables. The equilibrium Hamiltonian for passing particles is approximated by $\mathcal{H}_{\rm eq} = \frac{1}{2}mv_\parallel^2$, where the parallel velocity is expressed in terms of J_2 and J_3 as $v_\parallel = \frac{1}{mR_0}\left(J_3 - e\psi\left(J_2\right)\right)$. As explained in appendix E, we can approximate J_2 by the toroidal magnetic flux, i.e. $J_2 \approx e\Phi\left(\psi\right)$. Therefore, the gradient of $\mathcal{H}_{\rm eq}$ in the action-angle set of variables reads

$$\frac{\partial \mathcal{H}_{\rm eq}}{\partial J_3} = \frac{v_\parallel}{R}, \quad \frac{\partial \mathcal{H}_{\rm eq}}{\partial J_2} = \frac{v_\parallel}{qR} \tag{3.62}$$

Owing to the existence of two symmetric resonances $v_\parallel = \pm qR\omega_{\rm EGAM}$, we assume a perturbation of the form $\delta H = e\phi_1 \cos\alpha_2 \cos\left(\omega_{\rm EGAM}t\right) = \frac{1}{2}e\phi_1 \cos\left(\alpha_2 - \omega_{\rm EGAM}t\right) + \frac{1}{2}e\phi_1 \cos\left(\alpha_2 + \omega_{\rm EGAM}t\right)$ and write $\xi = \alpha_2 + M\omega_{\rm EGAM}t$, with $M = \pm 1$. The actions are perturbed as $J_i = J_{i,\rm res} + I\delta_{i,2}$, which allows one to write

$$\frac{{\rm d}\xi}{{\rm d}t} = \Omega_2 + M\omega_{\rm EGAM} = \frac{{\rm d}\Omega_2}{{\rm d}J_2} I = \frac{\partial \mathcal{K}}{\partial I} \tag{3.63}$$

$$\frac{{\rm d}I}{{\rm d}t} \equiv \frac{{\rm d}J_2}{{\rm d}t} = -\frac{\partial H}{\partial \alpha_2} = \frac{1}{2}e\phi_1 \sin\xi = -\frac{\partial \mathcal{K}}{\partial \xi} \tag{3.64}$$

where the effective Hamiltonian $\mathcal{K} = \frac{1}{2}CI^2 + \delta H$ has been introduced. The curvature C of the Hamiltonian is explicitly calculated as

$$C = \frac{{\rm d}\Omega_2}{{\rm d}J_2} = \frac{1}{mq^2R^2} \tag{3.65}$$

Note that $v_\parallel$ and I are related to each other following $I = qmR\left(v_\parallel + Mq\omega_{\rm EGAM}\right)$. Therefore, the effective Hamiltonian finally reads

$$\mathcal{K} = \frac{1}{2}m\left(v_\parallel + Mq\omega_{\rm EGAM}\right)^2 + \delta H \tag{3.66}$$

We can see that all particles around the resonance are passing at $\omega_c t = 5000$, which is consistent with the fact that at this instant, the mode still evolves linearly. The formation of the island can be observed later, when the system is close to the saturation but is still growing, for instance at $\omega_c t = 10000$. In this case, nonlinearities start appearing in the system, but the phase-space island is not large enough to compensate for the growth of the mode. However, at $\omega_c t = 15000$, the island has been widened and the system has completely saturated.

The saturation provided by the wave-particle trapping must result in a flattening of the distribution function around the resonance velocity [94]. Let us recall that we have obtained in this chapter the density of exchanged energy between wave and particles, given by equation 3.46. As we have shown, this energy is proportional to the integral over the μ-space of $\partial_E F_{eq}|_{|\zeta|=q\Omega}$, weighted by a positive polynomial $g\left(\bar{\mu}\right)$. Thus, the evolution of the exchanged energy must reflect any possible flattening of the distribution function. Figure 3.17a shows the time evolution of the density of exchanged energy between the mode and both thermal and fast ions. We observe that, at the beginning of the simulation, this energy remains constant and positive, which is consistent with the initial conditions. The mode then grows exponentially as long as the perturbation remains small and the exchanged energy subsequently decreases. More in-depth analysis of the saturation mechanism may be done by looking at the product $g\left(\bar{\mu}\right)\partial_E F_{eq}|_{|\zeta|=q\Omega}$ as

a function of the adiabatic invariant. This quantity will be positive if the particles feed the mode and negative otherwise, thus it provides a quantitative description of the excitation and saturation mechanisms and enables in particular to measure the energy gradient for passing and trapped particles separately.

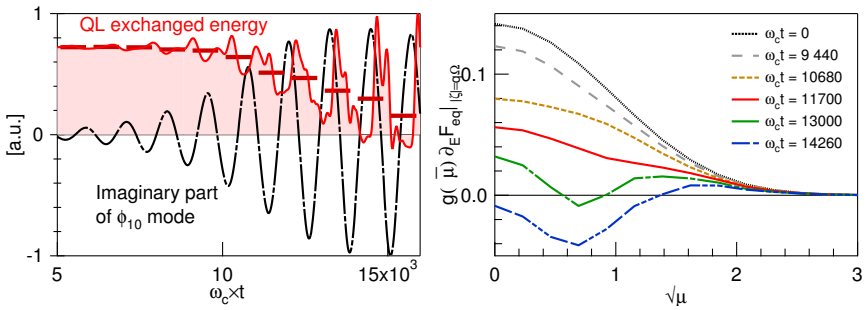

Figure 3.17: For a bump-on-tail instability. Left: density of exchanged energy per volume and time unit (solid curve) and its time average (horizontal lines). The imaginary part of the mode ϕ_{10} is represented here to compare the oscillations frequency. All quantities are normalized. Right: dependence of the derivative of the equilibrium distribution function at the resonance on the adiabatic invariant for various instants of the simulation.

Figure 3.17b shows this product at various instants corresponding to local minima of the density of exchanged energy. We observe that the derivative is positive for all μ at $t = 0$, which means that all the particles with a parallel velocity $\zeta = \pm q\Omega$ contribute to the excitation of the mode. Thus, **the saturation must only come from the exchange of energy between the particles and the mode, which is consistent with Fig. 3.17a and with the fact that the mode saturates *via* wave-particle trapping**. Nevertheless, we can observe that the flattening is not homogeneous in μ, i.e. it occurs at different instants depending on the perpendicular energy, and is more pronounced for particles with low μ.

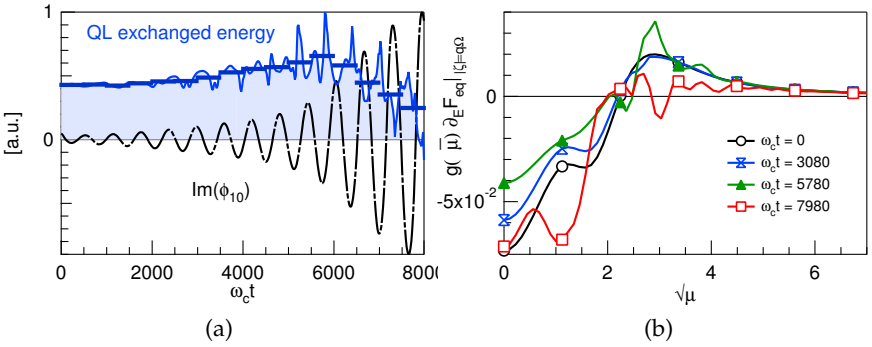

Figure 3.18: For a slowing-down instability. Density of exchanged energy (left) and derivative of the equilibrium distribution function at the resonance for different instants of the simulation (right).

The same kind of analysis for an instability driven by the slowing-down distribution function has been performed. Figure 3.18a shows the evolution of the exchanged energy

between waves and particles. In this case, we observe that the density of exchanged energy presents a maximum value before the saturation. As we have previously seen, the derivative of the initial distribution function with respect to the energy depends on both parallel and perpendicular velocity. In the case of the slowing-down, this derivative may be positive or negative depending on the value of the adiabatic invariant. Therefore, one needs to consider that only particles with sufficient perpendicular energy ($\mu > 5$) may contribute to the excitation of the mode at $t = 0$. Circles in figure 3.18b represent the derivative of the initial distribution with respect to the energy at the resonant velocity. We can see that high-μ particles excite the mode and the mode gives its energy to low-μ particles. A nonlinear energy transfer between trapped and passing particles in collisionless plasmas is then possible by means of GAM excitation. This transfer modifies the slope in $v_{||}$ of the distribution function at low μ as observed in figure 3.18b. Afterwards, passing particles become less stabilizing and the growth rate is modified. This self-organization of the system occurs during all the excitation until saturation is reached as a result of an equilibrium between the energy transferred from high- to low-μ particles via GAMs. For n_i remaining constant, n_h/n_i is just a multiplying factor that modifies the distribution function $F_{eq,h}$ acting in the same way on both classes of particles (exciting and stabilizing). Therefore, an increase of n_h/n_i increases identically the density of both exciting and stabilizing particles. As a result, the saturation level is therefore expected to be independent of n_h/ni, i.e. of the fast ion concentration. This means that, **even if wave-particle trapping is not excluded in the saturation mechanism of the slowing-down instability, the fact that some particles contribute to the mode damping introduces nonlinearities that have an impact on the saturation of the mode.**

3.6 Exploring the regimes under the linear instability threshold

We have seen that an instability coming from a situation where all resonant particles are destabilizing leads to a saturation dominated by the wave-particle trapping mechanism. The wave-particle trapping can be understood in that case as a decreasing of the linear growth rate down to zero, since in that case no damping exists. Mathematically, this decrease can be expressed as a modulation of the predicted linear growth rate by a damping factor as follows

$$\gamma_L(t) \sim \nu_L(\omega_B)\,\gamma_L \tag{3.67}$$

where $\gamma_L \propto \partial_E F_{\mathrm{eq}}|_{\mathrm{res}}(t=0)$ and $\nu_L(\omega_B)$ is a multiplying factor decreasing with the bounce frequency $\omega_B(t)$. If all resonant particles contribute to the excitation, saturation occurs only when $\langle \nu_L(\omega_B)\rangle_T = \gamma^{-1}\gamma_d$, where $\langle\cdots\rangle_T$ is an average over several EGAM cycles and γ_d is an external fixed damping rate. In the bump-on-tail instability where no collisions are accounted for, $\gamma_d = 0$ and the saturation occurs when $\langle \nu_L(\omega_B)\rangle_T = 0$. However, in the slowing-down instability, passing particles represent a resonant damping $\gamma_d(t)$. The case of kinetic modes resonantly driven and damped has been recently analysed in [96, 97]. It was shown therein the existence of some modes called *metastable*. They are characterized by an initial linearly stable phase, where the amplitude decreases for any initial perturbation, and a subsequent growth phase if the amplitude of the initial perturbation is large enough to reach the nonlinear regime. We have observed a similar behaviour in the case of GAMs driven by energetic ions. We plot in figure 3.19 the time evolution of the amplitude of the electrostatic potential for a set of parameters under the predicted linear threshold in the case of the slowing-down distribution function ($n_h/n_i = 0.011$). The described behaviour is clearly captured.

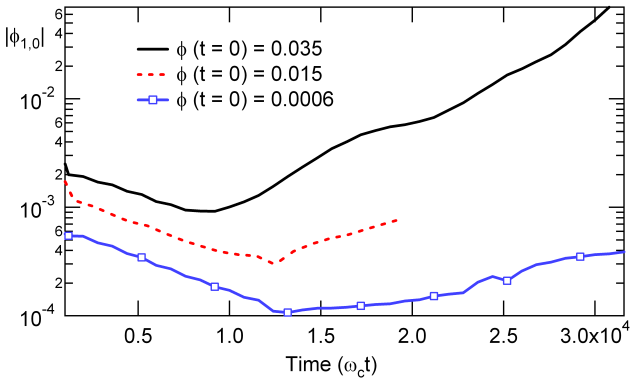

Figure 3.19: Time evolution of the amplitude of the electrostatic potential for three different initial conditions in the case of a slowing-down instability under the linear threshold.

3.7 Summary

In this chapter, we have analysed the excitation of GAMs by energetic particles. For this purpose, we have firstly derived a fully kinetic calculation of the GAM dispersion relation, which indicates that a strong Landau damping is expected for modes satisfying $\Im(\omega) \approx \Re(\omega)$. In practice, Landau damping only vanishes in the fluid limit ($\omega \gg c_{si}/qR$), where we recover the usual GAM oscillations. We have afterwards calculated analytically the exchanged energy between particles and waves via a variational principle. Based on this exchanged energy, a threshold for the excitation by fast ions has been established, leading to a quantitative description of the excitation mechanism. In particular, the expression that has been derived allows us to determine the nature of the particles that contribute to the excitation of the modes. Two examples have been studied analytically: the excitation by a double Maxwellian shifted in $v_{\|}$ (for the sake of simplicity called bump-on-tail in this paper) and the excitation by a slowing-down distribution function. It turns out that, although the resonance condition applies in the $v_{\|}$-space, the distribution of particles in μ-space is essential and mainly particles with high perpendicular energy are responsible for the mode excitation in the case of the slowing-down distribution function. Good agreement between gyrokinetic simulations using GYSELA code and the theoretically predicted linear threshold has been found for the two distribution functions, bump-on-tail and slowing-down. Density scan shows that the frequency of the excited mode decreases with the fast ion concentration as the linear growth rate increases. Nonlinear effects have been analysed in detail. Mode coupling has been excluded as a possible mechanism of the saturation. Flattening of the equilibrium distribution function around the resonance velocity due to wave-particle trapping has been found to be at the origin of the saturation in the case of a bump-on-tail distribution function, leading to a saturation level that increases with fast particles concentration. The flattening is more pronounced for low values of μ. In addition, the saturation must be understood as oscillations at the EGAM frequency between states of maximum and minimum density of exchanged energy, determined by the distribution in μ-space. In the case of a slowing-down distribution function, an energy transfer from high- to low-μ particles has been identified resulting in a constant saturation level. The excitation of linearly stable modes has been observed due to the resonant damping provided by passing particles in the slowing-down instability.

Chapter 4

Geodesic acoustic modes driven by energetic ions in the presence of turbulence

> No pretendo resolver el problema, entenderlo o asumirlo. Sólo es parte del viaje hacia donde voy: un lugar que reconoceré cuando llegue a él.
>
> Arturo Pérez-Reverte, *El pintor de batallas*

Contents

4.1 Introduction: a brief history of the GAM-ZF-turbulence paradigm

As explained in the introduction of this thesis, the control of turbulent transport reveals essential to achieve high tokamak performance, quantified by the amplification factor Q. In this first section we give some elements to understand the characteristics of turbulence as well as its control. The interested reader can find more details on the concepts introduced in this section in Ref. [98].

4.1.1 Flow shear effect

It is well-known that a shear of the poloidal component of the $E \times B$ velocity drift (and therefore a shear of the radial electric field, since $v_\theta \sim -E_r$) is a possible way to reduce the turbulence level [99]. This can be explained in a heuristic way by considering a vortex (isopotential line) embedded in a poloidal velocity field. This explanation is schematically illustrated in figure 4.1. In this figure, the arrows represent the poloidal velocity field, whose shear is constant in time. The vortex is represented by a closed line, which evolves from a circle at the initial time and is distorted by the sheared velocity field. This poloidal velocity field with (almost) constant shear can be due either to the so-called *zonal flows* [100] or to the mean radial electric field governed by the radial force balance.

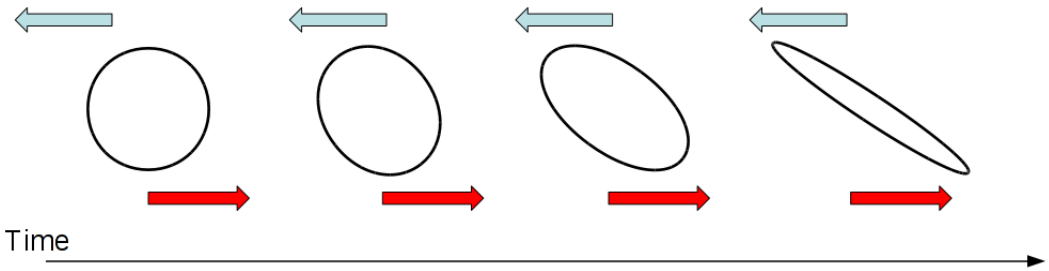

Figure 4.1: Schematic representation of a vortex sheared by a stationary poloidal velocity field.

Zonal flows are axisymmetric electric field perturbations independent of θ, but dependent on the radial position, i.e. $\partial_r^2 \phi_{00} \neq 0$. However, in the literature, GAMs are sometimes considered as zonal flows. To distinguish between both, some authors divide the zonal flows into *low frequency zonal flows* (LFZF) and GAMs. For the sake of clarity, we have decided to follow this terminology in this thesis. One can show that a sheared poloidal velocity field leads to a reduction of the radial extent of the vortex. Indeed, considering a mode of the form $e^{im\theta}$, an initial angle θ_0 will be transformed into $\theta = \theta_0 + \frac{1}{r}(r - r_0)\frac{\partial^2 \phi_{00}}{\partial r^2} t$ and the mode is written as $e^{im\theta_0 + i\frac{m}{r}(r-r_0)\frac{\partial^2 \phi_{00}}{\partial r^2} t}$. Therefore, the radial wavenumber becomes

$$k_r = k_r^{(0)} + k_\theta (r - r_0) \frac{\partial^2 \phi_{00}}{\partial r^2} t \tag{4.1}$$

where $k_r^{(0)}$ is the radial wavenumber in the absence of shearing. The importance of the shearing can be directly observed in expression (4.1). Since the radial wavenumber increases linearly with time, the radial structure, i.e. the vortex scale, becomes smaller and therefore the correlation between structures is partially lost. This mechanism introduces

a way to saturate the turbulence, different from profile relaxation, mode-mode coupling and dissipation of energy through ion Landau damping or collisions. A heuristic criterion for the stabilization *via* the shear is that the decorrelation rate of the ambient turbulence in the absence of shearing $\Delta\omega_T^{(0)}$, must be of the order of the absolute value of the shearing rate, namely $|\gamma_E| = |\frac{r}{q}\partial_r\left(\frac{q}{r}\frac{E_r}{B}\right)|$ in toroidal geometry [101], i.e.

$$|\gamma_E| \sim \Delta\omega_T^{(0)} \tag{4.2}$$

A more accurate description of the stabilization by means of a stationary shear is given by the modification of the radial correlation length Δr. It has been proposed that the correlation length is reduced with respect to its value in the absence of shearing rate Δr_0 as follows [101]

$$\frac{\Delta r_0}{\Delta r} = 1 + \left(\frac{\gamma_E}{\Delta\omega_T^{(0)}}\right)^2 \tag{4.3}$$

This reduction of the correlation length leads to a decrease of the amplitude of the perturbations [98]

$$\frac{\left\langle|\delta\phi|^2\right\rangle_{\text{stat}}}{\left\langle|\delta\phi^{(0)}|^2\right\rangle_{\text{stat}}} \approx \left(1 + \left(\frac{\gamma_E}{\Delta\omega_T^{(0)}}\right)^2\right)^{-1} \tag{4.4}$$

where $|\delta\phi^{(0)}|$ is the amplitude of the perturbations in the absence of shearing and $\langle\cdots\rangle_{\text{stat}}$ represents a statistical average. The question that rises from the previous discussion is how to create a sheared zonal flow allowing the stabilization of turbulence. This question leads us to the self-regulation of fluctuations. The temporal evolution of the poloidal velocity may be expressed in cylindrical geometry as [102]

$$\frac{\partial\left\langle v_\theta\right\rangle}{\partial t} = -\frac{1}{r^2}\frac{\partial}{\partial r}\left(r^2\Pi_{r\theta}\right) - \nu\left(\left\langle v_\theta\right\rangle - v_\theta^{\text{NC}}\right) \tag{4.5}$$

where v_θ^{NC} is the neoclassical prediction of the poloidal velocity and $\Pi_{r\theta}$ is the r,θ component of the Reynolds stress tensor, defined as $\Pi_{r\theta} = \langle\tilde{v}_r\tilde{v}_\theta\rangle$. Here, $\tilde{v}_r$ and $\tilde{v}_\theta$ are the fluctuations of the $E\times B$ velocity. This equation shows that zonal flows, which contribute to the stabilization of the fluctuations, are nonlinearly generated by the fluctuations themselves. This self-regulation of the turbulence has been invoked in the literature as the paradigm of the drift wave-zonal flow turbulence [98]. Note that even in the absence of electric shear, turbulence saturates due to both nonlinear coupling of unstable modes to stable modes and relaxation of radial profiles, i.e. flattening of equilibrium profiles. The level of saturation is however larger without than with ZFs.

The generation of zonal flows has been studied intensively during the last years. In particular, coherent analysis of nonlinear excitation of zonal flows developed by ITG turbulence has been predicted analytically and observed numerically in three-dimensional global gyrokinetic simulations [103]. Also, a secondary instability in drift wave turbulence has been invoked as an additional possible mechanism for zonal flow generation [104] and the nonlinear feedback on the background turbulence as the reason for zonal flow damping [105]. However, when talking about zonal flows as a key element for the turbulence stabilization and their damping on the underlying turbulence, one must keep in mind that, in addition, neoclassical damping of zonal flows due to ion-ion collisions may occur and have an effect on the turbulent transport. The collisional damping of zonal flows was firstly predicted analytically by Hinton and Rosenbluth [106] and

subsequently observed in gyrokinetic particle simulations by Lin *et al* [107], where the turbulent transport was found to increase with the ion-ion collision frequency and the neoclassical damping of zonal flows was invoked as the explanation of this behaviour. More recent analysis has been done regarding the impact of ion-ion collisionality on turbulence in full-f and global gyrokinetic simulations with GYSELA [108].

The oscillatory component of ZFs, namely the geodesic acoustic modes (GAMs) [12], though Landau damped (see previous chapter), are also thought to play a role in the nonlinear saturation of drift wave turbulence. However, because of their oscillatory behaviour, it has been claimed that their role is reduced compared to LFZFs. This can be analysed by considering a time-varying shearing rate $\gamma_E(t)$ evolving as

$$\gamma_E(t) = \gamma_E^{(0)} \mathrm{e}^{i\omega_s t} \tag{4.6}$$

In this case, it has been proposed that the effective shearing rate is given by [109]

$$\gamma_{E,\mathrm{eff}} = \gamma_E^{(0)} \frac{\left((1+3f)^2 + 4f^3\right)^{1/4}}{(1+f)\sqrt{1+4f}} \tag{4.7}$$

where $f = \left(\omega_s/\Delta\omega_T^{(0)}\right)^2$. This shearing rate is reduced with respect to the instantanous shearing rate and needs to be compared to the decorrelation rate of the ambient turbulence. An important reduction of turbulent transport is expected if the effective shearing rate exceeds the decorrelation rate. This effective shearing rate decreases with the frequency of the oscillations, which means that a time-dependent sheared flow will have relatively little effect on turbulence suppression. In particular, $\gamma_{E,\mathrm{eff}} \to 0$ when $f \to \infty$. This is schematically explained in figure 4.2, where an initial vortex is deformed by a time-varying sheared velocity field. From one instant t to the next one $t + \Delta t$, the shear is inverted, which makes the vortex deformation oscillate as well in time. Therefore, after many realizations, statistically, the vortex has not been effectively deformed if the frequency of the turbulence is much smaller than the frequency of the sheared field.

Gyrokinetic simulations [110] have shown that though generally less efficient than the LFZFs, the effect of GAMs on the saturation of turbulence sometimes appears to be dominant. Experimental evidence of the existence of GAMs in turbulence flows were reported in [111], where radially localized GAM-like oscillations of the poloidal flow $\tilde{v}_\theta$ were found at a frequency $\omega \ll \Delta\omega_T$. It was therefore suggested that these oscillations might contribute to the partial suppression of turbulence, but no other evidence was shown therein. Very recent experimental results have been reported in the context of turbulence regulation by GAMs during the analysis of the L-H transition in the ASDEX Upgrade tokamak [64]. In particular the presence of GAMs is accompanied by a suppression of turbulence during the L-mode phase and in the H-mode GAMs are not observed any longer, suppressed by the strengthened mean flow shearing. This behaviour remains for the moment unclear, but several theoretical works have been carried out in order to shed some light on these experimental evidences. One of these suggests that a pair of counter propagating GAMs might be coupled nonlinearly and give rise to a ZF, whose amplitude increases with the GAM amplitude. This mechanism, which is close to a wave beating phenomenon, represents an exchange of energy, whose level has been found to correlate with the level of symmetry breaking [63]. In a recent publication [112], the analysis of the efficiency of oscillating sheared flows compared to the efficiency of stationary shearing has been studied. It is therein suggested that the absence of GAMs could be the

key element to enable the transition to the H mode, which would be consistent with the experimental observations reported in [64].

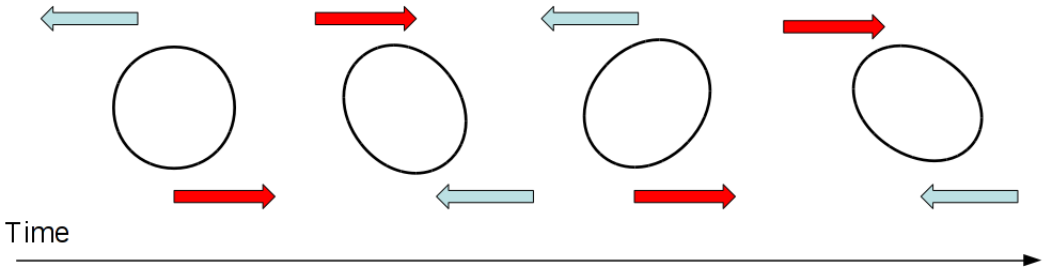

Figure 4.2: Schematic representation of a vortex sheared by a time-dependent poloidal velocity field.

In a more general case, where stationary zonal flows, GAMs and turbulence coexist, one needs to consider the coupling between the poloidally symmetric flows $(m = 0, n = 0)$, the $(m = 1, n = 0)$ perturbations and the ITG modes $(m \neq 0, n \neq 0)$ [60]

$$\frac{\partial \langle v_\theta \rangle}{\partial t} = -\frac{1}{r^2}\frac{\partial}{\partial r}\left(r^2 \Pi_{r\theta}\right) - \frac{2a}{n_{\mathrm{eq}} R}\langle p \sin\theta \rangle - \nu\left(\langle v_\theta \rangle - v_\theta^{\mathrm{NC}}\right) \tag{4.8}$$

$$\frac{\partial}{\partial t}\langle p \sin\theta \rangle = -\left\langle \left[\tilde{\phi}, \tilde{p}\right] \sin\theta \right\rangle + \left(\Gamma + \tau^{-1}\right) p_{\mathrm{eq}} \frac{a}{qR}\langle v \cos\theta \rangle + \left(\Gamma + \tau^{-1}\right) p_{\mathrm{eq}} \frac{a}{R}\langle v_\theta \rangle \tag{4.9}$$

$$\frac{\partial}{\partial t}\langle v \cos\theta \rangle = -\frac{a}{n_{\mathrm{eq}} qR}\langle p \sin\theta \rangle \tag{4.10}$$

where Γ is a ratio of specific heats and $\tau = T_i/T_e$. In these equations, we can distinguish (1) the coupling between $\langle v_\theta \rangle$ and $\langle p \sin\theta \rangle$ leading to the GAM oscillations, (2) the coupling between $\langle v_\theta \rangle$, $\langle p \sin\theta \rangle$ and $\tilde{\phi}$ reflecting the nonlinear generation of ZFs by turbulence *via* the Reynolds stress and the subsequent generation of up-down asymmetric perturbations *via* the curvature term and (3) the coupling between $\langle p \sin\theta \rangle$ and $\langle v \cos\theta \rangle$ leading to the sound wave equation. For high q, the two first couplings dominate over the third one. In the following we will focus our analysis on this case. Multiplying equations 4.8 and 4.9 by $\langle v_\theta \rangle$ and $\langle p \sin\theta \rangle$ respectively, one can in particular quantify the exchange of energy between zonal flows and turbulence and between $(1, 0)$ up-down asymmetric perturbations and turbulence [60]

$$\left.\frac{\mathrm{d}\mathcal{E}}{\mathrm{d}t}\right|_{ITG \to ZF} = -\frac{1}{r^2}\frac{\partial}{\partial r}\left(r^2 \Pi_{r\theta}\right)\langle v_\theta \rangle \tag{4.11}$$

$$\left.\frac{\mathrm{d}\mathcal{E}}{\mathrm{d}t}\right|_{ITG \to (1,0)} = -\left\langle \left[\tilde{\phi}, \tilde{p}\right] \sin\theta \right\rangle \langle p \sin\theta \rangle \tag{4.12}$$

These two terms are identified in figure 4.3, which is explained in subsection 4.1.3.

4.1.2 Envelope modulation of ambient turbulence

The interaction between LFZFs, GAMs and ambient turbulence and the effect of this interaction on the turbulent transport has been little analysed in experiments and remains

for the moment somewhat unclear. Experimentally, the modulation of the ambient turbulence by GAMs has been analysed in the edge of the plasma ($0.85 \leq r/a < 1$). This analysis makes sense since the frequency of GAMs is small compared to the characteristic frequency of the edge turbulence and the correction due to oscillating sheared flows is not significant. Therefore, a modulation of the high-frequency wave by the low-frequency wave is possible. First experimental results were obtained in the DIII-D tokamak [113] and subsequently corroborated in the JFT-2M tokamak. In these experiments the density and potential fluctuations were measured. It was observed that the potential oscillations at the GAM frequency and the temporal behaviour of the ambient turbulence, i.e. density perturbation, are coherent. In particular, in the JFT-2M tokamak, the high frequency components of the density fluctuations were observed to be modulated at the GAM frequency. In addition, this modulation seems to affect the local particle transport [114]. In recent experiments in the HL-2A tokamak [115], the interaction between ZFs, GAMs and ambient turbulence was closely analysed in the region $r/a \sim 0.9$. It was found that the ambient turbulence is modulated by both LFZFs and GAMs. In addition, GAMs are intermittently modulated by LFZFs. Even if this could shed some light on the famous ZF-turbulence paradigm through the interaction ZF-GAMs, much work remains to be done for deep and comprehensive explanations of the turbulence regulation *via* the modulation of turbulence at the GAM frequency. As we will see in section 4.5.6, a modulation of the turbulence has also been observed in the context of energetic GAMs in the simulations presented in this chapter. In this case, the modulation occurs at a frequency embedded in the turbulent spectrum. Possible explanations are provided for this modulation.

4.1.3 Role of energetic particles and outline of this chapter

As stated above, GAMs are Landau damped, but can be driven by the turbulence in a self-organized way. Therefore, no control on the amplitude of these GAMs is in principle possible. However, it has been found theoretically [13] and experimentally [14] that a population of energetic particles can drive GAMs unstable. These so-called EGAMs have been extensively analysed in the previous chapter by means of a variational approach and we have shown that they can also be observed in gyrokinetic simulations with GYSELA. Let us recall that this analysis was made in the absence of turbulence and with flat profiles. However, we know that real situations actually depart from the ones considered in the previous chapter. In particular, turbulent transport is present in fusion devices leading to diffusion coefficients that are higher than the ones predicted by the neoclassical theory. Taking this into account and considering that gyrokinetic simulations can now provide accurate predictions of the level of turbulence, it is clear that the excitation of EGAMs in gyrokinetic simulations in the presence of a well-developed electrostatic turbulence reveals interesting on the route towards the external control of sheared flows and therefore of turbulence. This idea was firstly invoked by Boswell *et al* [15] as *an external knob to regulate the turbulence diffusion*. Therefore, in this chapter we will extend the results of the previous one in order to explore the behaviour of turbulence in the presence of energetic GAMs.

For this purpose, we have considered necessary to stand back and identify each agent susceptible to play a major/minor role in the following. This identification is depicted in figure 4.3 and is summarized as follows:

- Poloidally asymmetric perturbations ($m \neq 0, n = 0$) are coupled to zonal flows ($m = 0, n = 0$) *via* the magnetic curvature. This coupling results in oscillations

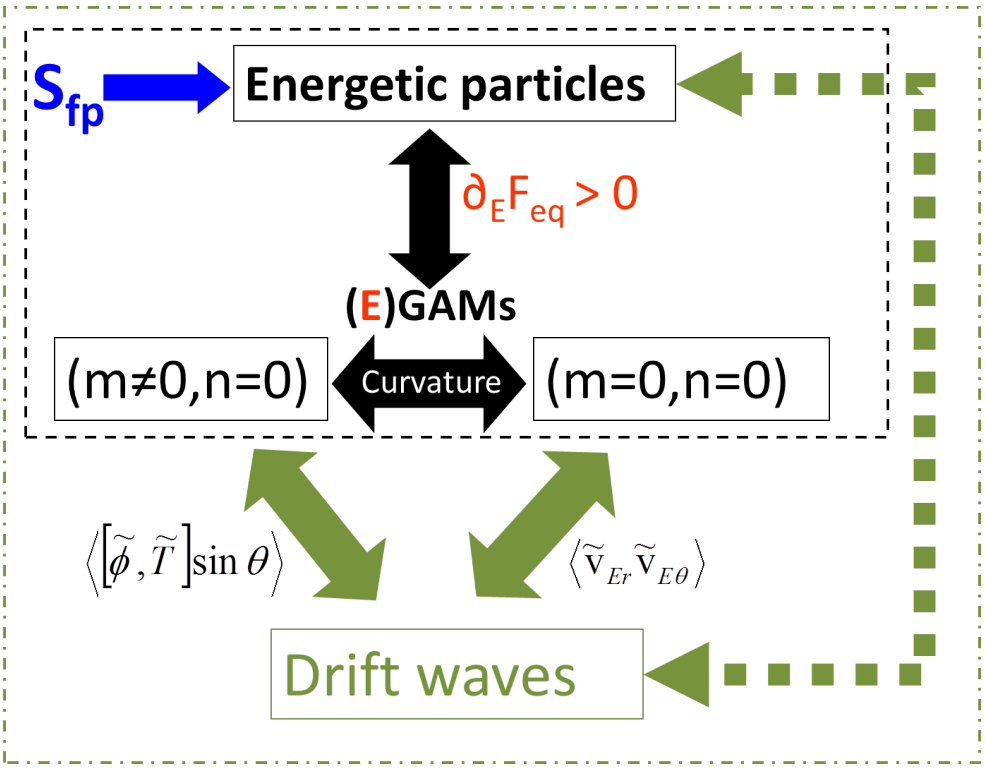

Figure 4.3: Schematic representation of the different possible interactions between energetic particles, drift waves, geodesic acoustic modes and zonal flows.

(GAMs) that are driven unstable when energetic particles are present in the system. This part was analysed in the previous chapter and is represented by black squares and arrows in figure 4.3.

- We will explain in section 4.2 the difficulties associated to the excitation of EGAMs in global and flux-driven gyrokinetic simulations in the presence of turbulence. This motivation will naturally lead to the implementation of a heating source to maintain the population of energetic particles enabling the excitation of EGAMs. This source is represented in blue and constitutes and external mean to control the EGAM excitation.

- The set of elements contained by the black dashed frame are the main ingredients of the neoclassical simulations presented in section 4.3.

- When introducing non axisymmetric modes in the system, there can be direct effects of the source on the marginal stability of ITG modes. This analysis will be done in detail in subsection 4.4 and is represented by a green dotted arrow.

- Due to the curvature coupling, the EGAM oscillations are present in both the $(m \neq 0, n = 0)$ perturbations and the zonal flows, which exchange energy with ITG modes *via* the Reynolds stress and the coupling between temperature and potential fluctuations. This exchange of energy is represented by green solid arrows and is analysed in section 4.5 with two GYSELA simulations. These simulations will enable also the analysis of the impact of the distribution function on the ITG turbulence.

4.2 Excitation of EGAMs in the presence of radial profiles

In the previous chapter, we analysed the excitation of EGAMs in a very special case, where neither radial gradients nor collision operator were accounted for. This situation allows one to perform simulations straightforwardly by initializing the distribution function as the sum of a local Maxwellian and an energetic particle distribution function. Since no radial dependence exists, the local Maxwellian reduces to a canonical Maxwellian and depends therefore on the motion invariants, namely the kinetic energy for this particular case. The energetic particle distribution function can be chosen to depend only on the energy. Therefore, no external source is required to excite EGAMs and the distribution function evolves following the Vlasov equation $\frac{\partial F}{\partial t} - [\mathcal{H}, F] = 0$. The distribution function does not evolve initially since it satisfies $[\mathcal{H}_{\text{init}}, F_{\text{init}}] = 0$, with $\mathcal{H}_{\text{init}} = 1/2 m v_{\parallel}^2 + \mu B$ the kinetic energy. However, the initial equilibrium is unstable due to a resonant energy exchange between particles and waves. After some EGAM cycles, the kinetic energy is not a motion invariant any longer because the amplitude of the electrostatic potential has increased. The increase of the potential perturbation needs to saturate and this is done mainly *via* the wave-particle trapping mechanism. In this chapter we are interested in analyzing any possible interaction between EGAMs and ITG turbulence. This means that radial gradients must be introduced in the physical system, especially temperature gradients. In the case of a local Maxwellian, building the inital temperature and density profiles is rather easy since the desired profiles $n_{i0}(r)$ and $T_{i0}(r)$ give straightforwardly the initial distribution function

$$F_{\text{M0}} = \frac{n_{i0}(r)}{\left[2\pi T_{i0}(r)/m\right]^{3/2}} \mathrm{e}^{-E/T_{i0}(r)}$$

However, with such a distribution function EGAMs cannot be excited. In order to excite EGAMs, we can modify the initial distribution function by implementing at $t = 0$ the following distribution function (see previous chapter)

$$F(t=0) = \frac{n_i(r)}{\left[2\pi T_i(r)/m\right]^{3/2}} \mathrm{e}^{-E/T_i(r)} + F_{M,h} e^{-\frac{v_{\parallel 0}^2}{2T_h}} \cosh\left(\frac{v_{\parallel 0} v_{\parallel}}{T_h}\right) \tag{4.13}$$

under the constraints

$$\int \mathrm{d}^3\mathbf{v} F(t=0) = n_{i0}(r) \quad \text{and} \quad \int \mathrm{d}^3\mathbf{v} E\, F(t=0) = n_{i0}(r)\, T_{i0}(r) \tag{4.14}$$

We encounter here a major difficulty. This distribution function does not depend on the motion invariants due to the radial dependence. In addition, the positive slope clearly represents an out-of-equilibrium state. The system will therefore evolve and can depart from the initial distribution function. Therefore, we propose the following solution. We can initialize the simulations with the local Maxwellian F_{M0} and then *deform* it (with no net particle injection) by means of an external source that will be called S_{fp} in the remainder of this thesis (*fp* stands for *fast particles*). The aim of this external source S_{fp} is to bring the system out of equilibrium by developing a bump on the tail of the Maxwellian distribution function. This way, the initial radial profiles are completely controlled by means of the initial local Maxwellian. Implementing this source term on the right-hand side of the gyrokinetic equation has another interest. In the framework of turbulent regimes, we can perform simulations without energetic particles and let the ITG

modes develop. Once a steady-state is achieved, by switching on the source $S_{\rm fp}$, the distribution function will be deformed and, once the excitation criterion is satisfied, EGAMs will be excited. It is obvious that the distribution function that we obtain with the source $S_{\rm fp}$ is not strictly the same as the one given by expressions 4.13 and 4.14. Therefore, we are implicitly allowing for a small departure with respect to the analytical situation analysed in the previous chapter. However, the situation presented in this chapter is clearly closer to experiments where additional heating, such as NBI heating, is switched on and EGAMs excited (see e.g. Refs. [15, 14]). Since EGAMs are excited in the presence of a broad turbulent spectrum, analysis of the interaction between EGAMs and turbulence is then possible. In the presence of this source, the equation satisfied by the distribution differs from the homogeneous Vlasov equation

$$\frac{\partial F}{\partial t} - [\mathcal{H}, F] = S_{\rm fp} \tag{4.15}$$

The choice of $F\left(t=0\right) = F_{\rm M0}$ means that large-scale polarization flows will be generated during the first instants of the simulation. This behaviour has been recently analyzed in detail [116] and leads to a distribution function solution of $[\mathcal{H}_{\rm end}, F_{\rm end}] = 0$. Together with this evolution, the source imposes another evolution towards a distribution function whose dependence on the motion invariants will be given by the source itself. In addition, the collision operator modifies the distribution function through diffusion/convection in $v_{\parallel}$ space. Finally, another source $S_{\rm th}$ representing the thermal energy in the inner region of the tokamak is introduced. This source injects energy in the inner boundary radial condition and the energy then propagates outwards. This propagation leads to another modification of the distribution function.

4.2.1 Energetic particle source in Gysela

As explained in the previous chapter, GYSELA solves the gyrokinetic equation with right-hand side terms corresponding to the binary Coulomb collision operator and the sources. A heat source makes it possible to perform simulations where the temperature evolves at $r_{\rm min}$. This kind of simulation is usually called *flux-driven* simulations, in contrast with simulations where the temperature at both radial boundaries is forced to remain constant (thermal bath) or simulations where the temperature gradient is fixed. Important differences between these regimes were pointed out in an earlier work [117]. First simulations of flux-driven systems with gyrokinetic codes were performed in a reduced model to describe the turbulence driven by trapped ions [118]. As for GYSELA code, first flux-driven simulations were presented in Ref. [119] and this kind of regimes have been recently explored in detail in Refs. [120, 121]. The explanation of the source $S_{\rm th}$ can by found in Ref. [119]. It is an isotropic source and its effect is schematically represented in figure 4.4a. It can be observed that this source takes particles at a vanishing velocity and accelerates them up to $v \approx 1.5 v_{\rm th}$. Regarding the source $S_{\rm fp}$, it is localized around the mid position $r_{\rm mid} = \left(r_{\rm min} + r_{\rm max}\right)/2$ and brings the distribution function out of the equilibrium by creating a positive slope in energy, i.e. it represents the energetic particles generation.

It is essential to analyse the effect of energetic particles when no other effects such as momentum, vorticity or mass injection are considered. The absence of parallel momentum injection, for symmetry reasons, may be satisfied by the following decomposition

$$S_{fp}\left(r, \theta, v_{\parallel}, \mu, t\right) = S_{+} + S_{-}$$

where $S_{-}\left(v_{\parallel}\right)=S_{+}\left(-v_{\parallel}\right)$. Each of these two terms does not inject neither vorticity nor mass. The absence of mass injection is essential in GYSELA simulations, because electrons are assumed adiabatic. Therefore, no radial particle transport exists and any injection of particles would result in accumulation of mass. In addition, we choose a source that injects only parallel energy. This kind of source is representative of NBI heating where the injectors are oriented in the tangent direction of the magnetic flux surfaces. On the contrary, ICRH systems can only heat the plasma in the perpendicular direction, as explained in chapter 2 of this thesis. The choice of parallel energy injection is justified since any perpendicular energy injected in GYSELA cannot be dissipated via the binary Coulomb collisions. In addition, accelarating particles only in the parallel direction makes it possible to use the already implemented gyrokinetic operator in GYSELA, consisting of a Padé approximation. The energetic particle source is decomposed by using projections onto Laguerre ($\mathcal{L}_l$) and Hermite ($\mathcal{H}_h$) polynomial basis, which enables a separation between injection of energy, parallel momentum and vorticity with a convenient choice of real coefficients c_{hl} [121]

$$S_{\pm}=\frac{1}{2}S_{fp,0}S\left(r\right)\mathrm{e}^{-\left(\bar{v}_{\parallel}\pm\bar{v}_{0}\right)^{2}}\mathrm{e}^{-\bar{\mu}B(r,\theta)}\sum_{h,l}c_{hl}\mathcal{H}_{h}\left(\bar{v}_{\parallel}\pm\bar{v}_{0}\right)\mathcal{L}_{l}\left(\bar{\mu}B\left(r,\theta\right)\right) \tag{4.16}$$

In this expression, $\bar{v}_{\parallel}=v_{\parallel}/\sqrt{2T_{s\parallel}}$, $\bar{v}_{0}=v_{0}/\sqrt{2T_{s\parallel}}$ and $\bar{\mu}=\mu/T_{s\perp}$, where velocities and temperatures are normalized to the thermal energy. The radial envelope, $S\left(r\right)$, is the sum of two hyperbolic tangents under the constraint that the integral over the minor radius is normalized. Its width and position can be chosen independently of each other. The parameter $S_{fp,0}$ gives the amplitude of the energy source. The source has been explicitly implemented so that no particle injection exists. Therefore, this source leads to a deformation of the distribution function in velocity space at constant particle density, i.e. the integral of the source over the velocity space vanishes. Details of the construction of a similar source may be found in [121]. For the sake of simplicity, we give here the final expression we have used, normalized to $S_{fp,0}S\left(r\right)/2$

$$\tilde{S}_{\pm}=\left[\left(\bar{v}_{\parallel}\pm\bar{v}_{0}\right)^{2}-\frac{1}{2}-Q_{fp}\left(2-\bar{\mu}B\right)\left(2\left(\bar{v}_{\parallel}\pm\bar{v}_{0}\right)-J_{\parallel}\right)\right]\mathrm{e}^{-\left(\bar{v}_{\parallel}\pm\bar{v}_{0}\right)^{2}}\mathrm{e}^{-\bar{\mu}B(r,\theta)} \tag{4.17}$$

where $Q_{fp}=J_{\parallel}/\left(2-J_{\parallel}^{2}\left(1+2\bar{v}_{0}^{2}\right)\right)$ and $J_{\parallel}=\vec{b}\cdot\vec{J}\sqrt{2T_{s\parallel}}/B$. The parallel current $J_{\parallel}$ is prescribed in GYSELA code. Figure 4.4b illustrates a schematic view of the dependence of the source $\tilde{S}_{\pm}$ on the parallel velocity. **It can be observed that this source takes particles around a given parallel velocity $v_{\parallel}\approx v_{0}v_{\mathrm{th}}$. Half of the extracted population is accelerated at parallel velocities $v_{\parallel}\approx 3.5v_{\mathrm{th}}$ and the remaining particles are slowed down in order to keep the density constant.**

Important differences must be stressed with respect to the source introduced in [121]. First, the source used here allows one to modify the distribution function around a non vanishing parallel velocity. This is extremely useful, since the excitation of GAMs by fast ions relies on the existence of a positive slope in energy of the distribution function at the resonant velocity. Therefore, a convenient choice of v_0 is essential for the excitation. Second, different normalizations for parallel and perpendicular velocities can be considered by introducing the temperatures $T_{s\parallel}$ and $T_{s\perp}$. The ratio $T_{s\parallel}/T_{s\perp}$ reveals important since the dependence of the distribution function on the adiabatic invariant may substantially

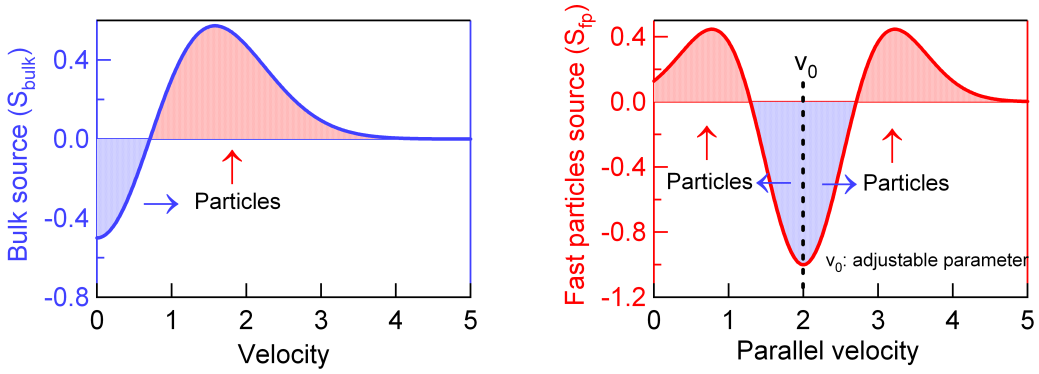

Figure 4.4: Schematic view of the energetic particle source as a function of the parallel velocity.

modify the excitation of GAMs, as established in the previous chapter. In what follows, this source will inject only parallel energy by creating two bumps on the tail of the initial distribution function. The effect of the source regarding the inversion of the slope of the distribution function has been optimized by choosing $v_0 = 2$, $T_{s\|} = 0.5$ and $T_{s\perp} = 1$. This case will be called in the remainder of this thesis *case with energetic particles*. It must be noted that the parameters v_0 and $T_{s\|}$ of this source can be chosen so that there is no inversion of the negative slope. In particular, by choosing $v_0 = 0$ and $T_{s\|} = 1$ the source $S_{\rm fp}$ reduces to a heating source injecting only parallel energy into the thermal particles, which are slightly accelerated, but no bump-on-tail is obtained. This case will be called in the following *case without energetic particles*.

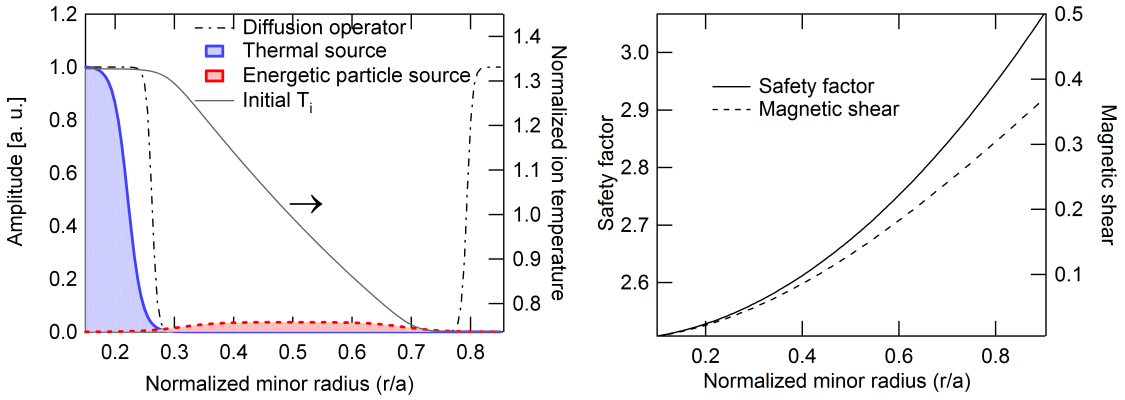

Figure 4.5: (Left) Radial profiles of the diffusion operator (dotted-dashed line), the thermal energy source (solid line) and the energetic particle source (dashed line). (Right) Radial dependence of the safety factor and magnetic shear.

4.3 Excitation of EGAMs in neoclassical regimes

Before analysing the excitation of EGAMs in the presence of a well-developed ITG turbulence, simulations to test the efficiency of the implemented source in neoclassical regimes are essential.

4.3.1 Description of the neoclassical simulations

In these regimes, only axisymmetric modes are retained. These simulations are crucial to analyse the excitation of EGAMs when the distribution function is built little by little with an external source, which is more relevant from the point of view of experiments than the situation explored in the previous chapter. In addition, in this chapter, collisions and diamagnetic effects are taken into account. For this purpose, we firstly present two simulations (with and without energetic particles). Both simulations are characterized by initial temperature and density gradients of $R/L_T = 4$ and $R/L_n = 2.2$, respectively. The safety factor profile is parabolic and characterized by a low magnetic shear $0 \leq s < 0.4$. The normalized ion Larmor radius is $\rho_\star = 1/75$. The maximum parallel velocity is $v_{\parallel,\max} = 7$ and the maximum value of the adiabatic invariant is $\mu_{\max} = 8$. Therefore, resonant passing particles are expected to play a more important role than resonant trapped particles. The time resolution is $\omega_c \Delta t = 15$. The collisionality is chosen in the banana regime: $\nu_\star = 0.1$. We use a thermal isotropic source located at $r_{\min}$ with amplitude $S_0 = 0.005$ and a temperature $T_s = 1.5$. An energetic particle source S_{fp} is used with an amplitude $S_{\text{fp},0} = 0.005$, localized across the mid radial position and sufficiently large so that the temperature profile is not significantly and locally deformed. Buffer regions are used in the inner and outer radial positions. The aim of these regions is to provide a diffusion in the radial and poloidal directions. In addition the collisionality is artificially increased inside the inner buffer region. This increase of the collisionality results in a regularization of the distribution function in the $v_\parallel$ direction and therefore a redistribution of the injected energy along the parallel motion. Figure 4.5a shows the radial profiles of the thermal source, the energetic particle source and the diffusion operator. Figure 4.5b illustrates the radial dependence of the safety factor and the magnetic shear. In the following, this first simulation in neoclassical regime will be called NC1 and the equivalent without energetic particles will be called NC1'.

To analyse the effect of the collisionality on the excitation and saturation of EGAMs, we present two additional simulations at lower collisionality ($\nu_\star = 0.02$). In one of these simulations (called NC2 in the following), we apply an energetic particle source with amplitude $S_{\text{fp}} = 3 \cdot 10^{-3}$. Since the collisionality is five times smaller, this amplitude needs to be reduced before obtaining negative values of the distribution function around the pumping velocity v_0. It has been subsequently reduced to $S_{\text{fp}} = 10^{-3}$ at $\omega_c t = 4.2 \cdot 10^4$. In the other simulation at low collisionality (called NC3 in the following), the amplitude $S_{\text{fp}} = 10^{-3}$ has been used from the beginning. In this case, the slope of the distribution function is expected to evolve slowly as compared to simulation NC2. We have not performed the simulations equivalent to NC2 and NC3 without energetic particles.

4.3.2 Modification of the distribution function and excitation of EGAMs

The equilibrium distribution function is defined as the flux surface average of the total distribution, as in the previous chapter. Its derivative with respect to the energy at the resonant velocity $v_\parallel = qR\omega_{\text{EGAM}}$ is plotted for different radial positions on figure 4.6a for

the simulation NC1. It can be observed that the initial negative slope is clearly inverted. However, the value of the derivative depends on the radial position, even if the source has a large radial extension. In particular, the effect of the energetic particle source is more visible for the radial positions $0.4 < \rho < 0.65$. As analysed in the previous chapter, this positive slope is expected to drive EGAMs unstable.

To analyse this excitation, we have extracted the imaginary part of the $(m, n) = (1, 0)$ component of the electrostatic potential, which is proportional to the up-down poloidally asymmetric part. The time trace is plotted in figure 4.6b for both simulations, NC1 (solid red line) and NC1' (dashed blue line). The first result is that energetic particles excite geodesic acoustic modes in the presence of temperature gradient, whereas when no energetic particles exist the only oscillations correspond to the initial GAMs (see inset frame at the bottom on figure 4.6b). These damped GAM oscillations occur in both cases with and without energetic particles, due to an initial self-organization of the physical system as analysed in [116]. The fact that we analyse only the oscillations of the imaginary part of the $(1, 0)$ perturbations does not mean that there is no $\cos\theta$ component. A stationary $\cos\theta$ component is expected in the presence of an anisotropic heating, following [122]. However, the amplitude of the oscillations in the $\cos\theta$ component are found to be ten times smaller than the amplitude of the oscillations of the $\sin\theta$ component. Therefore, in the following we focus our analysis on the imaginary part of $\phi_{1,0}$. The energetic particle mode that is excited here differs from the one observed in the previous chapter, where a single-frequency-mode was excited. In the present case, we can observe that there are two frequencies, with different growth rates and different saturation levels. These two frequencies are clearly observed in the upper inset on figure 4.6b, where we represent the Fourier transform performed over two time windows, $6 \cdot 10^4 \leq \omega_c t \leq 9 \cdot 10^4$ (dashed line) and $9 \cdot 10^4 \leq \omega_c t \leq 10^5$ (solid line). In particular it can be appreciated that these two frequencies are actually first and second harmonics of the same mode. The origin of this second harmonic in these simulations might be related to nonlinear effects in the presence of energetic particles, but this remains for the moment unclear and the results presented in this chapter deserve further analysis in this direction to shed some light on the excitation of these two frequencies. In figure 4.6 we give also two magnified views (frames A and B) of the slope of the distribution function and the electrostatic potential during the transition from the second harmonic to the EGAM frequency. In the frame A, the original signal has been smoothed to eliminate the EGAM oscillations. The resulted smoothed signal is represented by thick solid lines, only for the radial positions $\rho = 0.5$ and $\rho = 0.65$ to facilitate the interpretation of the results. These two views provide further information about the saturation of EGAMs in the presence of external sources, collisions and diamagnetic effects.

In the previous chapter, the nonlinear saturation of the mode has been found to be due mainly to wave-particle trapping. This mechanism results in a flattening of the distribution function around the resonant velocity. In the case presented in figure 4.6 we can observe that the saturation of the second harmonic ($\omega_c t = 8 \cdot 10^4$) is characterized by a slight decrease of the slope of the distribution function, whereas the saturation of the EGAM ($\omega_c t = 10^5$) is accompanied by a stronger reduction of the slope. Once the EGAM has saturated, the slope increases again, but the amplitude of the oscillations keeps decreasing. This phase represents a transient self-organization of the system to reach a stationary situation where an equilibrium between the energetic particle source, the collisions and the diamagnetic effects is found. After the increase of the slope ($10^5 < \omega_c t < 1.2 \cdot 10^5$), the amplitude of the oscillations starts increasing again and reaches a reduced saturation level,

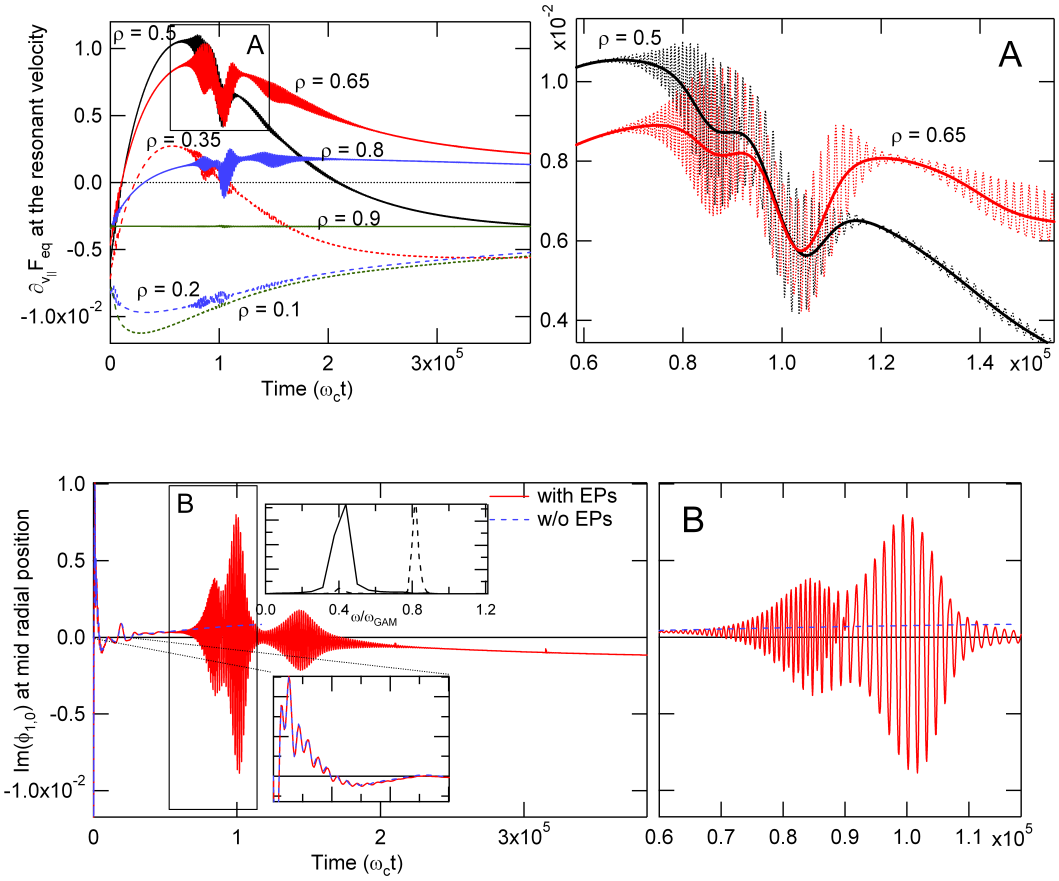

Figure 4.6: (Top-left) Time evolution of the derivative of the equilibrium distribution function with respect to the energy at the resonant velocity for the simulation NC1. (Bottom-left) Time evolution of the imaginary part of the mode $(m, n) = (1, 0)$ of the electrostatic potential at the mid radial position for the simulations NC1 and NC1′. (Right) Magnified views of the same evolutions during the saturation of the mode.

accompanied by a new time-averaged reduction of the slope of the distribution function. However, this last reduction is less important than the previous ones. Afterwards, collisions dominate over the energetic particle source, the slope decreases monotonically and so does the amplitude of EGAMs.

The results for the simulations NC2 and NC3 (evolution of $\partial_{v_\parallel} F_{\mathrm{eq}}$ and $\Im\left(\phi_{1,0}\right)$) are shown on figure 4.7 only for the mid radial position to facilitate the interpretation of the curves. Magnified views of the electrostatic potential are given on the right-hand side of the figure (frames C and D). Two important differences with respect to the previous simulation have been observed. First, the amplitude of EGAMs is the largest in NC1, then in NC2 and finally in NC3. This is consistent with the fact that the derivative of the distribution function follows the same ordering in these three simulations. In addition, the amplitude of the second harmonic decreases as well in the same way. The spectrograms of $\Im\left(\phi_{1,0}\right)$ given in figure 4.8 illustrates the time evolution of each harmonic for the three simulations analysed here. Second, during the first excitation/saturation/re-excitation phase the behaviour observed in simulation NC1 has been reproduced, i.e. the distribution function decreases but does not vanish during the saturation of the EGAM.

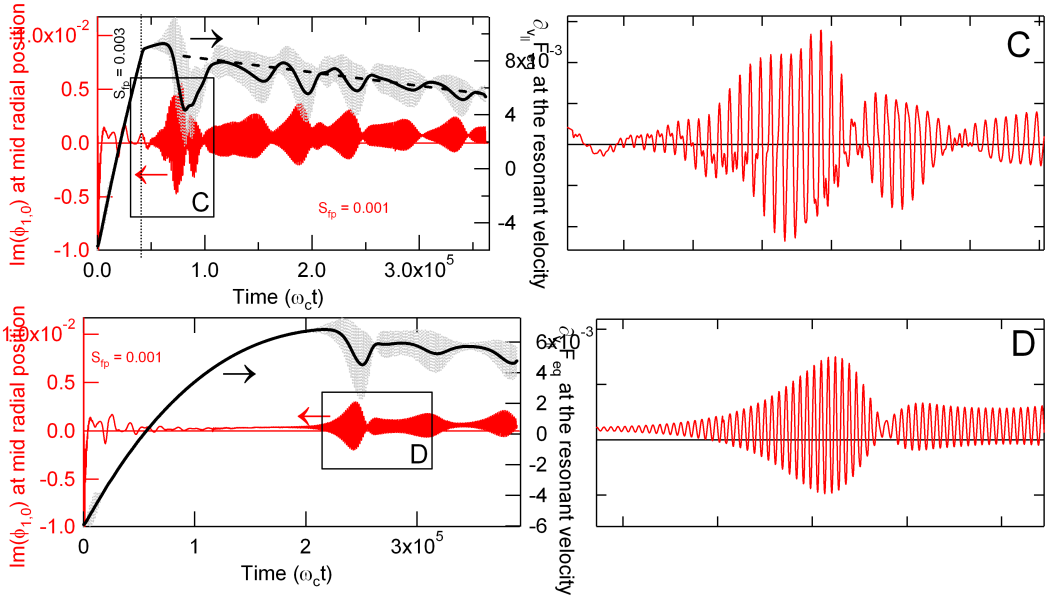

Figure 4.7: Time evolution of the derivative of the equilibrium distribution function with respect to the energy and imaginary part of the mode $(m, n) = (1, 0)$ of the electrostatic potential with $\nu_\star = 0.02$ for the simulations NC2 (top) and NC3 (bottom) explained in the text.

Afterwards, the linear drive is restored while the amplitude of EGAMs still decreases. Then, the EGAM seems to disappear, but it is re-excited after the linear drive has been restored. The main difference between NC1 and NC2/NC3 comes from the collisionality effects. This is captured in the quasi-periodic evolution of both the distribution function and the electrostatic potential. If the collisionality is large enough, this quasi-periodic behaviour is not observed since the distribution function converges to a local Maxwellian due to collisions and the linear drive disappears. However, when the collisionality is low, there is a competition between the wave-particle trapping mechanism that tends to flatten the distribution function, the energetic particle source that tends to invert the slope of the distribution function and collisions. The result is the quasi-periodic oscillations observed in figure 4.7. The evolutions of the distribution function and the EGAM amplitude are clearly correlated: the saturation of the mode in each *cycle* is accompanied by a reduction of the slope of the distribution function, which is restored during the decrease of the EGAM amplitude and the mechanism is reproduced quasi-periodically. The role of collisions can especially be appreciated by looking at the long-time evolution of the slope of the distribution function. In the same figure, we have represented this evolution by a dashed line, with a clear negative slope. Therefore, it can be observed three time-scales: (1) the oscillations at the EGAM frequency ($t \sim \omega_{\mathrm{EGAM}}^{-1}$), (2) the evolution of the equilibrium averaged over some EGAM cycles, resulting from the wave-particle trapping and the source and (3) the evolution at the collision time-scale, resulting from the competition between collisions and source ($t \sim \nu_{\mathrm{coll}}^{-1}$) . A similar quasi-periodic behaviour has been recently observed in numerical simulations to investigate the Berk-Breizman model. In particular, a nonchirping chaotic solution resulting from the competition between collisions, damping and source has been reported [123].

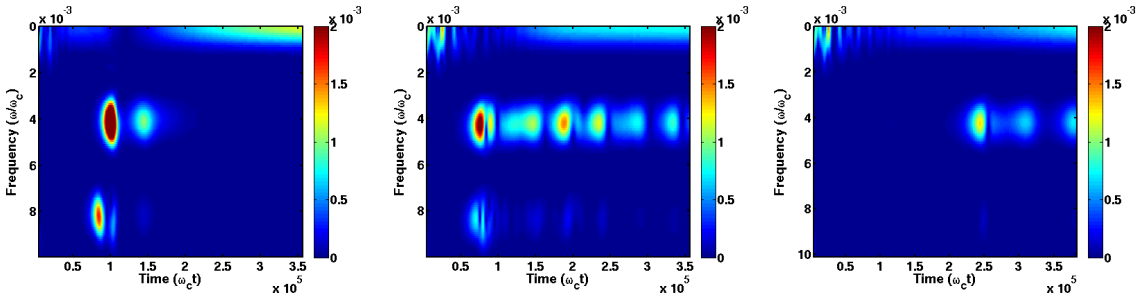

Figure 4.8: Spectrogram of the up-down asymmetric component of the electrostatic potential in neoclassical simulations, from left to right: NC1, NC2 and NC3.

4.3.3 Damping effects due to collisions and radial profiles

As we have mentioned, the slope of the distribution function at the resonant velocity does not completely vanish during the saturation of the mode. Therefore, wave-particle trapping cannot be the only mechanism responsible for the saturation in this case. In the previous chapter, we have presented collisionless simulations. In addition, we have claimed that diamagnetic effects do not play any role since the excited modes are axisymmetric and the distribution function does not depend on J_2. However, these two simplifications cannot be invoked here. On the one hand, collisions tend to widen the resonance. Therefore, large values of $\nu_\star$ are expected to reduce the growth rate and to amplify the damping. On the other hand, as explained in appendix E, the absence of diamagnetic effects is possible only when particles are described by a distribution function $F_{\rm eq} = F_{\rm eq}\left(\mu, \mathcal{H}, P_\varphi\right)$. However, for particles having a parallel velocity compared to $e\psi/Rm$, a more accurate description of the equilibrium consists of a distribution function $F_{\rm eq} = F_{\rm eq}\left(\mathcal{H}, J_2, P_\varphi\right)$, which straightforwardly leads to additional terms of the form $n_2 \partial_{J_2} F_{\rm eq} \delta\left(v_\parallel - qR\omega\right)$. Since $J_2 \approx e\Phi\left(J_3/e\right) + m/2\pi \oint v_\parallel {\rm d}s$ and $J_3 = e\psi + mRv_\parallel$, in the limit $\varepsilon \ll 1$ and for small $\rho_\star$, $J_2 \approx e\Phi\left(\psi/e\right)$. Therefore, the derivative with respect to J_2 results in a derivative with respect to the radial coordinate, i.e. passing particles can introduce diamagnetic effects even for axisymmetric modes. These diamagnetic effects do not exist for zonal flows ($m = 0, n = 0$) and are only present if $m \neq 0$. In addition, owing to the poloidal coupling between side-bands, the newly introduced diamagnetic effects vanish for symmetric distribution functions in parallel velocity. As a result, one needs to consider the growth rate provided by $\omega \partial_E F_{\rm eq}$ to which is subtracted the damping term

$$\gamma_{\rm d,dia} \approx -\frac{1}{eBr} \int {\rm d}\mu \left(\left.\frac{\partial F_{\rm eq}}{\partial r}\right|_{v_\parallel = qR\omega} - \left.\frac{\partial F_{\rm eq}}{\partial r}\right|_{v_\parallel = -qR\omega} \right) \tag{4.18}$$

where we consider that $\gamma_{\rm d,dia} > 0$ means *damping* of the mode. Figure 4.9 shows the antisymmetric part of $F_{\rm eq}$, i.e. $F_{\rm eq}\left(v_\parallel\right) - F_{\rm eq}\left(-v_\parallel\right)$, for three different radial positions. It can be observed that this function at the resonant velocity $v_{\rm res} = qR\omega$ decreases with the minor radius, meaning that $\gamma_{\rm d,dia} > 0$ and therefore this diamagnetic effect provides an additional damping for the EGAMs. In addition to this damping, the nonlinear reduction of the linear drive $\gamma_L \sim \partial_E F_{\rm eq}|_{\rm res}$ must be considered. This phenomenon has been theoretically analysed in a series of papers describing the saturation of a single mode driven by an energetic beam [124, 125, 126]. The Vlasov equation with collisions $\mathcal{C}\left(F\right)$ and sources S is analysed therein. One can find the general reduction [96] $\gamma_L \to c_0 \nu_\star \gamma_L$,

where $c_0 = \mathcal{O}(1)$ depends on the form of the whole term $S + \mathcal{C}(F)$. In our case, it represents the competition between the convergence of F towards a Maxwellian and the inversion of the slope of F, as mentioned before. Further analysis should be done to determine and quantify all the damping kinetic terms playing a role in the saturation phase of EGAMs.

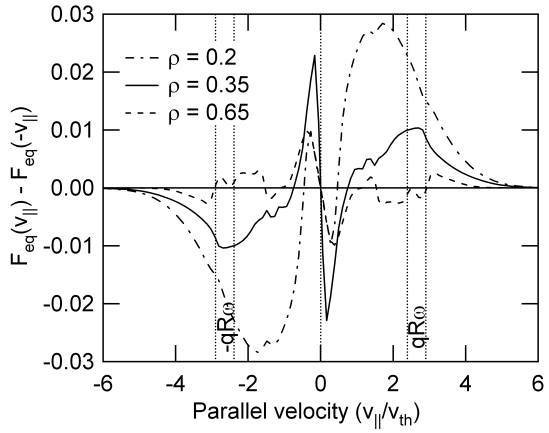

Figure 4.9: Antisymmetric part of the equilibrium distribution function for three radial positions.

4.3.4 Radial structure of the mode

Finally, these neoclassical simulations allow one to analyse the radial structure of the mode. For this purpose, we calculate the components $E_{r,\omega_{\mathrm{EGAM}}}$ and $E_{r,2\omega_{\mathrm{EGAM}}}$ of the radial electric field $E_r = -\nabla_r \phi_{00}$. The module of these components has been plotted in figure 4.10, at $\omega_c t \approx 10^5$ for the EGAM frequency and at $\omega_c t \approx 8.3 \cdot 10^4$ for the second harmonic, i.e. at the instant of maximum peak amplitude. It can be observed that in this case, the radial structure is not determined only by the radial boundary conditions, as occurred in the previous chapter, where the mode was localized in the whole simulation domain with a wave form $\phi_{1,0,\omega_{\mathrm{EGAM}}} \sim \sin\left(\pi \frac{r - r_{\min}}{r_{\max} - r_{\min}}\right)$. In the present case, the radial structure is determined by both the localization of the energetic particle source, i.e. the radial positions where $\partial_E F_{\mathrm{eq}}|_{\mathrm{res}} > 0$, and the drift orbit width of the resonant energetic particles [13, 14]. In that respect, even if the source is radially localized, due to the drift orbit width the mode can be excited at different radial positions. In particular, the radial extension of the mode increases with the energy of the resonant particles and the safety factor values as $\sim q\rho_{L,\mathrm{res}}$, with $\rho_{L,\mathrm{res}}$ the Larmor radius of resonant ions. This extension can be comparable to the size of the machine, leading to global modes. The radial profiles obtained here are consistent with the global structure of EGAMs invoked in [13].

4.4 Effect of the energetic particle source on the marginal stability of the ITG modes

It is important to note that from a fluid point of view the energetic particle source injects only parallel energy. One could think that such an ideal situation allows one to isolate

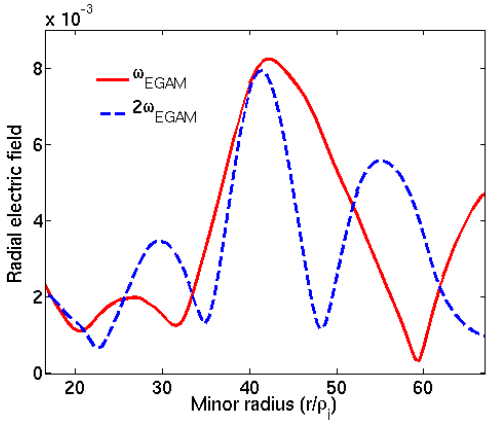

Figure 4.10: Radial structure of the electric field of the EGAM.

the effects of the energy, vorticity, mass and momentum injection. However, one must keep in mind that the injection of parallel energy is done by modifying the distribution function in the velocity space and bringing it far away from a thermodynamical equilibrium described by a Maxwellian distribution function. In particular, the particle orbits are modified for both trapped and passing particles. This can lead to some exotic effects, such as particle losses due to particle-trapping, modification of the radial electric shear due to radial currents induced by the displacements of particles and modification of the marginal stability of ITG modes. In this section we focus our analysis on the modification of the marginal stability of ITG modes due to the energetic particle source.

The energetic particle source that we have developed modifies the distribution function in two ways. First, it tends to deplete the population of particles located around $v_{\|} \sim 2v_{\rm th}$, where the factor 2 actually corresponds to the v_0 parameter. Second, it creates two bumps on the tail of the resulting distribution function, in view of triggering the bump-on-tail like EGAM instability. As we will see hereafter, the first effect is expected to lead to a reduction of ITG activity, consistently with what we observe in the numerical simulation (see section 4.5). Our analysis is based on the kinetic properties of the ITG instability, which we recall now.

One can make use of the variational principle introduced in the previous chapter to derive the expression of the Lagrangian in the general case where non axisymmetric modes are considered (let us recall that the excitation of EGAMs was analysed only for $n_3 = 0$). Using a Fourier decomposition on the action-angle variables, the Fourier mode $G_{\mathbf{n},\omega}$ yields (see appendix E)

$$G_{\mathbf{n},\omega} = -T_i \frac{\omega \partial_H \log F_{\rm eq} + n_3 \partial_{P_\varphi} \log F_{\rm eq}}{\omega - \mathbf{n}\cdot\mathbf{\Omega}} J_0 \cdot \phi_{\mathbf{n},\omega} \tag{4.19}$$

Therefore, the Lagrangian for a $(\mathbf{n} \neq \mathbf{0}, \omega)$ mode is ($\Xi \equiv \int \mathrm{d}^3\mathbf{x}\mathcal{L}$) [127]

$$\mathcal{L} = \mathcal{L}_{\rm adiab} + \mathcal{L}_{\rm non\,adiab} \tag{4.20}$$

where

$$\mathcal{L}_{\rm adiab} = |\phi_{\mathbf{n}\neq\mathbf{0},\omega}|^2 \left\{ \tau - T_i \int \mathrm{d}^3\mathbf{v} \partial_E F_{\rm eq} \right\} \tag{4.21}$$

$$\mathcal{L}_{\rm non\,adiab} = |\phi_{\mathbf{n}\neq\mathbf{0},\omega}|^2 \left\{ T_i \int \mathrm{d}^3\mathbf{v} \frac{\omega \partial_E F_{\rm eq} + n_3 \partial_{P_\varphi} F_{\rm eq}}{\omega - \mathbf{n}\cdot\Omega} \right\} \tag{4.22}$$

The denominator of the Lagrangian due to the non adiabatic response may be expressed for the resonant modes ($k_\parallel = 0$) as follows

$$\omega - \mathbf{n}\cdot\Omega = \omega - n_3\Omega_d = \omega - n_3\Omega_{dT}E \tag{4.23}$$

where, in circular unshifted magnetic flux surfaces, $\Omega_{dT} = \frac{q}{erB_0R_0}\bar{\Omega}_d$ and $\bar{\Omega}_d$ is a normalized frequency close to unity [128]. In the following, $\bar{\Omega}_d$ will be assumed constant, which means that no difference is made between trapped and passing particles. Therefore, the non adiabatic term reads

$$T_i\int \mathrm{d}^3\mathbf{v}\frac{\omega\partial_E F_{\mathrm{eq}} + n_3\partial_{P_\varphi}F_{\mathrm{eq}}}{\omega - \mathbf{n}\cdot\Omega} = -T_i\int \mathrm{d}^3\mathbf{v}\frac{\mathrm{E}_\omega\partial_E F_{\mathrm{eq}} + \Omega_{dT}^{-1}\partial_{P_\varphi}F_{\mathrm{eq}}}{E - \mathrm{E}_\omega} \tag{4.24}$$

where $\mathrm{E}_\omega = \frac{\omega}{n_3\Omega_{dT}}$. Following this simplified framework, the resonance takes place at the energy E_ω. This energy can be estimated as follows. Turbulence develops around the diamagnetic frequency $\omega_\star \sim k_\theta T/eBL_n$ [120], such that $\mathrm{E}_\omega \sim (m/nq)(T/\bar{\Omega}_d)R/L_n \sim (T/\bar{\Omega}_d)R/L_n$ for resonant modes characterized by $k_\parallel = 0$. It turns out that the chosen value of the R/L_n parameter in this simulation is $R/L_n = 2.2$. Coincidently, it then appears that the resonant normalized energy is $\mathrm{E}_\omega \sim 2.2$, which is close to the parallel energy at which the distribution function tends to be depleted by the energetic particle source, namely around $v_\parallel \sim 2v_{\mathrm{th}}$, or equivalently $E = (v_\parallel/v_{\mathrm{th}})^2/2 \sim 2$. Our particular choices of v_0 and R/L_n are then such that the energetic particle source reduces the number of resonant particles for the ITG instability. **One can therefore expect a reduction of the associated transport, which is qualitatively consistent with what is observed in the simulation (see section 4.5).**

As mentioned before, additional effects related to the marginal stability of ITG modes and the source must be analysed. For example, in the presence of a strong anisotropic heating not necessarily with energetic particles), marginally stable ITG modes might become unstable. In this context, the previous analysis applied to the case of an anisotropic Maxwellian provides additional information. The interested reader is encouraged to have a look at the analytical calculations presented in appendix F for further details. It is also briefly analysed therein a side effect observed in the neoclassical simulations presented in this chapter, which is the modification of the radial electric field in the presence of the energetic particle source.

4.5 Excitation of EGAMs in the presence of ITG modes

4.5.1 Description of the simulations presented in this section

In this section, two simulations (with and without energetic particles) in turbulent regime are presented, with a set of parameters in common: a normalized ion Larmor radius $\rho_\star = 1/150$, a collisionality $\nu_\star = 0.02$, initial gradients $R/L_T = 6.5$ and $R/L_n = 2.2$, $\omega_c\Delta t = 15$ and a bulk source amplitude $S_0 = 0.01$. For a deuterium plasma with a density $n = 2\cdot 10^{19}\,\mathrm{m}^{-3}$, a temperature $T = 1$ keV and a magnetic field $B = 1$ T, this source amplitude corresponds to a total injected power of $P_{\mathrm{add}} = 4$ MW [120]. This source is used alone in the time window $0 < \omega_c t < 2.7\cdot 10^5$. After $\omega_c t = 2.7\cdot 10^5$, the radially extended energetic particle source S_{fp} is added to the bulk source, located at the mid radial position. Its amplitude is $S_{\mathrm{fp},0} = 5\cdot 10^{-3}$, which is equivalent to a bulk heating of 2 MW located at r_{min}. The two simulations exhibit from that point a major difference: we use $v_0 = 2$ and $T_{\mathrm{s}\parallel} = 0.5$ for the simulation with energetic particles

and $v_0 = 0$ and $T_{s\|} = 1$ for the simulation without energetic particles. Whenever a comparison between these two simulations is made, they will be referred to as WEP (with energetic particles) and WOEP (without energetic particles). The simulations presented here have been performed with the following number of points: $N_r \times N_\theta \times N_\phi \times N_{v_\|} \times N_\mu = 256 \times 257 \times 129 \times 128 \times 20$ and represents $\sim 2.8 \cdot 10^6$ CPU-h on 2560 processors. A schematic time history of the heating in these simulations is illustrated in figure 4.11.

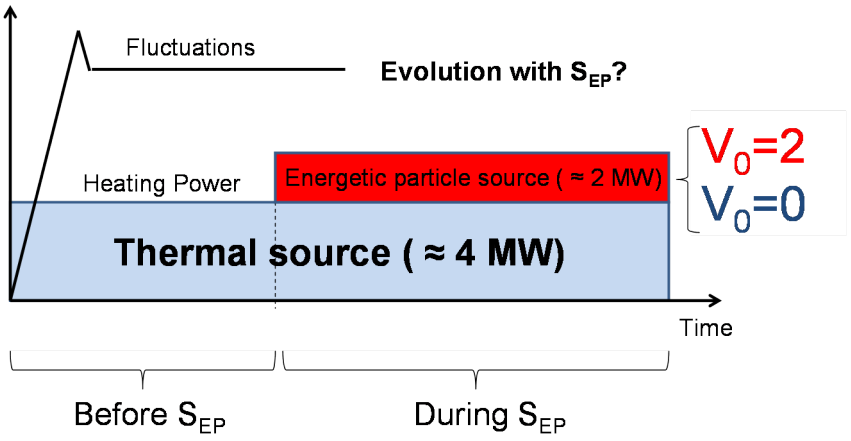

Figure 4.11: Schematic chronology of the heating in the turbulent GYSELA simulations presented in this section.

4.5.2 Brief overview of the obtained results

Before giving many technical details about these simulations, we have considered instructive to fly over the main physical results that are presented in the following and describe the chronology of the different observed phenomena. This chronology and the main results are summarized in figure 4.12, where we give a colormap of the $E \times B$ diffusivity (see expression 4.28).

The main results are: (1) **EGAMs are excited for the first time in the presence of a well-developed ITG turbulence**, (2) **EGAMs do not provide enough radial electric shear to stabilize the turbulence**, but (3) **turbulent transport is modulated at the EGAM frequency** and (4) **EGAM oscillations have been found to couple to avalanches, enabling the propagation of turbulence towards stable regions**. A secondary result is the suppression of the turbulence due to the modification of the distribution function by the energetic particle source, as explained earlier.

The chronology of the physical phenomena is the following. First of all, we have switched on the energetic particle source in a fully-developed turbulent regime. The distribution function is being deformed, but turbulence is not affected yet. This constitutes the phase A in figure 4.12. As predicted in the previous section, the ITG modes are expected to be linearly modified in the presence of energetic particles. This has been corroborated by means of the turbulence intensity, which has been found to decrease in the outer radial region of the simulation domain, where the distribution function is mainly modified. This state will be called in the following *transport barrier* and constitutes the phase B, where R/L_T increases. For the remainder of this section, the outer radial region will refer to the interval $0.5 < \rho < 0.8$, whereas the inner radial region will refer to the interval $0.2 < \rho < 0.5$. As far as the suppression of the turbulence is concerned,

we have excluded the effect of the radial electric shear due to the source since the shearing rate is modified only when the turbulence has been suppressed. This suggests that the cause is the reduction of the turbulence and the consequence the modification of the shear *via* the Reynolds stress. We have also excluded the effect of EGAMs because they are only observed well after the turbulence is reduced. In addition, the hypothesis that the turbulence is due to the modification of the distribution function is corroborated by the correlation between the decrease of the turbulence intensity and the time evolution of the distribution function. When the slope of the distribution function is high enough, the EGAMs are excited at the end of the phase B. They are characterized mainly by the frequency ω_{EGAM}. Afterwards, we have observed an increase of the turbulence and a bursty behaviour of EGAMs during the remainder of the simulation, which constitutes the phase C. Additional simulations in turbulent regimes with $\rho_\star = 1/150$ and $\rho_\star = 1/75$ have been performed. Similar behaviour regarding the turbulence reduction due to the modification of the distribution function and the EGAM excitation with subsequent destruction of the transport barrier has been observed.

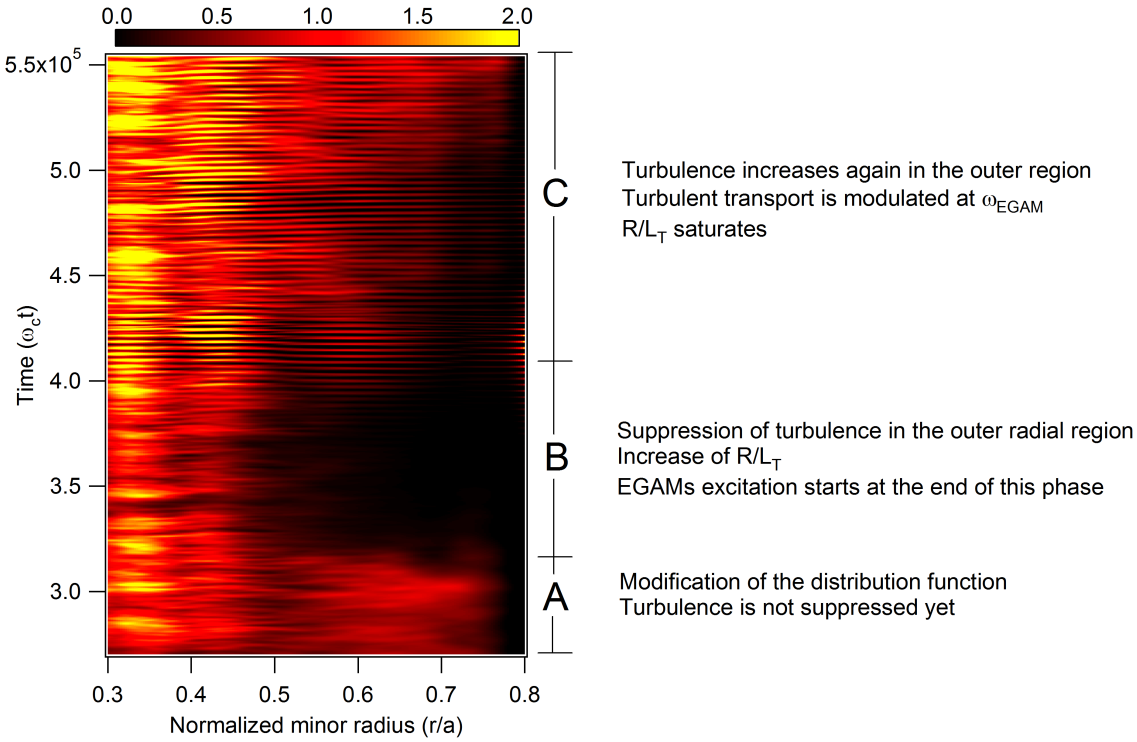

Figure 4.12: Colormap of the $E \times B$ diffusivity as defined by the expression 4.25. Main results of this section for each part (A, B, C) of the simulation are presented on the right-hand side.

The present section is structured as follows. In subsection 4.5.3 we analyse the modification of the distribution function by the energetic particle source, the EGAM excitation and give the spectrum of the ambient turbulence. In subsection 4.5.4 the reduction of the $E \times B$ transport is addressed. We compare the two simulations WEP and WOEP and analyse the reasons for the reduction of transport. In section 4.5.5, we study the different mechanisms potentially responsible for the increase of the $E \times B$ transport. Section 4.5.6 is devoted to the analysis of the modulation of turbulence at the EGAM frequency.

4.5.3 Evolution of the distribution function and excitation of EGAMs

As in the neoclassical case, the derivative of the distribution function is essential for the excitation of EGAMs. In addition, owing to the analysis done in the previous section, the evolution of the distribution function at $v_0 = 2$ and the increase of energetic particle population should be correlated to the modification of the turbulent transport. The mentioned quantities for the distribution function are given in figure 4.13. The sharp transition observed on figure 4.13a at $\omega_c t \approx 2.7 \cdot 10^5$ corresponds to the moment when the energetic particle source is switched on. This is highlighted by a vertical line. Afterwards, the slope increases until an equilibrium between energetic particle source, collisions and turbulence is achieved. Figure 4.13b illustrates the evolution of the distribution at $v_0 = 2$, normalized to its value before injecting the energetic particles, namely $F_{\mathrm{eq}}(v_0, t) / F_{\mathrm{eq}}(v_0, t = t_{\mathrm{init}})$. Figure 4.13c shows the evolution of the distribution function at the parallel velocity where the energetic particle population peaks normalized to the initial value, i.e. $F_{\mathrm{eq}}(\bar{\zeta}, t) / F_{\mathrm{eq}}(\bar{\zeta}, t = t_{\mathrm{init}})$. In figure 4.13a, it can be observed that, as occurred in neoclassical regimes, the modification of the slope of the distribution function is stronger in outer radial positions. In figures 4.13b and 4.13c, in order to compare inner and outer radial positions, we represent only the positions $\rho \in [0.35, 0.5, 0.65, 0.8]$. From the analysis of the ITG marginal stability in the presence of energetic particles and from the analysis done in the previous chapter and the simulations presented in neoclassical regimes in this chapter, we expect two main effects due to the presence of the energetic particle source. The first one is the reduction of the turbulent transport, mainly in the radial region $0.5 < \rho < 0.8$, but a reduction in the region $0.4 < \rho < 0.5$ cannot be totally excluded. The second effect consists of the **excitation of EGAMs only in the simulation WEP, which is possible due to the positiveness of the slope of the distribution function**. This excitation can already be observed in the evolution of the distribution function. As far as the slope is concerned, the EGAM oscillations are stronger in the outer region. In figure 4.13a, the time evolution of the derivative is represented by thin lines. Thick lines represent a time-average over several EGAM cycles. It is observed that the distribution function follows the same behaviour as in the neoclassical simulations NC2 and NC3 only in the region $\rho \geq 0.65$, i.e. there is a first overshoot characterized by a decrease of the slope and then we observe the beginning of the quasi-periodic behaviour only in the outer radial region.

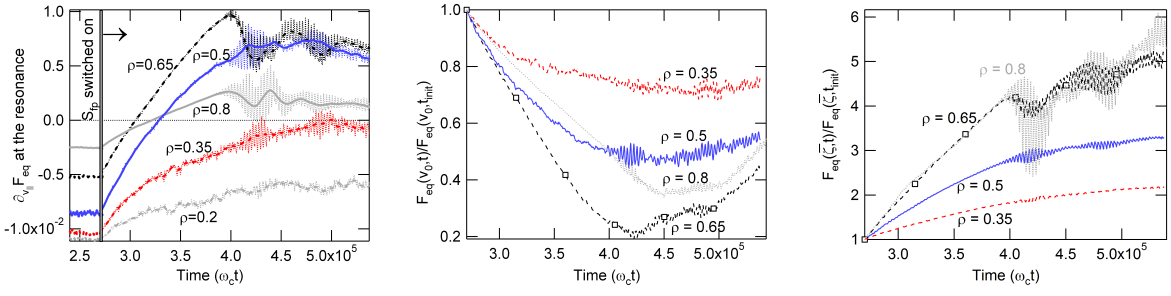

(a) (b) (c)

Figure 4.13: (4.13a) Derivative of the equilibrium distribution function with respect to the parallel velocity at the resonance (4.13b) Time evolution of the distribution function at the pumping velocity v_0 (4.13c) Time evolution of the distribution function at the velocity $\bar{\zeta}$.

Spectral analysis of the electrostatic potential before and after having switched on the energetic particle source allows one to determine the frequencies of both the ambient turbulence (AT) and the energetic particle mode. In figure 4.14a we represent the logarithm of the amplitude of the electrostatic modes at the mid radial position in the time window $2.3 \cdot 10^5 < \omega_c t < 2.7 \cdot 10^5$, i.e. before the energetic particle source is switched on. Only the resonant modes are considered, i.e. those satisfying $k_\parallel \propto m + nq = 0$. The frequency is normalized to the standard GAM frequency ω_{GAM}. Fourier transform of the up-down asymmetric component of the electrostatic potential reveals the same frequencies as those found in neoclassical simulations, i.e. $\omega_{\mathrm{EGAM}} \approx 0.4\omega_{\mathrm{GAM}}$ and the second harmonic at $2\omega_{\mathrm{EGAM}}$. The up-down asymmetric perturbations are coupled to the axisymmetric modes *via* the magnetic curvature, resulting in an oscillating radial electric shear at the same frequencies. In figures 4.14b and 4.14c we present the time evolution of the Fourier modes $E_{r,\omega_{\mathrm{EGAM}}}$ and $E_{r,2\omega_{\mathrm{EGAM}}}$ of the radial electric field $E_r = -\partial_r \phi_{00}$. This has been done by performing a spectrogram of the radial electric field after having switched on the energetic particle source over time windows covering 6 EGAM cycles. These time windows overlap each other over 4 EGAM cycles. As in the neoclassical simulations, the second harmonic exhibits small amplitude and large damping. **An important result is that the EGAM frequency is embedded in the AT spectrum (see yellow dashed line in figure 4.14a). This means that an interaction between the axisymmetric oscillating mode and the ITG modes is possible, but not straightforwardly predicted**. In this context, the gyrokinetic simulations that we present here provide important information to understand how the interaction occurs.

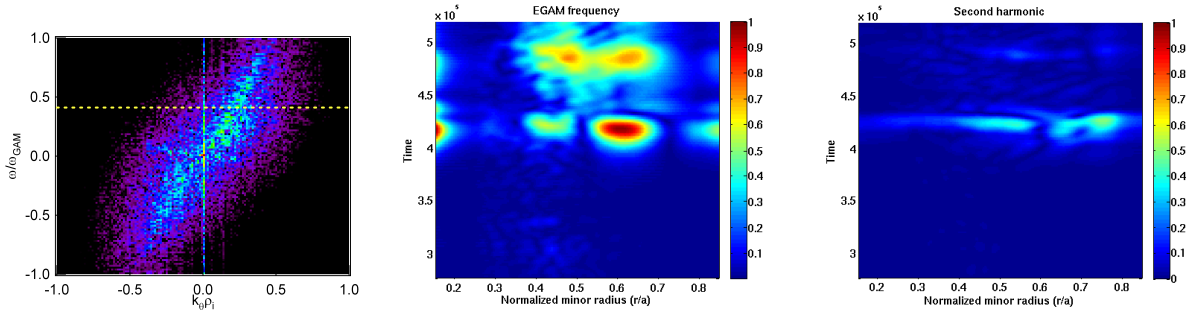

(a) (b) (c)

Figure 4.14: (4.14a) Logarithm of the amplitude of the resonant ITG modes as a function of the frequency and the poloidal wave number. The frequency is normalized to the standard GAM frequency. (4.14b) Colormap of the Fourier mode of the radial electric field at the EGAM frequency. (4.14c) Colormap of the Fourier mode of the second harmonic of the radial electric field.

4.5.4 Reduction of $E \times B$ transport in the outer region with energetic particles

A modification of the radial transport has been observed in the simulation with energetic particles. This is quantified by means of the effective $E \times B$ diffusivity, namely $\chi_{E\times B}$. For comparison, we calculate also the effective diffusivity associated to the curvature drift velocity χ_D. The definitions of these two quantities are

$$\chi_{E\times B} = -\frac{\left\langle \int v_{Er} E\, f\, \mathrm{d}^3\mathbf{v} \right\rangle_{\theta\varphi}}{n_i \nabla_r T_i} \tag{4.25}$$

$$\chi_{D} = -\frac{\left\langle \int v_{Dr} E\, f\, \mathrm{d}^3\mathbf{v} \right\rangle_{\theta\varphi}}{n_i \nabla_r T_i} \tag{4.26}$$

In the absence of EGAMs, these two quantities represent an accurate quantification of the turbulent and neoclassical diffusivities respectively. Figures 4.15a and 4.15b show these diffusivities for the two simulations presented in this section, namely WEP and WOEP. We plot in figure 4.16a only for the simulation WEP the $E \times B$ diffusivity in three selected radial regions, for comparison with the evolution of the distribution function.

We have observed that these curves are characterised by a choppy behaviour during the EGAM oscillations (an example of this can be observed in figure 4.16a). This is normal since the diffusivity χ_D oscillates in the same way as the mode $(m, n) = (0, 0)$ of the distribution function. The modulation of $\chi_{E\times B}$ will be analysed in subsection 4.5.6. For this reason, in figures 4.15a, 4.15b and 4.16a we plot the diffusivities averaged over some EGAM cycles for the simulation WEP. Only in figure 4.16a, the original signal for a radial position is given as an illustration of the large amplitude oscillations. In addition, for the sake of clarity and only for comparison between both simulations WEP and WOEP, in figures 4.15a and 4.15b we give the time evolution averaged over the outer radial region, namely $\langle\chi\rangle_{0.5<\rho<0.8}$, where the effect of the source on the turbulence is expected to be significant. Together with the diffusivities, we plot the time evolution of $|E_{r,\omega_{\mathrm{EGAM}}}|$ and $|E_{r,2\omega_{\mathrm{EGAM}}}|$ at the radial position $\rho = 0.6$, where the EGAM amplitude peaks, as observed in figure 4.14b.

Several results can be observed from these curves. First, the $E \times B$ diffusivity in the outer region of the simulation domain in the presence of energetic particles is reduced by more than 80%. This reduction occurs well before the onset of EGAMs, meaning that the energetic particle mode does not play any role in the stabilization of the turbulence at that time. From figure 4.16a we can say that the reduction of radial transport occurs indeed for $\rho \geq 0.5$, which is consistent with the time evolution of the distribution function illustrated in figure 4.13, as expected from the analysis of the previous section. Second, when the EGAM is excited, the $E \times B$ transport increases again and reaches at the end of the simulation the same value as at the beginning. This increase will be analysed in the next subsection. Third, the reduction of $E \times B$ transport is not observed in the absence of energetic particles with the same injected heating power. This means that kinetic effects lead to important differences regarding the radial transport even if from a fluid point of view the effect of the source is the same in both simulations. Finally, as a minor observation, the time-averaged neoclassical transport is not significantly affected by the modification of the distribution function nor by the excitation of EGAMs. We can see that $\chi_D < \chi_{E\times B}$ in three time windows: before the transport barrier formation ($\omega_c t < 3.2 \cdot 10^5$), between the two EGAM bursts ($4.4 \cdot 10^5 < \omega_c t < 4.7 \cdot 10^5$), and after the second burst at the end of the simulation ($\omega_c t > 5.2 \cdot 10^5$).

Other effects different from the evolution of the distribution function can impact the $E \times B$ transport. We analyse in this paragraph the effect of the electric shear only in the simulation with energetic particles. For this purpose, we plot in figure 4.16b the time evolution of the electric shearing rate γ_E normalized to the maximum estimated linear growth rate of the ITG modes, i.e. $\gamma_{\max} \approx 1.3 \cdot 10^{-3}$, for three radial regions. We can observe that only after the turbulence is reduced does the shear weakly increase in the region $0.45 < \rho < 0.7$. The shear remains on the contrary constant in the region

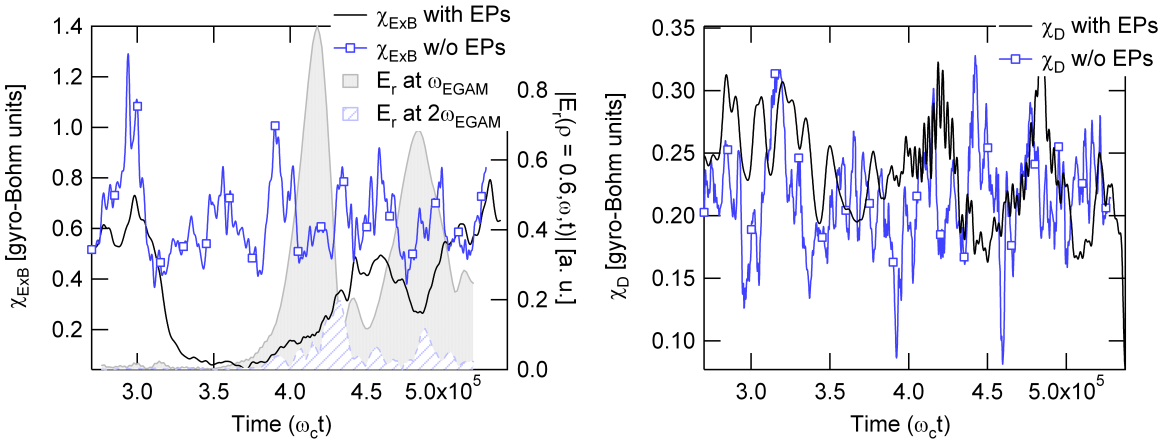

(a) (b)

Figure 4.15: Time evolution of the $E \times B$ (left) and curvature (right) effective diffusivities in the region $0.5 < \rho < 0.8$ for the simulations WEP and WOEP explained in the text. The time evolution of the amplitudes of the EGAM and the second harmonic is also given.

$0.3 < \rho < 0.4$. Since the modification of the shear occurs once the effective $E \times B$ diffusivity is reduced, we can conclude that the electric shear does not affect the turbulence stabilization in this simulation. These observations allow one to conclude that the modification of **the radial $E \times B$ transport does not rely upon fluid considerations. The modification of the distribution function seems to be the only possible mechanism for this stabilization, which is in qualitative agreement with the linear analysis detailed in the previous section.**

The radial profiles of $\chi_{E\times B}$ for the simulations WEP (solid curves) and WOEP (dashed blue curves) are given in figure 4.17a. In this figure, the profiles are averaged over three time windows representing the profiles during the transport barrier ($325000 < \omega_c t < 375000$) and the final profiles ($\omega_c t > 500000$). We give for reference the profile before switching on the source $S_{\rm fp}$ (dotted curve). As a consequence of the decrease of the radial $E \times B$ transport, the temperature gradient is increased in the outer region for the simulation WEP. A comparison between both simulations is given in figure 4.17b, where we plot R/L_T as a function of the normalized minor radius, averaged over the same time windows (the legend is the same in both figures). We can observe that the simulation WOEP exhibits a reduction of $E \times B$ transport in the inner region, leading to an increase of R/L_T. Since the source $S_{\rm fp}$ in the simulation WOEP does not invert the slope of the distribution function but only provides a parallel heating, we can approximate the distribution function by an anisotropic Maxwellian and analyse the modification of the turbulence as explained in appendix F. However, the predictions provided by this analysis are not consistent with the observed modification of transport in the inner region. This behaviour, which remains unclear, deserves further work in the future. Let us in the following focus our research on the simulation WEP and by studying the interaction between EGAMs and turbulence.

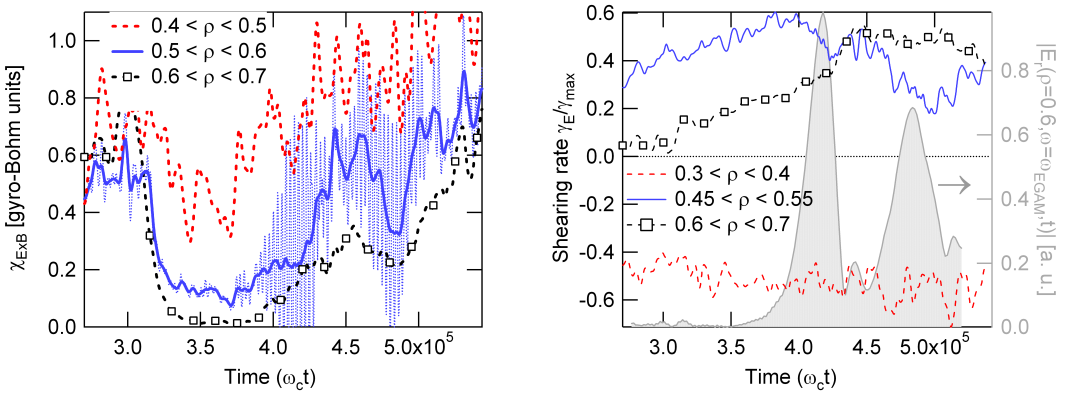

(a) (b)

Figure 4.16: For the simulation with energetic particles: (Left) Evolution of the time-averaged $E \times B$ diffusivity in three radial regions. Only for the region $0.5 < \rho < 0.6$, both signals the time-averaged and the original ones are given for illustration. (Right) Time evolution of the $E \times B$ shearing rate at three selected radial regions. The time evolution of the Fourier mode $E_{r,\omega_{\rm EGAM}}$ is also given.

4.5.5 Saturation of EGAMs and increase of the ITG turbulence

We examine in this subsection the different phenomena that occur during the saturation of EGAMs and the increase of radial transport in the turbulent simulations presented previously. As mentioned, the energetic particle mode appears when the radial transport has been reduced and exhibits mainly the frequency $\omega_{\rm EGAM}$. A major result observed in the simulation WEP is related to the increase of radial transport during the saturation of EGAMs. The different mechanisms that can be at the origin are: (1) Direct contribution of axisymmetric modes to the $E \times B$ transport, (2) interaction between EGAMs and ITG modes *via* the modification of the distribution function around v_0 and $\bar{\zeta}$ during the saturation of EGAMs, (3) propagation of turbulence by avalanches and (4) energy exchange between EGAMs, ITG modes and zonal flows, including an increase of the turbulent transport due a modulation of the phase between temperature and potential perturbations *via* the oscillating shear. Each of these mechanisms is analysed hereafter.

Contribution of axisymmetric modes to the radial $E \times B$ transport

The radial diffusivity defined in equation 4.25 can be decomposed into the contribution of axisymmetric and non axisymmetric modes as follows

$$\chi_{\rm E\times B,n=0} \approx i\frac{1}{r}\frac{\sum_m m p^{\dagger}_{m,0}\phi_{m,0}}{n_i \nabla_r T_i}, \qquad \chi_{\rm E\times B,n\neq 0} \approx i\frac{1}{r}\frac{\sum_{m,n\neq 0} m p^{\dagger}_{m,n}\phi_{m,n}}{n_i \nabla_r T_i} \tag{4.27}$$

where $p_{m,n}$ is the Fourier mode (m,n) of the pressure. If we consider the turbulent diffusivity as the one due to non axisymmtric modes, we can define the turbulent and neoclassical diffusivities as

$$\chi_{\rm turb} \equiv \chi_{\rm E\times B,n\neq 0} \tag{4.28}$$

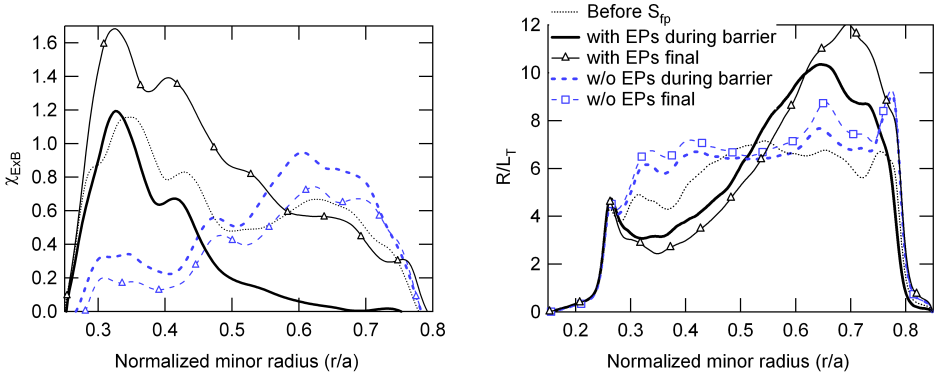

Figure 4.17: Comparison of $\chi_{E\times B}$ and R/L_T for the two simulations presented in this section. The dotted line represents the profiles before switching on S_{fp}. Black lines represent the profiles for the simulation WEP and blue lines for the simulation WOEP.

$$\chi_{\text{neo}} \equiv \chi_D + \chi_{\text{E}\times\text{B,n}=0} \tag{4.29}$$

Therefore, the $E\times B$ difusivity does not necessarily represent the turbulent diffusivity if axisymmetric modes are excited, which is the case in this section. It is legitimate to ask oneself if the increase that we observe in the radial transport is due to the non axisymmetric modes. The time evolution of $\chi_{\text{E}\times\text{B,n}\neq 0}$ and $\chi_{\text{E}\times\text{B,n}=0}$ is given in figure 4.18b only for two radial regions. In addition, the level of fluctuations is also quantified by

$$\delta\phi^2_{\text{axi}} = \sum_{m\neq 0} |\delta\phi_m|^2, \qquad \delta\phi^2_{\text{non axi}} = \sum_{m\neq 0} |\delta\phi_m|^2 \tag{4.30}$$

where $\delta\phi_{m,n}$ is the Fourier mode (m,n) of the fluctuation expressed as follows

$$\delta\phi = \phi - \frac{1}{(2\pi)^2}\iint \phi \mathrm{d}\theta\mathrm{d}\varphi \tag{4.31}$$

As can be observed in figure 4.18a the amplitude of the fluctuations associated to the axisymmetric modes is comparable to that of the fluctuations of non axisymmetric modes. The axisymmetric modes grow during the reduction of the turbulence. Afterwards, during the excitation of EGAMs, the amplitude of these fluctuations exhibits large amplitudes and exceeds temporarily that of the non axisymmetric modes. However, the contribution of the axisymmetric modes to the $E\times B$ diffusivity remains low and almost negligible during the whole simulation, as illustrated in figure 4.18b. The $E\times B$ axisymmetric diffusivity is modulated around zero and exhibits slight increases during the EGAM excitation and the saturation phase. To summarize, analysis of figure 4.18 reveals that **the increase of the $E\times B$ diffusivity is not due to the axisymmetric modes. Therefore, the $E\times B$ diffusivity represents an accurate measure of the turbulent diffusivity even in the presence of EGAMs**. Finally, it can be observed that the turbulent diffusivity χ_{turb} as defined in equation 4.28 follows the same trend as the non axisymmetric fluctuations.

Modification of the distribution function

Since the initial reduction of turbulence can be attributed to the modification of the distribution function (extraction of particles around v_0 and injection of particles around $\bar{\zeta}$),

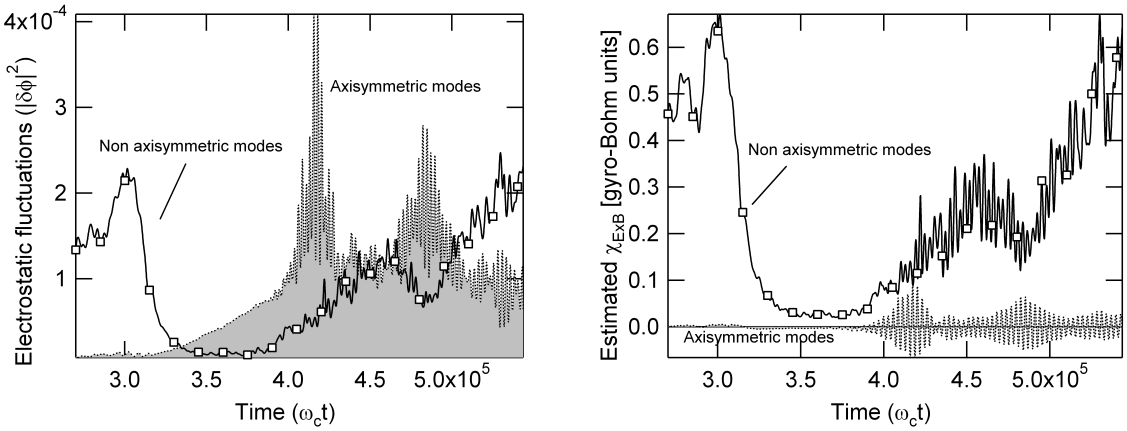

(a) (b)

Figure 4.18: Axisymmetric and non axisymmetric fluctuations of the electrostatic potential (left) and contributions to the $E \times B$ diffusivity (right).

the saturation of EGAMs could produce the inverse modification by wave-particle trapping. The resulting flattening might feed back the ITG modes. We could also imagine the opposite mechanism, i.e. an excitation of ITG modes and a subsequent feed back of the distribution function by turbulence. These two mechanisms are depicted in figures 4.19a and 4.19b respectively. On the left-hand panel, we illustrate the flattening as analysed in the previous chapter. In this case, the flattening occurs around the resonant velocity, resulting in an increase of the distribution function at v_0 (red dashed line) and a decrease at $\bar{\zeta}$ (dashed blue line). On the right-hand panel, the flattening is not significant, the distribution function decreases at $v_{\|} = 0$ (dashed blue line) and increases at v_0 and $\bar{\zeta}$ (red dashed line), likely due to the turbulent transport enhancement. We give hereafter some evidences that support the second mechanism.

First, the time evolution of the distribution function around v_0 and $\bar{\zeta}$ reveals that the decrease at $\bar{\zeta}$ occurs before the increase at v_0. In addition, when the distribution function starts increasing at v_0, it starts increasing also at $\bar{\zeta}$. Therefore, the distribution function at v_0 does not increase due to the flattening. Second, the distribution function at v_0 is mainly modified around $\rho = 0.65$ once the turbulence has increased again. In the other radial positions the modification is not significant. The values reached at $\rho = 0.65$ when the turbulence has increased are much smaller than the values when the turbulence was reduced. Thus, the final values of the distribution function are likely not sufficient to drive the ITG modes unstable again. Finally, the distribution function at $\rho = 0.65$ and $v_{\|} = 0$ is modified when EGAMs are excited and turbulence starts increasing again. This is shown in figure 4.20a. This suggests a depletion of the distribution function for $v_{\|} < v_0$ leading to an increase for $v_{\|} \geq v_0$. This modification cannot be due to the interaction between particles and EGAMs due to the distance in the phase space between $v_{\|} = 0$ and the resonance $v_{\mathrm{res}} = qR\omega_{\mathrm{EGAM}}$. Indeed, if any interaction between the resonant velocity and velocities around $v_{\|} = 0$ occurs, we should observe the EGAM frequency in the time trace of $F_{\mathrm{eq}}(v_{\|} = 0, t)/F_{\mathrm{eq}}(v_{\|} = 0, t_{\mathrm{init}})$. In figure 4.20b, we give the spectrogram of $F_{\mathrm{eq}}(v_{\|} = 0, t) - \langle F_{\mathrm{eq}}(v_{\|} = 0, t)\rangle$. The time evolution is not characterized by a single frequency. A wide spectrum is present instead, suggesting a modification around v_0 mainly due to the turbulence enhancement. The curves presented so far reflect the

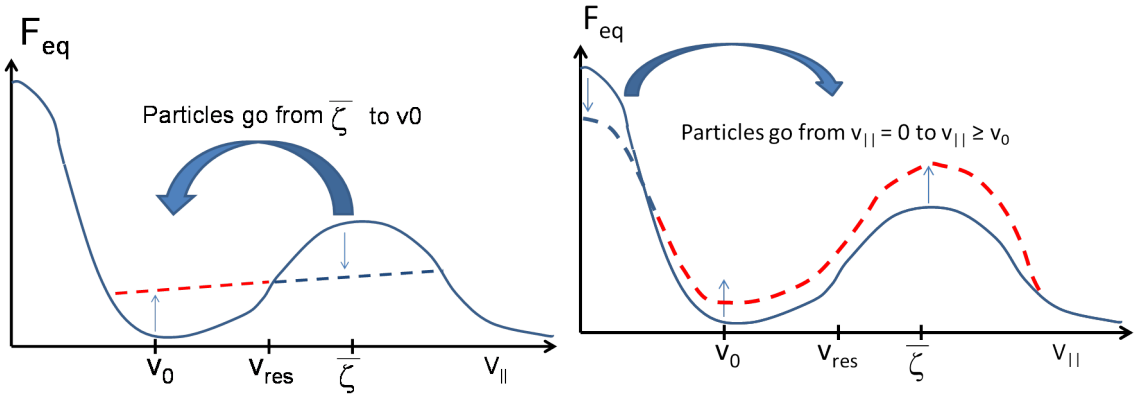

(a) (b)

Figure 4.19: Two possibilities of the modification of the equilibrium distribution function in the presence of EGAMs and turbulence: either the flattening affects the velocities v_0 and $\bar{\zeta}$ (left) or the ITG turbulence is excited, modifies the velocity $v_{\|} = 0$ which impacts the distribution function at suprathermal velocities (right).

evolution of the distribution function at several defined velocities ($v_{\|} = 0, v_0, \bar{\zeta}$), but in order to have a whole picture of the modification at other velocities, we plot in figure 4.20c three snapshots of the distribution function at $\rho = 0.65$ and $\mu = 0$. We can observe that the modification corresponds to the one depicted on the right-hand panel of figure 4.19. **Therefore, the following mechanism is proposed: (1) the turbulent transport is reduced due to the modification of the distribution function, (2) EGAMs are excited, (3) the turbulent transport is increased again, but this increase is not necessarily due to the modification of the distribution function, (4) the distribution function is subsequently modified by turbulence.** So far, the third point is not yet understood. We need to understand why the turbulence intensity increases during the EGAM excitation.

Radial propagation of turbulence

The previous discussions on the contribution of axisymmetric modes to the $E \times B$ radial transport and the modification of the equilibrium distribution function rises the following question: what is the mechanism that allows the turbulence to develop in the outer radial region once EGAMs start being excited? This region represents a linearly stable domain for ITG modes, as discussed in section 4.4. Different possibilities can be envisioned to understand the growth of turbulent transport, depending on the locality of the mechanism. First, local excitation of ITG modes is possible by three-waves parametric interaction between the axisymmetric modes excited at the EGAM frequency and the ITG modes. Similar phenomena were studied in the context of GAM excitation by drift-waves from fluid [68] and kinetic [66] points of view. Second, nonlocality can result in a radial propagation of turbulence, which meets two important phenomena extensively analysed in magnetic fusion devices: (1) turbulence spreading [129, 130, 131, 132, 133, 134, 135] and (2) avalanches [136, 137, 138, 139, 117, 140, 141, 142, 143, 104, 144, 145]. The former one relies upon the propagation of fluctuations energy from unstable to stable regions *via* the mode-mode toroidal coupling. Due to the axisymmetry of EGAMs, they can play a role in the toroidal coupling of ITG modes. This coupling involves a mode $(m \neq 0, n \neq 0)$

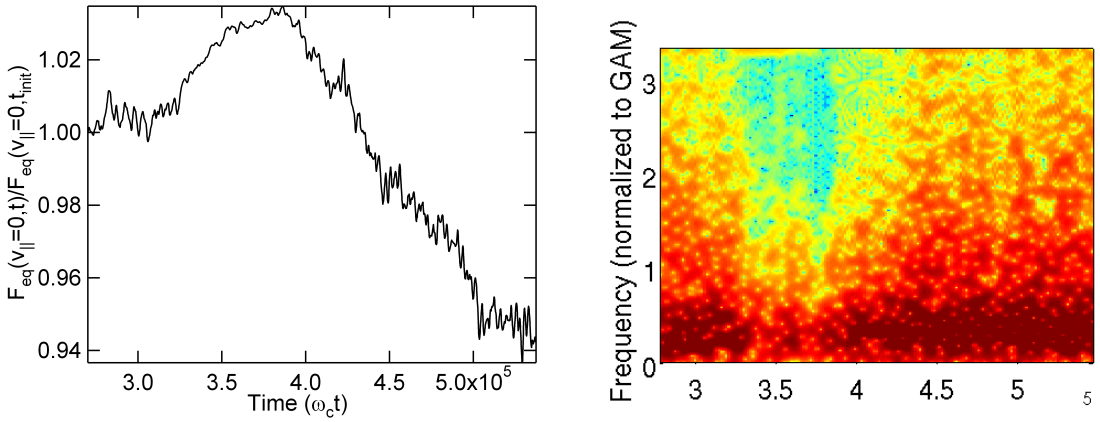

(a)

(b)

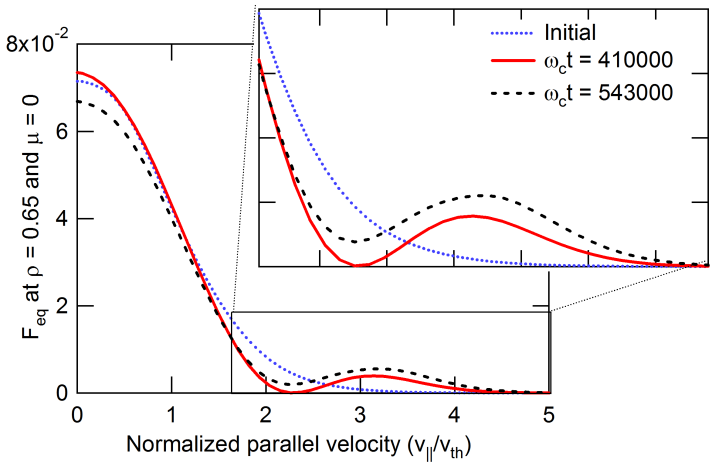

(c)

Figure 4.20: (4.20a-4.20b) Time evolution and spectrogram of the equilibrium distribution function at $v_{||} = 0$ and $\rho = 0.65$. (4.20c) Three snapshots of the distribution function during the simulation.

at a frequency ω_{EGAM} to its second harmonic at $2\omega_{\mathrm{EGAM}}$ and the $(1,0)$ perturbation at the EGAM frequency. The latter one is related to the critical gradient threshold in self-organized critical (SOC) systems, where avalanches are radial front propagations like in a sandpile. In this context, the avalanche-like phenomena may be related to the existence of *streamers* both in ITG [120] and ETG [146] turbulence. Streamers are radially extended convective cells [147] which enable the enhancement of transport [135]. The effectiveness of the streamers depends on the phase shift between temperature and potential fluctuations. Important characteristics regarding the streamers and the turbulent transport reduction were reported for the first time in [141]. In particular, the intrinsically nonlinear generation of streamers was evidenced, together with the reduction of turbulent radial flux due to the suppression of low frequencies. We are aware that a complete description of the simulation with energetic particles would require analysis of each possible mechanism pointed out here. However, this section does not aim at giving the whole picture of the existing physical phenomena, but only constitutes an attempt towards an acceptable

interpretation of the presented results. For this purpose, we focus our analysis on a main result that has been observed: the radial propagation of turbulence *via* avalanches, which are able to propagate by coupling to the coherent oscillations of the temperature gradient at the EGAM frequency.

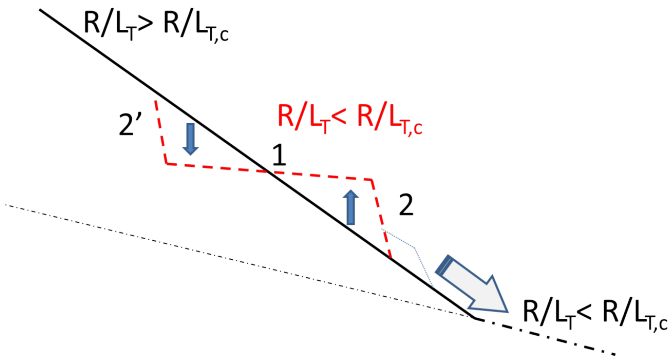

Figure 4.21: Schematic illustration of the avalanche mechanism.

Before detailing this mechanism, we consider necessary to explain in a heuristic way the front propagation leading to a radial spread of turbulence. This is schematically illustrated in figure 4.21. Let us assume a system with a temperature gradient above the critical value for ITG instability ($R/L_T > R/L_{T,c}$). Fluctuations grow and generate turbulent transport. Due to this transport, the temperature gradient decreases. This is represented by a red dashed line around the position 1. Since the energy is constant, this flatenning must lead to steep gradients downhill (position 2) and uphill (position 2'), represented by up/down arrows. Therefore, in positions 2 and 2' the gradient may exceed the critical value for ITG instability, fluctuations can grow there and the mechanism is reproduced, leading to a front propagation represented by an arrow oriented downhill. The front erodes when propagating, due to several stabilizing mechanisms. The avalanche may then stop when the gradient front is not large enough to excite turbulent modes. This is represented by the knee on figure 4.21.

The mechanism of avalanche-EGAM coupling that we propose is highlighted on figure 4.22, where we give two colormaps of the oscillating part of R/L_T, obtained as $R/L_T - \langle R/L_T \rangle$, where $\langle \cdot \rangle$ is a time average. These colormaps correspond to the first instants of the EGAM excitation at the end of the phase B (top panel) and to the phase where turbulence and EGAMs coexist, during the phase C (bottom panel). During the transport barrier, the inner region exhibits avalanche-like behaviour, as observed in figure 4.22a, with fronts propagating outwards and vanishing at $\rho \approx 0.5$. The propagation velocity can be estimated at $v_{\text{aval}} \approx 0.8 v_\star$, where $v_\star$ is the diamagnetic velocity. In the same figure, we observe static oscillations in the outer region, characterized by horizontal traces. By *static* we mean that there is no front propagation, i.e. the beginning of the EGAM oscillations does not exhibit avalanche-like behaviour for $\rho > 0.5$. These static oscillations can be explained as follows. The drive of the EGAM instability is the derivative of the distribution function in velocity space. The distribution function exhibits oscillations at the EGAM frequency and so does the neoclassical heat flux, which results in a temperature gradient oscillating at the same frequency. Since the drive of the EGAM instability is not the temperature gradient, R/L_T can oscillate at the EGAM frequency at the beginning of the excitation without propagating. However, a large perturbation propagating outwards in the inner region can run into another perturbation of the same sign in

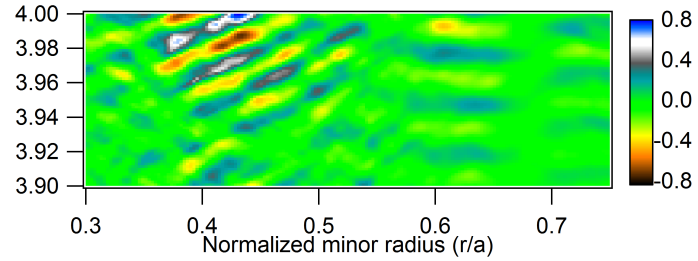

(a)

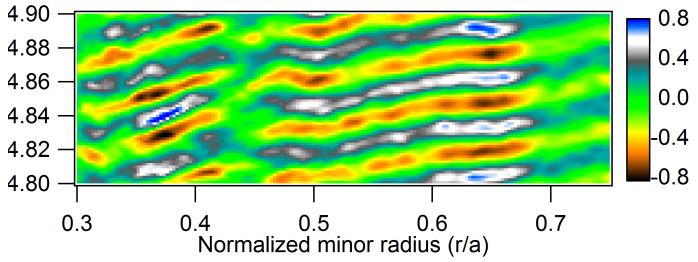

(b)

Figure 4.22: Colormap of the temperature gradient oscillations in two time intervals of the simulation WEP: at the end of phase B (top panel) and in the phase C (bottom panel).

the outer region. When this occurs, both perturbations are combined to give a larger perturbation which can exceed the local critical gradient to destabilize the turbulence. The inner avalanches can then propagate in the outer region and the energy can flow along the whole radial dimension. This is actually what happens in phase C, as observed in figure 4.22b. In this figure, we can see that there is not a single propagation velocity. This is attributed to the coexistence of both ITG instability and EGAMs. It is important to note here that **this mechanism requires a comparison with an analytical model. Nevertheless, even in the absence of this comparison, what we observe in figure 4.22 represents the first evidence of the coupling between turbulence and energetic particles *via* the EGAMs. Understanding the whole picture of this coupling still deserves further work.**

4.5.6 Modulation of the turbulent diffusivity at the EGAM frequency

An important result that has been obtained in the simulation with energetic particles is the modulation of the turbulent diffusivity at the EGAM frequency. This modulation is visible in the frequency Fourier transform of the oscillating part of the diffusivity at the mid radial position. The oscillating part is obtained as $\chi_{\text{turb}} - \langle\chi_{\text{turb}}\rangle$, where χ_{turb} is defined in the expression 4.28. The amplitude of the Fourier mode is plotted in figure 4.23 for two situations: (1) before the transport barrier, i.e. in the phase A of the simulation (dashed line) and (2) during the coexistence of EGAMs and turbulence, i.e. in the phase C (solid line). It can be observed that both cases exhibit a broad spectrum. The phase A presents a maximum around the EGAM frequency, which is consistent with the spectrum shown in figure 4.14a. Phase C exhibits a strong peak located exactly at the EGAM frequecy, which clearly dominates the spectrum. The Fourier transform of the turbulent diffusivity for the simulation WOEP has also been computed, but no significant difference has been observed with respect to the dashed line of figure 4.23.

The explanation for this modulation can be understood in two ways: (1) a kinetic

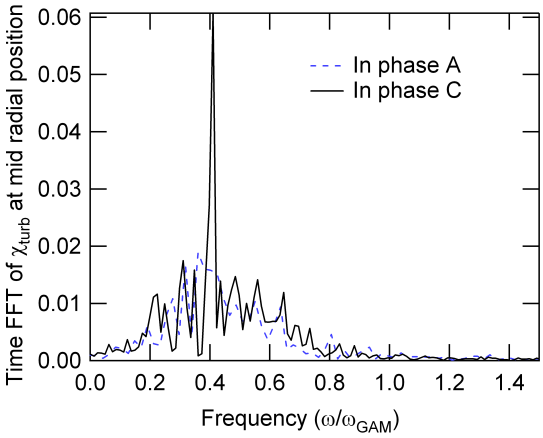

Figure 4.23: Fourier transform of the turbulent diffusivity before the transport barrier, i.e. phase A (dashed line) and during the coexistence of EGAMs and turbulence, i.e. phase C (solid line).

modulation, *via* the oscillations of the distribution function at $v_\parallel = v_0$, and (2) a modulation *via* the oscillating radial electric shear. These two mechanisms are detailed hereafter.

Kinetic modulation of the $E \times B$ diffusivity

The linear response 2.10 can be generalized to the case where $F_{\rm eq}$ oscillates at a frequency ω_0, as follows

$$\hat{F}_{\omega,\mathbf{n}} = -\frac{\mathbf{n}\cdot\partial_{\mathbf{J}}F_{{\rm eq},\omega_0}}{\omega - \mathbf{n}\cdot\mathbf{\Omega}}\hat{H}_{\omega-\omega_0,\mathbf{n}} \tag{4.32}$$

taking into account the expression for the total turbulent heat flux $Q_{\rm turb} = \left\langle \int {\rm d}^3\mathbf{v}\, EFv_{E,r}\right\rangle_{\theta,\varphi}$, we can approximate it as

$$Q_{\rm turb} \approx \int {\rm d}^3\mathbf{v} \sum_{\mathbf{n}}\sum_{\omega,\omega'} E\frac{\mathbf{n}\cdot\partial_{\mathbf{J}}F_{{\rm eq},\omega_0}}{\omega - \mathbf{n}\cdot\mathbf{\Omega}}\hat{H}_{\omega-\omega_0,\mathbf{n}}\hat{H}_{\omega',-\mathbf{n}}{\rm e}^{-i(\omega+\omega')t} \tag{4.33}$$

which gives straightforwardly the expression for the Fourier mode $\hat{Q}_{{\rm turb},\omega_0}$

$$\hat{Q}_{{\rm turb},\omega_0} \approx \int {\rm d}^3\mathbf{v} \sum_{\mathbf{n}}\sum_{\omega} E\frac{\mathbf{n}\cdot\partial_{\mathbf{J}}F_{{\rm eq},\omega_0}}{\omega - \mathbf{n}\cdot\mathbf{\Omega}}|\hat{H}_{\omega-\omega_0,\mathbf{n}}|^2 \tag{4.34}$$

The existence of this mode at $\omega_0 = \omega_{\rm EGAM}$ together with the oscillations at $\omega_{\rm EGAM}$ of the temperature gradient result in a modulation of the turbulent diffusivity. That the mode $\hat{Q}_{{\rm turb},\omega_{\rm EGAM}}$ exists can be demonstrated by the oscillations at the EGAM frequency of the distribution function at the resonant velocity for the ITG modes. This is indeed the case, as observed in figure 4.24, where we give the spectrogram of the oscillating equilibrium distribution function at $v = v_0$ and $\rho = 0.65$. We can observe that the spectrum (in logarithmic scale) peaks at the EGAM frequency.

Modulation by oscillating shear

In the introduction of this chapter, we mentioned that the self-regulation of fluctuations has been invoked in the literature as the drift-wave zonal flow paradigm. In this case, as

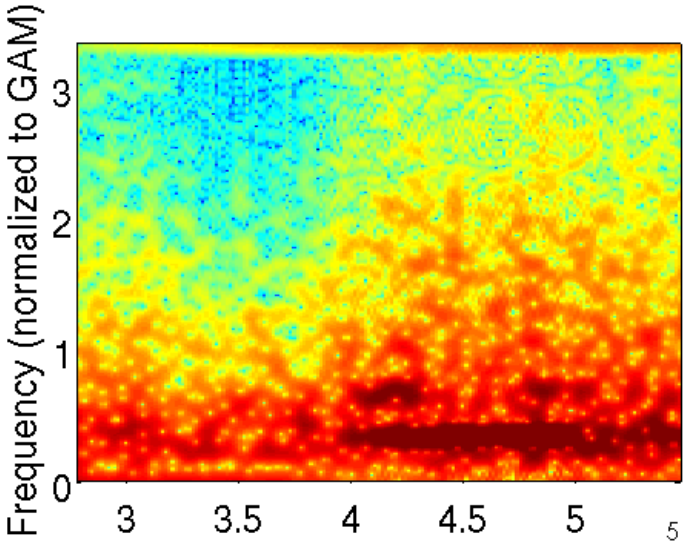

Figure 4.24: Spectrogram of the distribution function at $v_{\|} = v_0 = 2$.

explained earlier, zonal flows are nonlinearly generated by the fluctuations themselves and any control of the evolution of zonal flows then appears extremely challenging. In the present case, we are imposing externally the way zonal flows oscillate by means of both energetic particles and curvature coupling. In particular, the EGAM frequency is captured in the $E \times B$ shear evolution. Should the standard mechanism of regulation between sheared flows and turbulence apply, we would expect to observe oscillations at the frequency $2\omega_{\mathrm{EGAM}}$ in the time evolution of the turbulent diffusivity. This mechanism consists of a stabilization of turbulence depending only on the amplitude of the shearing rate, not on its sign (see criterion 4.2). This is illustrated in figure 4.25a. The solid line represents the shearing rate with its sign, whereas the dashed line represents the absolute value of the shearing rate. Therefore, in a simplified way, if $|\gamma_E| > \gamma_{\mathrm{crit}}$ the turbulent diffusivity is expected to decrease. This regulation results in a modulation of χ_{turb} at twice the frequency of the shearing rate. This is represented by the shadowed region in figure 4.25a. However, such an analysis of the impact of γ_E on turbulence is surely oversimplified to capture the complex interplay between γ_E oscillating at ω_{EGAM} and turbulence regulation. Also, it has been reported in a recent publication [148] that the growth rate of the ITG modes exhibits an asymmetry with respect to $\gamma_E = 0$. In particular, negative values of shearing rate increase the growth rate of the ITG modes before stabilization is achieved. Therefore, it would seem that the stabilization of turbulence depends on the sign of the shearing rate, as reported in Ref. [148]. Let us now consider a situation where if $-\gamma'_{\mathrm{crit}} < \gamma_E < \gamma_{\mathrm{crit}}$ the ITG modes are not stabilized, with $\gamma'_{\mathrm{crit}} > 0$. Let us assume that the shearing rate oscillates around a value $\langle\gamma_E\rangle$ and that the oscillations provided by energetic particles are such that $\gamma_E > -\gamma'_{\mathrm{crit}}$. In that case, the turbulent diffusivity is expected to oscillate at the EGAM frequency, as illustrated in figure 4.25b. Owing to the spectrum shown in figure 4.23, one could conclude that the mechanism illustrated in figure 4.25b could be at work. For this, it is necessary that the shearing rate and the turbulent diffusivity exhibit a predator-prey-like behaviour.

The oscillating part of the turbulent diffusivity in the simulation WEP is given by the colormap on figure 4.26a, together with the isocontours $\gamma_E = 0$, for the phase C of

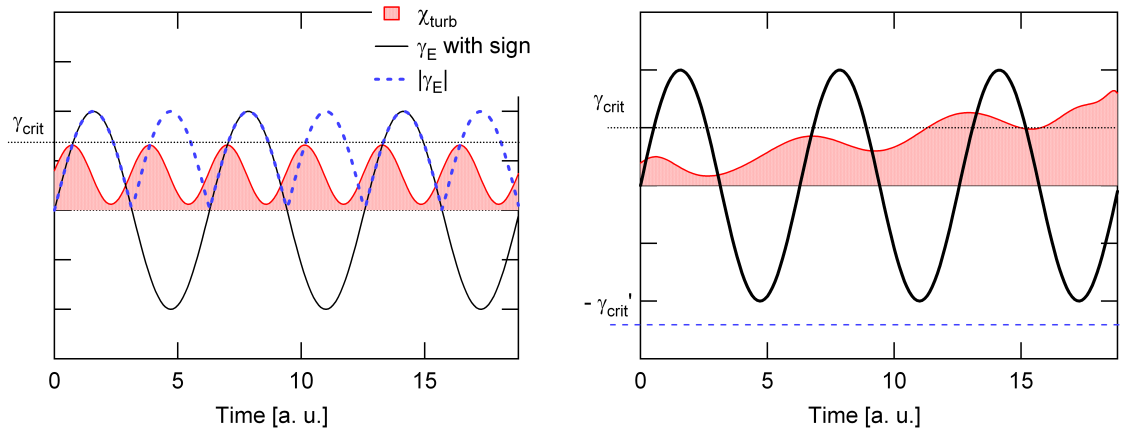

(a) (b)

Figure 4.25: Schematic illustration for the regulation of turbulence by a sheared flow depending on the condition for stabilization.

the simulation. We can see that the turbulent diffusivity is characterized by fast radial propagation. This behaviour is consistent with the one observed for the evolution of R/L_T in figure 4.22b. The time-trace at a given radial position shows that these two signals are not in phase and a maximum of $\chi_{\rm turb}$ always precedes a maximum of γ_E, which is consistent with the behaviour illustrated in figure 4.25b. The correlation between the two signals reveals a shift of $\omega_c \Delta t \approx 6 \cdot 10^2$.

4.6 Summary

In this chapter we have extended the collisionless theory of EGAMs to simulations in which radial profiles are taken into account. The necessity to implement a source term on the right-hand side of the gyrokinetic equation has been pointed out. The construction of this term has been detailed and the efficiency of the source has been tested in neoclassical simulations in the presence of temperature and density gradients. Two collisionality regimes in the banana regime have been explored. When collisions are less frequent, a quasi-periodic behaviour has been observed, characterized by a modulation of the EGAM amplitude. The slope of the distribution function is correlated to the amplitude of the mode, but the mode saturation does not require the slope to vanish. This has been explained by two mechanisms. First, the resonance in $v_\parallel$ space is widen in the presence of a finite collisionality. Second, damping effects associated to the radial gradients of the distribution function have been invoked. Further quantitative analysis needs to be done in this direction.

The implemented energetic particle source has been applied to turbulent simulations. In this context, it has been shown analytically that a departure of the distribution function from a Maxwellian can strongly modify the linear stability of ITG modes. In particular, the source used in this chapter stabilizes ITG modes in the outer region of the simulation domain *via* an extraction of particles that excite ITG modes. Subsequently, energetic particles excite EGAMs and two main results have been obtained: (1) Turbulence propagates from unstable to stable regions and (2) turbulent diffusivity is modulated at the EGAM

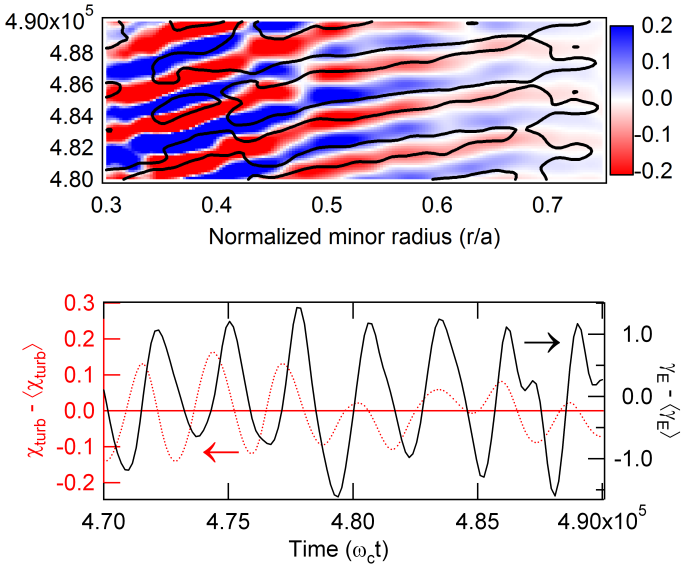

Figure 4.26: (Top) Colormap of the turbulent diffusivity and isocontours of the $E \times B$ shearing rate. (Bottom) Time trace for a given radial position of the oscillating parts of $\chi_{\rm turb}$ and γ_E.

frequency. A mechanism for the propagation of the turbulence has been proposed, based on the coupling between fronts propagating outwards and coherent oscillations of the temperature gradient at the EGAM frequency. Although further analytical verification is needed, the proposed mechanism can be understood as the first evidence of the interaction between turbulence and energetic particles *via* the EGAMs. As an illustration of this interaction, we give in figure 4.27 six snapshots of the poloidal cross-section of the perturbed electrostatic potential: the initial turbulent state ($\omega_c t = 270000$), the turbulence suppression in the outer radial region ($\omega_c t = 325000 - 370000$), the destruction of the transport barrier during the excitation of EGAMs and saturation of EGAMs ($\omega_c t = 420000 - 543000$). The duration of this mechanism is ≈ 2.7 ms, whereas the energy confinement time is $\tau_E \approx 3.8$ ms.

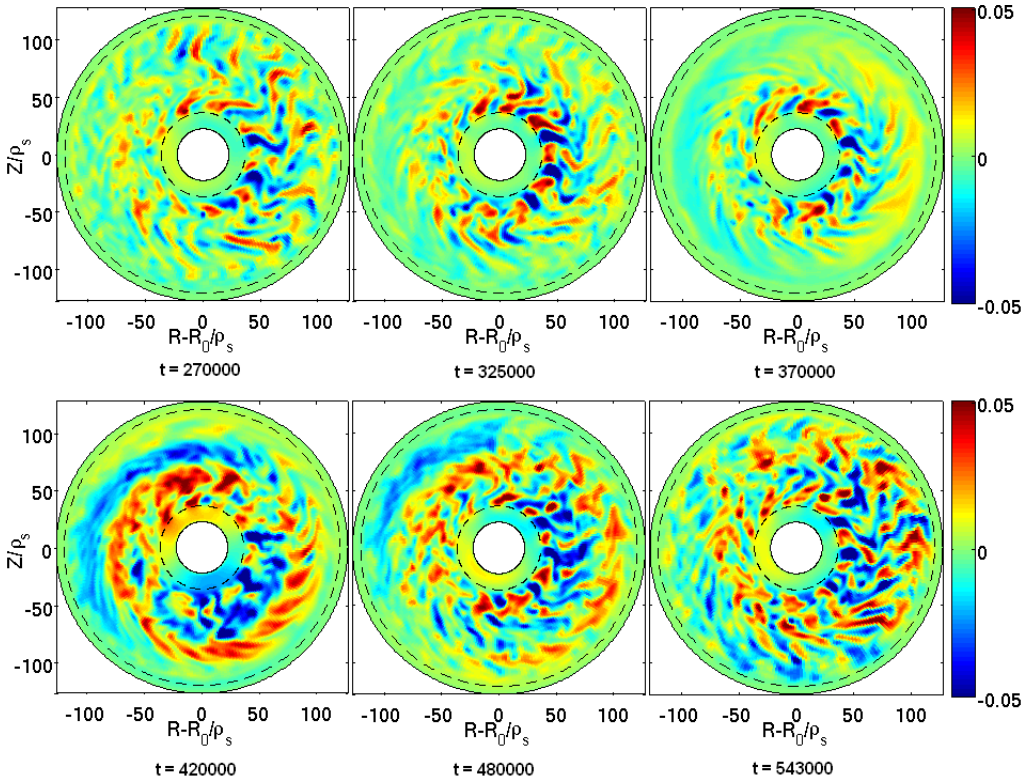

Figure 4.27: Snapshots of the poloidal cross-section of the electrostatic potential. At $\omega_c t = 270000$ the energetic particle source is switched on. In the time window $\omega_c t = 325000 - 370000$ the turbulence is suppressed in the outer region. At $\omega_c t = 420000$ occurs the first burst of EGAMs, with the increase of turbulent transport. At $\omega_c t = 480000$ occurs the second burst of EGAMs during a transient reduction of turbulence before reaching the final state where turbulence is increased and coexists with EGAMs at $\omega_c t = 543000$.

Chapter 5

Conclusions, open questions and perspectives

> In attempting to judge the success of a physical theory, we may ask ourselves two questions: (1) "Is the theory correct?" and (2) "Is the description given by the theory complete?"
>
> A. Einstein (1879-1955), in [149]

In this thesis, we addressed two essential phenomena regarding energetic particles in magnetic fusion devices: their generation and their impact on turbulence. Both of these subjects were studied from a kinetic point of view. By *kinetic point of view* we mean the way particles are distributed in the whole phase-space, i.e. velocity and position, and the way one can modify their distribution by external means, i.e. by sources. Three years of work on these exciting axes provided the author of this manuscript with the certainty that modeling a complex system such as an externally heated plasma in a tokamak cannot always be reduced to a fluid description. Throughout this manuscript, the reader was given mathematical tools, theoretical descriptions, numerical simulations and physical interpretations that support the mentioned certainty. To guide the reader along this hazardous route, the present research was structured in three main chapters.

In chapter 2, the generation of energetic particles in ICRF heating scenarios was analysed. This was done by means of a full-wave solver called EVE, coupled to a Fokker-Planck module called AQL. This module takes into account the anisotropy of the distribution function in velocity space, which is essential to model ICRF heating. The self-consistent response of the plasme was obtained for two ITER scenarios: second harmonic DT heating and fundamental DT(He^3) heating. The strong anisotropy of the distribution function was evidenced. It was also obtained that the effect of energetic particles is more pronounced in the second harmonic scenario, where the FWCD efficiency was reduced when the effects of energetic particles were added.

Afterwards, we focused our work on the effect of energetic particles on turbulent transport. The motivation relies upon the efficiency of large scale zonal flows (ZFs) to stabilize turbulence. While the efficiency of stationary sheared ZFs is now generally accepted, that of oscillating flows remains questionable. Our efforts were therefore directed towards the analysis of sheared flows oscillating in the acoustic range of frequencies,

namely the geodesic acoustic modes (GAMs). These modes are damped in the core of a tokamak. The interest of externally controlling and maintaining the oscillating sheared flows structured the remaining of the research in two steps, summarized hereafter.

First, we analysed in chapter 3 how a population of energetic particles can excite oscillating sheared flows. By means of a variational approach, we found that GAMs are damped in a Maxwellian background. The necessity of using energetic particles to excite them in steady-state was then evidenced and a linear criterion for the destabilization derived. In this case, the GAMs are called energetic GAMs, or EGAMs. The predicted criterion was verified numerically in gyrokinetic simulations using the GYSELA code, with flat profiles in the absence of turbulence. The structure of the distribution function in perpendicular velocity space revealed essential to understand the behaviour of the system wave-particles close to the saturation. In particular, nonlinear exchange of energy between stabilizing particles, destabilizing particles and the wave was proposed during the excitation of the mode leading to a saturation level independent of the energetic particle density for a slowing-down distribution function. This nonlinear interaction leads to the excitation of linearly stable modes.

In chapter 4, we applied these results to turbulent simulations and analysed the interaction between turbulence and EGAMs in GYSELA. This chapter led to very promising and surprising results and, though extremely short taking into account the difficulty of the subject, it constitutes the natural ending of the whole thesis, which acquires complete significance. It is important to note that the results of chapter 4 were obtained for the first time in flux-driven simulations run with a global full-f code. We demonstrated that each of these three ingredients (flux-driven, global and full-f) is essential to account for the enormous complexity of the interaction between EGAMs and turbulence. We highlighted the necessity of implementing a source term on the right-hand side of the gyrokinetic equation. This term mimics the effect of heating sources that generate energetic particles. For this reason, the source was called *energetic particle source*. This new element was implemented and revealed essential to excite EGAMs in simulations with radial gradients, both in neoclassical and turbulent regimes. As far as neoclassical regimes are concerned, the results of chapter 3 were extended regarding the nonlinear saturation in very long flux-driven simulations. In the presence of turbulence the source was firstly found to reduce the transport in the outer region of the simulation domain. Afterwards, EGAMs were excited and an increase of the transport was observed, modulated at the EGAM frequency. This increase was attributed to the coupling between propagating avalanches and coherent oscillations of the temperature gradient at the EGAM frequency in the outer region. However, two more mechanisms that have not been explored but only mentioned in the present manuscript can be at work, namely the parametric destabilization of turbulence *via* a three-waves coupling between EGAMs and ITG modes and the turbulence spread *via* a toroidal coupling. Finally, it was found that the turbulent diffusivity oscillates at the EGAM frequency, as occurs with the shearing rate. This modulation is not in agreement with the most acceptable stabilization mechanism, based on the module of γ_E and not on its sign. This finding suggests two possible explanations: (1) the growth rate of the ITG modes is not symmetric with respect to the shearing rate sign, (2) the modulation comes from the oscillations of the distribution function, suggesting a kinetic modulation. The latter one was analysed and we concluded that this mechanism can indeed be at work when turbulence and EGAMs coexist with similar frequencies.

This PhD work resulted in many open questions that led to different future research axes. We enumerate hereafter those that are considered more relevant (the open questions

related to chapter 4 are given in order of importance from the point of view of the author of this manuscript).

- The role of additional terms on the right-hand side of the Vlasov equation was pointed out in chapter 2. This term accounted for energy losses that cannot be redistributed *via* collisions among the existing thermal species. This term should be modeled and added to AQL for a more realistic description of ICRF heating. In addition, the coupling between EVE and AQL needs to be improved to give the real time evolution of the electromagnetic field and the distribution function.

- In chapter 3 we gave some examples of linearly stable modes that can be driven unstable due to resonant damping and energy exchange between stabilizing and destabilizing particles. These examples illustrate to what extent the excitation of EGAMs can be sensitive to minor modifications of the distribution function. These modifications cannot be retained by linear analysis. Therefore, further work to generalize the linear developments of this manuscript should be considered. In this direction, first efforts have been made in [150] to explain the generation of the second harmonic.

- A comparison between the mechanism of radial propagation proposed in chapter 4 and an analytical model needs to be made. This model should be based on the coupling of two equations: the wave-energy and the heat transfer equations, as analysed in [145]. A new element is to be added: the oscillations of the temperature gradient in a linearly stable region.

- We should understand the possible excitation of ITG modes by (1,0) perturbations oscillating at the EGAM frequency. This should be done as mentioned earlier in the framework of the three-waves coupling mechanism. This work can be conducted in a wave-kinetic framework, like that reported in [66].

- Additional elements should be provided to know whether the stabilization of ITG modes based on the amplitude of γ_E is applicable to the case of oscillating sheared flows in the ITG range of frequency.

- Finally, in chapter 4, we pointed out the kinetic effects of a source and demonstrated how a source which injects only energy can result in unexpected effects depending on the structure in phase-space. We demonstrated in particular the existence of kinetic effects on the modification of the turbulence. Further work needs to be done for a complete description of a source, especially in gyrokinetic simulations where kinetic considerations might reveal essential. For this purpose, the author of this manuscript proposes the following analysis. First, since the distribution function modified by a source may depart considerably from a Maxwellian, the neoclassical theory should be revisited. In this context, some pioneering works have been carried out in the particular case of an anisotropic Maxwellian [151, 152]. A general case different from a Maxwellian could be studied numerically, to analyse the modification of the neoclassical transport. Second, if the source affects mainly the viscosity boundary layer, dramatic modifications of the neoclassical theory are expected. For this purpose, one can use the implemented energetic particle source and perform a scan on the parameters v_0 and $T_\parallel$ (see section 4.2.1) at constant parallel injected power. A measure of the neoclassical diffusivity $\chi_{\rm neo}$ could provide additional clues to unveil the impact of the source on the transport. The effect of a

thermal source on turbulent transport should be analysed in detail. In particular, the calculations presented in appendix F can provide additional information for the stabilization of ITG modes. But additional work needs to be done to give a complete explanation for the reduction of turbulence in the inner region in the absence of energetic particles.

Publications

- Y. Sarazin, G. Dif-Pradalier, D. Zarzoso, X. Garbet, Ph. Ghendrih and V. Grandgirard 2009 *Plasma Phys. Control. Fusion* **51** 115003
- M. N. A. Beurskens, T. H. Osborne, P. A. Schneider, E. Wolfrum, L. Frassinetti, R. Groebner, P. Lomas, I. Nunes, S. Saarelma, R. Scannell, P. B. Snyder, D. Zarzoso, I. Balboa, B. Bray, M. Brix, J. Flanagan, C. Giroud, E. Giovannozzi, M. Kempenaars, A. Loarte, E. de la Luna, G. Maddison, C. F. Maggi, D. McDonald, R. Pasqualotto, G. Saibene, R. Sartori, Emilia R. Solano, M. Walsh, L. Zabeo, DIII-D Team, ASDEX Upgrade Team, and JET-EFDA Contributors *Phys. Plasmas* **18**, 056120 (2011)
- D. Zarzoso, M.N.A. Beurskens, L. Frassinetti, E. Joffrin, F.G. Rimini, E.R. Solano and JET EFDA contributors 2011 *Nucl. Fusion* **51** 112001
- D. Zarzoso, X. Garbet, Y. Sarazin, R. Dumont, and V. Grandgirard *Phys. Plasmas* **19**, 022102 (2012)
- R. Dumont and D. Zarzoso 2012 *Nucl. Fusion* "*Heating and current drive by Ion Cyclotron waves in the activated phase of ITER*" to be published
- D. Zarzoso, X. Garbet, Y. Sarazin, A. Strugarek, R. Dumont, J. Abiteboul, Th. Cartier-Michaud, G. Dif-Pradalier, Ph. Ghendrih, V. Grandgirard, G. Latu, C. Passeron and O. Thomine "*Effect of the anisotropic heating on the marginal stability of ion temperature gradient turbulence*", submitted to *Phys. Plasmas*
- D. Zarzoso, Y. Sarazin, X. Garbet, R. Dumont, A. Strugarek, J. Abiteboul, Th. Cartier-Michaud, G. Dif-Pradalier, Ph. Ghendrih, V. Grandgirard, G. Latu, C. Passeron and O. Thomine "*Impact of energetic particle driven geodesic acoustic modes on turbulence*", submitted to *Phys. Rev. Lett.*

Appendix A

Guiding-centre motion in the adiabatic limit

We derive in this appendix the parallel and perpendicular components of the guiding-centre velocity in the so-called adiabatic limit. This derivation can also be found in many references (see for instance Refs. [153, 154]).

A.1 Defining the adiabatic limit

The adiabatic limit for the motion of a charged particle in an electromagnetic field is defined by the condition

$$\frac{\mathrm{d}\log B}{\mathrm{d}t} \ll \omega_c \equiv \frac{eB}{m} \tag{A.1}$$

This condition on the total time derivative leads to the following ordering

$$\frac{\omega}{\omega_c} \ll 1 \tag{A.2}$$

$$\frac{\rho_i}{R} \ll 1 \tag{A.3}$$

Condition (A.2) means that the motion of the particles around the magnetic field lines occurs in a time much shorter than the characteristic time of the motions along the filed lines and in the poloidal and radial directions. Condition (A.3) means that the spatial variations of the physical quantities occur in a scale larger than the Larmor radius.

A.2 Velocity of charged particle in the adiabatic limit

The motion of a charged particle is governed by the 2^{nd} Newton equation

$$m\frac{\mathrm{d}\mathbf{v}}{\mathrm{d}t} = e\left(\mathbf{E} + \mathbf{v}\times\mathbf{B}\right) \tag{A.4}$$

The velocity, electric and magnetic fields can be decomposed as

$$\left\{\begin{array}{c}\mathbf{v}\\ \mathbf{E}\\ \mathbf{B}\end{array}\right\} = \left\{\begin{array}{c}\mathbf{v}_{\mathrm{G}}\\ \mathbf{E}_{\mathrm{G}}\\ \mathbf{B}_{\mathrm{G}}\end{array}\right\} + \left\{\begin{array}{c}\tilde{\mathbf{v}}\\ \tilde{\mathbf{E}}\\ \tilde{\mathbf{B}}\end{array}\right\} \tag{A.5}$$

where $\mathbf{A}_{\mathrm{G}}$ is the average of any quantity $\mathbf{A}$ over the cyclotron motion, i.e. $\mathbf{A}_{\mathrm{G}} \equiv \langle \mathbf{A} \rangle = \oint \frac{\mathrm{d}\varphi_c}{2\pi} \mathbf{A}$. With these definitions, the equation (A.4) yields

$$\frac{\mathrm{d}\mathbf{v}_{\mathrm{G}}}{\mathrm{d}t} + \frac{\mathrm{d}\tilde{\mathbf{v}}}{\mathrm{d}t} = \frac{e}{m}\left(\mathbf{E}_{\mathrm{G}} + \tilde{\mathbf{E}} + \mathbf{v}_{\mathrm{G}} \times \mathbf{B}_{\mathrm{G}} + \mathbf{v}_{\mathrm{G}} \times \tilde{\mathbf{B}} + \tilde{\mathbf{v}} \times \mathbf{B}_{\mathrm{G}} + \tilde{\mathbf{v}} \times \tilde{\mathbf{B}}\right) \tag{A.6}$$

Averaging over φ this expression we obtain the following equations for the guiding-centre and perturbed velocities

$$\frac{\mathrm{d}\mathbf{v}_{\mathrm{G}}}{\mathrm{d}t} = \frac{e}{m}\left(\mathbf{E}_{\mathrm{G}} + \mathbf{v}_{\mathrm{G}} \times \mathbf{B}_{\mathrm{G}} + \left\langle \tilde{\mathbf{v}} \times \tilde{\mathbf{B}} \right\rangle\right) \tag{A.7}$$

$$\frac{\mathrm{d}\tilde{\mathbf{v}}}{\mathrm{d}t} = \frac{e}{m}\left(\tilde{\mathbf{E}} + \mathbf{v}_{\mathrm{G}} \times \tilde{\mathbf{B}} + \tilde{\mathbf{v}} \times \mathbf{B}_{\mathrm{G}} + \tilde{\mathbf{v}} \times \tilde{\mathbf{B}} - \left\langle \tilde{\mathbf{v}} \times \tilde{\mathbf{B}} \right\rangle\right) \tag{A.8}$$

We can now proceed as in the quasi-linear approach, where the perturbations are written up the lowest order and the second-order terms are only conserved in the equation of the equilibrium quantities. Within this approach, the last equation yields

$$\frac{\mathrm{d}\tilde{\mathbf{v}}}{\mathrm{d}t} = \frac{e}{m}\tilde{\mathbf{v}} \times \mathbf{B}_{\mathrm{G}} \tag{A.9}$$

whose solution leads to the well-known cyclotron motion

$$\tilde{\mathbf{v}} = \frac{e}{m}\boldsymbol{\rho}_c \times \mathbf{B}_{\mathrm{G}} \tag{A.10}$$

In order to determine the contribution of the second-order term in the evolution of the guiding-centre velocity, we need to calculate explicitly the expression $\left\langle \tilde{\mathbf{v}} \times \tilde{\mathbf{B}} \right\rangle$. For this purpose, we will write a Taylor expansion for the magnetic field

$$\mathbf{B} = \mathbf{B}_{\mathrm{G}} + \boldsymbol{\rho}_c \cdot \nabla \mathbf{B}|_{\mathbf{x}=\mathbf{x}_{\mathrm{G}}} + \mathcal{O}\left(\rho_c^2\right) \tag{A.11}$$

which gives

$$\left\langle \tilde{\mathbf{v}} \times \tilde{\mathbf{B}} \right\rangle \approx \frac{e}{m}\left\langle \left(\boldsymbol{\rho}_c \times \mathbf{B}_{\mathrm{G}}\right) \times \left(\boldsymbol{\rho}_c \cdot \nabla \mathbf{B}|_{\mathbf{x}=\mathbf{x}_{\mathrm{G}}}\right)\right\rangle \tag{A.12}$$

The vector products will be expressed in tensorial form as follows

$$\left\langle \tilde{\mathbf{v}} \times \tilde{\mathbf{B}} \right\rangle \cdot \mathbf{e}_i \approx \frac{e}{m}\left\langle \epsilon_{ijk}\epsilon_{jmn}\rho_m B_n \rho_p \nabla_p B_k \right\rangle \tag{A.13}$$

where the subscript G has been omitted for the sake of readiness, the Einstein notation has been used and ϵ_{ijk} is the Levi-Civita symbol (also called permutation symbol), whose expression in three dimensions reads

$$\epsilon_{ijk} = \frac{(j-i)\,(k-i)\,(k-j)}{2} \tag{A.14}$$

In particular, it is useful to use the contracted product of two Levi-Civita symbols to obtain an important relation between the permutation symbol and the Kronecker symbol

$$\epsilon_{ijk}\epsilon_{imn} = \delta_{jm}\delta_{kn} - \delta_{jn}\delta_{km} \tag{A.15}$$

Therefore, expression (A.13) reads

$$\left\langle \tilde{\mathbf{v}} \times \tilde{\mathbf{B}} \right\rangle \cdot \mathbf{e}_i \approx \frac{e}{m}\left\langle \rho_k \rho_p B_i \nabla_p B_k - \rho_i \rho_p B_k \nabla_p B_k \right\rangle \tag{A.16}$$

Expressing the Larmor radius in an orthogonal basis allows one to obtain the tensor $\langle \rho_i \rho_j \rangle$

$$\boldsymbol{\rho}_c = \rho_c \begin{pmatrix} \cos\varphi_c \\ \sin\varphi_c \\ 0 \end{pmatrix} \Rightarrow \langle \rho_i \rho_j \rangle = \frac{1}{2}\rho_c^2 \delta_{ij}^{\perp} \tag{A.17}$$

where $\delta_{ij}^{\perp}$ is the Kronecker symbol projected onto an orthogonal plane. The magnetic field is evaluated at the guiding-centre position, which means that the only dependence on φ_c comes from $\boldsymbol{\rho}_c$. Therefore, we can write

$$\left\langle \tilde{\mathbf{v}} \times \tilde{\mathbf{B}} \right\rangle \approx -\frac{e\rho_c^2}{2m} \left(\mathbf{B}\nabla_{\perp} \cdot \mathbf{B}_{\perp} - \frac{1}{2}\nabla_{\perp} B^2 \right) \tag{A.18}$$

Using the divergenceless of the magnetic field, the perpendicular divergence of the perpendicular component of $\mathbf{B}$ equals $-\nabla_{\parallel} B$ so that

$$\left\langle \tilde{\mathbf{v}} \times \tilde{\mathbf{B}} \right\rangle \approx -\frac{\mu}{e}\nabla B \tag{A.19}$$

The evolution of the guiding-centre velocity is finally governed by the equation

$$\frac{\mathrm{d}\mathbf{v}_{\mathrm{G}}}{\mathrm{d}t} = \frac{e}{m}\left(\mathbf{E}_{\mathrm{G}} + \mathbf{v}_{\mathrm{G}} \times \mathbf{B}_{\mathrm{G}}\right) - \frac{\mu}{m}\nabla B \tag{A.20}$$

The guiding-centre velocity can be decomposed into a parallel velocity and a perpendicular velocity

$$\mathbf{v}_{\mathrm{G}} = \mathbf{v}_{\mathrm{G}\parallel} + \mathbf{v}_{\mathrm{G}\perp} = \left(\mathbf{v}_{\mathrm{G}} \cdot \mathbf{b}\right)\mathbf{b} + \mathbf{v}_{\mathrm{G}\perp} \tag{A.21}$$

A.2.1 Expression of the perpendicular velocity

The equation (A.20) can be projected onto the perpendicular direction

$$\left.\frac{\mathrm{d}\mathbf{v}_{\mathrm{G}\parallel}}{\mathrm{d}t}\right|_{\perp} + \left.\frac{\mathrm{d}\mathbf{v}_{\mathrm{G}\perp}}{\mathrm{d}t}\right|_{\perp} = \frac{e}{m}\left(\mathbf{E}_{\mathrm{G}\perp} + \mathbf{v}_{\mathrm{G}\perp} \times \mathbf{B}_{\mathrm{G}}\right) - \frac{\mu}{m}\nabla_{\perp} B \tag{A.22}$$

The adiabatic limit allows one to neglect the second term of the left-hand side of the previous equation, leading to the following expression for the parallel guiding-centre velocity

$$v_{G\parallel}\frac{\mathbf{N}}{R} = \frac{e}{m}\mathbf{E}_{\mathrm{G}\perp} + \frac{e}{m}\left(\mathbf{v}_{\mathrm{G}\perp} \times \mathbf{B}\right) - \frac{\mu}{m}\nabla_{\perp} B \tag{A.23}$$

where $\mathbf{N}$ is the normal vector and R is the curvature radius. From this expression, one can obtain the perpendicular component of the guiding-centre velocity

$$\mathbf{v}_{\mathrm{G}\perp} = \frac{\mathbf{E} \times \mathbf{B}}{B^2} + \frac{m{v_{G\parallel}}^2}{eB}\frac{\mathbf{B}}{B} \times \frac{\mathbf{N}}{R} + \frac{\mu B}{eB}\frac{\mathbf{B} \times \nabla B}{B^2} \tag{A.24}$$

We can make use of the identity $\mathbf{N}/R = \mathbf{b} \cdot \nabla\mathbf{b} = \mathbf{b} \times \left(B^{-1}\nabla \times \mathbf{B} - B^{-2}\mathbf{B} \times \nabla B\right)$ to rewrite the perpendicular velocity as the sum of the electric drift velocity, the curvature velocity and the current terms

$$\mathbf{v}_{\mathrm{G}\perp} = \underbrace{\frac{\mathbf{E} \times \mathbf{B}}{B^2}}_{\mathbf{v}_E} + \underbrace{\frac{m{v_{G\parallel}}^2 + \mu B}{eB}\frac{\mathbf{B} \times \nabla B}{B^2}}_{\mathbf{v}_D} + \frac{m{v_{G\parallel}}^2}{eB^2}\nabla \times \mathbf{B}|_{\perp} \tag{A.25}$$

In the low-β limit, i.e. in the limit where the kinetic pressure is negligible compared to the magnetic pressure, the perpendicular velocity reduces to the electric drift $\mathbf{v}_E$ and the curvature drift $\mathbf{v}_D$.

A.2.2 Expression of the parallel velocity

Projecting equation (A.20) onto the parallel direction yields

$$\left.\frac{\mathrm{d}\mathbf{v}_{\mathrm{G}\parallel}}{\mathrm{d}t}\right|_{\parallel} + \left.\frac{\mathrm{d}\mathbf{v}_{\mathrm{G}\perp}}{\mathrm{d}t}\right|_{\parallel} = \frac{e}{m}\mathbf{E}_{\mathrm{G}\parallel} - \frac{\mu}{m}\nabla_{\parallel}B \tag{A.26}$$

The second term of the left-hand side reduces to

$$\left.\frac{\mathrm{d}\mathbf{v}_{\mathrm{G}\perp}}{\mathrm{d}t}\right|_{\parallel} \approx v_{G\parallel}\left(\nabla_{\parallel}\mathbf{v}_{\mathrm{G}\perp}\right)\cdot\mathbf{b} \tag{A.27}$$

where the adiabatic limit has been assumed. This expression represents the coupling between the electric drift velocity and the inhomogeneities of the magnetic field

$$v_{G\parallel}\left(\nabla_{\parallel}\mathbf{v}_{\mathrm{G}\perp}\right)\cdot\mathbf{b} = v_{G\parallel}\frac{\mathbf{E}\times\mathbf{B}}{B^2}\cdot\frac{\nabla B}{B} \tag{A.28}$$

Appendix B

Variational principles and electromagnetic Lagrangian

This appendix has been written based on the Ref. [155], which constitutes an excellent introduction to the universe of Variational Principles. For further details, the interested reader is encouraged to explore that reference. It is usual to use the words *variational principle* as a kind of "magical recipe" which will give us straightforwardly the solution we are looking for. However, strictly speaking, there is no one single variational principle (in singular), but variational principles (in plural). These are the mathematical expression of the natural convergence towards an optimal solution in any physical situation. *Mathematical expression* means that they are universal. Fermat (1601-1665) was the first who introduced the idea of optimal solution by stating that nature always takes the path it can pursue most quickly. This principle (called obviously Fermat's principle) leads naturally to the concept of least time and has been present in very recent theories like the Theory of Relativity, where the trajectory of light was calculated in the presence of gravity and a curvature following the geodesic lines was obtained. Note that the geodesic lines are the curves $\gamma : \mathcal{S} \subset \mathbb{R} \to \mathbb{S} \subset \mathbb{R}^3$ such that the distance between two fixed points a and b is minimum. Here, γ is a function of class $\mathcal{C}^1$, $\mathcal{S}$ is a segment and $\mathbb{S}$ is a surface in the three-dimensional space. The distance between a and b is defined as

$$d\left(a, b, \gamma\right) = \int_{t_a}^{t_b} \left|\gamma'\left(t\right)\right| \mathrm{d}t \tag{B.1}$$

where $\{a, b\} = \gamma\left(\{t_a, t_b\}\right)$. We see that the optimization is performed with respect to a function, i.e. the problem reduces to make the expression (B.1) minimum for any variation of γ at a and b fixed. This is the reason why an expression like (B.1) is in general called *functional* or *action*. The concept of action was introduced by Maupertuis in the principle named after him in 1744, which resulted in the principle of *Least Action*:

- Any physical system is characterized by a Lagrangian $\mathcal{L}\left(\mathbf{x}, \dot{\mathbf{x}}, t\right)$.
- For any trajectory between $\mathbf{x}_1$ and $\mathbf{x}_2$ we define the action

$$\mathcal{A} = \int_{t_1}^{t_2} \mathcal{L}\left(\mathbf{x}, \dot{\mathbf{x}}, t\right) \mathrm{d}t \tag{B.2}$$

Then, the only possible trajectory is the one for which the action is minimum. It must be stressed that the Lagrangian is not unique, since the integral of any time derivative of a

function $f(\mathbf{x}, t)$ gives

$$\int_{t_1}^{t_2} \frac{\mathrm{d}}{\mathrm{d}t} f(\mathbf{x}, t)\, \mathrm{d}t = f(\mathbf{x}(t_2), t_2) - f(\mathbf{x}(t_1), t_1)$$

and this terms remains unchanged for any variation of $\mathbf{x}$ satisfying $\delta\mathbf{x}(t_{1,2}) = 0$. Therefore, for a Lagrangian

$$\mathcal{L}' = \mathcal{L} + \frac{\mathrm{d}f}{\mathrm{d}t}$$

the equations of the motion are not modified. The most difficult point is the calculation of the Lagrangian and, in particular, the Lagrangian of a particle embedded in an electromagnetic field. This is the case of interest in this thesis. To derive the whole electromagnetic Lagrangian, we will start with the Lagrangian of a free particle in a three-dimensional space. Such a particle evolves following the Galileo's inertia principle: the motion is characterized by the invariance with respect to any (1) time translation, (2) linear space translation, (3) rotation and (4) change of Galilean system. Since the Lagrangian depends on time, space and velocity, properties (1) and (2) imply that $\mathcal{L} = \mathcal{L}(\dot{\mathbf{x}})$. Property (3) implies that the dependence on the velocity is reduced to a dependence on the modulus of the velocity. The invariance with respect to any change of Galilean system means that $\partial_{v^2}\mathcal{L} = \text{constant}$. It is convenient to choose a constant which reprensents the dynamics of a particle. Following Einstein's idea of equivalence of mass, this constant will be $m/2$. Therefore, the Lagrangian for a free particle is given by

$$\mathcal{L}_{\text{part}} = \frac{1}{2} m v^2 \tag{B.3}$$

Let us now consider many charged particles characterized by a density ρ in an electrostatic field, characterized by an electric potential ϕ. The potential energy of particles is

$$\mathcal{E}_{\text{pot}} = \int \mathrm{d}^3\mathbf{x} \rho\phi$$

and the energy of the electric field is

$$\mathcal{E}_{\text{elect}} = \frac{1}{2}\epsilon_0 \int \mathrm{d}^3\mathbf{x} |\nabla\phi|^2$$

It is obvious that the system will tend to equal both energies (note that this condition is global since it is imposed on an integral over the whole space, i.e. it is not local). Therefore, the solution ϕ makes the following action minimum

$$\mathcal{A} = \int \mathrm{d}^3\mathbf{x} \left(\frac{1}{2}\epsilon_0 |\nabla\phi|^2 - \rho\phi \right) \tag{B.4}$$

for any variation of ϕ. Note that this is equivalent to minimize the action

$$\mathcal{A} = \int \mathrm{d}^3\mathbf{x} \left(\epsilon_0 \nabla\phi \cdot \nabla\phi^\dagger - \rho\phi^\dagger \right) \tag{B.5}$$

for any variation of $\phi^\dagger$, where the symbol † means *complex conjugate*. The Least Action principle gives

$$\delta\mathcal{A} = \int \mathrm{d}^3\mathbf{x} \left(\epsilon_0 \nabla\phi \cdot \nabla\delta\phi^\dagger - \rho\delta\phi^\dagger \right) = 0 \tag{B.6}$$

Integrating by parts the first term, the variation of the action yields

$$\delta\mathcal{A} = -\int \mathrm{d}^3\mathbf{x}\left(\epsilon_0\nabla^2\phi\delta\phi^\dagger + \rho\delta\phi^\dagger\right) = 0 \tag{B.7}$$

which implies that the integrand must vanish. This condition leads to the Poisson equation, which is a local condition satisfied by the solution. Therefore, we have used a global principle to obtain a local condition, which constitutes the main advantage of the variational principles. Finally, we have identified the following Lagrangian

$$\mathcal{L} = \mathcal{L}_{\text{field}} + \mathcal{L}_{\text{int}} + \mathcal{L}_{\text{part}} \tag{B.8}$$

where

$$\mathcal{L}_{\text{field}} = \epsilon_0\nabla\phi\cdot\nabla\phi^\dagger$$
$$\mathcal{L}_{\text{int}} = -\rho\phi^\dagger$$

The last term represents the interaction between the electrostatic field and particles. Note that the minimization of the action has been performed without considering the free particles Lagrangian, since any variation of $\phi^\dagger$ gives the same form of $\mathcal{L}_{\text{part}}$. If we add now a magnetic field, we need to introduce the potential $\mathbf{A}$ such that $\mathbf{B} = \nabla\times\mathbf{A}$. As in the case of a particle embedded in an electrostatic field, we will look for a Lagrangian that will be decomposed as (B.8). Let us recall that a scalar product is an invariant with respect to any Lorentz transformation. If we are interested in any Lorentz-invariant Lagrangian, one possible choice is to impose that $\mathcal{L}_{\text{int}}$ is written as the scalar product of the two quadrivectors $(\phi^\dagger/c, \mathbf{A}^\dagger)$ and $(c\mathrm{d}t, d\mathbf{x})$

$$\mathcal{L}_{\text{int}} = \mathbf{j}\cdot\mathbf{A}^\dagger - \rho\phi^\dagger \tag{B.9}$$

which leads to total Lagrangian of a non relativistic particle embedded in an electromagnetic field

$$\mathcal{L} = \frac{1}{2}mv^2 + \epsilon_0\mathbf{E}\cdot\mathbf{E}^\dagger + \frac{1}{\mu_0}\mathbf{B}\cdot\mathbf{B}^\dagger + \mathbf{j}\cdot\mathbf{A}^\dagger - \rho\phi^\dagger \tag{B.10}$$

Appendix C

Numerical implementation of the Fokker-Planck equation in AQL

The second-order differential equation 2.48 will be solved by using a finite central difference method. The functions $F_{h,m}^{(k+1)}(u)$ and $\alpha_{h,m,n}^{(k,l)}(u)$ will be written in the form

$$F_{h,m}^{(k+1)}(u) \to F_{h,m}^{(k+1)}(u_p) \tag{C.1}$$

$$\alpha_{h,m,n}^{(k,l)}(u) \to \alpha_{h,m,n}^{(k,l)}(u_p) \tag{C.2}$$

and the derivatives of $F_{h,m}^{(k+1)}$ approached by second-order differences. The system 2.48 has the form

$$\begin{aligned}\frac{F_{h,m}^{(k+1)}(u_p) - F_{h,m}^{(k)}(u_p)}{\Delta t} = \\ \alpha_{h,m,n}^{(k,2)}(u_p)\frac{F_{h,m}^{(k+1)}(u_{p+1}) - 2F_{h,m}^{(k+1)}(u_p) + F_{h,m}^{(k+1)}(u_{p-1})}{\Delta u^2} + \\ \alpha_{h,m,n}^{(k,1)}(u_p)\frac{F_{h,m}^{(k+1)}(u_{p+1}) - F_{h,m}^{(k+1)}(u_{p-1})}{2\Delta u} + \\ \alpha_{h,m,n}^{(k,0)}(u_p)F_{h,m}^{(k+1)}(u_p)\end{aligned} \tag{C.3}$$

If we rearrange the terms of this expression, we may rewrite

$$\begin{aligned}\left(\frac{\alpha_{h,m,n}^{(k,1)}(u_p)}{2\Delta u} - \frac{\alpha_{h,m,n}^{(k,2)}(u_p)}{\Delta u^2}\right) F_{h,m}^{(k+1)}(u_{p-1}) \\ + \left(\frac{1}{\Delta t} - \alpha_{h,m,n}^{(k,0)}(u_p) + \frac{2\alpha_{h,m,n}^{(k,2)}(u_p)}{\Delta u^2}\right) F_{h,m}^{(k+1)}(u_p) \\ - \left(\frac{\alpha_{h,m,n}^{(k,2)}(u_p)}{\Delta u^2} + \frac{\alpha_{h,m,n}^{(k,1)}(u_p)}{2\Delta u}\right) F_{h,m}^{(k+1)}(u_{p+1}) = \frac{F_{h,m}^{(k)}(u_p)}{\Delta t}\end{aligned} \tag{C.4}$$

with $n = 0, \ldots, L$ and $p = 0, \ldots, N$. This system has $(L+1)(N+3)$ unknowns and only $(L+1)(N+1)$ equations. Therefore, we need to include $2(L+1)$ equations from the boundary conditions, leading to the system

$$\left(\mathbf{I} - \Delta t^{-1}\mathbf{M}^{(k)}\right) \cdot \mathbf{F}^{(k+1)} = \mathbf{F}^{(k)} \tag{C.5}$$

where

$$\mathbf{M}^{(k)} = \left\{\mathbf{M}^{(k)}_{\alpha,\beta}\right\}, \quad \mathbf{F}^{(k+1)} = \begin{pmatrix} F^{(k+1)}_{h,0}(u_0) \\ \vdots \\ F^{(k+1)}_{h,0}(u_N) \\ F^{(k+1)}_{h,1}(u_0) \\ \vdots \\ F^{(k+1)}_{h,1}(u_N) \\ \vdots \\ F^{(k+1)}_{h,L-1}(u_0) \\ \vdots \\ F^{(k+1)}_{h,L-1}(u_N) \end{pmatrix}$$

The matrix $\mathbf{M}^{(k)}$ is composed of L^2 tridiagonal submatrices representing the coupling between the the Legendre polynomials. This is schematically represented as follows (for three Legendre polynomials)

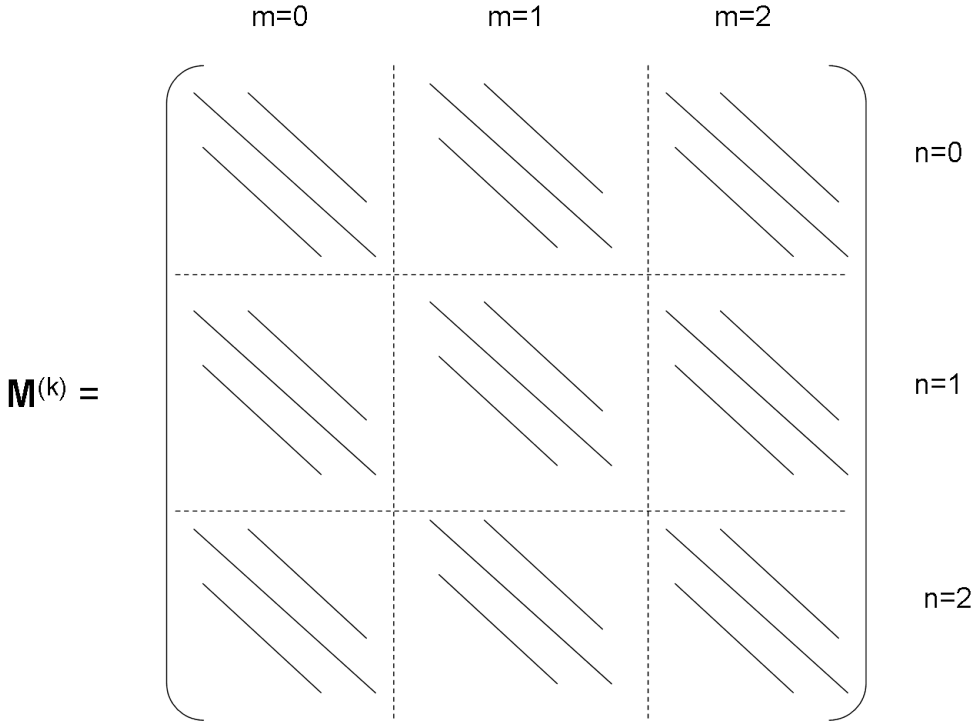

Appendix D

Formalism of action-angle variables

The motion of a charged particle in an electromagnetic field can be described by the Newton equation as shown in appendix A. When coupling this law to the Maxwell's equations, one can find a more powerful tool, consisting of the least action principle, as explained in appendix B. However, this principle as introduced by Lagrange differs from the one detailed in appendix B. The actual form of the principle has been derived by Hamilton in 1834 and is embedded in a more general framework leading to the expression of the physical laws, namely the canonical formulation of analytical mechanics.

D.1 Canonical variables system and Hamilton equations

Let us consider a physical system for which the existence of the Lagrangian $\mathcal{L}\left(\{x_i\},\{\dot{x}_i\},t\right)$ will be assumed (for a charged particle embedded in an electromagnetic field we have already shown in appendix B the form of such Lagrangian). We define the canonical momentum p_i as

$$p_i = \frac{\partial \mathcal{L}}{\partial \dot{x}_i} \tag{D.1}$$

whose time evolution is given by the Euler-Lagrange equation

$$\dot{p}_i = \frac{\partial \mathcal{L}}{\partial x_i} \tag{D.2}$$

The idea is to describe the evolution of a system with the variables $\{x_i\}$ and $\{p_i\}$ that will be called generalized coordinates and generalized momenta respectively instead of $\{x_i\}$ and $\{\dot{x}_i\}$. The interest will be highlighted when discussing the canonical transformations. Let us for the moment define a function called *Hamiltonian* by means of the Legendre transformation on the Lagrangian

$$\mathcal{H} = p_i\dot{x}_i - \mathcal{L} \tag{D.3}$$

It is obvious that the linear application (usually called total differential) $\mathrm{d}\mathcal{H} = p_i\mathrm{d}x_i + \dot{x}_i\mathrm{d}p_i - \{\mathrm{d}x_i\partial_{x_i} + \mathrm{d}\dot{x}_i\partial_{\dot{x}_i} + \mathrm{d}t\partial_t\}\,\mathcal{L}$ can be reduced, by using (D.1) and (D.2), to the following expression

$$\mathrm{d}\mathcal{H} = -\dot{p}_i\mathrm{d}x_i + \dot{x}_i\mathrm{d}p_i - \mathrm{d}t\partial_t\mathcal{L} \tag{D.4}$$

which leads to Hamilton equations

$$\dot{x}_i = \frac{\partial \mathcal{H}}{\partial p_i} \tag{D.5}$$

$$\dot{p}_i = -\frac{\partial \mathcal{H}}{\partial x_i} \tag{D.6}$$

These equations are symmetric with respect to any interchange of variables $x_i \leftrightarrow p_i$ and $\dot{x}_i \leftrightarrow \dot{p}_i$ (up to a change of sign). Note in particular that the Hamiltonian will remain constant if the Lagrangian does not depend explicitly on time.

D.2 Poisson brackets and total time derivative

If the existence of these generalized postions and momenta is proved, one can define the Poisson brackets of two quantities A and B as

$$[A, B] = \frac{\partial A}{\partial x_i}\frac{\partial B}{\partial p_i} - \frac{\partial A}{\partial p_i}\frac{\partial B}{\partial x_i} \tag{D.7}$$

If a function F depends on x_i, p_i and t, then its time derivative is expressed in terms of the Poisson bracket as follows

$$\frac{\mathrm{d}F}{\mathrm{d}t} = \frac{\partial F}{\partial t} - [\mathcal{H}, F] \tag{D.8}$$

This formulation reveals elegant and powerful since the evolution of the system is only governed by one single quantity, namely the Hamiltonian of the system. However, the guiding-centre coordinates are not generalized coordinates in the sense that they do not satisfy the Hamilton equations. Therefore, the guiding-centre description detailed in appendix A does not provide any canonicity and canonical transformations are needed to expressed the motion of a charged particle with such a powerful formulation.

D.3 Canonical transformations

As seen before, if we exchange the coordinates $\{x_i\} \leftrightarrow \{p_i\}$, the form of the Hamilton equations remain unchaged. This change of variables belong to a more general kind of change of variable that keep the motion equations invariant. These are called *canonical transformations*. A canonical transformation is defined as

$$X_i\left(\{x_i\}, \{p_i\}, t\right), P_i\left(\{x_i\}, \{p_i\}, t\right) \tag{D.9}$$

so that together with the new Hamiltonian H' written as

$$H'\left(\{X_i\}, \{P_i\}, t\right) \tag{D.10}$$

satisfies the equations

$$\dot{X}_i = \frac{\partial H'}{\partial P_i}, \dot{P}_i = -\frac{\partial H'}{\partial X_i} \tag{D.11}$$

Owing to the quasi-periodicity of the motion of a particle in a tokamak, one can find canonical transformations leading to generalized positions and momenta. The generalized positions will be the three angles $\boldsymbol{\alpha}$ characterizing the quasi-periodic motion of the

particle in the tokamak and the generalized momenta will consist of the three actions $\mathbf{J}$, or motion invariants at the equilibrium. An extensive derivation of this set of variables can be found in Refs. [156, 96] and we give hereafter some elements of this derivation. They can be obtained from the expression of the Lagrangian of the guiding-centre following [157]

$$\mathrm{d}\mathcal{L}_{gc} = P_\theta \mathrm{d}\theta + P_\varphi \mathrm{d}\varphi + P_{\varphi_c}\mathrm{d}\varphi_c - \mathcal{H}_0 \mathrm{d}t \tag{D.12}$$

where

$$P_\theta = \frac{m v_\parallel B_\theta}{B_0} + e\Phi \tag{D.13}$$

$$P_\varphi = \frac{m v_\parallel I}{B_0} + e\psi \tag{D.14}$$

$$P_{\varphi_c} = \frac{m}{e}\mu \tag{D.15}$$

Here we have used the coordinates $(\psi, \theta, \varphi, \varphi_c)$, i.e. the poloidal magnetic flux, the poloidal angle, the toroidal angle and the gyrophase respectively. The magnetic field $\mathbf{B}_0$ is considered axisymmetric $\mathbf{B}_{\mathrm{eq}} = \boldsymbol{\nabla}\psi \times \boldsymbol{\nabla}\varphi + I\boldsymbol{\nabla}\varphi$, with the flux label $I = R^2\mathbf{B}_{\mathrm{eq}} \cdot \boldsymbol{\nabla}\varphi$. In the adiabatic limit, the magnetic momentum is an invariant. Therefore, P_{φ_c} is one of the invariants, called J_1, and the associated angle $\alpha_1 = \varphi_c$. In axisymmtric systems, the Lagrangian does not depend on φ. Thus, P_φ is another invariant, that will be called J_3, with the associated angle $\alpha_3 = \varphi$. Taking into account that P_θ depends only on θ, $\mathcal{H}_0$, P_{φ_c} and P_φ, one can make use of the Poincare-Helmholtz invariant to define J_2

$$J_2 = \frac{1}{2\pi}\oint \mathrm{d}\theta P_\theta \tag{D.16}$$

Using the generating function $\mathcal{G} = \varphi_c J_1 + \varphi J_3 + \int_0^\theta \mathrm{d}\tilde{\theta} P_\theta$, the new coordinates satisfy

$$P_{\varphi_c} = \partial_{\varphi_c}\mathcal{G} = J_1 \quad P_\theta = \partial_\theta \mathcal{G} \quad P_\varphi = \partial_\varphi \mathcal{G} = J_3 \tag{D.17}$$

$$\boldsymbol{\alpha} = \partial_{\mathbf{J}}\mathcal{G} \tag{D.18}$$

which means that $(\boldsymbol{\alpha}, \mathbf{J})$ represents a set of action-angle coordinates. It can be shown that the angle associated to J_2 is

$$\alpha_2 = 2\pi \left(\oint \frac{\mathrm{d}\theta}{\dot{\theta}}\right)^{-1} \int_0^\theta \frac{\mathrm{d}\theta}{\dot{\theta}} \tag{D.19}$$

The coordinates (α_2, J_2) are associated to the bounce motion of the particles, characterized by the bounce frequency

$$\Omega_b \equiv \Omega_2 = 2\pi \left(\oint \frac{\mathrm{d}\theta}{\dot{\theta}}\right)^{-1} \tag{D.20}$$

and (α_3, J_3) are associated to the toroidal drift motion, characterized by the drift frequency

$$\Omega_3 = \Omega_b \oint \frac{\mathrm{d}\theta}{2\pi}\frac{\dot{\varphi}}{\dot{\theta}} \tag{D.21}$$

The time evolution of the poloidal angle is approximately given by the parallel velocity. Therefore, one can write

$$\Omega_2 = 2\pi \left(\oint \frac{\mathrm{d}\theta}{\mathbf{b}\cdot\boldsymbol{\nabla}\theta} v_\parallel\right)^{-1} \tag{D.22}$$

and considering that $\dot{\varphi} - q\dot{\theta} \approx \mathrm{d}_\psi q\psi\dot{\theta} + \mathbf{v}_\perp \cdot \boldsymbol{\nabla}(\varphi - q\theta)$ one obtains

$$\Omega_3 \approx q\Omega_b\delta_{\text{passing}} + \Omega_b \oint \frac{\mathrm{d}\theta}{2\pi\dot{\theta}} \left(-\mathrm{d}_\psi q\dot{\psi}\theta + \mathbf{v}_\perp \cdot \boldsymbol{\nabla}(\varphi - q\theta)\right) \tag{D.23}$$

These angle-action coordinates allow one to described the unperturbed motion of a charged particle embedded in an electromagnetic field by means of the Hamilton equations

$$\dot{\boldsymbol{\alpha}} = \frac{\partial \mathcal{H}_0}{\partial \mathbf{J}} \tag{D.24}$$

$$\dot{\mathbf{J}} = -\frac{\partial \mathcal{H}_0}{\partial \boldsymbol{\alpha}} = 0 \tag{D.25}$$

and the Vlasov equation in the form D.8. This formulation reveals extremely powerful and will be used throughout this thesis and the explicit expression for the frequencies and generalized momenta will be used whenever necessary.

Appendix E

Non adiabatic part of the perturbed distribution function

The gyrokinetic equation can be written as follows

$$\frac{dF}{dt} = \partial_t F - [\mathcal{H}, F] = 0 \tag{E.1}$$

where F and $\mathcal{H}$ are expressed in terms of the equilibrium and a perturbation

$$F\left(\mu, \mathcal{H}, P_\varphi, \alpha_2, \alpha_3\right) = F_{\mathrm{eq}}\left(\mu, \mathcal{H}, P_\varphi\right) + F_{\mathrm{eq}}\left(\mu, \mathcal{H}_{\mathrm{eq}}, P_\varphi\right) G \tag{E.2}$$

$$H = H_{\mathrm{eq}} + \delta H \tag{E.3}$$

Here we have made the assumption that the dependence of the distribution function on the motion invariants reduces to the dependence on μ, $\mathcal{H}$ and P_φ. The function G is called the non adiabatic part of the perturbed distribution function and contains the dependence of F on α_2 and α_3. A Taylor expansion gives

$$F_{\mathrm{eq}}\left(\mu, \mathcal{H}, P_\varphi\right) = F_{\mathrm{eq}}\left(\mu, \mathcal{H}_{\mathrm{eq}}, P_\varphi\right) + \delta\mathcal{H}\partial_{\mathcal{H}} F_{\mathrm{eq}}|_{\mathcal{H}=\mathcal{H}_{\mathrm{eq}}} \tag{E.4}$$

Thus

$$F\left(\mu, \mathcal{H}, P_\varphi\right) = F_{\mathrm{eq}} + \delta\mathcal{H}\partial_{\mathcal{H}} F_{\mathrm{eq}} + F_{\mathrm{eq}} G \tag{E.5}$$

where

$$F_{\mathrm{eq}} \equiv F_{\mathrm{eq}}\left(\mu, \mathcal{H}_{\mathrm{eq}}, P_\varphi\right)$$

$$\partial_{\mathcal{H}} F_{\mathrm{eq}} \equiv \partial_{\mathcal{H}} F_{\mathrm{eq}}|_{\mathcal{H}=\mathcal{H}_{\mathrm{eq}}}$$

The linearized gyrokinetic equation reads

$$\partial_{\mathcal{H}} F_{\mathrm{eq}} \partial_t \delta\mathcal{H} + F_{\mathrm{eq}} \partial_t G - [\mathcal{H}_{\mathrm{eq}}, G]\, F_{\mathrm{eq}} - [\mathcal{H}_{\mathrm{eq}}, \delta\mathcal{H}]\, \partial_{\mathcal{H}} F_{\mathrm{eq}} - [\delta\mathcal{H}, F_{\mathrm{eq}}] = 0 \tag{E.6}$$

The Poisson bracket can be written in terms of angle-action variables to simplify the previous expression

$$\begin{aligned} [\mathcal{H}_{\mathrm{eq}}, \delta\mathcal{H}]\, \partial_{\mathcal{H}} F_{\mathrm{eq}} + [\delta\mathcal{H}, F_{\mathrm{eq}}] = & \quad -\boldsymbol{\Omega} \cdot \partial_{\boldsymbol{\alpha}} \delta\mathcal{H} \partial_{\mathcal{H}} F_{\mathrm{eq}} + \partial_{\boldsymbol{\alpha}} \cdot \delta\mathcal{H} \partial_{\mathbf{J}} F_{\mathrm{eq}} \\ = & \quad -\boldsymbol{\Omega} \cdot \partial_{\boldsymbol{\alpha}} \delta\mathcal{H} \partial_{\mathcal{H}} F_{\mathrm{eq}} + \boldsymbol{\Omega} \cdot \partial_{\boldsymbol{\alpha}} \delta\mathcal{H} \partial_{\mathcal{H}} F_{\mathrm{eq}}|_{J_1, J_3} + \\ & \quad \partial_{\boldsymbol{\alpha}} \delta\mathcal{H} \cdot \partial_{\mathbf{J}^\star} F_{\mathrm{eq}}|_{\mathcal{H}} \\ = & \quad \partial_{\alpha_1} \delta\mathcal{H} \partial_{J_1} F_{\mathrm{eq}} + \partial_{\alpha_3} \delta\mathcal{H} \partial_{J_3} F_{\mathrm{eq}} \end{aligned} \tag{E.7}$$

where $\mathbf{J}^\star = (J_1, J_3)$. Since in the electrostatic limit $\delta\mathcal{H} = eJ_0 \cdot \phi$. In addition, in the framework of the gyrokinetic theory, $\partial_{\alpha_1}\delta\mathcal{H} = 0$. Owing to the equivalence between α_3 and φ, $\partial_{\alpha_3} \equiv \partial_\varphi$. The Vlasov equation satisfied by the non adiabatic part G can finally be written as follows

$$\partial_t G - [\mathcal{H}_{\text{eq}}, G] = -T_i \partial_{\mathcal{H}} \log F_{\text{eq}} \partial_t J_0 \cdot \phi + \partial_\varphi J_0 \cdot \phi T_i \partial_{P_\varphi} \log F_{\text{eq}} \tag{E.8}$$

where the electric potential is normalized to T_i/e, T_i being an equilibrium ion temperature. The last term, on the right-hand side accounts for spatial inhomogeneities of F_{eq}, the so-called diamagnetic effects. With these notations, the distribution function is expressed under the form

$$F = F_{\text{eq}} \left(1 + T_i \partial_{\mathcal{H}} \log F_{\text{eq}} J_0 \cdot \phi + G\right) \equiv F_{\text{eq}} + \delta F \tag{E.9}$$

The action-angle variables description reveals useful to derive the expression of the non adiabatic part of the perturbed distribution function. This can be done by projecting the solution onto a Fourier basis as follows

$$\left\{ \begin{array}{c} G \\ \phi \end{array} \right\} = \sum_{\mathbf{n},\omega} \left\{ \begin{array}{c} G_{\mathbf{n},\omega} \\ \phi_{\mathbf{n},\omega} \end{array} \right\} \mathrm{e}^{i(\mathbf{n}\cdot\alpha - \omega t)} \tag{E.10}$$

Equation (E.8) reads

$$-i\omega G_{\mathbf{n},\omega} + i\mathbf{n}\cdot\mathbf{\Omega} G_{\mathbf{n},\omega} = i\omega T_i \partial_{\mathcal{H}} \log F_{\text{eq}} J_0 \cdot \phi_{\mathbf{n},\omega} + in_3 J_0 \cdot \phi_{\mathbf{n},\omega} T_i \partial_{P_\varphi} \log F_{\text{eq}} \tag{E.11}$$

Therefore, the solution $G_{\mathbf{n},\omega}$ is written as follows

$$G_{\mathbf{n},\omega} = -T_i \frac{\omega \partial_{\mathcal{H}} \log F_{\text{eq}} + n_3 \partial_{P_\varphi} \log F_{\text{eq}}}{\omega - \mathbf{n}\cdot\mathbf{\Omega}} J_0 \cdot \phi_{\mathbf{n},\omega} \tag{E.12}$$

Note that in a rigorous way, $(J_0 \cdot \phi)_{\mathbf{n},\omega} \neq J_0 \cdot \phi_{\mathbf{n},\omega}$, due to the dependence of J_0 on the magnetic field. However, the correction introduced would be of second order on ε. Note also that the diamagnetic effects appear here only due to the dependence on P_φ. This comes from a very particular choice of distribution function, where the radial dependence is given only by the toroidal momentum. In general the equilibrium distribution function depends on three motion invariants. Owing to the existence of the angle-action variables, the most general case is $F_{\text{eq}} = F_{\text{eq}}(J_1, J_2, J_3)$. However, one can replace one of the three actions by a motion invariant $\mathcal{A} = \mathcal{A}(J_1, J_2, J_3)$. So far, we have decided to replace J_2 by the unperturbed Hamiltonian $\mathcal{H}_{\text{eq}}$, leading to diamagnetic effects of the form $\partial_{P_\varphi} F_{\text{eq}}$. This description is valid if the parallel velocity of the particles remains small, i.e. if J_3 is close to a radial coordinate. Indeed, for small $\rho_\star$ and in the limit $\varepsilon \ll 1$, the second action can be approximated by $J_2 \approx e\Phi_T(\psi/e)$ [158]. Therefore, for small $v_\parallel$, both J_2 and J_3 describe the radial dependence of F_{eq} and the choice $F_{\text{eq}} = F_{\text{eq}}(\mu, \mathcal{H}, P_\varphi)$ is legitimate. If the parallel velocity becomes comparable to $e\psi/mR$, a more accurate description is $F_{\text{eq}} = F_{\text{eq}}(\mathcal{H}, J_2, P_\varphi)$. In that case, equation E.8 is generalized as follows

$$\partial_t G - [\mathcal{H}_{\text{eq}}, G] = -T_i \partial_{\mathcal{H}} \log F_{\text{eq}} \partial_t J_0 \cdot \phi - \frac{1}{eq} \partial_\theta J_0 \cdot \phi T_i \partial_\psi \log F_{\text{eq}} + \partial_\varphi J_0 \cdot \phi T_i \partial_{P_\varphi} \log F_{\text{eq}} \tag{E.13}$$

where we have made use of the equivalence $\alpha_2 \equiv \theta$. The non adiabatic part of the perturbed distribution function finally reads

$$G_{\mathbf{n},\omega} = -T_i \frac{\omega \partial_{\mathcal{H}} \log F_{\rm eq} - n_2 e^{-1} q^{-1} \partial_\psi \log F_{\rm eq} + n_3 \partial_{P_\varphi} \log F_{\rm eq}}{\omega - \mathbf{n} \cdot \mathbf{\Omega}} J_0 \cdot \phi_{\mathbf{n},\omega} \tag{E.14}$$

which means that even for axisymmetric modes ($n_3 = 0$), diamagnetic effects can play a role due to the poloidal structure of the electrostatic potential.

Appendix F

Additional comments on the kinetic effects of a source

We analyse in this appendix two effects that must be considered when using a source term on the right-hand side of the gyrokinetic equation: (1) the modification of the marginal stability of ITG modes due to an anisotropic heating and (2) the possible modification of the radial electric field.

F.1 Analysis of the effect of the anisotropy of the distribution function on the marginal stability of ITG modes

We now assume that the equilibrium distribution function is given by

$$F_{\mathrm{eq}} = \frac{n_i}{\left(2\pi T_i/m\right)^{3/2}} \mathrm{e}^{-\mathcal{E}} \mathrm{e}^{-\beta u} \tag{F.1}$$

with $n_i = n_i\left(P_\varphi\right)$, $T_i^{3/2} = T_\parallel^{1/2} T_\perp$, $T_\parallel = T_\parallel\left(P_\varphi\right)$, $T_\perp = T_\perp\left(P_\varphi\right)$, $\beta = \frac{T_\parallel}{T_\perp} - 1$, $u = \frac{\mu B}{T_\parallel}$ and $\mathcal{E} = \frac{E}{T_\parallel}$. The β parameter contains the degree of anisotropy of the distribution function. In particular, if $\beta = 0$, we recover the isotropic case. With this anisotropic distribution of thermal ions and neglecting the gradients of the magnetic field, the diamagnetic frequency is generalized as follows

$$\Omega_{dT}^{-1} \partial_{P_\varphi} F_{\mathrm{eq}} = \left[\Omega_n^* + \left(\mathcal{E} - \frac{1}{2}\right)\Omega_{T_\parallel}^* + \left(\beta u - 1\right)\Omega_{T_\perp}^* + u\left(\Omega_{T_\perp}^* - \Omega_{T_\parallel}^*\right)\right] F_{\mathrm{eq}} \tag{F.2}$$

where $\Omega_n^* = \Omega_{dT}^{-1} \frac{1}{n_i} \frac{\mathrm{d}n_i}{P_\varphi}$, $\Omega_{T_\parallel}^* = \Omega_{dT}^{-1} \frac{1}{T_\parallel} \frac{\mathrm{d}T_\parallel}{P_\varphi}$ and $\Omega_{T_\perp}^* = \Omega_{dT}^{-1} \frac{1}{T_\perp} \frac{\mathrm{d}T_\perp}{P_\varphi}$. Note that the derivative with respect to P_φ of a quantity decreasing with the minor radius is positive. Therefore, for profiles decreasing with the minor radius we have Ω_n^*, $\Omega_{T_\parallel}^*$, $\Omega_{T_\perp}^* > 0$. The integral is performed with respect to the energy and the adiabatic invariant in order to conveniently analyse the resonance. Therefore, the integral in velocity space is transformed as follows

$$\int \cdots \mathrm{d}^3\mathbf{v} = T_\parallel^{3/2} \frac{4\pi}{m^2} \sqrt{\frac{m}{2}} \int_0^\infty \mathrm{d}\mathcal{E} \int_0^{\mathcal{E}} \cdots \frac{\mathrm{d}u}{\sqrt{\mathcal{E} - u}}$$

where we have assumed that everything inside the integral is even in $v_\parallel$.

The fluid limit can be obtained by Taylor-expanding the denominator up to the second order in E/E_ω. The dispersion relation reads (with $\tau = 1$ and $n_{\mathrm{eq}} = n_i$)

$$\mathcal{L}\left(\mathcal{E}_\omega\right) \approx \tilde{\mathcal{L}}\left(\mathcal{E}_\omega\right) = \mathcal{E}_\omega^2 + A_1 \mathcal{E}_\omega + A_0 = 0 \tag{F.3}$$

where

$$A_1 = \left[\Omega_n^\star - \frac{1}{2}\Omega_{T_\parallel}^\star - \Omega_{T_\perp}^\star + \left(\Omega_{T_\parallel}^\star - 1\right)\left\langle \mathcal{E}\right\rangle + \tilde{\beta}\left\langle u\right\rangle\right]\frac{T_i}{T_\parallel} \tag{F.4a}$$

$$A_0 = \left[\left(\Omega_n^\star - \frac{1}{2}\Omega_{T_\parallel}^\star - \Omega_{T_\perp}^\star\right)\left\langle \mathcal{E}\right\rangle + \left(\Omega_{T_\parallel}^\star - 1\right)\left\langle \mathcal{E}^2\right\rangle + \tilde{\beta}\left\langle u\mathcal{E}\right\rangle\right]\frac{T_i}{T_\parallel} \tag{F.4b}$$

and

$$\left\langle \mathcal{E}\right\rangle = \frac{2}{\sqrt{\pi}}\left(\frac{T_\parallel}{T_i}\right)^{3/2}\int_{\mathbb{R}} x^3 g_1\left(x\right)\mathrm{e}^{-x^2}\mathrm{d}x \tag{F.5}$$

$$\left\langle \mathcal{E}^2\right\rangle = \frac{2}{\sqrt{\pi}}\left(\frac{T_\parallel}{T_i}\right)^{3/2}\int_{\mathbb{R}} x^5 g_1\left(x\right)\mathrm{e}^{-x^2}\mathrm{d}x \tag{F.6}$$

$$\left\langle u\right\rangle = \frac{2}{\sqrt{\pi}}\left(\frac{T_\parallel}{T_i}\right)^{3/2}\int_{\mathbb{R}} x g_2\left(x\right)\mathrm{e}^{-x^2}\mathrm{d}x \tag{F.7}$$

$$\left\langle u\mathcal{E}\right\rangle = \frac{2}{\sqrt{\pi}}\left(\frac{T_\parallel}{T_i}\right)^{3/2}\int_{\mathbb{R}} x^3 g_2\left(x\right)\mathrm{e}^{-x^2}\mathrm{d}x \tag{F.8}$$

where we have introduced the functions

$$g_1\left(x\right) = \int_0^x \mathrm{e}^{-\beta\left(x^2-y^2\right)}\mathrm{d}y \tag{F.9a}$$

$$g_2\left(x\right) = \int_0^x \left(x^2-y^2\right)\mathrm{e}^{-\beta\left(x^2-y^2\right)}\mathrm{d}y \tag{F.9b}$$

and the parameter

$$\tilde{\beta} = \beta\Omega_{T_\perp}^* + \Omega_{T_\perp}^* - \Omega_{T_\parallel}^* \tag{F.10}$$

The marginal stability curve is obtained by assuming that the imaginary part of ω is small compared to the real part, i.e. $\Im\left(\omega\right) \ll \Re\left(\omega\right)$, and Taylor-expanding the expression F.3 up to the first order in $\Im\left(\omega\right)$. The dispersion relation is then solved by imposing $\tilde{\mathcal{L}} = 0$ and $\partial_{\mathcal{E}_\omega}\tilde{\mathcal{L}} = 0$, i.e.

$$A_1^2 = 4A_0 \tag{F.11}$$

Solving this dispersion relation when the distribution function is anisotropic ($\beta \neq 0$, $\tilde{\beta} \neq 0$) leads to a rather complicated nonlinear system. However, one can simplify the problem by considering a marginally stable reference situation where the distribution function is isotropic. In this case, we obtain the fluid dispersion relation

$$\mathcal{E}_\omega^2 + \left(\Omega_n^\star - \frac{3}{2}\right)\mathcal{E}_\omega + \frac{3}{2}\left(\Omega_n^\star + \Omega_T^\star - \frac{5}{2}\right) = 0 \tag{F.12}$$

and the stability curve is given by

$$\Omega_T^\star = \frac{5}{2} - \Omega_n^\star + \frac{1}{6}\left(\Omega_n^\star - \frac{3}{2}\right)^2 \tag{F.13}$$

From that situation, we can introduce a modification in the temperature of the system to create an anisotropy. We analyse in the following three types of modification: (i) parallel heating, (ii) perpendicular heating or (iii) vorticity injection without net heating. The effect of the vorticity injection without net heating on the parallel and perpendicular temperatures can be interpreted as an exchange of energy between parallel and perpendicular motions. These three modifications are expressed as follows

$$T_\parallel = T + \epsilon_\parallel \delta T, \quad T_\perp = T + \epsilon_\perp \delta T \tag{F.14}$$

with $(\epsilon_\parallel, \epsilon_\perp) = (1, 0)$ and $\delta T > 0$ for parallel heating, $(\epsilon_\parallel, \epsilon_\perp) = (0, 1)$ and $\delta T > 0$ for perpendicular heating, $(\epsilon_\parallel, \epsilon_\perp) = (1, -1)$ and $|\delta T| < T$ for vorticity injection without net heating. This modification allows one to address two issues: (1) the possibility to excite or destabilize ITG modes when the system lives out of the marginality and (2) the existence of a marginally stable anisotropic solution. The dispersion relation F.3 is solved for the three aforementioned situations. The curve of marginal stability in the hydrodynamic limit is plotted in figure F.1. The space (δT, $\partial_r \delta T$) is divided into a region where ITG modes are stable and a region where they are unstable. In addition, the localization of these two regions in the plane (δT, $\partial_r \delta T$) depends on the heating scheme. If a parallel heating is applied to a marginally stable isotropic state while keeping the perpendicular temperature constant, the region where the difference $T_\parallel - T_\perp$ increases (resp. decreases) with the minor radius becomes stable (resp. unstable). If a perpendicular heating is applied instead, the situation can be inverted. An intermediate situation is obtained when a parallel heating is accompanied by a perpendicular cooling with no net injection of energy. Therefore, by conveniently choosing the heating scheme we can bring the system towards a situation where ITG modes are unstable in a radial region and stable elsewhere.

F.2 Modification of the radial electric field

A side effect that we have observed in the neoclassical simulations presented in chapter 3 is the modification of the mean radial electric field when using the energetic particle source. Figure F.2a shows the time evolution of the shear of the radial electric field for the simulations NC3 (solid black line) and without energetic particles (dashed blue line). It can be observed that the shear in the presence of energetic particles is increased, even before the excitation of EGAMs. This means that the modification of the radial electric field is due to the effect of the source, probably related to the modification of the particle orbits. Figure F.2a shows the radial profiles of the electric field averaged over two different time windows of the simulation, highlighted by vertical lines in figure F.2b. This large electric shear might provide additional damping, as invoked in [64]. In the modification of the radial electric field by the source is attributed to the modification of the particle orbits, it is expected that this effect plays a minor role for low $\rho_\star$ simulations.

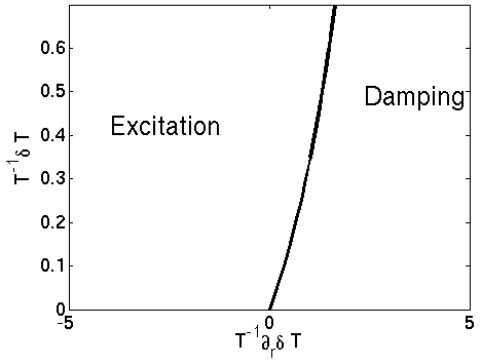

(a)

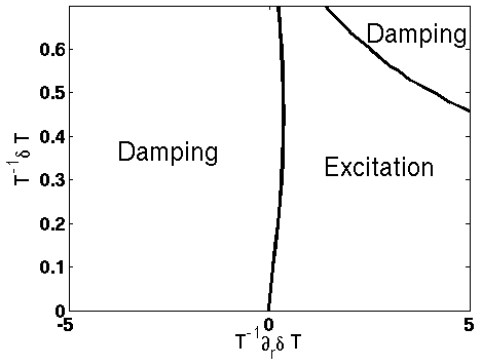

(b)

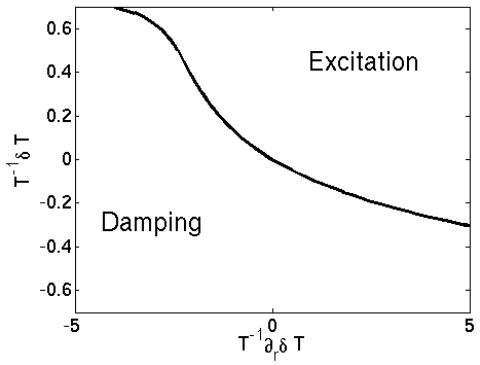

(c)

Figure F.1: Marginal stability curves in the hydrodynamic limit for (top) parallel heating, (middle) perpendicular heating and (bottom) energy exchange between parallel and perpendicular motions.

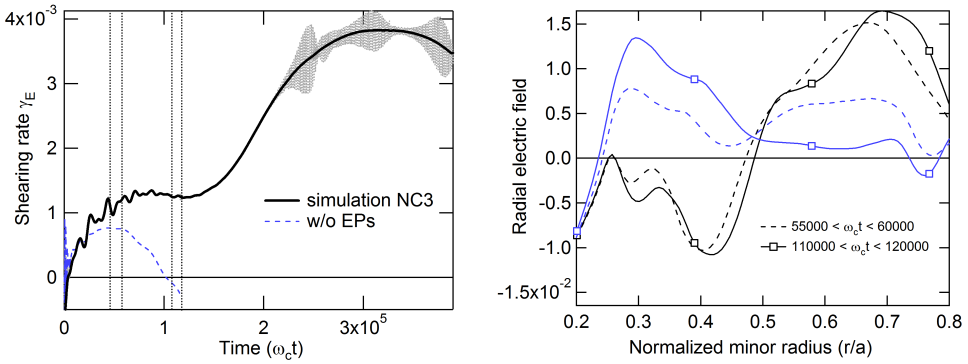

Figure F.2: (Left) Time evolution of the radial electric shear at the mid radial position. (Right) Radial profiles of the radial electric field for different instants of the simulations.

Bibliography

[1] R.D. Hazeltine and J.D. Meiss. *Plasma confinement*. Dover Pubns, 2003.

[2] J.M. Rax. Physique des plasmas: cours et applications (coll. sciences sup). *Recherche*, 67:02, 2005.

[3] K. Miyamoto. *Plasma physics and controlled nuclear fusion*, volume 38. Springer Verlag, 2005.

[4] J.M. Rax. *Physique des Tokamaks*. Ecole Polytechnique, 2011.

[5] J. Wesson. *Tokamaks*, volume 149. Oxford Univ Press, 2011.

[6] J.C. Maxwell. *A treatise on electricity and magnetism*, volume 1. Clarendon Press, 1873.

[7] S.I. Newton. *Philosophiae naturalis principia mathematica*, volume 1. Excudit Georgius Brookman; impensis TT et J. Tegg, 1833.

[8] J.D. Lawson. Some criteria for a power producing thermonuclear reactor. *Proceedings of the Physical Society. Section B*, 70:6, 1957.

[9] Liu Chen, R. B. White, and M. N. Rosenbluth. Excitation of internal kink modes by trapped energetic beam ions. *Phys. Rev. Lett.*, 52:1122–1125, Mar 1984.

[10] W. W. Heidbrink, Ralph Hay, and J. D. Strachan. Confinement of fusion reaction products during the fishbone instability. *Phys. Rev. Lett.*, 53:1905–1908, Nov 1984.

[11] B. Coppi and F. Porcelli. Theoretical model of fishbone oscillations in magnetically confined plasmas. *Phys. Rev. Lett.*, 57:2272–2275, Nov 1986.

[12] N. Winsor, J.L. Johnson, and J.M. Dawson. Geodesic acoustic waves in hydromagnetic systems. *Physics of Fluids*, 11:2448, 1968.

[13] GY Fu. Energetic-particle-induced geodesic acoustic mode. *Physical review letters*, 101(18):185002, 2008.

[14] R. Nazikian, GY Fu, ME Austin, HL Berk, RV Budny, NN Gorelenkov, WW Heidbrink, CT Holcomb, GJ Kramer, GR McKee, et al. Intense geodesic acousticlike modes driven by suprathermal ions in a tokamak plasma. *Physical review letters*, 101(18):185001, 2008.

[15] CJ Boswell, HL Berk, DN Borba, T. Johnson, SD Pinches, and SE Sharapov. Observation and explanation of the jet n= 0 chirping mode. *Physics Letters A*, 358(2):154–158, 2006.

[16] HL Berk, CJ Boswell, D. Borba, ACA Figueiredo, T. Johnson, MFF Nave, SD Pinches, and SE Sharapov. Explanation of the jet n= 0 chirping mode. *Nuclear fusion*, 46:S888, 2006.

[17] W. Horton. Drift waves and transport. *Reviews of Modern Physics*, 71(3):735–778, 1999.

[18] WE Drummond and D. Pines. Nucl. fusion suppl. 3, 1049 1962; aa vedenov, ep velikhov, and rz sagdeev. *Nucl. Fusion*, 1:82, 1961.

[19] AA Vedenov, EP Velikhov, and RZ Sagdeev. Nonlinear oscillations of rarified plasma. *Nuclear Fusion*, 1:82, 1961.

[20] Y.A. Romanov and GF Filippov. Interaction of fast electron beams with longitudinal plasma waves. *Zhur. Eksptl'. i Teoret. Fiz.*, 40, 1961.

[21] T.H. Stix. Heating of toroidal plasmas by neutral injection. *Plasma Physics*, 14:367, 1972.

[22] RJ Dumont. Variational approach to radiofrequency waves in magnetic fusion devices. *Nuclear Fusion*, 49:075033, 2009.

[23] CFF Karney. Fokker-planck and quasilinear codes. *Comput. Phys. Rep.*, 4(3-4):183, 1986.

[24] M. Brambilla. *Kinetic Theory of Plasma Waves: Homogeneous Plasmas*, volume 1. 1998.

[25] M. Brambilla. Quasi-linear ion distribution function during ion cyclotron heating in tokamaks. *Nuclear fusion*, 34:1121, 1994.

[26] A. Messiaen, M. Vervier, P. Dumortier, D. Grine, PU Lamalle, F. Durodié, R. Koch, F. Louche, and R. Weynants. Preparing iter icrf: development and analysis of the load resilient matching systems based on antenna mock-up measurements. *Nuclear Fusion*, 49:055004, 2009.

[27] R. Carruthers, PA Davenport, and JTD Mitchell. Economic generation of power from thermonuclear fusion. Technical report, United Kingdom Atomic Energy Authority, Abingdon (England). Culham Lab., 1967.

[28] N.J. Fisch. Theory of current drive in plasmas. *Reviews of Modern Physics*, 59(1):175, 1987.

[29] T. Ohkawa. New methods of driving plasma current in fusion devices. *Nuclear Fusion*, 10:185, 1970.

[30] DJH Wort. The peristaltic tokamak. *Plasma Physics*, 13:258, 1971.

[31] N.J. Fisch and C.F.F. Karney. Current generation with low-frequency waves. *Physics of Fluids*, 24:27, 1981.

[32] Nathaniel J. Fisch. Confining a tokamak plasma with rf-driven currents. *Phys. Rev. Lett.*, 41:873–876, Sep 1978.

[33] C.F.F. Karney and N.J. Fisch. Numerical studies of current generation by radio-frequency traveling waves. *Physics of Fluids*, 22:1817, 1979.

[34] S. Bernabei, C. Daughney, P. Efthimion, W. Hooke, J. Hosea, F. Jobes, A. Martin, E. Mazzucato, E. Meservey, R. Motley, J. Stevens, S. Von Goeler, and R. Wilson. Lower-hybrid current drive in the plt tokamak. *Phys. Rev. Lett.*, 49:1255–1258, Oct 1982.

[35] P.T. Bonoli and R.C. Englade. Simulation model for lower hybrid current drive. *Physics of Fluids*, 29:2937, 1986.

[36] G. Kuang, Y. Liu, J. Shan, W. Xu, X. Zhang, D. Liu, F. Liu, Y. Zhu, C. Zhang, G. Zheng, et al. Lower hybrid current drive experiments and improved performance on the ht-7 superconducting tokamak. *Nuclear Fusion*, 39:1769, 1999.

[37] N. J. Fisch and A. H. Boozer. Creating an asymmetric plasma resistivity with waves. *Phys. Rev. Lett.*, 45:720–722, Sep 1980.

[38] V. Krivenski, I. Fidone, G. Giruzzi, G. Granata, RL Meyer, and E. Mazzucato. Improving current generation in a tokamak by electron cyclotron waves. *Nuclear fusion*, 25:127, 1985.

[39] RW Harvey, MG McCoy, and GD Kerbel. Power dependence of electron-cyclotron current drive for low-and high-field absorption in tokamaks. *Physical review letters*, 62(4):426–429, 1989.

[40] K. Matsuda. Ray tracing study of the electron cyclotron current drive in diii-d using 60 ghz. *Plasma Science, IEEE Transactions on*, 17(1):6–11, 1989.

[41] V. Erckmann and U. Gasparino. Electron cyclotron resonance heating and current drive in toroidal fusion plasmas. *Plasma physics and controlled fusion*, 36:1869, 1994.

[42] CC Petty, RI Pinsker, ME Austin, FW Baity, SC Chiu, JS DeGrassie, CB Forest, RH Goulding, RW Harvey, DJ Hoffman, et al. Fast wave and electron cyclotron current drive in the diii-d tokamak. *Nuclear fusion*, 35:773, 1995.

[43] TC Luce, YR Lin-Liu, RW Harvey, G. Giruzzi, PA Politzer, BW Rice, JM Lohr, CC Petty, and R. Prater. Generation of localized noninductive current by electron cyclotron waves on the diii-d tokamak. *Physical review letters*, 83(22):4550–4553, 1999.

[44] Z. A. Pietrzyk, C. Angioni, R. Behn, S. Coda, T. P. Goodman, M. A. Henderson, F. Hofmann, and O. Sauter. Long-pulse improved central electron confinement in the tcv tokamak with electron cyclotron heating and current drive. *Phys. Rev. Lett.*, 86:1530–1533, Feb 2001.

[45] YR Lin-Liu, VS Chan, and R. Prater. Electron cyclotron current drive efficiency in general tokamak geometry. *Physics of Plasmas*, 10:4064, 2003.

[46] J. Lohr, YA Gorelov, K. Kajiwara, D. Ponce, RW Callis, JL Doane, RL Ellis, HJ Grunloh, CP Moeller, J. Peavy, et al. The electron cyclotron resonant heating system on the diii-d tokamak. *Fusion science and technology*, 48(2):1226–1237, 2005.

[47] NJ Fisch. Current generation by minority-species heating. *Nuclear Fusion*, 21:15, 1981.

[48] T. Hellsten, J. Carlsson, and L.-G. Eriksson. Minority ion cyclotron current drive in tokamaks. *Phys. Rev. Lett.*, 74:3612–3615, May 1995.

[49] GT Hoang, P. Monier-Garbet, T. Aniel, C. Bourdelle, RV Budny, F. Clairet, L.G. Eriksson, X. Garbet, C. Grisolia, P. Platz, et al. An h minority heating regime in tore supra showing improved l mode confinement. *Nuclear fusion*, 40:913, 2000.

[50] M. Laxåback and T. Hellsten. Modelling of minority ion cyclotron current drive during the activated phase of iter. *Nuclear fusion*, 45:1510, 2005.

[51] RW Harvey, KD Marx, and MG McCoy. Non-linear fokker-planck studies of rf current drive efficiency. *Nuclear Fusion*, 21:153, 1981.

[52] JG Cordey, T. Edlington, and DFH Start. A theory of currents induced by radio-frequency waves in toroidal plasmas. *Plasma Physics*, 24:73, 1982.

[53] SC Chiu, VS Chan, JY Hsu, GE Guest, R. Prater, and JM Rawls. Current driven by asymmetrical minority heating in icrf. *Nuclear Fusion*, 23:499, 1983.

[54] A. Becoulet. Heating and current drive regimes in the ion cyclotron range of frequency. *Plasma Physics and Controlled Fusion*, 38:A1, 1996.

[55] DA Ehst and CFF Karney. Approximate formula for radiofrequency current drive efficiency with magnetic trapping. *Nuclear fusion*, 31:1933, 1991.

[56] EF Jaeger, DB Batchelor, and DC Stallings. Influence of various physics phenomena on fast wave current drive in tokamaks. *Nuclear fusion*, 33:179, 1993.

[57] L. Chen, J. Vaclavik, and GW Hammett. Ion radial transport induced by icrf waves in tokamaks. *Nuclear fusion*, 28:389, 1988.

[58] K. Hallatschek and D. Biskamp. Transport control by coherent zonal flows in the core/edge transitional regime. *Physical Review Letters*, 86(7):1223–1226, 2001.

[59] M. Ramisch, U. Stroth, S. Niedner, and B. Scott. On the detection of reynolds stress as a driving and damping mechanism of geodesic acoustic modes and zonal flows. *New Journal of Physics*, 5:12, 2003.

[60] N. Miyato, Y. Kishimoto, and J. Li. Global structure of zonal flow and electromagnetic ion temperature gradient driven turbulence in tokamak plasmas. *Physics of plasmas*, 11:5557, 2004.

[61] Y. Nagashima, K. Hoshino, A. Ejiri, K. Shinohara, Y. Takase, K. Tsuzuki, K. Uehara, H. Kawashima, H. Ogawa, T. Ido, Y. Kusama, and Y. Miura. Observation of nonlinear coupling between small-poloidal wave-number potential fluctuations and turbulent potential fluctuations in ohmically heated plasmas in the jft-2m tokamak. *Phys. Rev. Lett.*, 95:095002, Aug 2005.

[62] K. Miki, Y. Kishimoto, N. Miyato, and JQ Li. Intermittent transport associated with the geodesic acoustic mode near the critical gradient regime. *Physical review letters*, 99(14):145003, 2007.

[63] M. Sasaki, K. Itoh, S.I. Itoh, and N. Kasuya. Zonal flows induced by symmetry breaking with existence of geodesic acoustic modes. *Nuclear Fusion*, 52:023009, 2012.

[64] GD Conway, C. Angioni, F. Ryter, P. Sauter, and J. Vicente. Mean and oscillating plasma flows and turbulence interactions across the lh confinement transition. *Physical Review Letters*, 106(6):65001, 2011.

[65] K. Itoh, K. Hallatschek, and SI Itoh. Excitation of geodesic acoustic mode in toroidal plasmas. *Plasma physics and controlled fusion*, 47:451, 2005.

[66] F. Zonca and L. Chen. Radial structures and nonlinear excitation of geodesic acoustic modes. *EPL (Europhysics Letters)*, 83:35001, 2008.

[67] F. Zonca, L. Chen, and Z. Qiu. Kinetic theory of geodesic acoustic modes: radial structures and nonlinear excitations. In *Proc. 22nd Int. Fusion Energy Conf. 2008 (Geneva, Switzerland, 2008)*, 2008.

[68] N. Chakrabarti, R. Singh, PK Kaw, and PN Guzdar. Nonlinear excitation of geodesic acoustic modes by drift waves. *Physics of plasmas*, 14:052308, 2007.

[69] PN Guzdar, N. Chakrabarti, R. Singh, and PK Kaw. Excitation of geodesic acoustic modes by ion temperature gradient modes. *Plasma Physics and Controlled Fusion*, 50:025006, 2008.

[70] K. Hallatschek. Diamagnetic gam drive mechanism. 2009.

[71] K. Hallatschek and G.R. McKee. Theory of external geodesic acoustic mode excitation. *Bulletin of the American Physical Society*, 56, 2011.

[72] Robert Hager and Klaus Hallatschek. Nonlinear dispersion relation of geodesic acoustic modes. *Phys. Rev. Lett.*, 108:035004, Jan 2012.

[73] GD Conway. Amplitude behaviour of geodesic acoustic modes in the asdex upgrade tokamak. *Plasma Physics and Controlled Fusion*, 50:085005, 2008.

[74] HL Berk and T. Zhou. Fast excitation of egam by nbi. *Nuclear Fusion*, 50:035007, 2010.

[75] Z. Qiu, F. Zonca, and L. Chen. Nonlocal theory of energetic-particle-induced geodesic acoustic mode. *Plasma Physics and Controlled Fusion*, 52:095003, 2010.

[76] JH Malmberg and CB Wharton. Collisionless damping of electrostatic plasma waves. *Physical Review Letters*, 13(6):184–186, 1964.

[77] N.G. Van Kampen. On the theory of stationary waves in plasmas. *Physica*, 21(6-10):949–963, 1955.

[78] J. H. Malmberg, C. B. Wharton, R. W. Gould, and T. M. O'Neil. Plasma wave echo experiment. *Phys. Rev. Lett.*, 20:95–97, Jan 1968.

[79] B.D. Fried and S.D. Conte. The plasma dispersion function. *The Plasma Dispersion Function, New York: Academic Press, 1961*, 1, 1961.

[80] T. Watari, Y. Hamada, T. Notake, N. Takeuchi, and K. Itoh. Geodesic acoustic mode oscillation in the low frequency range. *Physics of plasmas*, 13:062504, 2006.

[81] T. Watari, Y. Hamada, A. Fujisawa, K. Toi, and K. Itoh. Extension of geodesic acoustic mode theory to helical systems. *Physics of plasmas*, 12:062304, 2005.

[82] WW Heidbrink, EJ Strait, MS Chu, and AD Turnbull. Observation of beta-induced alfvén eigenmodes in the diii-d tokamak. *Physical review letters*, 71(6):855–858, 1993.

[83] R. Sabot, F. Clairet, GD Conway, L. Cupido, X. Garbet, G. Falchetto, T. Gerbaud, S. Hacquin, P. Hennequin, S. Heuraux, et al. Recent results on turbulence and mhd activity achieved by reflectometry. *Plasma Physics and Controlled Fusion*, 48:B421, 2006.

[84] VS Udintsev, M. Goniche, G. Giruzzi, GTA Huysmans, F. Imbeaux, P. Maget, X. Garbet, R. Sabot, JL Ségui, F. Turco, et al. Studies of high frequency hot ion instabilities by means of correlation ece on tore supra. *Plasma physics and controlled fusion*, 48:L33, 2006.

[85] C. Nguyen, X. Garbet, R. Sabot, LG Eriksson, M. Goniche, P. Maget, V. Basiuk, J. Decker, D. Elbeze, GTA Huysmans, et al. Excitation of beta alfvén eigenmodes in tore-supra. *Plasma Physics and Controlled Fusion*, 51:095002, 2009.

[86] T. Dannert, S. Günter, T. Hauff, F. Jenko, X. Lapillonne, and P. Lauber. Turbulent transport of beam ions. *Physics of Plasmas*, 15:062508, 2008.

[87] J. Abiteboul, X. Garbet, V. Grandgirard, SJ Allfrey, P. Ghendrih, G. Latu, Y. Sarazin, and A. Strugarek. Conservation equations and calculation of mean flows in gyrokinetics. *Physics of Plasmas*, 18:082503, 2011.

[88] V. Grandgirard, Y. Sarazin, X. Garbet, G. Dif-Pradalier, P. Ghendrih, N. Crouseilles, G. Latu, E. Sonnendrücker, N. Besse, and P. Bertrand. Computing itg turbulence with a full-f semi-lagrangian code. *Communications in Nonlinear Science and Numerical Simulation*, 13(1):81–87, 2008.

[89] AJ Brizard and TS Hahm. Foundations of nonlinear gyrokinetic theory. *Reviews of modern physics*, 79(2):421, 2007.

[90] MN Rosenbluth and FL Hinton. Poloidal flow driven by ion-temperature-gradient turbulence in tokamaks. *Physical review letters*, 80(4):724–727, 1998.

[91] H. Sugama and TH Watanabe. Collisionless damping of geodesic acoustic modes. *Journal of plasma physics*, 72(6):825–828, 2006.

[92] Y. Sarazin, V. Grandgirard, G. Dif-Pradalier, E. Fleurence, X. Garbet, P. Ghendrih, P. Bertrand, N. Besse, N. Crouseilles, E. Sonnendrücker, et al. Impact of large scale flows on turbulent transport. *Plasma physics and controlled fusion*, 48:B179, 2006.

[93] Z. Qiu and L. Chen. Kinetic theories of geodesic acoustic modes: Radial structure, linear excitation by energetic particles and nonlinear saturation. *Plasma Science and Technology*, 13:257, 2011.

[94] T. O'Neil. Collisionless damping of nonlinear plasma oscillations. *Physics of Fluids*, 8:2255, 1965.

[95] HL Berk, BN Breizman, and H. Ye. Scenarios for the nonlinear evolution of alpha-particle-induced alfvén wave instability. *Physical review letters*, 68(24):3563–3566, 1992.

[96] C. Nguyen. Magneto-hydrodynamic activity and energetic particles-application to beta alfven eigenmodes. *Arxiv preprint arXiv:0912.2613*, 2009.

[97] C. Nguyen, H. Lütjens, X. Garbet, V. Grandgirard, and M. Lesur. Existence of metastable kinetic modes. *Physical review letters*, 105(20):205002, 2010.

[98] PH Diamond, SI Itoh, K. Itoh, and TS Hahm. Zonal flows in plasmas - a review. *Plasma Physics and Controlled Fusion*, 47:R35, 2005.

[99] H. Biglari, PH Diamond, and PW Terry. Influence of sheared poloidal rotation on edge turbulence. *Physics of Fluids B: Plasma Physics*, 2:1, 1990.

[100] A. Hasegawa, C.G. Maclennan, and Y. Kodama. Nonlinear behavior and turbulence spectra of drift waves and rossby waves. *Physics of Fluids*, 22:2122, 1979.

[101] TS Hahm and KH Burrell. Flow shear induced fluctuation suppression in finite aspect ratio shaped tokamak plasma. *Physics of Plasmas*, 2:1648, 1995.

[102] G. I. Taylor. Eddy motion in the atmosphere. *Philosophical Transactions of the Royal Society of London, Series A*, 215:1–26, 1915.

[103] L. Chen, Z. Lin, and R. White. Excitation of zonal flow by drift waves in toroidal plasmas. *Physics of Plasmas*, 7:3129, 2000.

[104] PH Diamond, S. Champeaux, M. Malkov, A. Das, I. Gruzinov, MN Rosenbluth, C. Holland, B. Wecht, AI Smolyakov, FL Hinton, et al. Secondary instability in drift wave turbulence as a mechanism for zonal flow and avalanche formation. *Nuclear fusion*, 41:1067, 2001.

[105] MA Malkov, PH Diamond, and A. Smolyakov. On the stability of drift wave spectra with respect to zonal flow excitation. *Physics of Plasmas*, 8:1553, 2001.

[106] FL Hinton and MN Rosenbluth. Dynamics of axisymmetric and poloidal flows in tokamaks. *Plasma physics and controlled fusion*, 41:A653, 1999.

[107] Z. Lin, TS Hahm, WW Lee, WM Tang, and PH Diamond. Effects of collisional zonal flow damping on turbulent transport. *Physical review letters*, 83(18):3645–3648, 1999.

[108] G. Dif-Pradalier, V. Grandgirard, Y. Sarazin, X. Garbet, and Ph. Ghendrih. Interplay between gyrokinetic turbulence, flows, and collisions: Perspectives on transport and poloidal rotation. *Phys. Rev. Lett.*, 103:065002, Aug 2009.

[109] TS Hahm, MA Beer, Z. Lin, GW Hammett, WW Lee, and WM Tang. Shearing rate of time-dependent e$\times$ b flow. *Physics of Plasmas*, 6:922, 1999.

[110] RE Waltz and C. Holland. Numerical experiments on the drift wave–zonal flow paradigm for nonlinear saturation. *Physics of Plasmas*, 15:122503, 2008.

[111] M. Jakubowski, R. J. Fonck, and G. R. McKee. Observation of coherent sheared turbulence flows in the diii-d tokamak. *Phys. Rev. Lett.*, 89:265003, Dec 2002.

[112] YZ Zhang, T. Xie, and SM Mahajan. Analysis on the exclusiveness of turbulence suppression between static and time-varying shear flow. *Physics of Plasmas*, 19(2):020701–020701, 2012.

[113] G.R. McKee, R.J. Fonck, M. Jakubowski, K.H. Burrell, K. Hallatschek, R.A. Moyer, D.L. Rudakov, W. Nevins, G.D. Porter, P. Schoch, et al. Experimental characterization of coherent, radially-sheared zonal flows in the diii-d tokamak. *Physics of Plasmas*, 10:1712, 2003.

[114] T. Ido, Y. Miura, K. Hoshino, K. Kamiya, Y. Hamada, A. Nishizawa, Y. Kawasumi, H. Ogawa, Y. Nagashima, K. Shinohara, et al. Observation of the interaction between the geodesic acoustic mode and ambient fluctuation in the jft-2m tokamak. *Nuclear fusion*, 46:512, 2006.

[115] AD Liu, T. Lan, CX Yu, HL Zhao, LW Yan, WY Hong, JQ Dong, KJ Zhao, J. Qian, J. Cheng, et al. Characterizations of low-frequency zonal flow in the edge plasma of the hl-2a tokamak. *Physical review letters*, 103(9):095002, 2009.

[116] G. Dif-Pradalier, V. Grandgirard, Y. Sarazin, X. Garbet, P. Ghendrih, and P. Angelino. On the influence of initial state on gyrokinetic simulations. *Physics of Plasmas*, 15:042315, 2008.

[117] X. Garbet, Y. Sarazin, P. Beyer, P. Ghendrih, RE Waltz, M. Ottaviani, and S. Benkadda. Flux driven turbulence in tokamaks. *Nuclear Fusion*, 39:2063, 1999.

[118] G. Darmet, P. Ghendrih, Y. Sarazin, X. Garbet, and V. Grandgirard. Intermittency in flux driven kinetic simulations of trapped ion turbulence. *Communications in Nonlinear Science and Numerical Simulation*, 13(1):53–58, 2008.

[119] V. Grandgirard, Y. Sarazin, P. Angelino, A. Bottino, N. Crouseilles, G. Darmet, G. Dif-Pradalier, X. Garbet, P. Ghendrih, S. Jolliet, et al. Global full-f gyrokinetic simulations of plasma turbulence. *Plasma Physics and Controlled Fusion*, 49:B173, 2007.

[120] Y. Sarazin, V. Grandgirard, J. Abiteboul, S. Allfrey, X. Garbet, P. Ghendrih, G. Latu, A. Strugarek, and G. Dif-Pradalier. Large scale dynamics in flux driven gyrokinetic turbulence. *Nuclear Fusion*, 50:054004, 2010.

[121] Y. Sarazin, V. Grandgirard, J. Abiteboul, S. Allfrey, X. Garbet, P. Ghendrih, G. Latu, A. Strugarek, G. Dif-Pradalier, PH Diamond, et al. Predictions on heat transport and plasma rotation from global gyrokinetic simulations. *Nuclear Fusion*, 51:103023, 2011.

[122] M. Taguchi. Generation of poloidal electric field by anisotropic heating. *Journal of the Physics Society Japan*, 62(10):3486–3491, 1993.

[123] M Lesur. Nonlinear categorization of the energetic-beam driven instability with drag and diffusion. *Nuclear Fusion*, to be published, 2012.

[124] HL Berk and BN Breizman. Saturation of a single mode driven by an energetic injected beam. i. plasma wave problem. *Physics of Fluids B Plasma Physics*, 2(9):2226, 1990.

[125] HL Berk and BN Breizman. Saturation of a single mode driven by an energetic injected beam. ii. electrostatic universal destabilization mechanism. *Physics of Fluids B Plasma Physics*, 2(9):2235, 1990.

[126] HL Berk and BN Breizman. Saturation of a single mode driven by an energetic injected beam. iii. alfvén wave problem. *Physics of Fluids B Plasma Physics*, 2(9):2246, 1990.

[127] D Edery, X Garbet, J P Roubin, and A Samain. Variational formalism for kinetic-mhd instabilities in tokamaks. *Plasma Physics and Controlled Fusion*, 34(6):1089, 1992.

[128] F. Zonca, P. Buratti, A. Cardinali, L. Chen, J.-Q. Dong, Y.-X. Long, A.V. Milovanov, F. Romanelli, P. Smeulders, L. Wang, Z.-T. Wang, C. Castaldo, R. Cesario, E. Giovannozzi, M. Marinucci, and V. Pericoli Ridolfini. Electron fishbones: theory and experimental evidence. *Nuclear Fusion*, 47(11):1588, 2007.

[129] X. Garbet, L. Laurent, A. Samain, and J. Chinardet. Radial propagation of turbulence in tokamaks. *Nuclear fusion*, 34:963, 1994.

[130] Z. Lin and TS Hahm. Turbulence spreading and transport scaling in global gyrokinetic particle simulations. *Physics of Plasmas*, 11:1099, 2004.

[131] T.S. Hahm, PH Diamond, Z. Lin, K. Itoh, and SI Itoh. Turbulence spreading into the linearly stable zone and transport scaling. *Plasma physics and controlled fusion*, 46:A323, 2004.

[132] Liu Chen, Roscoe B. White, and F. Zonca. Zonal-flow dynamics and size scaling of anomalous transport. *Phys. Rev. Lett.*, 92:075004, Feb 2004.

[133] RE Waltz and J. Candy. Heuristic theory of nonlocally broken gyro-bohm scaling. *Physics of plasmas*, 12:072303, 2005.

[134] Ö.D. Gürcan, PH Diamond, TS Hahm, and Z. Lin. Dynamics of turbulence spreading in magnetically confined plasmas. *Physics of plasmas*, 12:032303, 2005.

[135] ÖD Gürcan, PH Diamond, and TS Hahm. Nonlinear triad interactions and the mechanism of spreading in drift-wave turbulence. *Physical review letters*, 97(2):24502, 2006.

[136] P.H. Diamond and TS Hahm. On the dynamics of turbulent transport near marginal stability. *Physics of Plasmas*, 2:3640, 1995.

[137] BA Carreras, D. Newman, VE Lynch, and PH Diamond. A model realization of self-organized criticality for plasma confinement. *Physics of Plasmas*, 3:2903, 1996.

[138] X. Garbet and R.E. Waltz. Heat flux driven ion turbulence. *Physics of Plasmas*, 5:2836, 1998.

[139] Y. Sarazin and P. Ghendrih. Intermittent particle transport in two-dimensional edge turbulence. *Physics of Plasmas*, 5:4214, 1998.

[140] P. Beyer, Y. Sarazin, X. Garbet, P. Ghendrih, and S. Benkadda. 2d and 3d boundary turbulence studies. *Plasma physics and controlled fusion*, 41:A757, 1999.

[141] P. Beyer, S. Benkadda, X. Garbet, and PH Diamond. Nondiffusive transport in tokamaks: Three-dimensional structure of bursts and the role of zonal flows. *Physical Review Letters*, 85(23):4892–4895, 2000.

[142] Y. Sarazin, X. Garbet, P. Ghendrih, and S. Benkadda. Transport due to front propagation in tokamaks. *Physics of Plasmas*, 7:1085, 2000.

[143] P. A. Politzer. Observation of avalanchelike phenomena in a magnetically confined plasma. *Phys. Rev. Lett.*, 84:1192–1195, Feb 2000.

[144] J. Candy and RE Waltz. Anomalous transport scaling in the diii-d tokamak matched by supercomputer simulation. *Physical review letters*, 91(4):45001, 2003.

[145] X. Garbet, Y. Sarazin, F. Imbeaux, P. Ghendrih, C. Bourdelle, Ö.D. Gürcan, and PH Diamond. Front propagation and critical gradient transport models. *Physics of Plasmas*, 14(12):122305–122305, 2007.

[146] F. Jenko, W. Dorland, M. Kotschenreuther, and BN Rogers. Electron temperature gradient driven turbulence. *Physics of Plasmas*, 7:1904, 2000.

[147] J. F. Drake, P. N. Guzdar, and A. B. Hassam. Streamer formation in plasma with a temperature gradient. *Phys. Rev. Lett.*, 61:2205–2208, Nov 1988.

[148] P Hill, S Saarelma, B McMillan, A Peeters, and E Verwichte. Perpendicular wavenumber dependence of the linear stability of global ion temperature gradient modes on exb flows. *Plasma Physics and Controlled Fusion*, 54(6):065011, 2012.

[149] A. Einstein, B. Podolsky, and N. Rosen. Can quantum-mechanical description of physical reality be considered complete? *Physical review*, 47(10):777, 1935.

[150] GY Fu. On nonlinear self-interaction of geodesic acoustic mode driven by energetic particles. *Journal of Plasma Physics*, 77(4):457, 2011.

[151] M. Taguchi. Neoclassical transport theory for tokamak plasma with anisotropic temperature in the banana regime. *Journal of the Physics Society Japan*, 67(3):863–869, 1998.

[152] M. Taguchi. Effects of temperature anisotropy on neoclassical transport in the plateau and banana-plateau regimes. *Journal of the Physics Society Japan*, 68(1):97–103, 1999.

[153] Y. Sarazin. *Transport et turbulence dans les plasmas magnétisés*.

[154] Y. Sarazin. Interactions multi-échelles en turbulence des plasmas de fusion. *Habilitation dissertation, University of Provence (Aix-Marseille I), France*, 2008.

[155] J.L. Basdevant and C. Kopper. *Principes variationnels et Mécanique analytique*.

[156] X. Garbet. Instabilités, turbulence et transport dans un plasma magnétisé. *Habilitation dissertation, University of Marseille, France*, 2001.

[157] R.G. Littlejohn. Variational principles of guiding center motion. *Journal of Plasma Physics*, 29(1), 1983.

[158] X. Garbet, G. Dif-Pradalier, C. Nguyen, Y. Sarazin, V. Grandgirard, and P. Ghendrih. Neoclassical equilibrium in gyrokinetic simulations. *Physics of Plasmas*, 16:062503, 2009.